Structural and chemical effects of charge transfer across metal organic interfaces

Thesis for Degree of Doctor of Philosophy

Department of Condensed Matter Physics

of the Universidad Autónoma de Madrid

Christian Urban

Madrid, December 2011

This thesis has been co-directed by Dr. Roberto Otero Martín and Dr. José María Gallego Vázquez in the Surface Science group at the Universidad Autónoma de Madrid.

The cover picture is an artistic interpretation of one of the consequences that charge transfer may have: The assembly mechanism of TCNQ on Cu(100) and the intermolecular interaction is mediated by the surface, which is distorted due to the strong bonds to the adsorbate as a result of charge transfer.

Abstract

In the present dissertation charge transfer at the interface between organic acceptors and a metal Cu(100)-single crystal surface is identified as one of the main factors in determining the molecular adsorption geometry, the possible surface reconstruction upon adsorption, the molecular ordering upon self assembly and the nature of the chemical reaction that the molecules can undergo when adsorbed on a metal surface. Four molecule-substrate systems are investigated with experimental techniques like STM, XPS, XAS and work function measurements, the findings are presented together with theoretical support. The results of this thesis evidence the inadequacy of the gas-phase picture in which the only role of the surface is supporting the adsorbates, while their interactions and geometries are those of the gas-phase.In particular, our experiments show that charge transfer at organic-metal interfaces, which is expected at many technologically relevant situations, affects in a very decisive way the morphology of the interface and must be taken into consideration in the atomic-scale engineering of such interfaces.

Resumen

En esta tesis se identifica la transferencia de carga en la intercara entre moléculas aceptoras y la superficie de Cu(100) como uno de los factores determinantes para la geometría de adsorción, la reconstrucción de la superficie metálica en presencia de adsorbatos, el orden molecular que surja del proceso de auto ensamblaje, y la naturaleza de las reacciones químicas que pueden sufrir las moléculas adsorbidas sobre superficies metálicas. Cuatro sistemas aceptor/Cu(100) han sido investigados con técnicas experimentales como STM, XPS, XAS y medidas de la función de trabajo. Los resultados son presentados con apoyo teórico. Los resultados de esta tesis demuestran la invalidez del enfoque en el cual el único papel de la superficie es de soporte de las moléculas que se comportarían como si estuvieran en fas gas. En particular, nuestros experimentos demuestran que la transferencia de carga en la intercara metal-orgánica, importante en muchas situaciones de interés tecnológico, determina de manera decisiva su morfología, y debe ser tenida en cuenta a la hora de diseñar estas intercaras a nivel atómico.

Acknowledgements

A scientific work, like this thesis, consists of contributions of many different people and I would like to thank them for their help and support during the experiments and the writing of this manuscript. I am aware that without them, elaborating this thesis would have been impossible.

First of all, I would like to thank my direct supervisors, Dr. Roberto Otero and Dr. Jose Maria Gallego for their support in every kind of imaginable direction. Their scientific knowledge and their explanations guided me through all the very different and difficult phases of this thesis letting me at the same time the freedom to develop my capabilities and knowledge. Their personal support und their trust gave me the motivation and the power to master all challenges on the way to the PhD and also in hard times they did not lose their faith in me.

I also acknowledge Prof. Rodolfo Miranda, the head of the laboratory, who gave me the opportunity to work with the best people and the newest material during my thesis with the freedom to concentrate on science without worrying about the financial aspects. He helped me, too, with his huge background in physics and bringing together the right people to solve all arising problems.

This brings me to thank as well the collaborators for their specialist knowledge in theory and chemistry and also their great practical part in the present work, especially the group of Prof. Nazario Martín and the group of Prof. Fernando Martín.

My thanks also go to all the colleagues of the whole laboratory, especially to David É. who introduced me into many secrets of the former experimental system and Jonathan, who was always there to help me whenever I needing him, and also to Marta, as well as to all persons who visited the laboratory, Juan-Carlos, Graziano, Anaís, Michi, Maria, Katrin and Andrey, for a helping hand and an interesting and positive atmosphere.

The technical support for the experimental system was fundamental, also apart from the usual working hours, and therefore I acknowledge especially the help of all technicians, Santiago, Andres, Rosa and Juan.

Thanks to Elsa, the whole administration of the department in one person, I made it through all the complex paperwork, thank you.

Apart from the colleagues, there are also a lot of persons outside the university who deserve my acknowledgements, like many friends, Javi, Guille, Michele, July, Nelson, Bea, Caro, David S., Lorena, Marcos, Lara, Arturo, David P. and all my flatmates, who all together were a kind of a chosen family in this foreign country and they supported me in my hardest times in several ways and with a lot of patience. Without them forming part of my private life I wouldn’t have been able to elaborate this thesis.

Contents

1 Introduction and motivation

1.1 Background and motivation

Discovery and creation of new materials is surely one of the most important factors in the progress of technology and development of inventions in human history. One example are the piezoelectric ceramics which made possible the invention of the scanning tunneling microscope (STM)[1] one of the main experimental techniques of our surface science group. Piezoelectric ceramics are used to position the STM-tip with atomic precision at distances of Ångstroms close to the object of interest. Without this material the STM invention, awarded with the Nobel Prize in 1986[2], would not have been possible. Another example is related to the Giant Magnetoresistance effect in sandwich structures of ferromagnetic layers separated by non magnetic spacers. They exhibited such a sensibility to magnetic fields that enormous data densities could be achieved on hard discs drives. This discovery received the Nobel Prize in Physics 2007[3].

Organic chemistry is in general defined as the chemistry of carbon and its compounds. Carbon can form up to four bonds to other elements or other carbon atoms with three different types of bonds (covalent single, double and triple bonds); this leads to aliphatic, alicyclic, aromatic, and heterocyclic compounds. Moreover the covalent C-C-bond is so strong that on one hand carbon chains with up to thousands of atoms are possible, and on the other hand many functional groups (-Br, -OH, -CN) can be attached to a carbon skeleton without altering the basic structure. Due to this bond strength, the high number of possible bonds, and the bond type flexibility, the number of organic compounds is infinite (only the number of the isomers of a $C_{30}H_{62}$-alkane chain is $4.11 \cdot 10^{9}$)[4].This makes organic chemistry a research field with an enormous potential with respect to the discovery of materials with new interesting properties. Some important areas of synthetic organic chemistry are explosives, plastics, drugs, dyes, synthetic fabrics, building materials, insecticides, food, petrochemicals and many others[4].

The promising properties of organic materials has motivated the investigation of new compounds and the improvement of existing ones. Organic compounds were found in the middle of the last century which showed high conductivity and semiconductor properties (in 1954: perylene-iodine complex[4, 6] and the first charge transfer salt in 1973: TTF-TCNQ[7, 8]), which before was known only metals. What started as a playground for scientists, turned into the current huge research area of organic electronics, including important applications like OLEDs, solar cells and field effect transistors. The original scientific motivation was reinforced due to its fast success and immense impact on the technological market. New applications in such different fields like heterogeneous catalysis, coatings, with materials exhibiting switchable properties, sensors, organic based batteries and plastic electronics with molecular components were and are in the focus of research. Some advantages of organic materials over others are the possibility of large-area electronic production, biodegradability or environmental friendliness, the simple processability, their light weight, the physical flexibility, the easy accessibility of the required materials (no rare metals and minerals are necessary), the rather low temperatures and purity demand on the production stage, the low price and the low production costs and the virtually unlimited room for further material modification

and improvement. A concrete example in organic electronics is the first anthracene-based OLED device in 1965[9]; organic solar cells and field effect transistor followed shortly after. These examples will be explained in the following.

1.2 Applications

1.2.1 Organic light emitting diode (OLED)

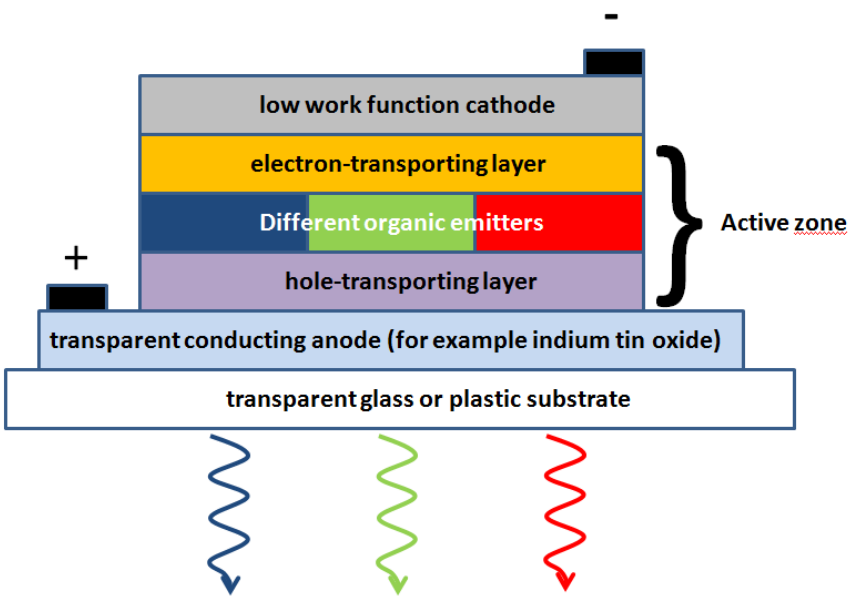

Figure 1: General scheme of an organic light emitting diode: At the interface of the active layer with the electron- or the hole-transport media the charge carriers which recombine radiatively under emission of the desired wavelength. The whole active layer can be one material or in the case of highly sophisticated OLEDs a grade of three different materials combined. For the electron injection a cathode with a low work function is desirable and the anode in this emission geometry must be transparent and conducting.

The general working scheme of an OLED consists of an active layer sandwiched between two electrodes where a voltage is applied, which leads to an injection of electrons on the cathode side and injection of holes on the anode side. Both types of charge meet and recombine, emitting light, in the active zone which can consist of only one material, of several films or even of a graded composition of different materials (described in the following). This general scheme is applicable to all working OLEDs. Therefore the understanding of the active layer including the different interfaces is crucial in order to control and improve the transport and injection of the different charge carriers (Fig. 1).

The first reported successful experiments to generate light from an organic material were done in 1965 with a 5 mm thick anthracene crystal between two electrodes and a bias voltage between 100 V and 1000 V[9] (as a consequence of the high internal resistance to charge migration in the organic solid). Electrons and holes were injected from the respective electrodes into the organic material and recombined after migration to an area, the active zone, near the hole-injecting electrode. This zone reached approximately 2 mm into the crystal from where blue light was emitted. After ultrathin film growth technology was available, which allowed the growth of pin-hole-free layers with a reduced thickness, the structures became

more sophisticated. The first report about a practical OLED is dated in 1987[10]. The device had a double-layer structure of organic thin films, which were prepared by vapor deposition. The injection of electrons was achieved by an alloyed Mg:Ag cathode and the holes were provided through an indium-tin-oixide anode. In the interface region electrons recombined radiatively with the holes with electroluminescent emission of green light. A quantum efficiency of 1 % photon/electron, a luminous efficiency of 1.5 lm/W, a brightness > 1000 cd/m^2 and a driving voltage below 10 V were reported. One example of the state of the art of an OLED in 2010 is a combination of hole-, electron-transporting materials and the green phosphorescent emitter *fac*-tris(2-phenylpyridine) iridium (III) into a single, graded composition emissive layer of 100 nm thickness[11]. The composition is continuously graded to realize nearly 100 % hole transport material at the anode and nearly 100 % electron transport material at the cathode. Peak external quantum and power efficiencies of η_{EQE} = (19.3 ± 0.4) % and η_P = (66.5 ± 1.3) lm/W are realized at a luminance level of 600 cd/m^2. These results depend strongly on the morphology, which thus has to be controlled precisely.

Although the active medium structure has grown increasingly sophisticated and improved strongly, room to optimize OLED devices still remains, concerning, for example, the charge carrier creation, the injection efficiency, the charge mobility and the efficiency of the radiative recombination. All this calls for more detailed studies of the physics of organic materials especially at the involved interfaces and about the control over the growth and thus the morphology at the nanoscale, two topics which are in the focus of our research.

1.2.2 Organic photovoltaic cell (OPVC)

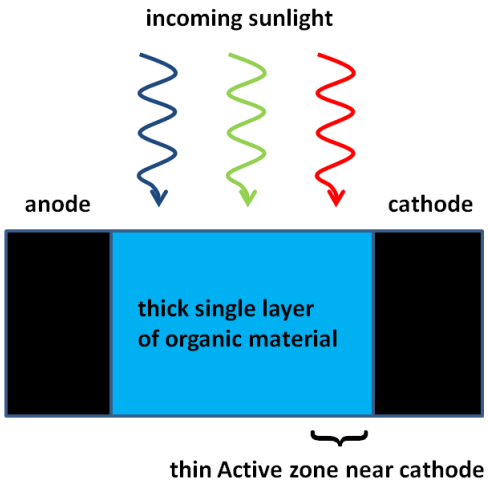

Figure 2: Schematic model of a single layer organic solar cell: The light comes from above and excites tightly bound electrons-hole pairs known as excitons, which diffuse up to 100 nm before they recombine. This is why only the excitons created close to the cathode can be separated due to the intrinsic electric field created by the work function difference the cathode and the anode.

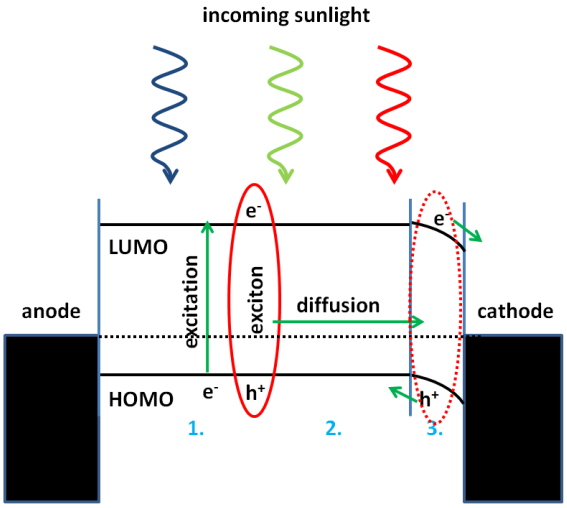

Figure 3: Band scheme of a p-type single layer organic solar cell: The incoming light transfers its energy to en electron which is excited from the HOMO to the LUMO. An exciton (1.) which diffuses (2.) and can be separated due to the band bending close to the cathode (3.). There the electrons are collected and the holes diffuse back to the anode.

Solar energy seems to have the potential to solve several current and urgent problems of global magnitude. This technology may provide humanity with a renewable cheap energy source consisting of environmentally friendly material in times of a threatening energy crisis due to the decreasing fossil resources and nuclear power plant accidents with disastrous consequences. Moreover global warming caused by greenhouse gases like CO_2, a consequence of modern energy production, is a thread for life and the need for solutions is a big motivation for detailed studies for improvements. Organic compounds exhibit different physical properties than inorganic materials and depending on the field of application offer advantages, like flexibility and low production cost, over other solar technologies.

In 1958 a single component organic photovoltaic cell (Fig. 2) was used to create a photocurrent through an active layer of Mg-phthalocyanines, which is a p-type semiconductor[12]. Photons of different wavelengths excite electrons which are then still bound coulombically to the created hole. These pseudo-particles are called excitons and move randomly jumping from molecule to molecule. Their mean free path before the electron recombines with the hole is between 10 and 100 nm[13-15] and before that happens they have to be separated and then the free charges can be driven to the electrodes. This last step is achieved by the different work functions of the anode and cathode, which leads, in the picture of the Fermi level alignment, to a band bending near the cathode and thus to a zone of charge depletion (Fig. 3). This is the dissociation area for the arriving excitons where the coulombic interaction is overcome by the electric field. Once the charges are separated the holes move back through the active zone to the anode while the electrons arrive at the cathode[16]. In order to create an intrinsic electrical field through band bending the anode is made typically of indium tin oxide, that has a high work function, while the cathode consists of materials which have low work functions (Al, Mg, Ca). The functioning of such a device is based on only a very thin part of the whole organic crystal. Excitons created further away from the dissociation area than their mean free path cannot be separated before they recombine and do not contribute to the photocurrent.

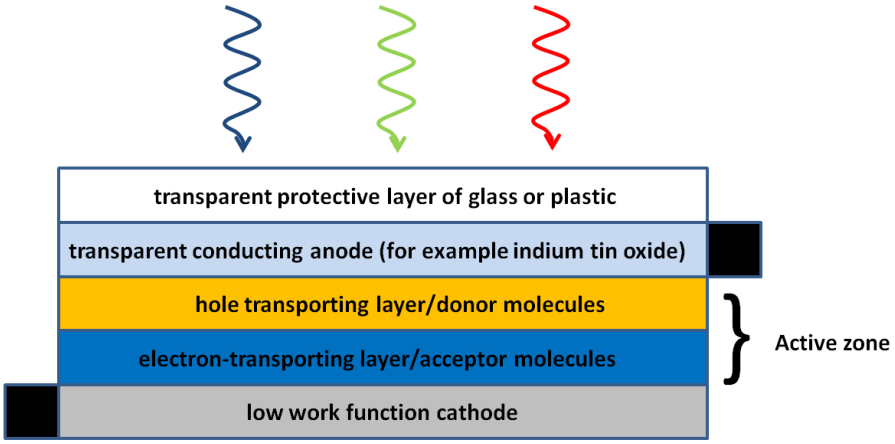

Figure 4: Sunlight comes from above and passes first the protective layer of glass or plastic then the conductive layer which is connected to the cathode, and then it excites electrons in the active bilayer of electron-donor and electron-acceptor molecular layers. The formed excitons are separated at the interface of both organic materials. Electrons are transported to the anode and holes to the cathode.

An OPVC with an active zone consisting of two films of donor- and acceptor molecules overcomes that geometric restriction and improves as well charge separation[17] (Fig. 4). The separation of a strongly bound exciton can take place at the interface between the two organic materials if the following condition is verified: $I_d - A_a < U_c$ (I_d is the ionization potential of the photo excited donor state, A_a is the electron affinity of the acceptor material and U_c is the effective coulomb interaction of the excitons)[18]. When the excitons reach the interface between the donor and acceptor molecules, the electrons jump from the LUMO of the donor material to the energetically lower lying LUMO of the acceptor molecules and are transported to the anode, which usually has a low work function, while the holes move to the cathode which has a high work function (Fig. 5). At the interface, the charge transfer rate is several orders of magnitude faster than competing recombination rate[19]. In such a double film structure the loss mechanisms depend therefore only on the defect concentration. At an impurity, for example, an electron can de-excite and loses its energy. In a heterojuntion OPVC the charge carrier generation is therefore independent of the intrinsic field and the photocurrent is proportional to the light intensity[15, 17, 20]. Moreover the fill factor, which is the ratio of the maximum experimental power and the theoretical power limit, is larger than in single layer devices[21].

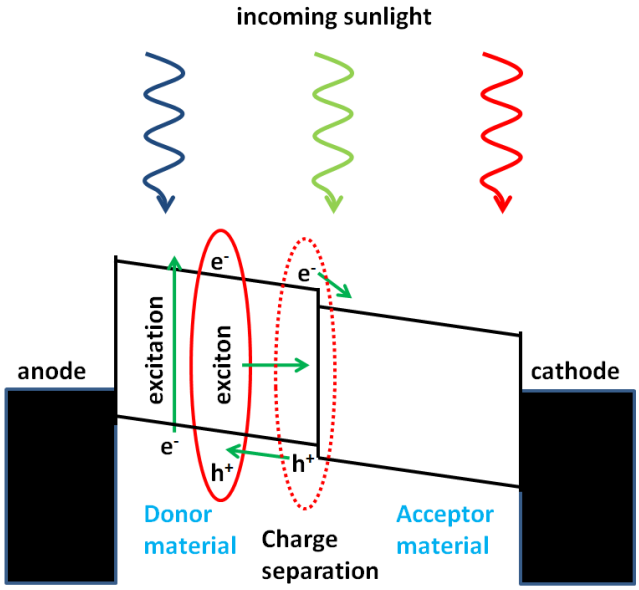

Figure 5: Band scheme of a double film photovoltaic device without band bending: The sunlight creates again excitons which only have to diffuse to the interface between organic donor and acceptor material to be separated. There the coulombian bond is broken and the charges are separated. The electrons diffuse to the cathode and the holes are collected at the anode.

A further improvement is achieved in the bulk or dispersed heterojuntion device, which is still based on the dissociation zone between donor and acceptor molecules. Here the two organic materials are physically mixed to maximize the interface area between both, in such a way that the active zone is dispersed over the whole bulk volume (Fig. 6 a)[22]. As a consequence excitons reach the active zone after a shorter diffusion in the average than in the double film device. This renders the bulk OPVC more effective due to a higher percentage of excitons which can be dissociated and thus contribute to the photocurrent. Two interpenetrating materials are necessary to conduct the free charges to the respective electrodes. Therefore the nanoscale morphology of OPVC is as important to be controlled precisely as in the OLED devices.

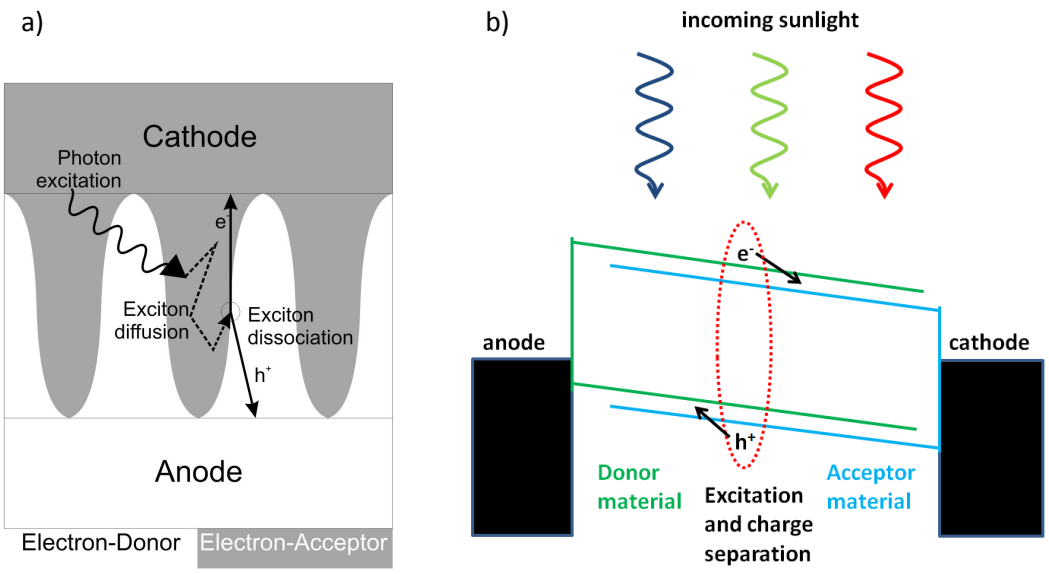

Figure 6: Model of a photovoltaic device consisting of a blend of donor and acceptor molecules **a)** with the band scheme without considering band bending **b)**: The sunlight creates excitons which after a very short diffusion path are separated at the interface between intermixed organic donor and acceptor materials.

Summarizing, the functioning of OPVC depends on the photon absorption, on the energy levels at the donor-acceptor-interfaces where the excitons dissociates, on the transport properties for the hole and electron conductors (impurity level and crystallinity of the used material) and on the energy levels at the electrodes where the charges are adsorbed and where injection has to be facilitated (work functions). As in the case of the OLEDs the interfaces between the donor-acceptor-materials and the electrodes play a crucial role, which is object of our research. The short mean free paths of the excitons limit the device thickness to the nanometer scale. The controlled growth of ultrathin films with a desired morphology and a maximum crystallinity at this scale is therefore an important requirement for a high efficiency of OPVC.

1.2.3 Organic field effect transistor (OFET)

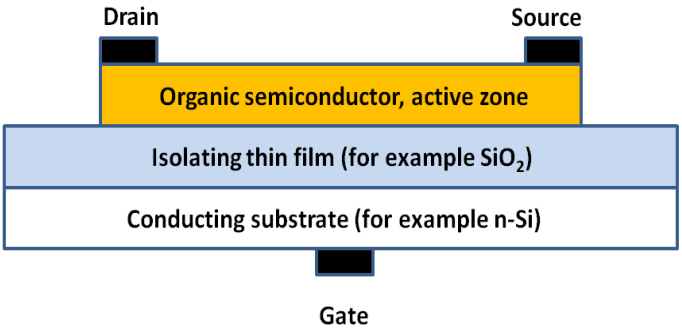

Figure 7: Schematic model of an organic field effect transistor: The OFET consists of an organic semiconductor as active material with the drain and source electrodes situated on top of it. The semiconductor layer is separated from the conducting gate electrode by an isolating film. The current between source and drain can be changed by orders of magnitude applying a voltage at the gate.

A basic OFET consists of a source and a drain electrode connected to a semiconducting organic material which is situated above an insulator. The insulator film is very often made of SiO_2 and sits on top of a conducting substrate which is connected to the gate electrode (Fig. 7). The control over the source-drain current originates from a potential applied to this gate electrode. This voltage produces a polarity dependent band bending at the semiconductor/insulator interface. The consequence is the reduction or the increase of the amount of majority charge carriers in the conduction bands of the semiconductor (Fig. 8). If a negative voltage is applied to a n-type semiconductor, the band bends upwards and a depletion of the majority charge carriers (electrons in the n-type semiconductor) is the result. The resistance between source and drain electrode increases. A positive voltage results in a downward bent band and electrons accumulate at the organic-insulator interface with the consequence of a reduced source-drain resistance. In a p-type semiconductor the effect of the gate voltage is inversed because majority charge carriers are holes and not electrons (a description and explanation about the inversion regimes and the threshold voltage as well as more details can be found elsewhere[23, 24, 25]).

After reports about the success in the area of organic solar cells, investigation about the basic electrical parameters of molecular single crystal showed in 1970 that a field effect on transport in those materials could be achieved[26]. Later on reports followed of a field effect in other organic materials[27], but only in 1987 the potential of the new materials for organic electronics was realized and the functioning of a practical field effect transistor was proved. The active organic semiconductor layer consisted of a structure of electrochemically polymerized polythiophene[28]. The source-drain current in the first practical OFET[28] could be changed by a factor of 10^2–10^3. Nowadays all necessary layers can be deposited and patterned at room temperature by a combination of low-cost solution-processing and direct-write printing, which makes them ideally suited for realization of low-cost, large-area electronic functions on flexible substrates[29].

Nevertheless the crucial elements have still to be improved. These are, as in the case of the OLEDS and the OVPDs, the injection and extraction of charge carriers (holes and electrons) at the interfaces to the metal electrodes, the mobility inside the organic semiconductor and the

band structure at the interface of the active zone with the insulator connected to the gate electrode. The morphology of interfaces between organic materials or to metals as the physics behind this and the charge injection is an active part of our investigation.

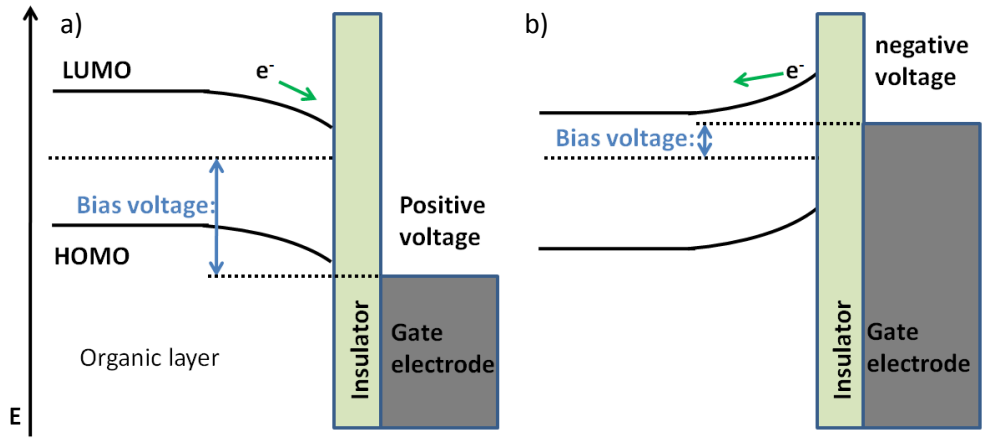

Figure 8: Band scheme of an OFET with **a)** positive bias voltage and **b)** with negative bias voltage. In a) majority charge carriers diffuse into the interface region between semiconductor and insulator and thus reduce the resistance between source and drain (source and the gate electrode are related to the same potential). In b) a depletion of majority carriers is obtained at the interface due to a negative bias voltage. The result is a high resistance between source and drain.

Summarizing, the main electronic processes in the three devices presented here, and in organic electronics in general, are the injection, collection, creation and mobility of charge carriers, which in principle could be improved by learning about the different interfaces involved (between donor and acceptor or between metal electrode and organic material), including the possible interface effects and its influence on the properties of the involved materials. These are topics of this thesis.

1.3 Problems of organic electronics and interface effects

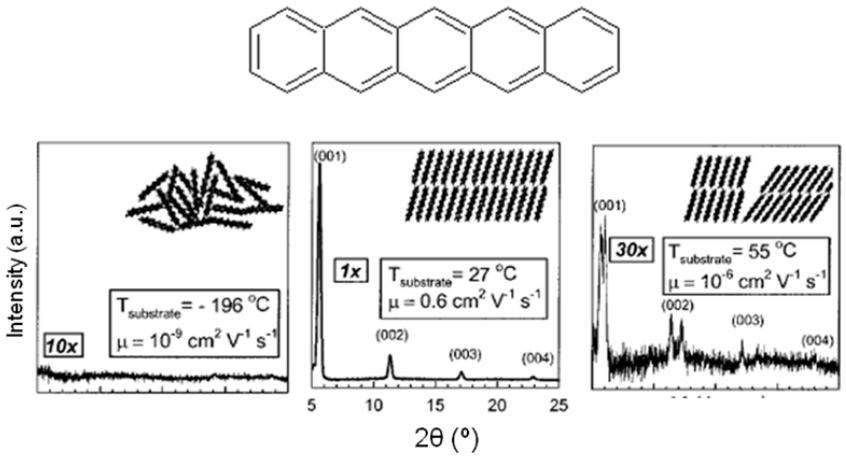

Figure 9: Conductivity measurements depending on the order of pentacene films[Taken from 30]: The higher the degree of order or crystallinity in the organic semiconductor pentacene, the higher is the conductivity, more than 8 orders of magnitude difference is observed.

Controlling the morphology of organic semiconductors at the nanoscale, including the impurity level and the crystallinity, is a way to improve the transport and mobility of charge carriers which usually have short mean free paths because they move by thermally assisted hopping from molecule to molecule[31]. This has been shown for pentacene: Crystalline order leads to an increase of the conductivity by several orders of magnitude compared to a disordered morphology[30] (Fig. 9). Exploiting the self assembly properties of tailored molecular building blocks is an approach to achieve a desired morphology of an organic thin film. Structural investigation of thus created ultrathin films is part of the present thesis.

Another possibility to improve the issue of mobility of charge carriers in organic devices is using polymer materials[32] and including aromatic functional groups or a conjugated π-electron system facilitating the delocalization of the orbital wave function of the charge carrier. Additionally, electron withdrawing or donating functional groups can be attached with an effect on mobility, while other functional groups provide a means for the band gap tuning[33, 33]. Poly thiophene, which was discovered in the late 1970, is an example of a conjugated polymer with an improved mobility[31]. Inducing polymerization reactions of functionalized molecular units on the desired surface is an alternative route to create well conducting layers instead of depositing the already synthesized polymer. The topic of polymerization will be treated in Chapter 4.

Other unsolved problems of organic compounds for devices require more investigation, additional to ours, like the delamination of electrode material after intensive use, the stability against oxidation and reduction, the device degradation over time by recrystallization and temperature variations and the atomic electro migration of sodium and indium from glass substrates.

Other research fields among organic materials exist, too: the poorly developed n-type OFETs, which exhibit an unsatisfactory performance compared to p-type organic semiconductors[34], the new promising organic heterostructures for OFET which appeared recently in literature[35],

the idea of injection laser (i.e. an organic diode laser) based on polymer materials and nonvolatile memory elements based on OFETs with a polymeric gate electret[36, 37]; also ambipolar light-emitting OFET[38, 39] are promising new devices calling for detailed investigation but which will not be treated here.

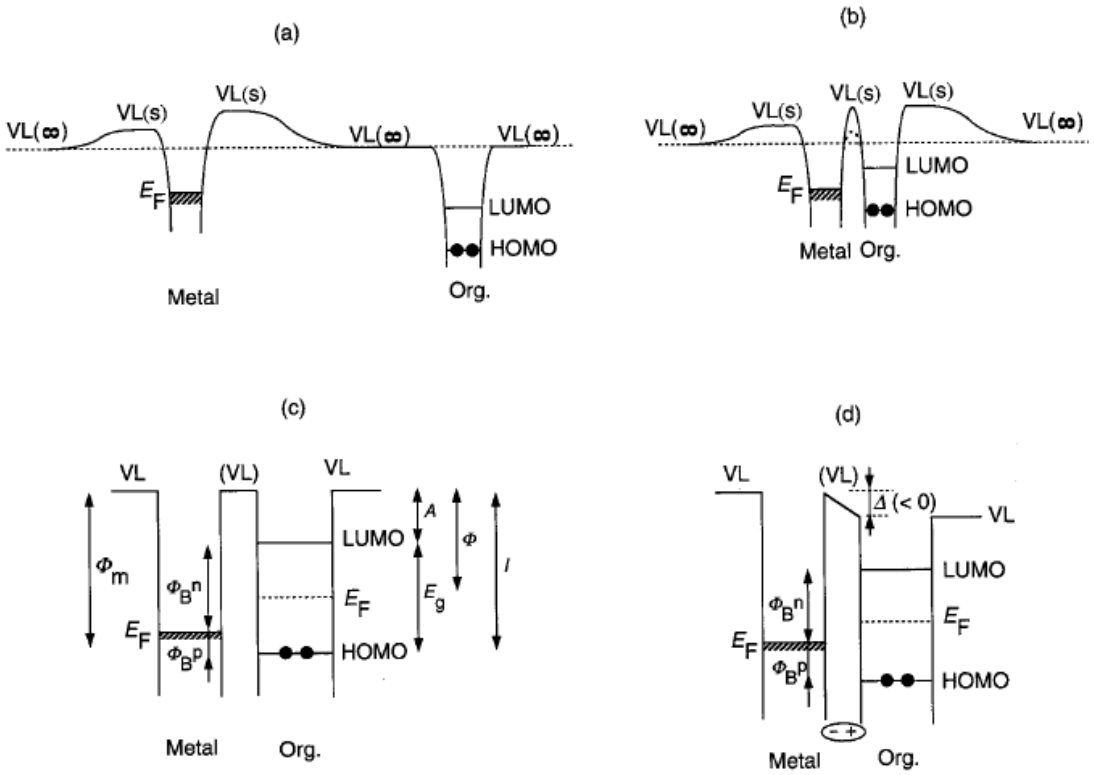

Figure 10 [Taken from 40]**:** a) Electronic structure of a metal and an organic solid at infinite distance. b) Contact of a metal and a thin organic solid layer. The organic layer is within the electric field of the surface dipole layer of the metal, and the interfacial VL is common. When the two solids come into contact, the actual potential well may become as shown by the broken line. c) Schematic energy diagram representation of a) assuming common (virtual) VLs at the interface. A is the electron affinity, E_g is the band gap, Φ is the Fermi level and I is the ionization potential of the molecule. Φ_B^n and Φ_B^p denote the injection barriers for electron and hole, E_F is the Fermi level, $\Phi_m$is the work function of the metal surface. d) Interfacial energy diagram with a shift Δ of the VL at the interface due to dipole layer formation. In this figure, the organic side is charged positively, making this side more comfortable (low energy) for an electron, and making the sign of Δ negative.

All organic electronic devices are based on similar principles and their functioning is determined, as shown previously, by a very thin active layer, mostly the interface between two materials like the electrode and the organic emitting layer or the organic donor and acceptor layers. Understanding the physics behind these interfaces is crucial and allows the improvement and optimization of organic devices. This means controlling the work function and the electronic band structure in order to solve and improve some of the previously mentioned issues. The energy which has an electron just outside a solid at the vacuum level close to the surface, VL(s), determines the work function (difference to Fermi Level) as well as the energy barriers for electrons and holes Φ_B^n and Φ_B^p (Fig. 10). It has been shown that the traditional assumption of a common vacuum level is invalid due to the difference of VL(s) and the energy at infinite distance, at VL(∞)[41, 40]. These quantities are all influenced by surface dipoles (Fig. 10), as is shown experimentally by a change in the work function of metal electrodes, upon adsorption of a layer of molecules with an intrinsic electric dipole moment[42,

[43, 44, 45]. Even fully saturated hydrocarbons adsorbed on noble metal surfaces produce an interface dipole by a lateral displacement of the electronic charge caused by the quantum mechanical phenomenon referred to as exchange repulsion (the so-called “pillow” effect)[41].

For example, non planar molecules with a halogen atom at an off-center position exhibit an inherent electric dipole moment This is the case of Cl-subphtalocyanine, which has a cone shape with a Cl-atom at the apex, and has a dipole moment of 4.5 D[46]. These molecules can adsorbs on the Cu(111) surface in two different ways, Cl-up or Cl-down, which can be influenced by a post-deposition annealing. That would, in principle, give control over the resulting work function of this system.

An important origin of an interface dipole arises from a net charge transfer between the surface and the adsorbed molecule. For example, adsorbing donor molecules (methyl viologen bipyridinylidene, MVO) on Au(111) reduces the work function of the sample from 5.5 eV of the pristine metal to 3.3 eV. The organic material donates negative charge to the metal substrate and influences the electron transport layers deposited on top of the modifying MVO-layer. The consequence is a reduction of the electron injection barrier of 0.65 eV for a transport layer of C_{60}[47].

With electron acceptor molecules the energy-level alignment at interfaces can also be varied. Depositing F4-TCNQ on gold prior to an electro-active conjugated organic material provides certain control over the energy level alignment at the interface by varying the pre-coverage of the electron acceptor. This way the hole-injection barrier could be lowered by as much as 1.2 eV; photoelectron spectroscopy revealed that the electron transfer from the substrate to the adsorbed F4-TCNQ was responsible[48, 49]. Charge transfer between adsorbates and surfaces is therefore an important effect which affects deeply the electronic coupling for charge injection and the energy levels at the interfaces[50]. An important charge transfer mechanism which leads to an interface dipole can be described with the text book example of carbon monoxide adsorbed on a metal surface[51]. The HOMO (5σ orbital) is localized on the carbon end of the C-O-molecule and interacts strongly with the metal forming hybrid electronic states. Negative charge from the 5σ states is thus donated to the metal. The LUMO (2π* orbital) is extended symmetrically along the axis of the molecule and the bond geometry is therefore determined by localization of the 5σ orbitals which render the overlap with the metal states most favorable if located close to the surface. This determines the adsorption geometry of C-O to be perpendicular to the surface. Charge is therefore located in the interface region between the adsorbate and the metal and an interface dipole is created. The LUMO also receives charge from the metal by the process of back donation, and as it is an antibonding orbital, the bond strength between the C- and the O-atom is slightly reduced. This leads to another effect of charge transfer: a higher reactivity of C-O due to the interaction with a metal surface.

The net charge transfer across an organo-metallic interface, seen from the adsorbate side, is determined by the gain (negative charge transfer from the surface) and the loss (back donation to the surface) of electrons. In principle an electron transfer to the substrate takes place if the HOMO of a free molecule far away from the surface is above the Fermi Level of the metal, which is often the case for donor molecules and metals with a large work function. As a consequence, upon adsorption the HOMO will be partially emptied[52]. If the LUMO of the free molecule lies below the Fermi Level of the metal, a charge transfer from the substrate to the

adsorbate will take place, filling partially the LUMO; this occurs for many acceptor molecules and small work function metals. Back donation of charge may also occur through the interaction of deeper lying molecular orbitals which can hybridize with metal states[41, 53, 54] (for example σ-states localized on –CN substituents[49]). The back donation of charge is difficult to predict without sophisticated calculations. In a charge transfer complex the HOMO of the donor lies above the LUMO of the acceptor molecule, like in TTF and TCNQ, which form a charge transfer-salt (TTF-TCNQ[7, 8]) without any external energy after bringing them into physical contact.

For example, adsorbing the electron acceptor TCNQ on top of Cu(100),a surface with a work function of 4.5 ± 0.1 eV leads to a large charge transfer of electrons from the surface to the molecules (Chapter 3). On the contrary, TCNQ only physisorbs on Au(111), due to the higher work function of 5.3 ± 0.1 eV of the substrate. This is different for a very similar, but stronger acceptor molecule adsorbed on the same surface. Photoemission data provides direct evidence for a charge transfer interaction of F4-TCNQ with Au surfaces[48]. In other words the charge transfer is minimal for TCNQ/Au(111)[55] but large for F4-TCNQ due to the different LUMO energies. The combination of TCNQ and F4-TCNQ on Cu(100) and Au(111) emphasize therefore the role of the difference in binding energy between one of the two molecular frontier orbitals and the Fermi level of the metal substrate. This binding energy difference determines the direction and the amount of charge transfer.

There are several other examples of organo-metallic systems with a charge transfer and certain typical combinations of chemical elements with metals can be identified. A strong adsorbate - substrate interaction often occurs due to the availability of electron lone pairs which can bind to the surface through mixing with the d_z^2-states of the metals. Examples are O, N and S, molecules containing these elements tend to chemisorb with a charge transfer to reactive metal surfaces. Depending on the systems, charge transfer can lead to many different effects. For example, small oxygen containing molecules bind strongly (chemisorptions) on palladium surfaces through the lone-pair and decompose to CO[56], depending on the sample temperature. Sulphur binds often strongly to gold as in the case of the electron donor-molecules exTTF/Au(111)[58] and TTF/Au(111)[52]. In the latter system, for low coverages (<< 1 ML), a long range repulsive interaction between the single molecules with an assembly at a certain minimum distance is observed as a result of the negative charge donated to the substrate. Nitrogen often binds strongly to silver, TCNE/Ag(100)[59], or to copper, TCNE on Cu(100)[60]. In the latter case an interesting effect of the charge transfer is a strong structural modification of the surface, which causes a chain-like assembly of the molecules. F4-TCNQ also chemisorbs via their cyano groups on Au(111), Cu(111) and Ag(111), with the charge transfer causing a geometrical distortion of the molecular backbone[49], as shown in the case of Cu(111) by x-ray standing waves experiments and confirmed by first principle calculations[54]. The work function of this system can be increased by 0.6 eV at a coverage of 1 ML compared to the pristine metal surface.

Being able to predict the interface charge transfer and to identify the possibly arising effects makes it possible to tailor the work function and the strength of electronic coupling for charge transport across the interface. These are fundamental parameters which influence the organic electronic device performance. However, a charge transfer between substrate and adsorbed molecules affects not only the work function, but it also alters the interaction between

adsorbates and the substrate with consequences for the self assembly, the adsorption geometry, the chemical reactivity and other important characteristics of adsorbed molecules. These non-electronic effects of charge transfer have not been studied in depth before but, as will be seen in the discourse of the present thesis, they are of utmost importance to understand the structure of organic-metal interfaces. All described and also additional effects of charge transfer might arise at the interfaces of devices in organic electronics and future studies will have to take them into account in order to control their performance.

In this thesis we present organic/metal systems where charge transfer causes effects different from those mentioned in the previous examples. In Chapter 3, for example, the causal connection between charge transfer and the substrate mediated interaction between the adsorbates, which form thus ordered islands, is demonstrated in the system of TCNQ on Cu(100)[61 and this work]. As in the case of F4-TCNQ/Cu(111)[54], the negative charge transfer to TCNQ affects several molecular bonds and thus the adsorption geometry. This facilitates a strong interaction with the surface, which leads to a lifting of selected Cu-atoms and to a substrate mediated self assembly of the adsorbates simila to the previously mentioned case of TCNE/Cu(100)[60]. This, for the first time clearly drawn, causal connection is supported by an unprecedented variety of experimental techniques like STM, XPS, XAS and work function measurements combined with DFT-calculations. Further new results presented in this thesis are the identification of charge transfer as the origin of an increased chemical reactivity and the subsequent polymerization of TCPQ- and TCTQ-molecules on Cu(100), and the role charge transfer plays in the isomerization of DCNQI/Cu(100) (Chapter 4 and 5, respectively).

1.4 Outline of this thesis

First the structural properties of selected organic molecules on a typical electrode material, copper, in particular the Cu(100)-surface, is investigated with respect to the understanding of self assembly and the morphology. The selected molecules are TCNQ, which is a model molecule for strong electron acceptors and as such used in electronic devices like OPVC[62] and OFETs[29, 63, 64], and three derivatives with a variation of the two types of functional elements of the parent molecule: the number of cyano groups and the number of aromatic carbon rings at the molecular backbone, in order to learn about the influence each of the two functional moieties can have on the behavior of the organic adsorbates. After providing arguments for charge transfer in the treated systems, its consequences for the adsorption geometry, the substrate distortion, the self assembly, the chemical reactivity and the isomerization are described with results which will have to be taken into account in research about organic electronics.

Chapter 2 describes the used UHV-system and its expansion during the course of this thesis with the main experimental methods.

Chapter 3 deals with the results of the adsorption of TCNQ on Cu(100) and the effect of the observed charge transfer on the adsorption geometry of the adsorbate with a consequences for the Cu-surface distortion, and the resulting indirect assembly mechanism of the molecules.

Chapter 4 describes the findings of the adsorption of TCPQ and TCTQ on Cu(100). These have the same number of cyano groups as its parent molecule but the number of carbon rings fused to the central quinone ring varies. This inhibits a substrate mediated self assembly as seen in Chapter 3 but results in an enhanced chemical reactivity due to the charge transfer which leads upon annealing to the formation of a polymer with a highly functionalized backbone.

Chapter 5 identifies charge transfer as responsible for the appearance of two island types of DCNQI on Cu(100) due to the lowering of the energy barrier for molecular isomerization.

1.5 Bibliography

References

1. Binnig, G. & Rohrer, H. Scanning tunneling microscopy. *Surf. Sci.* **126**, 236-244 (1983).

2. http://nobelprize.org/nobel_prizes/physics/laureates/1986/index.html.

3. http://www.nobelprize.org/nobel_prizes/physics/laureates/2007/.

4. Roberts, J. D. & Caserio, M. C. Basic Principles of Organic Chemistry. *W. A. Benjamin, Inc., Menlo Park, CA. ISBN 0-8053-8329-8* (1977).

5. Little, W. A. Possibility of Synthesizing an Organic Superconductor. *Phys. Rev.* **134**, A1416 (1964).

6. Naarmann, H. in *Ullmann's Encyclopedia of Industrial Chemistry* (Wiley-VCH Verlag GmbH & Co. KGaA, 2000).

7. Ferraris, J., Cowan, D. O., Walatka, V. & Perlstein, J. H. Electron transfer in a new highly conducting donor-acceptor complex. *J. Am. Chem. Soc.* **95**, 948-949 (1973).

8. Anderson, P. W., Lee, P. A. & Saitoh, M. Remarks on giant conductivity in TTF-TCNQ. *Solid State Commun.* **13**, 595-598 (1973).

9. Helfrich, W. & Schneider, W. G. Recombination Radiation in Anthracene Crystals. *Phys. Rev. Lett.* **14**, 229 (1965).

10. Tang, C. & VanSlyke, S. Organic electroluminescent diodes. *Appl. Phys. Lett.* **51**, 913 (1987).

11. Erickson, N. C. & Holmes, R. J. Highly efficient, single-layer organic light-emitting devices based on a graded-composition emissive layer. *Appl. Phys. Lett.* **97**, 083308 (2010).

12. Kearns, D. & Calvin, M. Photovoltaic Effect and Photoconductivity in Laminated Organic Systems. *J. Chem. Phys.* **29**, 950 (1958).

13. Peumans, P., Yakimov, A. & Forrest, S. Small molecular weight organic thin-film photodetectors and solar cells. *J. Appl. Phys.* **93**, 3693 (2003).

14. Pettersson, L., Roman, L. & Inganäs, O. Modeling photocurrent action spectra of photovoltaic devices based on organic thin films. *J. Appl. Phys.* **86**, 487 (1999).

15. Halls, J., Pichler, K., Friend, R., Moratti, S. & Holmes, A. Exciton diffusion and dissociation in a poly(p-phenylenevinylene)/C60 heterojunction photovoltaic cell. *Appl. Phys. Lett.* **68**, 3120 (1996).

16. Bello, C. d. Principles of Organic Chemistry. *Decibel-Zanichelli*, 93 (1993).

17. Tang, C. Two-layer organic photovoltaic cell. *Appl. Phys. Lett.* **48**, 183 (1986).

18. Lee, C. H. *et al*. Sensitization of the photoconductivity of conducting polymers by C60: Photoinduced electron transfer. *Phys. Rev. B* **48**, 15425 (1993).

19. Zerza, G., Brabec, C. J., Cerullo, G., De Silvestri, S. & Sariciftci, N. S. Ultrafast charge transfer in conjugated polymer-fullerene composites. *Synth. Met.* **119**, 637-638 (2001).

20. Hoppe, H. & Sariciftci, N. S. Organic solar cells: An overview. *J. Mater. Res.* **19**, 1924 (2004).

21. Ma, W., Yang, C., Gong, X., Lee, K. & Heeger, A. ?. Thermally Stable, Efficient Polymer Solar Cells with Nanoscale Control of the Interpenetrating Network Morphology. *Advanced Functional Materials* **15**, 1617-1622 (2005).

22. McGehee, M. D. & Topinka, M. A. Solar cells: Pictures from the blended zone. *Nat Mater* **5**, 675-676 (2006).

23. Shur, M. Physics of Semiconductor Devices. *Englewood Cliffs, NJ: Prentice-Hall. ISBN 0-13-666496-2.* (1990).

24. Sze, S. M. Physics of Semiconductor Devices. *2nd Edition, Wiley-InterScience, New York* (1981).

25. Horowitz, G., Hajlaoui, R., Bourgouiga, R. & Hajlaoui, M. Theory of Organic FieldEffect Transistors. *Synth. Met.* **101**, 401 (1999).

26. Barbe, D. F. & Westgate, C. R. Surface state parameters of metal-free phthalocyanine single crystals. *Journal of Physics and Chemistry of Solids* **31**, 2679-2687 (1970).

27. Kudo, K., Yamashina, M. & Moriizumi, T. Field Effect Measurement of Organic Dye Films. *Jpn. J. Appl. Phys.* **23**, 130 (1983).

28. Koezuka, H., Tsumura, A. & Ando, T. Field-effect transistor with polythiophene thin film. *Synth. Met.* **18**, 699-704 (1987).

29. Sirringhaus, H. Device Physics of Solution-Processed Organic Field-Effect Transistors. *Adv Mater* **17**, 2411-2425 (2005).

30. Dimitrakopoulos, C. D. & Malenfant, P. R. L. Organic Thin Film Transistors for Large Area Electronics. *Adv Mater* **14**, 99-117 (2002).

31. Horowitz, G. Organic Field-Effect Transistors. *Adv Mater* **10**, 365-377 (1998).

32. Hamilton, R. *et al*. High-Performance Polymer-Small Molecule Blend Organic Transistors. *Adv Mater* **21**, 1166-1171 (2009).

33. Rivers, N. P. Leading edge research in solar energy. *Nova Science Publishers ISBN: 1-60021-336-7* (2007).

34. Yamashita, Y. Organic semiconductors for organic field-effect transistors. *Science and Technology of Advanced Materials* **10**, 024313 (2009).

35. Zhu, F., Yang, J., Song, D., Li, C. & Yan, D. Single-crystal-like organic heterojunction with 40 nm thick charge accumulation layers. *Appl. Phys. Lett.* **94**, 143305 (2009).

36. Singh, T. *et al*. Nonvolatile organic field-effect transistor memory element with a polymeric gate electret. *Appl. Phys. Lett.* **85**, 5409 (2004).

37. Narayanan Unni, K., de Bettignies, R., Dabos-Seignon, S. & Nunzi, J. A nonvolatile memory element based on an organic field-effect transistor. *Appl. Phys. Lett.* **85**, 1823 (2004).

38. Schidleja, M. *et al*. The impact of contact formation on the light emission from ambipolar transistors. *Appl. Phys. Lett.* **95**, 113303 (2009).

39. Seo, H., Zhang, Y., An, M. & Choi, J. Fabrication and characterization of air-stable, ambipolar heterojunction-based organic light-emitting field-effect transistors. *Organic Electronics* **10**, 1293-1299 (2009).

40. Ishii, H., Sugiyama, K., Ito, E. & Seki, K. Energy Level Alignment and Interfacial Electronic Structures at Organic/Metal and Organic/Organic Interfaces. *Adv Mater* **11**, 605-625 (1999).

41. Witte, G., Lukas, S., Bagus, P. S. & Woll, C. Vacuum level alignment at organic/metal junctions: “Cushion” effect and the interface dipole. *Applied Physics Letters* **87**, 263502-263502-3 (2005).

42. Campbell, I. H. *et al*. Controlling Schottky energy barriers in organic electronic devices using self-assembled monolayers. *Phys. Rev. B* **54**, R14321 (1996).

43. Nüesch, F., Rotzinger, F., Si-Ahmed, L. & Zuppiroli, L. Chemical potential shifts at organic device electrodes induced by grafted monolayers. *Chemical Physics Letters* **288**, 861-867 (1998).

44. Zuppiroli, L. *et al*. Self-assembled monolayers as interfaces for organic opto-electronic devices. *Eur. Phys. J. B* **11**, 505-512 (1999).

45. Tour, J. M. *et al*. Synthesis and Preliminary Testing of Molecular Wires and Devices. *Chemistry - A European Journal* **7**, 5118-5134 (2001).

46. Trelka, M. *et al*. Subphthalocyanine-based nanocrystals. *Chem. Commun.* **47**, 9986-9988 (2011).

47. Bröker, B. Gold work function reduction by 2.2 eV with an air-stable molecular donor layer. *Appl. Phys. Lett.* **93**, 243303 (2008).

48. Koch, N., Duhm, S., Rabe, J. P., Vollmer, A. & Johnson, R. L. Optimized Hole Injection with Strong Electron Acceptors at Organic-Metal Interfaces. *Phys. Rev. Lett.* **95**, 237601 (2005).

49. Rangger, G. M. *et al*. F4TCNQ on Cu, Ag, and Au as prototypical example for a strong organic acceptor on coinage metals. *Phys. Rev. B* **79**, 165306 (2009).

50. Zhu, X. -. Electronic structure and electron dynamics at molecule-metal interfaces: implications for molecule-based electronics. *Surface Science Reports* **56**, 1-83 (2004).

51. Kolasinski, K. W. in *Surface Science - Foundation of Catalysis and Nanoscience* (John Wiley & Sons Ltd, Baffins Lane, Chichester, England, 2002).

52. Fernandez-Torrente, I. *et al*. Long-Range Repulsive Interaction between Molecules on a Metal Surface Induced by Charge Transfer. *Phys. Rev. Lett.* **99**, 176103 (2007).

53. Triguero, L. Spin uncoupling in surface chemisorption of unsaturated hydrocarbons. *J. Chem. Phys.* **108**, 1193 (1998).

54. Romaner, L. *et al*. Impact of Bidirectional Charge Transfer and Molecular Distortions on the Electronic Structure of a Metal-Organic Interface. *Phys. Rev. Lett.* **99**, 256801 (2007).

55. Torrente, I. F., Franke, K. J. & Pascual, J. I. Structure and electronic configuration of tetracyanoquinodimethane layers on a Au(1 1 1) surface. *International Journal of Mass Spectrometry* **277**, 269-273 (2008).

56. Luth, H., Rubloff, G. W. & Grobman, W. D. Chemisorption and decomposition reactions of oxygen-containing organic molecules on clean Pd surfaces studied by UV photoemission. *Surf. Sci.* **63**, 325-338 (1977).

57. Duhm, S. *et al*. Weak Charge Transfer between an Acceptor Molecule and Metal Surfaces Enabling Organic/Metal Energy Level Tuning. *J Phys Chem B* **110**, 21069-21072 (2006).

58. Urban, C. *et al*. Growth and Structure of Self-assembled Monolayers of a TTF Derivative on Au(111). *J. Phys. Chem. C* **114**, 6503-6510 (2010).

59. Wegner, D. *et al*. Single-Molecule Charge Transfer and Bonding at an Organic/Inorganic Interface: Tetracyanoethylene on Noble Metals. *Nano Letters* **8**, 131-135 (2008).

60. Bedwani, S., Wegner, D., Crommie, M. F. & Rochefort, A. Strongly Reshaped Organic-Metal Interfaces: Tetracyanoethylene on Cu(100). *Phys. Rev. Lett.* **101**, 216105 (2008).

61. Tzu-Chun Tseng, e. a. Charge-transfer-induced structural rearrangements at both sides of organic/metal interfaces. *Nature Chemistry* (2010).

62. Opitz, A. *et al*. Mixed crystalline films of co-evaporated hydrogen- and fluorine-terminated phthalocyanines and their application in photovoltaic devices. *Organic Electronics* **10**, 1259-1267 (2009).

63. Hajlaoui, R. *et al*. Improved field-effect mobility in short oligothiophenes: Quaterthiophene and quinquethiophene. *Adv Mater* **9**, 389-391 (1997).

64. Yamagishi, M., Tominari, Y., Uemura, T. & Takeya, J. Air-stable n-channel single-crystal transistors with negligible threshold gate voltage. *Appl. Phys. Lett.* **94**, 053305 (2009).

2 Experimental methods and theoretical background

In the introduction (Chapter 1) we have seen that detailed studies about organic on solid surfaces are important due to their influence in determining the functioning of technological devices. In particular, charge transfer at the metal-organic interface has been demonstrated to affect strongly the structural and electronic properties. In order to study these effects, adequate analysis techniques, like scanning tunneling microscopy (STM), x-ray photoelectron spectroscopy (XPS) and x-ray absorption spectroscopy, have been used. STM provides the means to investigate structurally ultrathin films and single molecules with atomic or molecular resolution on a variety of surfaces. Spectroscopic methods like XPS and XAS can provide detailed chemical and electronic information about the element composition, the chemical bonds, energy levels and also, in the case of XAS, structural information about the spatial orientation of molecules on surfaces. These experimental tools will be described in detail in the following.

2.1 Scanning tunneling microscopy (STM)

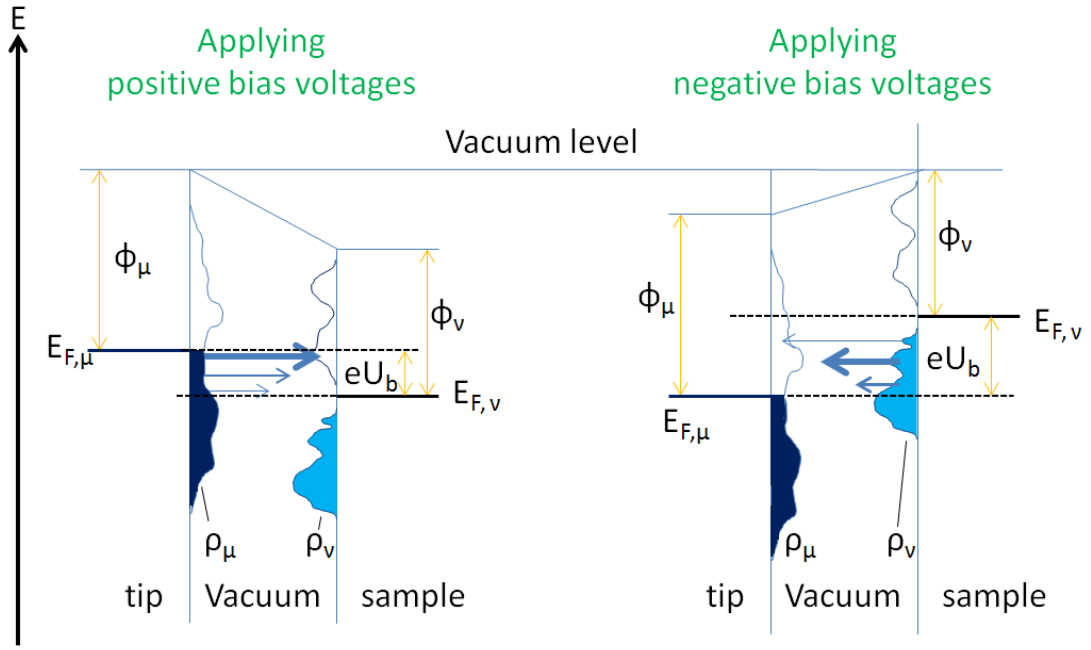

Figure 1: Energy diagram of the tunnel effect between tip and sample, applying a bias voltage to the sample (as in the STM used in this thesis): In the case of a positive voltage U_b, electrons from the tip tunnel through the vacuum to the sample. They come from occupied states in an energy window between the Fermi level of the tip and eU_b and tunnel into empty states of the sample in an energy window between the Fermi level of the sample ($E_{F,v}$) and $E_{F,v}$- eU_b, depending also on the densities of states. When a negative voltage is applied, the tunnel direction is inverted and occupied states of the sample from an energy interval [$E_{F,v}$; $E_{F,v}$- eU_b] contribute to the tunnel current into the unoccupied states of the tip ($E_{F,\mu}$) from $E_{F,\mu}$ up to $E_{F,\mu}$+ eU_b , also as a function of the density of states (illustrated with arrows of different thickness).

STM has been an investigation technique of many of the previous PhD thesis in our surface science group. Therefore a number of extensive descriptions of the working principle of this instrument already exist, so I will limit this section to the basic theory and the technical specialties of the STM I worked with.

The STM is a method to investigate conducting microscopic structures and morphologies of metal surfaces in real space with atomic resolution. It was developed in 1981 by G. Binning and H. Rohrer[1] (Nobel Prize in Physics in 1986[2]), and since then it has become one of the most important tools in surface science. The method is based on the quantum mechanical effect of electron tunneling between two electrodes separated, in our case by a vacuum gap, and connected to two different potentials. One electrode is the metallic STM tip (often made of tungsten or platinum-iridium), usually connected to ground, and the second electrode is the sample, to which a voltage of a few volts can be applied. Bringing the two electrodes in close proximity leads to a current in the range of pA to nA, due to the potential difference and due to the extension of the wavefunctions of the electrons over the gap. This tunneling current depends, among other parameters, on the potential applied and the electrode distance (the tip-sample distance). Changing the distance 1 Å decreases or increases the tunnel current typically an order of magnitude[3]. If the bias voltage (U_b) applied to the sample is negative, only electrons from the occupied states in an energy window between the Fermi level of the sample ($E_{F,\mu}$) up to $E_{F,\mu}+ eU_b$ participate in the tunneling process (Fig. 1). They tunnel to empty states in the tip in an energy range between the Fermi level of the tip ($E_{F,v}$) and $E_{F,v}- eU_b$. With positive bias voltages, the tunneling direction is inverted and electrons from the tip in an energy interval from $E_{F,v}$ to $E_{F,v}-eU_b$ contribute to the tunneling current. These tip electrons tunnel to empty sample states between $E_{F,\mu}$ and $E_{F,\mu}+ eU_b$ (Fig. 1). The theoretical modeling of the process shows that the tunnel current depends also on the density of states of tip and sample: the more electrons come from an energy interval of the origin electrode and the higher the density of unoccupied states in the target electrode, the higher is the tunnel current.

An STM image is produced by measuring the tunnel current at different points on the surface along the x- and y- directions (both directions are within the surface plane). This is called “scanning” and is achieved with piezo-electric materials which expand and contract by applying a voltage and can thus position the tip precisely over any part of the surface. Such an x-y-matrix of points, with a value of the tunnel current at each point, contains then information about the geometry and the electronic structure of the scanned area: this is the STM image. Different measuring modes exist: first the constant height mode, which refers to measuring the STM image while the z-height of the tip is fixed. Second, the usually used constant current mode (our case), which refers to the imaging of the surface with a constant current and a height that changes to keep this current at its reference value. This is achieved with a feedback controller which automatically approaches or retracts the STM-tip in order to maintain the current. This offers the advantage of being able to scan surfaces with large changes in z-height; otherwise the tip could crash into the surface or the tunnel current could be so low that no reasonable signal-to-noise ratio would be obtained. The measurement parameter in the constant current mode is the voltage applied to the piezo element controlling the z-height.

2.1.1 Theoretical modeling of the tunnel process

The Tersoff-Hamann model[4] of the tunneling process between tip and sample describes the dependence of the tunnel current with a 3D-tip model of spherical shape, with the assumption that many electrons tunnel simultaneously with different probabilities[5], and including the work functions of the metal electrodes, which gives the vacuum barrier a more realistic shape, unlike a rectangular form in the simplest approach of the potential barrier. The current is then in first-order perturbation theory:

$$\mathrm{I} = \frac{2\pi e}{\hbar}\sum_{\mu,\nu} f(\mathrm{E}_\mu)\left[1 - f(\mathrm{E}_\mu + \mathrm{eU}_b)\right]\left|M_{\mu\nu}\right|^2 \delta(\mathrm{E}_\mu - \mathrm{E}_\nu)$$

The bias voltage is U_b; E_μ and E_ν are the energy eigen values of the states of the tip (φ_μ) and the sample (φ_ν) and $M_{\mu\nu}$ is the tunneling matrix element between both, which is given, according to the Bardeen formalism[5], by:

$$M_{\mu\nu} = \frac{2\pi e}{\hbar}\int d\vec{S}\left(\varphi_\mu^* \Delta\varphi_\nu - \varphi_\nu \Delta\varphi_\mu^*\right),$$

with $d\vec{S}$ being an infinitesimal surface element within the vacuum barrier between tip and sample. Assuming, for the description of the tip spherical wave functions (s-waves), a bias voltage close to 0 V ($\mathrm{E}_\nu \approx \mathrm{E}_F$) and temperatures close to 0 K ($\mathrm{f}(\mathrm{E}_F) \approx 1$), the matrix elements $M_{\mu\nu}$ follow the proportionality:

$$M_{\mu\nu} \sim R \cdot e^{kR}\varphi_\mu(\vec{r}_0),$$

where R is the curvature of the tip-apex, centered around the vector $\vec{r}_0$, and $k = \hbar^{-1}\sqrt{2m\Phi}$, which is the inverse decay length of the wave function in vacuum. The tunnel current dependence can then be expressed in the following way:

$$\mathrm{I} \sim \sum_\mu \mathrm{U}_b R^2 e^{2kR}\left|\varphi_\mu(\vec{r}_0)\right|^2 \delta(\mathrm{E}_\mu - \mathrm{E}_F).$$

The above expression, using the exponentially decaying wave function:

$$\left|\varphi_\mu(\vec{r}_0)\right|^2 \sim e^{-2k(R+d)},$$

with d being the tip-sample distance, results in the following proportionality of the tunnel current I:

$$\mathrm{I} \sim \mathrm{U}_b R^2 e^{-2kd}.$$

This exponential dependence of the tunnel current on the tip-sample distance is the reason for the high sensitivity of the STM in the z-direction on the sample (z is the coordinate orthogonal to the surface plane). Moreover, the tunnel current is proportional to the bias voltage which maintains Fermi levels of the electrodes at different energies and therefore causes a flow of electrons. This confirms the process mentioned previously: when a positive bias voltage is applied to the sample, a current of electrons flows from the occupied states of the tip between

$E_{F,\mu}$ and $E_{F,\mu} - eU_b$ to the unoccupied states of the sample between $E_{F,\nu}$ and $E_{F,\nu} + eU_b$. For negative bias voltages the tunneling direction is inverted. The probability P, of finding in the sample an electron coming from the state φ_μ of the tip is proportional to the following expression:

$$P \sim |\varphi_\mu(d)|^2 e^{-2kd}.$$

The tunnel current is the sum of the probabilities of all states in the energy interval $[E_F, E_F - eU_b]$.

$$I \sim \sum_{E_\mu = E_F - eU_b}^{E_F} |\varphi_\mu(\vec{r}_0)|^2 e^{-2kd}$$

With the definition of the local density of states (LDOS):

$$\rho(x,E) = \frac{1}{\varepsilon} \sum_{E_\mu = E_F - eU_b}^{E_F} |\varphi_\mu(\vec{r}_0)|^2$$

the tunnel current can be expressed as a function of the density of states:

$$I \sim eU_b \rho(0, E_F) e^{-2kd}$$

This underlines, as described above, that not only the tip-sample distance, but also the LDOS, influences the tunnel current which is thus a convolution of the electronic and geometric structure of the electrodes. This has to be taken into account when interpreting STM-data.

2.1.2 The Aarhus STM

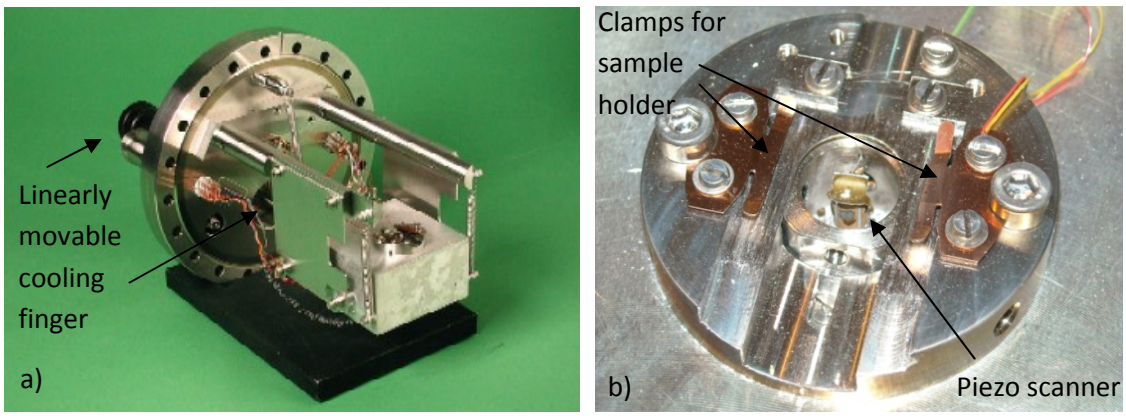

Figure 2: Variable temperature Aarhus-STM: The whole microscope is mounted on a CF150-flange, a). Cooling of the microscope is achieved with liquid nitrogen through a linear feedtrough which is pressed against the block. The cubic aluminium block in the center hosts the piezo-scanner, which can be seen in b). The sample is mounted facing down in a holder which is fixed by two clamps to the aluminum block.

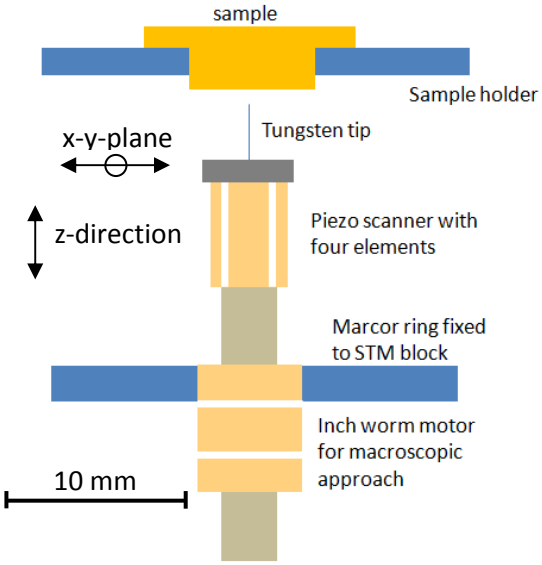

Figure 3: Schematic representation of the Aarhus STM piezo scanner: The whole tube scanner and approach motor is thermally and electrically insulated from the sample, so it can be maintained at RT (with a counter heating diode, not represented). The scanner is a cylindrical tube made of piezo-electric ceramics with four electrodes on its surface for the movement in the x-y-plane. The macroscopic approach is achieved by another piezo tube with three elements, the inch worm, which is fixed to the STM block by a macor ring.

The microscope used in the present thesis is the commercial Aarhus STM from "Specs" (Fig. 2) with a very small and light piezo scanner in tube form (Fig. 3) which makes possible a very fast movement of the STM tip (up to video rate with the appropriate electronics). The piezo tube has a single common electrode on the inside and four electrodes on its outside that control the lateral movement of the tip in the x- and y-direction (Fig. 3). This is achieved by applying asymmetric voltages (between -200 and 200 V) to contract and expand opposite piezo elements, deflecting thus the whole piezo cylinder in any desired direction. By applying a bias voltage to the inner electrode, the stretching or contraction of the whole tube scanner along the z-axis is achieved, and thus the distance to the sample is controlled in a range of nm. The macroscopic approach of the tip to the sample is achieved by another piezo tube, the inchworm, with three horizontal elements (Fig. 3). By applying a sequence of voltages to these three elements, they expand and contract in such a way that the piezo scanner can be moved upwards or downwards with a speed of approximately 1 mm per minute. Some drawbacks of this design are the slightly stronger curvature in the z-direction during a wide x-y-scan, compared to longer scanners, and the smaller scan range (1 µm x 1 µm) due to material curvature limits.

An important advantage is the possibility to cool the sample. This is achieved by liquid nitrogen which provides together with the possibility of heating using a Zener-diode, a measurement temperature range of 90 to 400 K. The piezo scanner is always maintained at RT which on one hand provides the possibility to work with only one length scale calibration, but on the other hand it makes the system more sensitive to drift, due to the temperature difference between the tip and the sample. Another big advantage is the possibility to deposit material on a cool sample while scanning. Thus, phenomena like diffusion or temperature dependent phase transitions (e.g. Chapter 5) can be studied.

2.2 Spectroscopic methods

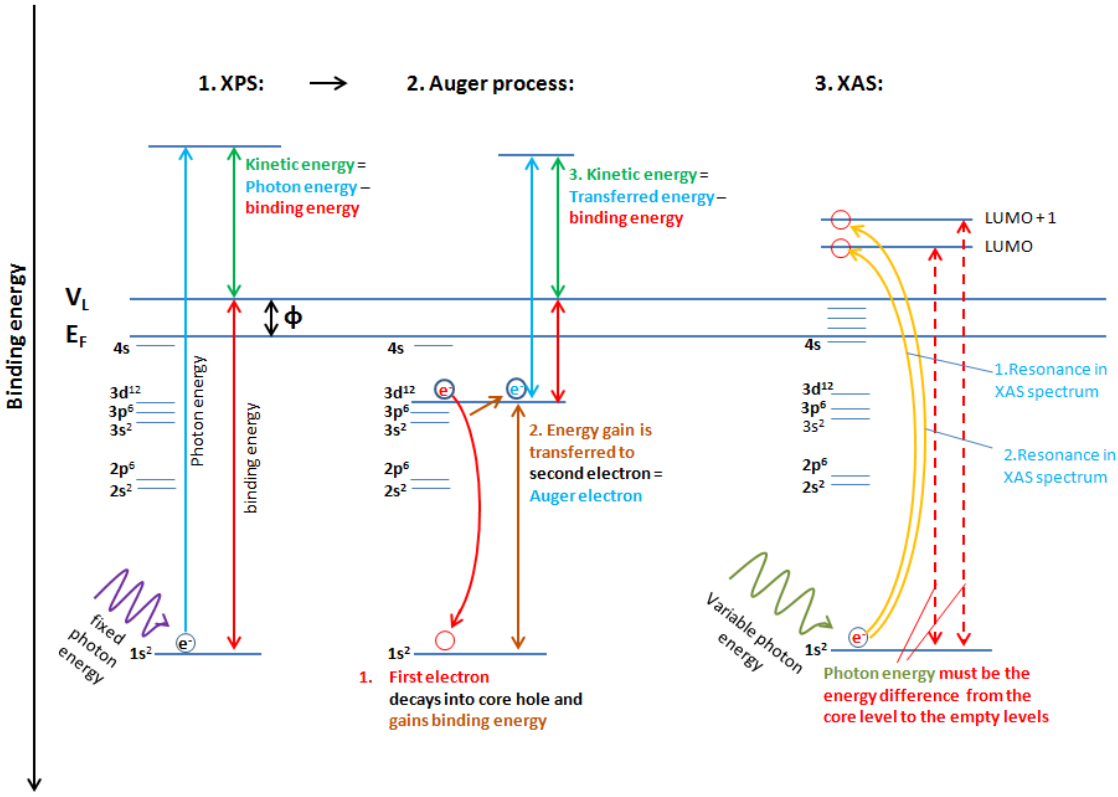

Figure 4: Energy diagrams of the different electronic processes which are used for x-ray photoelectron spectroscopy, Auger electron spectroscopy and x-ray absorption spectroscopy. In XPS a photon with a fixed energy excites a core level electron which is ejected with a kinetic energy equal to the photon energy minus its original binding energy. Knowing the excitation energy, the binding energy can be calculated by measuring the kinetic energy of the photoelectron. The core holes left by the photoelectron can be filled by electrons from higher levels. The gained binding energy can be transferred to a second electron (Auger electron), which can thus leave the atom with a kinetic energy that depends only on the levels involved and is then characteristic for the element. In XAS, if the photon energy equals the energy difference between an occupied and an empty state, an electron transition will take place. This will be registered as a peak in the total yield - or Auger electron intensity- vs. photon energy measurements. In this way information about the electronic (and even spatial) structure can be obtained.

Several spectroscopic methods can provide different information about the electronic structure of metal-organic interfaces. The tools presented here are based on the electronic excitation of the samples by light. X-ray photoelectron spectroscopy (XPS), for example, makes use of the photoelectric effect: The electrons ejected by an incident x-ray photon carry information about the orginal binding energy of the electron (Fig. 4, left side). The ionized atoms will fill the created core holes after a very short time through any of the different relaxation processes. One of the relaxation mechanisms is the Auger effect (Fig. 4, center): A second electron of the excited atom can fill the core hole. The energy gained is then transferred to another electron (the Auger electron) which is ejected into the vacuum. The origin of a photoelectron and an Auger electron are different, but both carry information characteristic of the element. Their kinetic energy is measured by an electron energy analyzer.

In X-ray absorption spectroscopy the photon energy is varied to excite electron transitions from occupied core levels into empty states to probe thus the initial and final states (Fig. 4, right side). The absorption of light depends on the x-ray incidence angle, which can provide information about the spatial orientation of the empty orbitals and thus about the adsorption geometry of molecules on surfaces. These methods will be described in more detail in the following.

2.2.1 X-ray photoelectron spectroscopy (XPS)

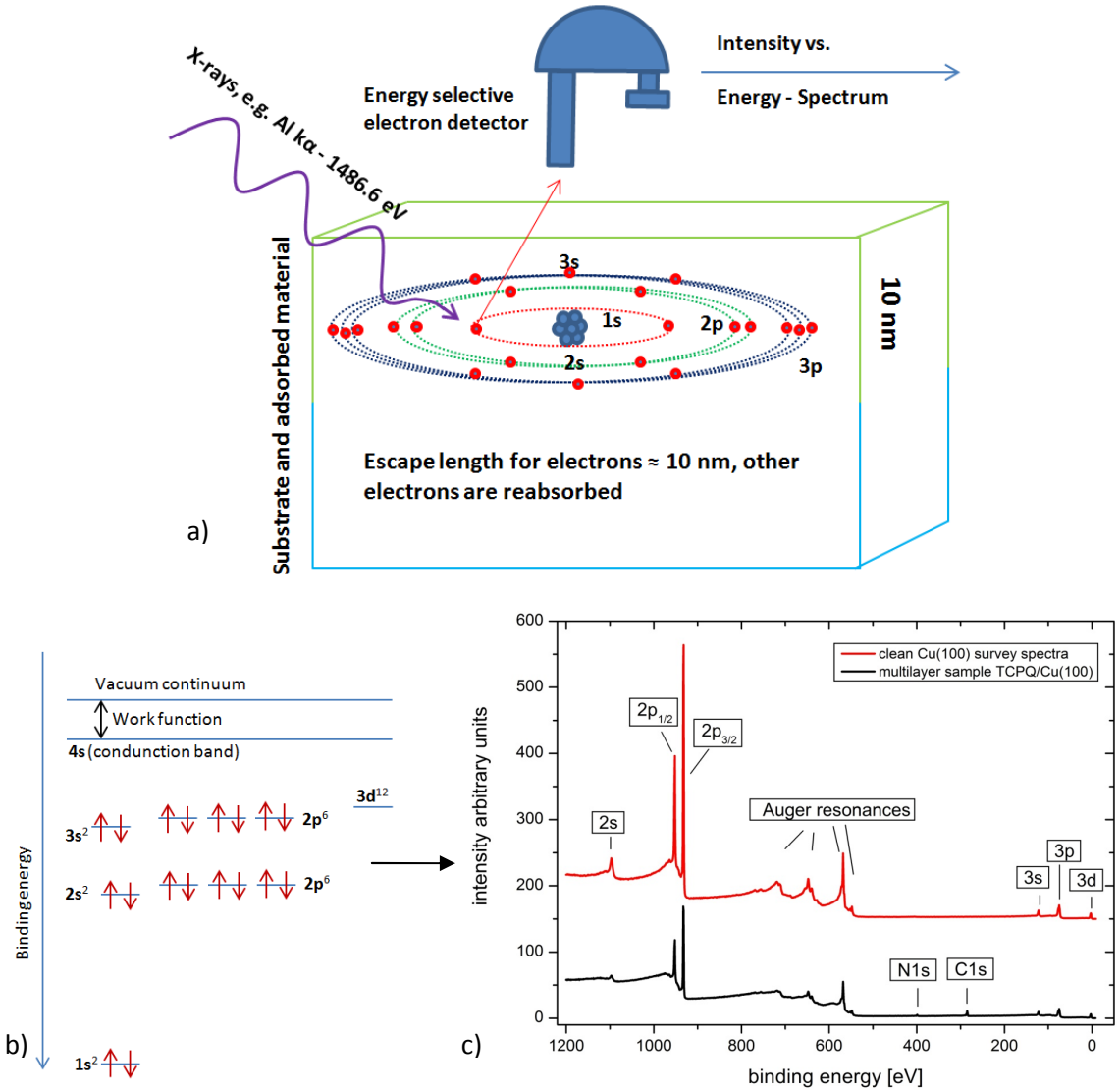

Figure 5: XPS technique: **a)** X-ray radiation leads to the removal of electrons of all shells within the energy range of the incident light. The intensity of these photoelectrons is measured as a function of their kinetic energy (spectra in **c)**), providing information about their origin and chemical state **b)**.

XPS is a spectroscopic method which is based on the photoelectric effect. If the energy hν of a photon is larger than the binding energy E_b of a core level electron in an atom ($h\nu > E_b$), then the electron-photon interaction can excite and remove the electron. The energy of the exciting light must therefore be in the range of keV. The electron leaves then the atom with a kinetic energy E_{kin} that carries chemical information about the atom of origin. The intensity of these photoelectrons is measured in a detector as a function of their kinetic energy (Fig. 5). In order to quantify this energy, it has to be taken into account that electrons gain energy in the absorption process in the analyzer. This energy gain is equal to the work function difference $\Delta\phi = \phi_{detector} - \phi_{sample}$ of the electron analyzer and the sample (Fig. 6). The equation of Einstein for the photoelectric effect yields then:

$$E_{kin} + \phi_{detector} = h\nu - E_{bind} + \phi_{sample} \rightarrow E_{bind} = h\nu - E_{kin} + \Delta\phi$$

The measured binding energies can provide two types of information about the samples. On one side, the core level binding energies of two neighboring elements in the periodic table vary more than 100 eV ($E_{b,\,N1s} - E_{b,\,C1s} \approx 115$ eV). Literature values help therefore to identify clearly the involved chemical elements. On the other side, the binding energy of core level electrons of an atom changes slightly (between 0.1 - 5 eV) if the bond configuration changes. This is called chemical shift and will be discussed later in this chapter.

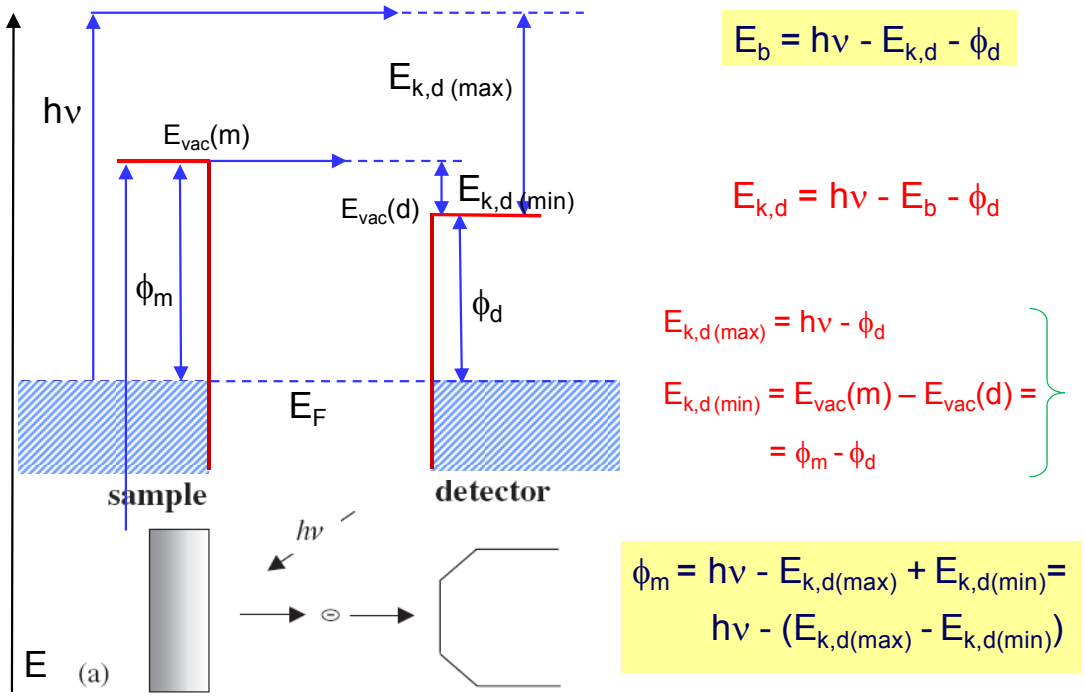

Figure 6: Energy diagram of processes photoelectrons undergo: Electrons from states with a binding energy smaller than the photon energy subtracting the work function are removed from the sample. Not all reach the detector where the local work function changes the kinetic energy of the electrons upon absorption due to the different analyzer work function. The spectrum consists of a fraction of the excited electrons due to losses and due to filtering of the secondary electrons. The ones from the Fermi level exhibit the maximal kinetic energy measured in the detector and electrons at the secondary electron cut-off represent the minimum kinetic energy measurable. Subtracting from the photon energy the "width" of the measurable spectrum yields the sample work function.

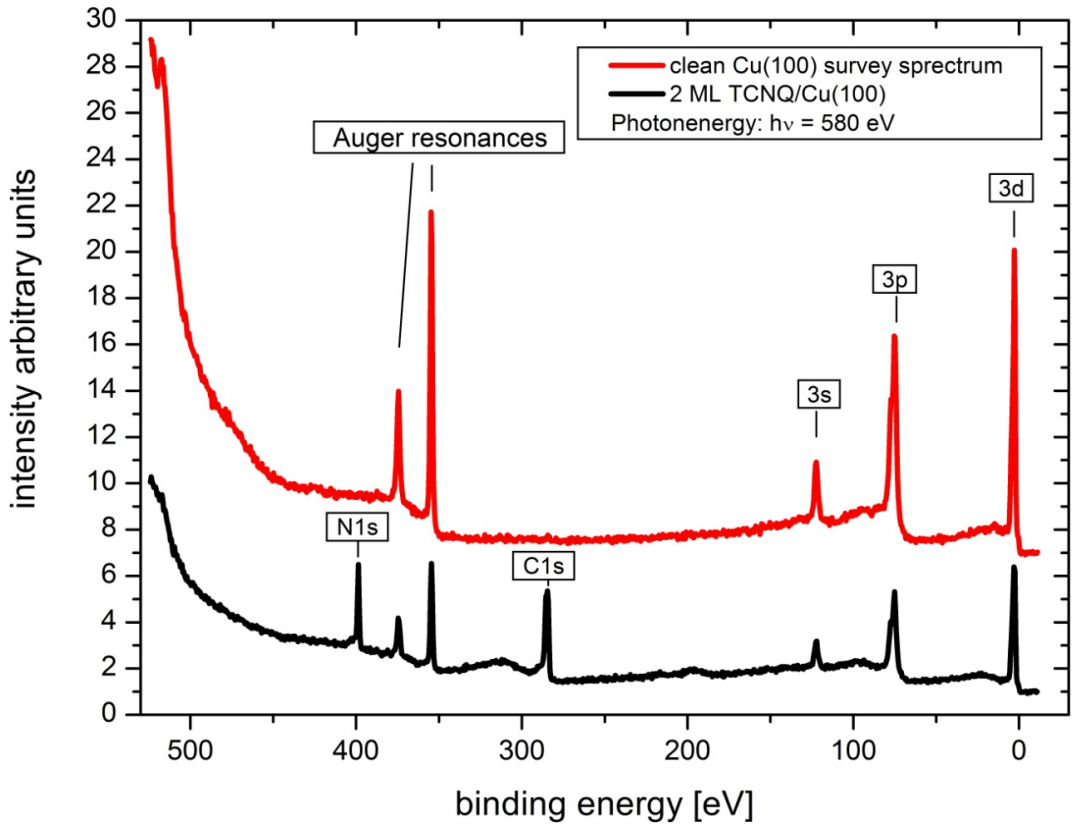

Figure 7: Typical XPS-spectra of Cu(100) at a synchrotron radiation facility: The excitation energy of the light is 580 eV and in the spectrum of the clean sample some characteristic peaks from the shells close to the Fermi level can be seen. Auger resonances from the L-absorption edge are also present. In the spectrum of the samples with the molecules on the substrate additional peaks provide information about the chemical elements on the surface. The peaks can be identified with literature values of the binding energy: carbon and nitrogen.

2.2.1.1 Quantitative analysis

A quantitative analysis of the chemical composition can be obtained after recording a spectrum of a sample because the photoelectrons contain in principle information about the stoichiometry in or on the measured surface. A spectrum is obtained measuring the electron intensity as a function of the binding energy (Fig. 7). It shows the part of the electronic configuration from the Fermi level to deeper lying states, depending on the photon energy. The occupied states of the investigated sample appear in the spectrum as a number of characteristic peaks on top of an electron background (Fig. 7). The area of any of the peaks from one element is a measure of the amount of this material in the surface or on top of it. The peak area a_{ij} of the peak j from Element i can be expressed in the following way:

$$a_{ij} = n_i \cdot A \cdot T(E_{kin}) \cdot L_{ij} \cdot \sigma_{ij} \cdot \lambda(E_{kin}) \cdot \cos(\theta).$$

n_i is the atomic concentration of element i, A is an instrument constant, $T(E_{kin})$ the transmission function of the analyzer, L_{ij} represents the angular asymmetry factor of orbital j of element i, σ_{ij} is the photoionization cross-section of peak j of element i, $\lambda(E_{kin})$ is the inelastic mean free path

length and θ is the emission angle (angle with the surface) of the photoelectrons. In this way the experimental atomic concentration c_i of a sample surface can be determined.

$$c_i = \frac{n_i}{\sum_i n_i} = \frac{\frac{a_{ij}}{\sigma_{ij}\lambda(\mathrm{E}_{kin})}}{\sum_i \frac{a_{ij}}{\sigma_{ij}\lambda(\mathrm{E}_{kin})}}$$

Defining the sensitivity factor $s_i = \sigma_{ij} \cdot \lambda(E_{kin})$ of the core level j of element i leads to :

$$c_i = \frac{\frac{a_{ij}}{\mathrm{s}_i}}{\sum_i \frac{a_{ij}}{\mathrm{s}_i}}$$

X-ray sensitivity factors can be found in the literature[6] and thus, by comparing the concentrations of all elements, the expected element ratio from the chemical model of the adsorbates can be verified (e.g. C:N-ratio, Chapter 4, the sensitivity factors in this thesis are taken from the home page[6] of the synchrotron radiation facility ELETTRA in Trieste, Italy). Stoichiometry can thus give detailed information about chemical reactions possibly taking place on the surface or to ensure, for example, that the molecules are adsorbed in an intact and unchanged way after the sublimation.

2.2.1.2 Chemical shift

The chemical environment, which is the specific combination of all direct bond partners of an atom, influences the binding energy of electrons. A change of a bond partner will therefore cause a shift of the binding energy. The process of oxidation of carbon can be identified, for example. The binding energy of an electron of a carbon atom bound to other C-atoms is increased upon oxidation because the large electronegativity of oxygen polarizes the new C-O-bond with a larger negative charge density on the side of the O-atom than in the original C-C-bond. The reduced electron density on the C-atom increases the attractive interaction of the core with the electrons and the binding energy of the electrons grows slightly. This shift can be measured. A shift in the opposite direction is observed when negative charge is added to an existing bond. Then the binding energy of the bound electrons of all involved atoms reveal a shift in the direction of lower binding energy, since the larger screening of the attractive positive nucleus makes less costly to remove an electron. The chemical shift is usually between 0.1 eV to 5 eV, and leads often to the existence of several very close peaks from the same element but with different chemical environments. A deconvolution based on the experimental spectra, literature values, apparatus characteristics and experience has to be done to obtain quantitative results. Such an XPS-analysis can yield results about the relative amounts of a specific element in different bonds or charge states. For example, due to a

different charging of the cyano groups, the contact with the surface of the first molecular layer (XPS section, Chapter 4) leads to a different binding energy of the nitrogen core levels compared to the topmost layers, which are isolated from the substrate.

2.2.1.3 Work function

Secondary electrons from the sample background which reach the detector with zero kinetic energy define the start of the energy scale (Fig. 6). This point in the spectra is called "secondary electron cut-off" (SECO). The Fermi edge on the other side of the energy spectrum is defined by electrons with the maximum kinetic energy (or with the minimum binding energy): this is the end of the energy scale. The work function can therefore be calculated subtracting from the photon energy the difference between the minimum and the maximum kinetic energies or the start and the end of the energy scale. This method is independent of the detector work function (Fig. 6):

$$\varphi = E_{photon} - (E_{SECO} - E_F)$$

In order to measure the SECO of the sample, a negative bias voltage (often -5 or -10 V) is applied to the sample to displace the spectrum and identify doubtlessly the electron cut-off related to sample electrons from those coming from the analyzer.

As described already in the introduction, a charge transfer leads to an induced dipole at the interface between the adsorbate and the surface. This dipole moment is then responsible for a change in the energy, necessary to remove an electron from the interface region of the surface. This change in the work function is therefore a direct measure of the interface dipole and can then (with the help of the theory) be related to a charge transfer process.

2.2.1.4 Screening effect

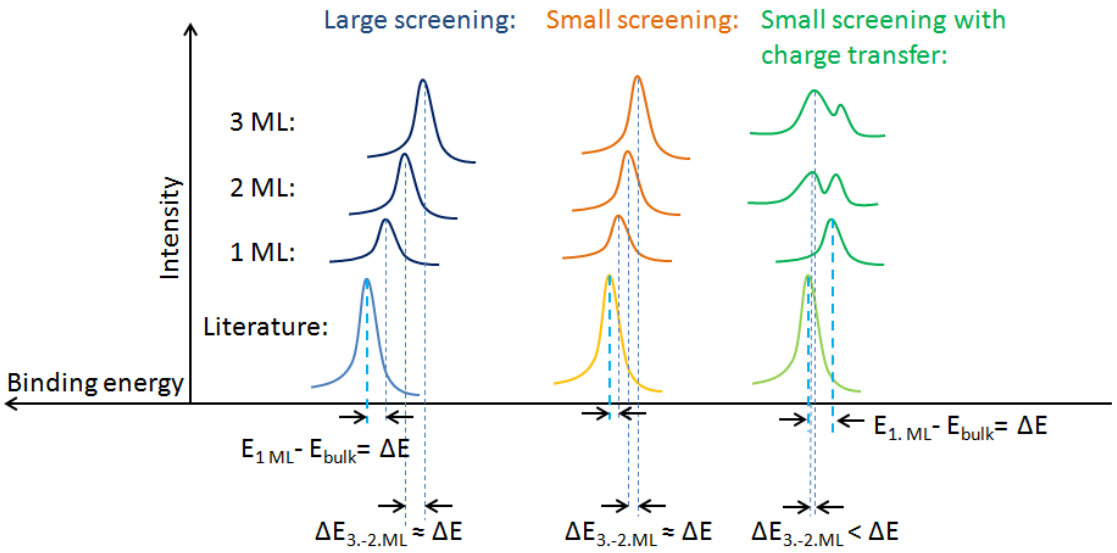

Figure 8: Schematic illustration of a strong (left case) and a small screening effect (center case) compared to the situation with an additional binding energy shift caused by charge transfer (right case): A screening causes a binding energy shift of all peaks of adsorbates on metal samples, and has been observed for thicknesses up to three layers[7]. The binding energy values of a material deposited on a metal substrate are therefore different than in the bulk form. The strength of the screening can be estimated roughly by the binding energy shift rate with coverage in the regime of a few monolayers. If the shift rate is small (center case), a small difference between binding energies values of the pure compound and the corresponding component in the first three layers on the metal sample would be expected. Only if another effect, like charge transfer, changes the binding energy of the first layer, a bigger shift to the bulk literature value will be observed (right case).

Metal samples have very mobile electrons at their surfaces. The core hole of an excited atom attracts therefore negative charges which can screen the electric field of the core hole immediately after its creation. This can decrease the energy which is necessary to bring a photoelectron to the vacuum level compared to the situation without the metal. Screening can therefore shift the binding energy and has to be taken into account when interpreting the energy positions of the core level electrons.

An experimental possibility to identify and estimate the strength of the metal screening effect is to compare the binding energies of a core level from samples with varying thickness (few monolayer regime, Fig. 8, left and center cases). A strong screening effect in Xenon layers on palladium has been observed, for example[7]. There, the core level binding energy of the Xe $5p_{1/2}$-peak of a bilayer sample is shifted several eV compared to the monolayer and an energy difference of some eV is also observed from the bi- to the trilayer sample. These shifts are related to the screening by the metal substrate. The comparison of these binding energy shifts provides thus a method to estimate the strength of a screening in other adequate systems. A large binding energy difference between the second and third layer indicate therefore a strong screening by the surface (Fig. 8, left case). A small shift between a bilayer and trilayer sample would be related to a weak screening effect (Fig. 8, center case). If additionally, in the case of a weak screening effect, a shift of the binding energy between the first layer and a bulk sample (or the literature value for the pure compound) is observed (Fig. 8, right case), then another

effect, like charge transfer, must involved. A charge transfer would affect mainly the organic material in direct contact with the surface, in contrast to a screening effect which influences several layers (Chapter 4). This method provides the possibility to estimate roughly the binding energy shift caused purely by a screening of the metal surface. Comparing this estimation to the shift of the binding energy between a monolayer and the second layer can reveal the existence of other effects, like charge transfer, with an influence on the binding energy of the layer in direct contact with the surface.

2.2.1.5 Shake-up satellites

A “shake up”-resonance is a peak appearing at the high binding energy side of a core level peak, displaced some electrons volts. This phenomenon can be observed in high-resolution spectra of all elements (N1s- and C1s-regions, for example) of a sample that contains aromatic structures, unsaturated bonds, transition metal ions or the element nitrogen, for example. In a naive picture, part of the photoelectrons removed from a core level is considered to interact with the frontier orbitals exciting an electron from the valence band to an unoccupied level. The photoelectron decreases then its kinetic energy, giving rise to a satellite in the low kinetic energy side (high binding energy side) of the main peak. (This is incorrect for a quantitative theory, however.) In the case of organic molecules, the excitation usually takes place from the HOMO to the LUMO. However, the energy difference between the shake-up satellite and the main peak does not correspond exactly to the energy gap, because the transition between the neutral organic compound and the ionized molecule has to be considered.

2.2.1.6 Surface sensitivity

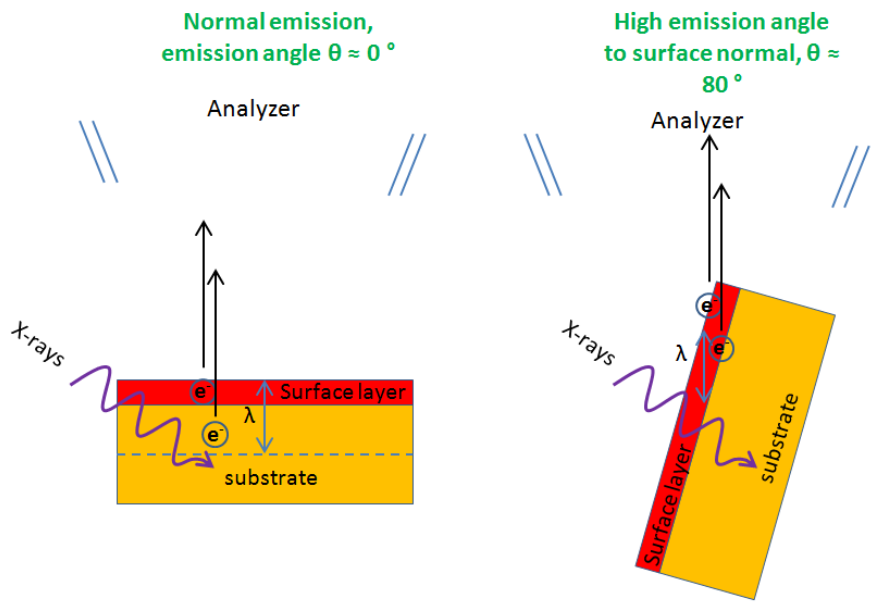

Figure 9: Comparison of photoelectron contribution to the measured intensity under different emission angles θ: As the mean free path limits the measurement of photoelectrons to a thin surface region of the sample, changing the emission angle causes a higher portion of electrons from an even smaller surface region to be detected with the same mean free path λ.

In XPS, only a part of all excited electrons reach the detector with its original kinetic energy, because depending on the position of the ionized atom within the solid, the photoelectron may interact with other particles or quasi-particles. The mean free path is therefore defined as the average distance an electron travels without any interaction which could change the kinetic energy. With the mean free path an estimation for the width of the surface layers contributing to the detected photoelectrons is possible, because the closer the position of the excited atom within the solid to the surface, the larger is the escape probability of the photoelectrons. In general, only electrons from the first 10 nm of a solid surface reach the analyzer, although the mean free path depends on the kinetic energy in a way described by the "universal curve"[8]. That dependence can be used to select the photoelectrons and to achieve even higher surface sensitivity which in our case is important, because the amounts of organic material are adsorbed on the surfaces are usually small. Therefore, a kinetic energy of about 100 eV is desirable, because then, the detected photoelectrons with the chemical information originate only from a surface region of a few nm[9], all other electrons are reabsorbed within the solid or loose kinetic energy in inelastic processes. The optimum surface sensitivity adjusting the kinetic energy of the photoelectrons can only be achieved at synchrotrons. With a fixed energy from a laboratory source a geometrical optimization can be done to obtain a maximal surface sensitivity. The angle of the surface towards the detector can be changed from normal emission (analyzer receives electrons escaping the substrate under 90 ° to the surface) to a high electron emission angle which leads to the detection of photoelectrons leaving the sample at a small angle to the surface (Fig. 9). With the same mean free path more

photoelectrons from the surface layer reach the detector compared to normal emission, because the mean free path λ limits electrons from the deeper layers to escape the solid under this angle.

2.2.2 Technical details

2.2.2.1 Light sources

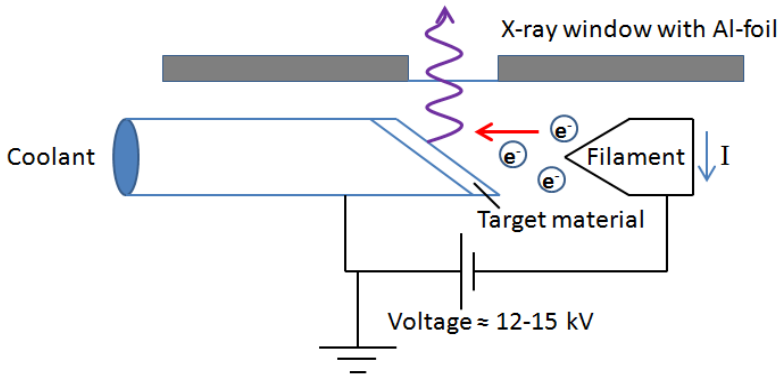

Figure 10: Schematic diagram of an x-ray source: Electrons from a hot filament are accelerated by a voltage of 12-15 kV onto the anode material where x-rays are excited due to the relaxation of an ionized aluminum target. The light leaves the source through a window while the electrons are retained by a foil.

The light can be provided by laboratory sources with different metal anodes or at particle accelerators, which emit synchrotron radiation of a wide spectrum (in our case, Chapter 3, at BESSY in Berlin, for example). In the latter case the necessary energy can then be selected with tunable monochromators. This is an advantage over fixed laboratory source because the surface sensitivity can thus be adjusted considering the escape length of photoelectrons.

The used x-ray source in our laboratory, XR 50 M from SPECS, provides photon energy of 1486.6 eV by the aluminum K α-transition, which is excited by electrons from a filament. These electrons accelerate due to a voltage up to 15 kV (400 W) and hit the aluminum anode. The anode atoms are excited and relax emmiting x-ray radiation (Fig. 10). In order to avoid an overheating of the anode material a coolant (water) must take away the thermal energy, which otherwise can damage the target material. A second anode, parallel mounted to the Al-target, provides the possibility to produce x-rays with higher energies (Ag L α = 2984 eV, 600 W).

2.2.2.2 Monochromator

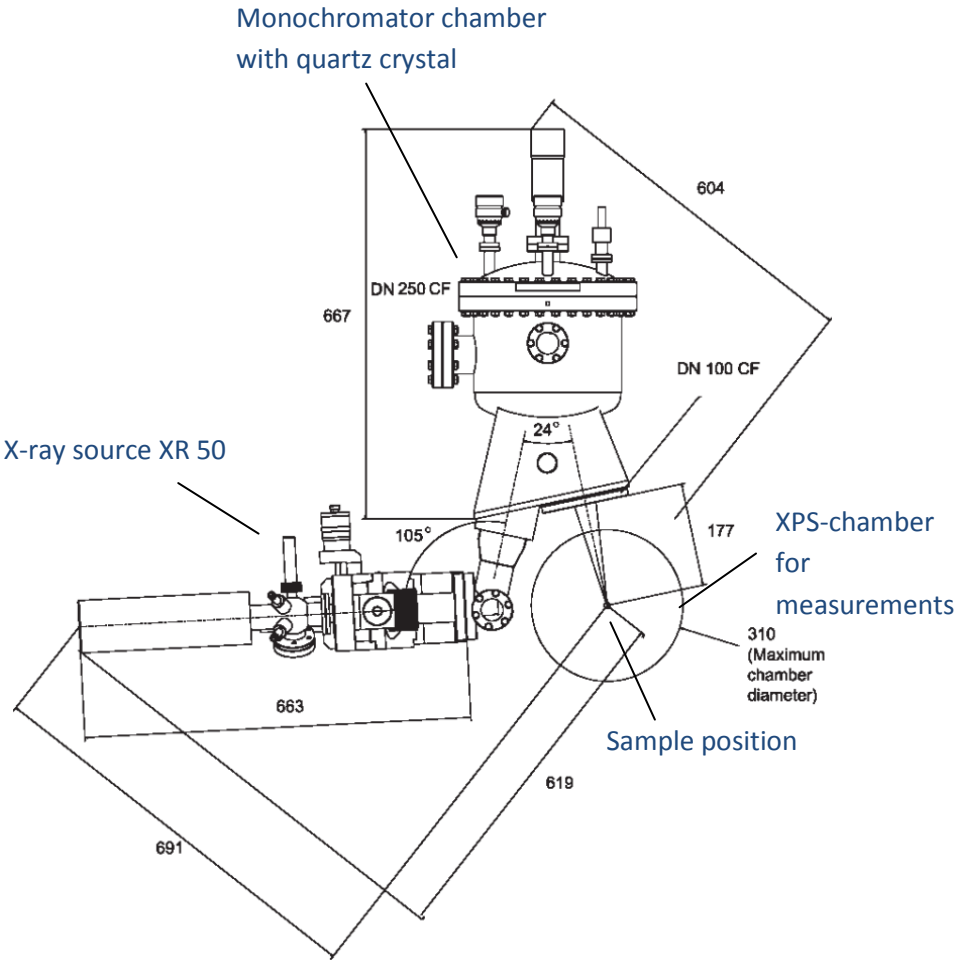

Figure 11[taken from SPECS homepage 10]: Dimensions of the monochromator with the x-ray source: The source produces Al Kα or Ag Lα x-ray radiation which is reflected and focuses by the ellipsoidal quartz crystal inside the monochromator chamber onto the sample. The quartz position and angles can be adjusted from outside of the UHV.

Our XPS chamber is equipped with a commercial, ellipsoidal quartz crystal monochromator from SPECS, FOCUS 500, to reduce the line width of the x-ray source (Fig. 11). The functioning is based on Bragg's Law:

$$2d\sin\theta = n\lambda$$

The x-ray source emits radiation in the direction of the crystal which reflects and focuses the light on the sample (Fig. 12). A specific wavelength λ is selected by mounting the crystal under an angle θ, adjustable in a small range (n is the diffraction order and d is the distance of the planes of the quartz crystal). Depending on the desired energy and the used anode, the first order Bragg reflection for the aluminum target or the second order for the silver anode can be selected. The reflected intensity versus the angle of incidence of the X-rays for a given crystal type is known as the rocking curve. For quartz crystals the rocking curve width is about 160 meV which provides the basic energy resolution of the x-ray source. The experimental energy resolution of the system is usually obtained measuring the Ag $3d_{5/2}$-peak of a silver sample. In

our case the full width at half maximum intensity is 0.8 eV at a pass-energy of 12 eV (400 W, 15 kV, Al Kα-anode, non focusing mode and 600 kcounts).

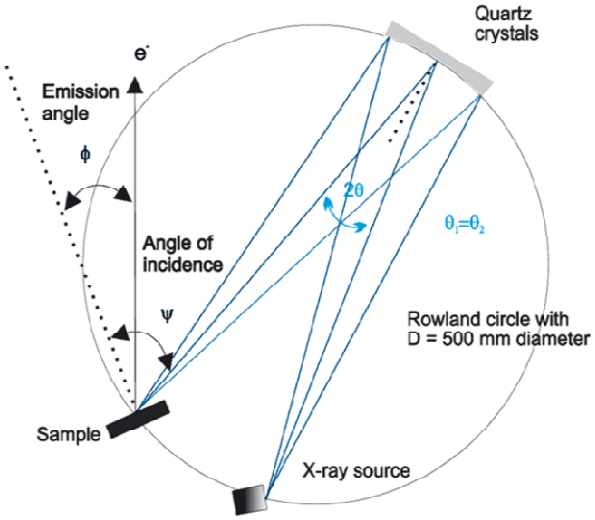

Figure 12[taken from SPECS homepage 10]: Schematic path of x-rays: From the source the x-rays fall onto the ellipsoid quartz crystal which reflects only a small part of the radiation around the desired wavelength onto the sample. All three elements lie on a circle, the Rowland circle. The line width of the x-rays is thus reduced.

2.2.2.3 Electron energy analyzer

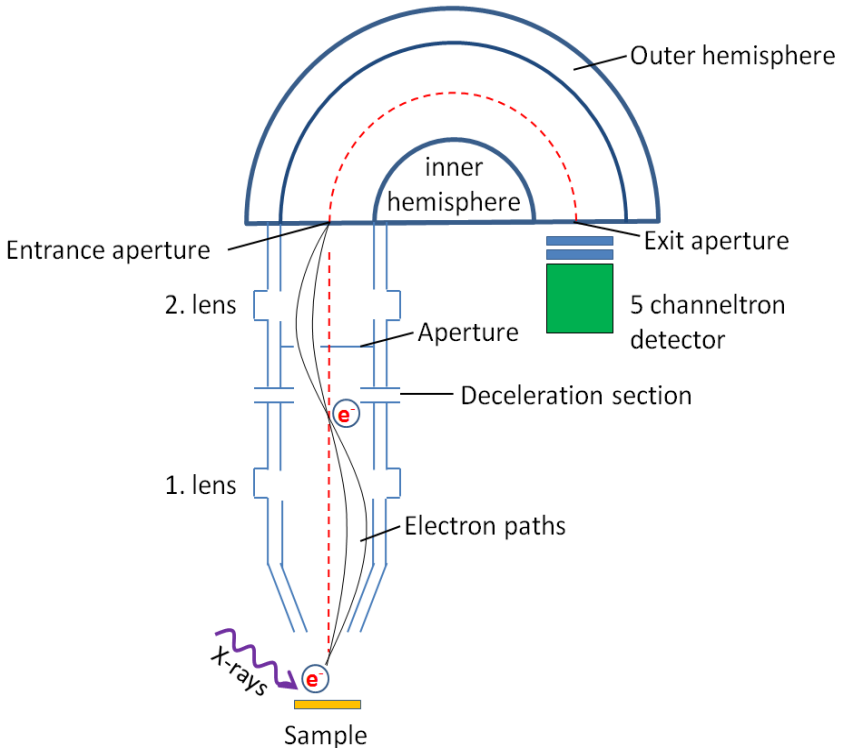

Figure 13: Schematic draw of PHOIBOS 150 electron energy analyzer: The x-ray electrons excited from the sample are collected and transmitted by electrical lenses into the hemispherical energy analyzer. The detectors, in our case, are 5 channeltrons.

The commercial detector-set from SPECS, "PHOIBOS 150 MCD 5", of the XPS-system consists of an electrical transfer lens system for the photoelectrons at the entrance, a hemispherical energy analyzer and five exchangeable channeltrons (Fig. 13). The work function has been determined to be 4.51 ± 0.03 eV. Several pairs of entrance slits and exit slits can be used from outside the UHV to optimize the energy resolution and the angular spread of the photoelectrons. The detector can be operated with many different lens modes in order to adapt to angular or spatially more resolving studies.

2.2.2.4 Line widths

The natural irreducible line width Γ of a core level state depends on its lifetime:

$$\Gamma_{natural} = \frac{2h}{\tau}$$

h is Plank's constant, τ is the core hole lifetime.

It can be shown[11] that the peak-shape of any transition has therefore originally Lorentzian character but the experimental set-up broadens the natural line width by inhomogeneous

broadening mechanisms with a Gaussian line shape, the measured XPS-peak is therefore a convolution of both types of line shapes. The total line width w_{total} can be written as:

$$w_{total} = \sqrt{\Gamma_{natural}{}^2 + \Gamma_{x-rays}{}^2 + \Gamma_{analyser}{}^2 + \Gamma_{surface\ charge}{}^2}$$

Γ_{x-rays} is the line width of the exciting light which irradiates the sample, $\Gamma_{analyser}$ is the line width of the analyzer depending on it characteristics (e.g. geometrical properties, electrical lenses) and $\Gamma_{surface\ charge}$ is a contribution to the line width cause by a surface charge when the sample is insulating. The use of a monochromator reduces Γ_{x-rays} and the entry slits of the analyzer reduce $\Gamma_{analyser}{}^2$, at the expense of the number of measured electrons. If there is a surface charge, it can be reduced by improving the conduction or providing electrons (low energy electron flood gun).

2.2.2.5 Energy calibration

Every electron analyzer has different physical properties, like the work function or geometrical characteristics. These system properties influence the measured energies and in order to be able to compare to literature values, all experimental XPS spectra have to be calibrated to a reference peak, well known in literature. Usually substrate peaks serve as good energy reference because the photoelectrons from deeper layers exhibit always a constant binding energy. In contrast, peaks from the deposited material can change due to possible surface reactions. In all XPS-data here presented (Chapters 3-4), Cu(100) is the substrate and the Cu2p- (932.6 eV[12]) or the Cu3p-peaks (75.1 eV[13]) are used as a reference.

2.2.2.6 Background intensity

The background signals in a XPS-specrum originate in photoelectrons which have interacted inelastically on their way to the detector. They have lost kinetic energy and appear therefore on the higher binding energy side of the peak related to the state where they originate from. This leads to a stepwise increase in background going from low binding energy to high binding energy, after every intense peak. These secondary electrons cause an intense tail ranging from 0 eV kinetic energy ($E_{bind} = E_{hv} - E_{kin}$ = 580 eV) to about 100 eV (E_{bind} = 480 eV) into the spectrum (Fig. 14)

In order to simplify the peak analysis of a high resolution spectrum in a specific region, sometimes a background treatment is suggested. It consists of subtracting a spectrum of the clean substrate from the spectra of the surface with adsorbates. This provides a method to disentangle the measured peaks from the substrate contribution, especially in the case of submonolayer coverage, where the substrate features can be a strong part of the spectra. Although the substrate features are slightly attenuated by the material on top and a subtraction of a clean sample spectrum overestimates therefore slightly the contribution of the surface, this background treatment works well, as can be seen in the example of N1s-spectra in the XPS-section of Chapter 5 and is explained in the appendix of Chapter 5.

2.2.2.7 Necessity of UHV:

UHV is fundamental in surface science in order to achieve a well defined and atomically clean surface during the measuring time. Ambient pressure would lead, on one side, to the absorption of unknown compounds on the sample and, on the other, to oxidization reactions of the substrate or the organic material deposited on the surfaces. Additionally, for XPS a technical limit is that the electrons have to be able to reach the detector, which is often about a meter away from the sample. UHV provides therefore the necessary mean free path for the photoelectrons, but limits the technique to solid samples, although in the last years new differential pumping methods have been developed which also allow the measurement at ambient pressures by differential pumping methods.

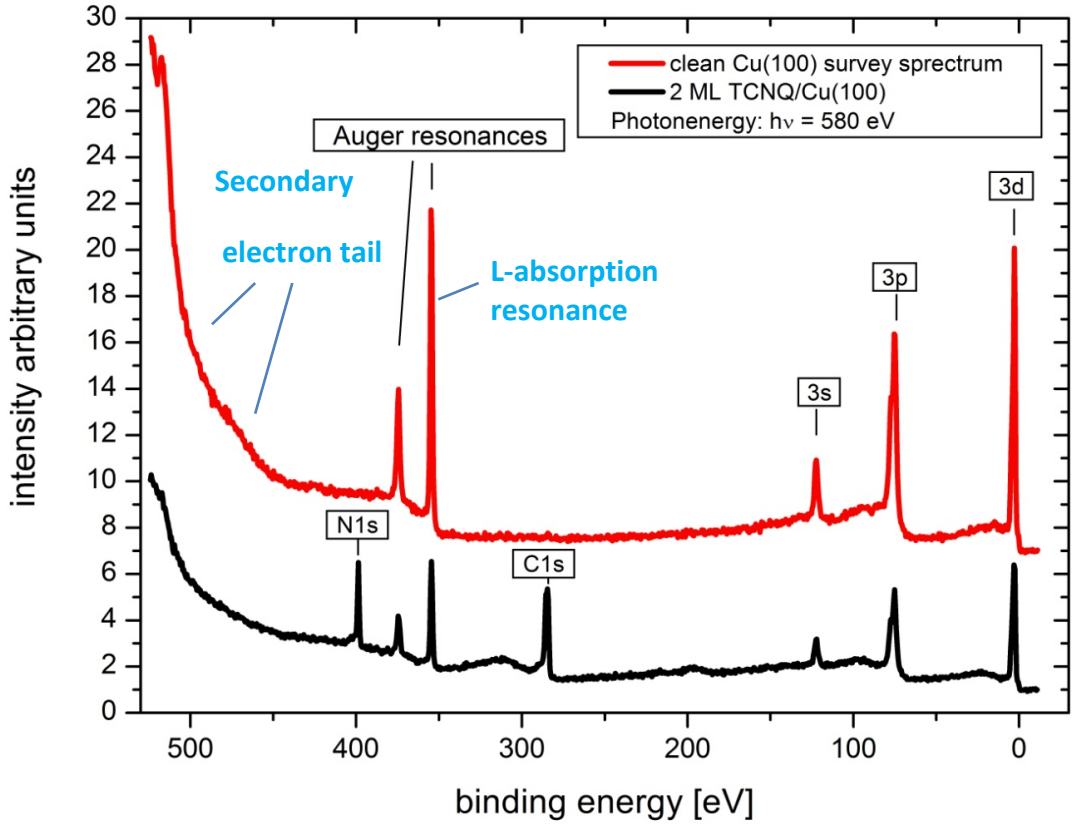

Figure 14: XPS-spectra of Cu(100) at a synchrotron radiation facility: The excitation energy of the light is 580 eV and the secondary electron cause a broad peak from 0 to about 100 eV kinetic energy (which means 580 to 480 eV binding energy). The tail can be seen at the high binding energy side of the spectra. Some Auger resonances from the L-absorption edge caused by the removal of the Cu 2p3/2- and Cu 2p1/2-electrons can be seen, too (at 352.6 eV).

2.2.3 X-ray absorption spectroscopy (XAS)

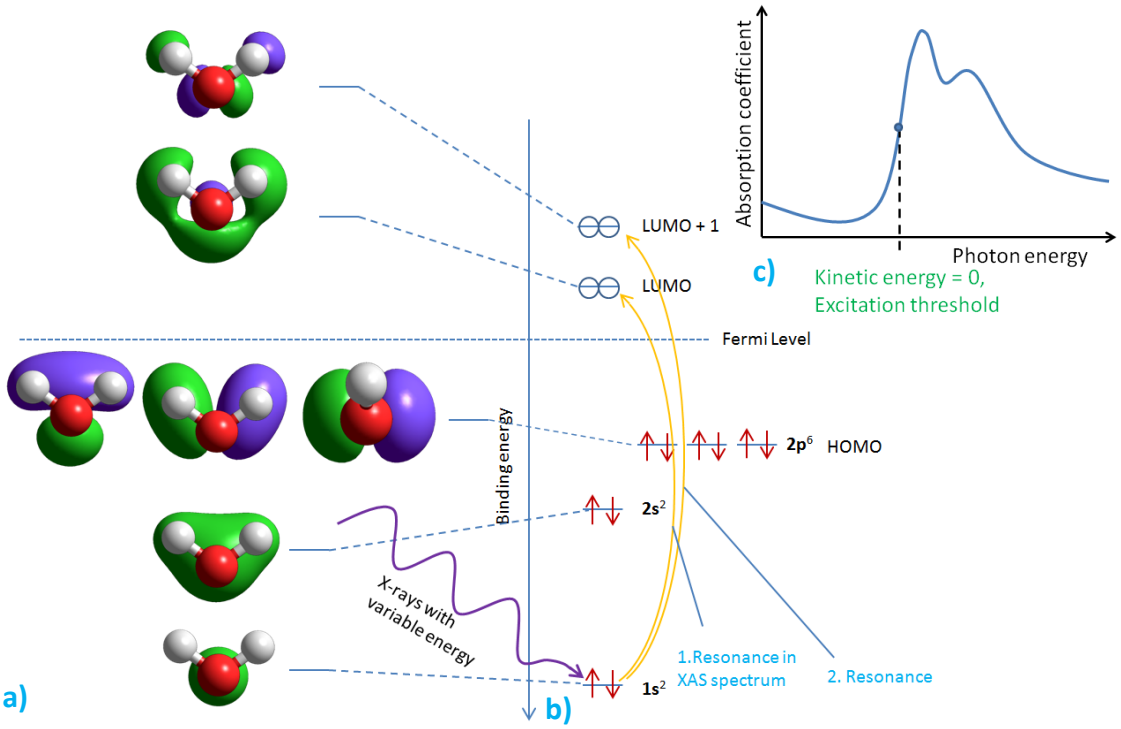

Figure 15: Working scheme of XAS: On the example of a water molecule with the molecular orbital in **a)**, the energy levels are shown, **b)**, and the transitions which occur, if the exciting energy exhibits the energy difference between an occupied and an empty state. Every atomic shell (n=1, 2…) gives rise to a new excitation threshold in the spectrum in **c)**, and every transition (yellow arrows, b) produce a peak in the XAS spectra, c).

X-ray absorption spectroscopy (XAS) is a powerful technique to study the electronic structure: varying the wavelength of the exciting x-ray radiation electron transitions from occupied core levels to empty states or to the ionization continuum of a medium can be produced (Fig. 15). Only synchrotrons provide the possibility to change the photon energy continuously. Provided that the x-ray energy is big enough to excite core levels, the general form of a XAS-spectrum consists of a series of excitation thresholds corresponding to the excitation from the shells n=1, n=2, n=3 and so on, called K-, L-, M- … edges. The K-edge is a single edge. Higher edges are a collection of edges close together, because L- and higher edges, with more than one orbital angular momentum, participate in more transitions. The region from 0 to 50 eV above an edge shows spectroscopic fine structures of a type which contains details about the unoccupied density of states and the transition probability, apart from other information. This region of the spectra is called near edge absorption fine structure (NEXAFS) and we will focus in the following only on that particular region of XAS spectra.

2.2.3.1 Near edge x-ray absorption fine structure (NEXAFS)

Although the NEXAFS region may be very complex (it is determined by details of the final density of states, the transition probability, resonance and many-body effects), it can reveal the geometrical orientation of empty orbitals of adsorbates on surfaces, which helps to determine the adsorption geometry of molecules[14]. For that reason the K-edges, which are single edges, of carbon or other light elements are studied. As previously mentioned, in XAS the photon energy is varied continuously to excite different electron transitions. X-ray photons with the right energy for transition of 1s-core level electrons into the empty states cause peaks at the K-edge, each corresponding to at least one unoccupied orbital. The electrons after the transition can relax by different mechanisms, emitting a photon or by ionizing an Auger electron. In lighter elements the Auger process is favored. As the yield of Auger electrons is proportional to the number of core holes, the total yield of Auger electrons provides a measure for the absorption of x-ray radiation. Additionally, the mean free path of Auger electrons is below 10 nm and provides therefore intrinsically a high surface sensitivity. A second method to measure absorption is the total yield detection with a biased metal plate close to the sample, connected to a picoammeter. But in this case, apart from the Auger electrons of the element of interest, other elements and probably contamination contribute to the low energy tail of secondary electron emission. Therefore the spectra have to be disentangled from the influence of the electrons of the substrate and the beam line contamination, which is often done by dividing the spectra of the samples by a normalization spectrum recorded of the clean substrate.

Synchrotron radiation is polarized and the photon absorption by adsorbates on surfaces depends thus on the relative orientation to the incident light. Analyzing the dependence of the dominant resonances in the spectra on the x-ray incidence angle gives information about the orientation of the adsorbates. In a first step the resonances have to be identified. This is often possible even in bigger molecules because, in principle, the core level electrons are excited very locally into the empty states (Fig. 15) and the spectra can be analyzed, in a simple picture, as a superposition of resonances from different functional groups (building block approach). This approach may break down if the empty molecular orbitals are extended over more, chemical identical atoms than only over the atoms of one functional group. Calculations of the location of the empty orbitals can provide this information and moreover lead to an identification of the resonances by their energy above the Fermi level. In smaller adsorbates it is a simpler chemical structure which provides this information. Single bonds are related to transitions into σ*-orbitals which are very broad and some electron volts higher in energy than the narrower peaks related to transition into π*-orbitals. The latter are associated with p-atomic orbitals participating in double, triple and aromatic bonds. Another hint can be provided by a splitting of a resonance which in gas phase is observed as one peak. This can occur among adsorbates with triple bonds due to a different interaction of the π-electrons of these bonds with the surface and identifies the split resonances as the two π*-orbitals related to the triple bond (example in Chapter 3).

After relating the bonds to the observed peaks, the area analysis of one peak at different x-ray incidence angles delivers the angle between the bond and the surface.

2.2.3.2 Theoretical background[15]:

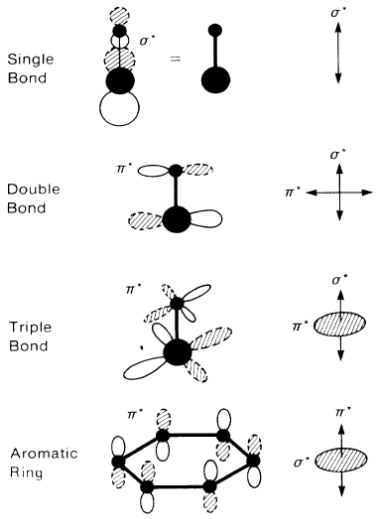

Figure 16[taken from 15]**:** Definition of orbital vectors for the calculation of bond angles with the substrate from XAS-data: A single π*-orbital formed by two p-orbitals of every participating atom of a double bond, lies perpendicular to the sigma bond of these two atoms. A triple bond has an additional π*- orbital orthogonal to the first one and thus a plane is defined parallel to the atomical p-orbitals and represented by it normal vector. In an aromatic ring the σ*-bonds define also a plane and all π*-bonds are parallel, thus a vector can be defined for this case.

The theoretical models are derived from the condition of maximum light absorption when the E-field vector $\vec{E}$ of the x-rays with the correct resonance energy is parallel to the dipole matrix element between the initial core level state and the final empty state. For a σ-bond the direction of such vector is related to the so called bond vector $\vec{\sigma}^*$ along the unoccupied orbitals of the final electron state, (Fig. 16) which is defined parallel to the connection line between two bound atoms. In a double bond the atomic p-orbitals, which form the interatomic π-orbital with its antibonding orbitals π*, are perpendicular to the σ-bond and the defined bond-vector $\vec{\pi}^*$ is parallel to these p-orbitals (Fig. 16). In the case of a triple bond and two degenerate π-bonds, a plane is spanned by two p-orbitals of one atom, called π*-plane which is determined by its normal $\vec{n}^{\pi}$ (Fig. 16). A plane parallel to an aromatic carbon ring along all σ-bonds is defined as σ*-plane also characterized by its normal $\vec{n}^{\sigma}$, while all atomic p-orbitals define again a bond-vector $\vec{\pi}^*$ as previously (Fig. 16). In the analysis, it has to be distinguished therefore between the two cases of vector-like and plane-like antibonding orbitals.

The knowledge about the orbital character (σ*- or π*-orbital) has to be taken into account for the interpretation of the experimental data in order to find the angle of the bond with the normal of the surface. As mentioned previously the shape of the peaks in the NEXAFS spectra can distinguish the two orbital types; also calculations of the orbital energy above the Fermi level can identify the orbital character.

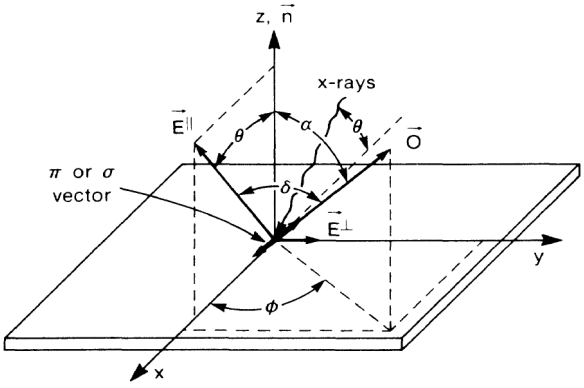

Figure 17[taken from 15] : Coordinate system defining the geometry of a σ*- and a π*- vector-like orbital represented by $\vec{O}$: The incident x-rays are represented by two components of the E-field vector $\vec{E}^{\parallel}$ and $\vec{E}^{\perp}$ with an angle δ to the orientation of the orbital $\vec{O}$ and an angle θ to the normal of the surface, described by its normal $\vec{n}$. The incidence angle θ is changed around the rotation axis y in the experiment and the angle δ is affected which reflects the absorption intensity change.

The E-field vector components of the incident x-ray beam and the surface normal are defined for the vector-like case in Figure 17. The angle between the parallel component of the E-field vector $\vec{E}^{\parallel}$ and the surface normal $\vec{n}$ is θ. The orbital vector $\vec{O}$ represents the bond-vectors $\vec{\pi}^*$ and $\vec{\sigma}^*$. The angle between the orbital vector $\vec{O}$, and the surface normal $\vec{n}$ is α, which is to be determined by the fit of the experimental data. Changing the incidence angle θ influences the angle δ between $\vec{E}^{\parallel}$ and $\vec{O}$ and this affects directly the resonance intensity. In a similar way the geometry can be defined for the plane-like case. Describing then the σ*- and π*-resonances as in the molecular-orbital picture as dipole transitions from s initial states to the p component of the σ*- and π*-final states leads, with Fermi's Golden Rule, to a resonance intensity proportional to the matrix element

$$I \sim \left|\langle f|\vec{E}\cdot\vec{p}|i\rangle\right|^2$$

The electric field vector is $\vec{E}$, $\vec{p}$ is the dipole operator, $|i\rangle$ and $|f\rangle$ are the initial and final states. The intensity can be rewritten:

$$I \sim \left|\vec{E}\cdot\langle f|\vec{p}|i\rangle\right|^2$$

For a 1s initial state, the vector matrix element will be directed along the p-like final-state orbital which transform the equation for the resonance intensity into:

$$I = A\cos^2\delta$$

A describes the angle-integrated cross section and δ is the previously defined angle between the electric field vector $\vec{E}$ and the direction of the final state orbital $\vec{O}$, that means the direction of maximum orbital amplitude. In the plane-like case integration over all azimuthal angles in a plane with the normal $\vec{n}^{\pi,\sigma}$ yields

$$I_P = B\ sin^2\varepsilon$$

with ε being the angle between $\vec{E}$ and $\vec{n}^{\pi,\sigma}$. After expressing the angle δ (ε for the plane like type) as a function of θ (γ, for the plane-like type), the polar angle α and the azimuthal angle ϕ, the angular dependence of the resonance intensities for vector-like ($I_v^{\parallel}, I_v^{\perp}$) and plane-like ($I_p^{\parallel}, I_p^{\perp}$) orbitals within threefold or higher symmetry systems can then be reduced and deconvoluted into the following parallel and orthogonal components of the two orbital types[15]:

For vector-like orbitals:

$$I_v^{\parallel} = A\left(\cos^2\theta\,\cos^2\alpha + \frac{1}{2}\sin^2\theta\,\sin^2\alpha\right)$$

$$I_v^{\perp} = \frac{1}{2}\,\mathrm{A}\,\sin^2\alpha$$

For plane-like orbitals:

$$I_p^{\parallel} = B\left(1 - \cos^2\theta\,\cos^2\gamma - \frac{1}{2}\sin^2\theta\,\sin^2\gamma\right)$$

$$I_p^{\perp} = \frac{1}{2}\,B\,(1 + \cos^2\gamma)$$

In addition, the synchrotron radiation is not perfectly polarized. Therefore the measured peak intensities $I_{v,p}^{total}$ are a linear combination of the parallel ($I_v^{\parallel}, I_p^{\parallel}$)) and the orthogonal ($I_v^{\perp}, I_p^{\perp}$) vector-like (plane-like) orbital contribution weighted with the polarization factors ψ and 1 – ψ (ψ is characteristic for the beam line, 0.8 for the BESSY II synchrotron radiation facility), *C* is a normalization parameter[15]:.

$$I_{v,p}^{total} = C\left(\psi\, I_{v,p}^{\parallel} + (1-\psi)\, I_{v,p}^{\perp}\right)$$

The experimental data can be fitted with the formula of $I_{v,p}^{total}$ using α (γ) and *C* as free parameter.

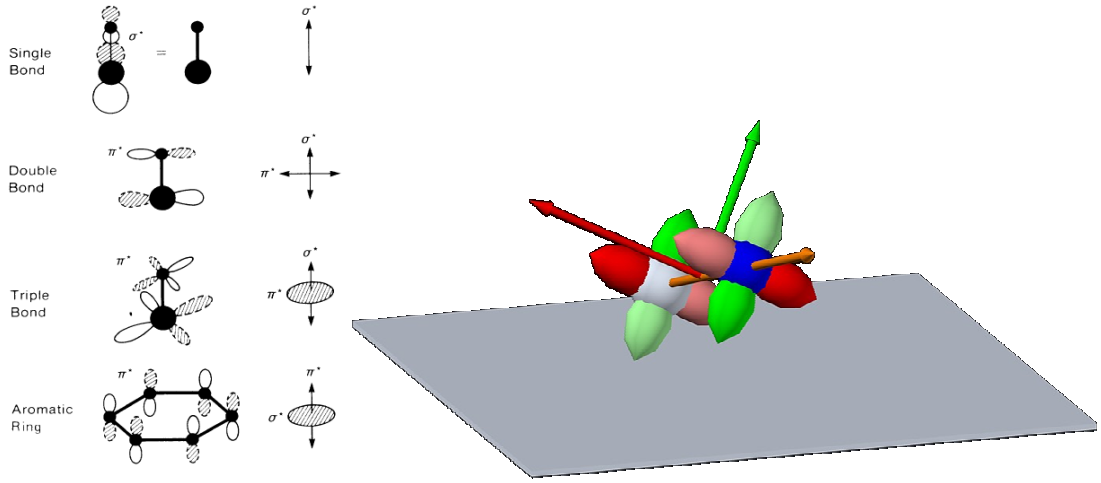

Figure 18: Interpretation of the results for a split triple bond: **a)** Taking into account the definition of the π*- orbitals and the representative vectors which lie perpendicular to the connection between the bound atoms (gray and blue spheres) a solution with two experimentally found vectors (red and green) is shown in **b)**. One π*- orbital is parallel to the red vector and the other to the green one and that defines with the conditions of orthogonality between the two π*- orbitals the direction of the triple bond (orange vector).

The bonding angles with the surface are then in all cases 90 - α or 90 – β, except in a triple bond (recalling the definition for α and β being the angles between the orbital vector $\vec{O}$, and the surface normal $\vec{n}$). A triple bond consisting of two degenerate π*-orbitals can split in energy due to the interaction with the surface (Chapter 3), and then it cannot be treated as a plane like orbital type. The two resonances have to be analyzed first independently in the vector-like formalism for π*-orbitals of a double bond. The two resulting angles are connected by the condition that the π*-orbitals are orthogonal. Regarding the definition of the π*-orbital and the bond direction (Fig. 18 a) shows that the bond angle of the triple bond must be orthogonal to both π*-orbital angles which are also perpendicular to each other (Fig. 18 b). The mathematical analysis reveals that the triple bond angle γ with the surface depends on the split π*-orbital angles as follows:

$$\cos(90° - \gamma) = \sqrt{\sin^2\alpha - \cos^2\beta}$$

An example of the determination of a split triple bond by NEXAFS and the described method is given in Chapter 3.

2.3 TIREMISU UHV-system

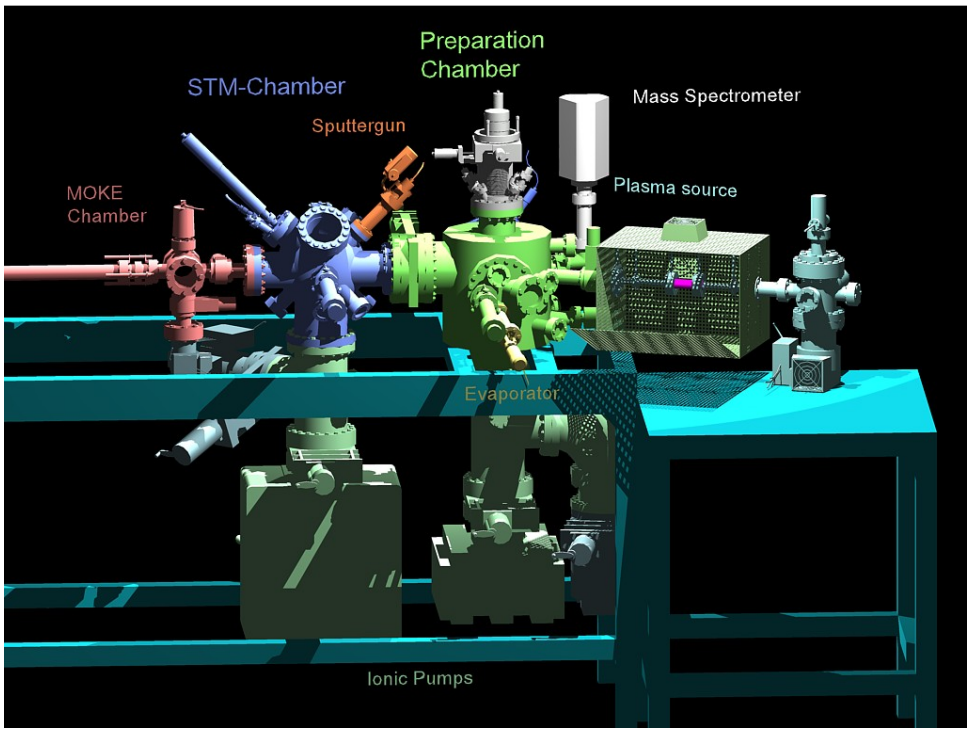

Figure 19: UHV system until 2007: The main chambers were the STM chamber, where the samples were sputtered and annealed and the preparation chamber with a LEED-apparatus on the back. The preparation chamber served to deposit atomic nitrogen from the plasma source or molecules from the evaporator and to control the samples with LEED. The UHV-pumping system consisted of a large turbo molecular pump and two ionic pumps which were placed under the main chambers. A a mass spectrometer, a sputter gun and a linear actuator for the sample bombardment, annealing and storage complete the system. Additionally a small chamber with two windows provided the possibility to integrate a MOKE system. This small extra chamber was used also to deposit molecules.

Most of the presented experimental results have been obtained with the TIREMISU-UHV-system within the surface science group of the “Universidad Autonoma de Madrid”. The original setup (Fig. 19) consisting of an UHV-STM-chamber interconnected to the preparation-LEED-chamber, was first extended with an optimized preparation chamber (Fig. 20). Two years later the system has been completely reconstructed and restructured to integrate an XPS-chamber with detector, monochromator and x-ray source, as part of the present thesis (Fig. 22).

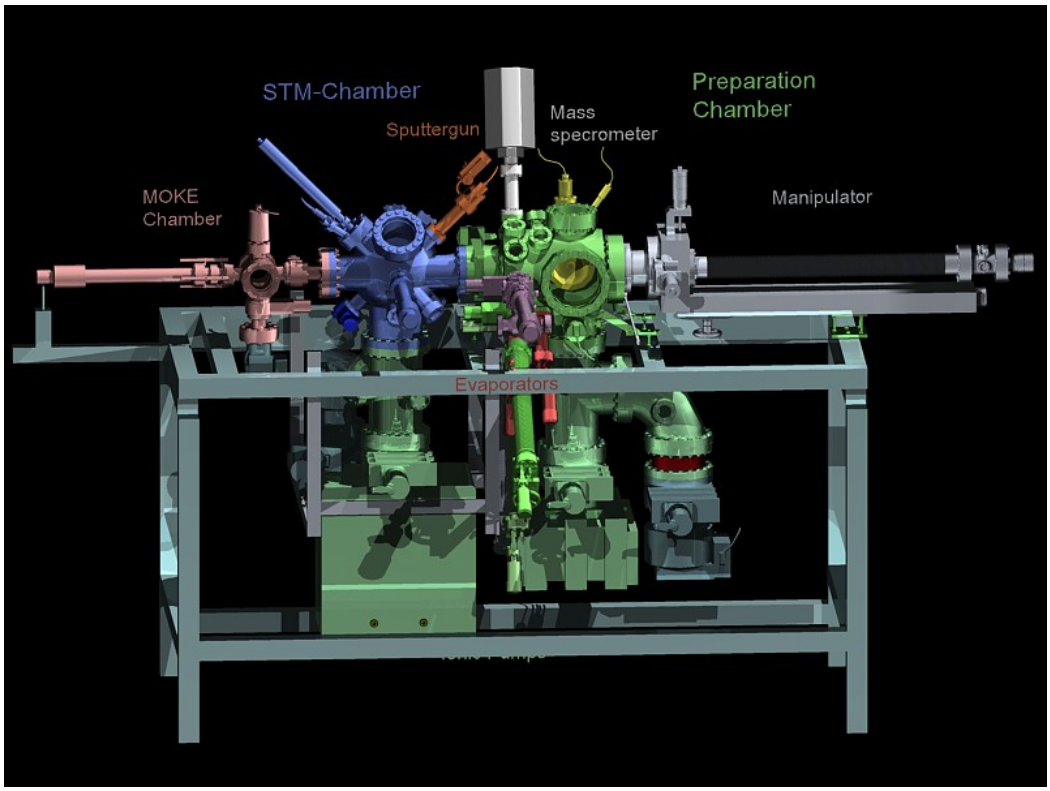

Figure 20: UHV system from 2007 until 2009: The main chamber with the STM has been maintained while the plasma source and the old preparation chamber have been removed. An easy accessible new preparation chamber with the LEED-apparatus and a precision manipulator has been added. The whole sample preparation could be done in the new chamber having a back-up system in the STM chamber for sputtering and annealing. The sample transport and the positioning have been improved by installing a manipulator with z-motor. A small load lock with a manipulator bar has also been added (purple color in front). The possibility to connect a MOKE apparatus and to deposit molecules in the small chamber on the left side of the STM has been conserved, too. The biggest advantages apart from the uncomplicated fast handling were the possibilities to introduce new samples and new molecules without breaking the vacuum and without being limited by the flange number in addition to the possibility of co-depositing different materials.

2.3.1 The new preparation chamber

The old UHV-system consisted of two interconnected chambers (Fig. 20). The main one, which is still integrated in the actual system, hosts a fast scanning, variable temperature Arhus-type microscope (100 - 400 K). In this chamber, the samples can be stored on a linear actuator, where they can be bombarded with Ar^+-ions with a sputter gun and annealed up to 1000 K. With the help of a transfer bar, the samples can be moved between the linear actuator, the STM and a very long transfer bar which brings the samples into the preparation chamber. This transfer was rather complicated but was necessary in order to deposit molecules, use the LEED apparatus or to access the plasma generator. The reasons for the difficulties were the not optimized geometric conditions between the very long, imprecise bar and the tiny sample slot of the manipulator on top of the preparation chamber. As a consequence, a new chamber fully adapted to all needs has been designed, built and implemented as part of this thesis. The

guidelines were: to be able to prepare the sample outside the STM chamber, to have several flanges for depositing material or gases onto the sample and to place a mass spectrometer, a sputter gun and a load lock. Furthermore the new chamber should have a large viewport in front of the LEED instrument, which had to be integrated as well into this new chamber. An X-Y-Z-manipulator was also necessary for a precise movement and positioning of the samples in front of the LEED and the sputter gun. An easy sample transfer to the STM chamber and to the load lock were also basic necessities. A “flange-revolver”- system integrated into a cylindrical chamber with big flanges for the pumping, the viewport, access for the manipulator and the LEED instrument fulfills all criteria. 10 Flanges are arranged in one plane pointing to the long axis of the chamber. Therefore at one specific position the sample can easily be introduced, sputtered, annealed and metals and different organic molecules can be co-deposited by only changing the rotation angle of the manipulator. More flanges of different sizes are available, e.g. for the mass spectrometer, the electro spray deposition system (described briefly in the following), pressure gauges, gas lines and other instruments. With the installation of the new preparation chamber several advantages were achieved: the fast introduction of new samples into the UHV chamber by the new smaller load lock (small pumping volume), the separation of the main sample preparation from the STM chamber, which keeps the latter at an UHV pressure, the very good accessibility to the LEED screen, the possibility of co-depositing all kind of evaporable materials, the integration of the electro spray deposition system (described in the following) and the precise and fast displacement of the samples within the chamber and to the STM.

The integration of a manipulator with the possibility for annealing made necessary the design of an electrically isolated, high temperature resistant sample holder. This has been achieved with the materials molybdenum and macor, which are temperature resistant and the latter additionally electrically insulating. Two sockets, isolated from ground, provide space for the integration of two commercial filaments for annealing. Passive, resistive annealing by current through the filaments and electron bombardment assisted annealing using voltages up to the kV-range is possible. Two thermo couples have also been integrated for temperature control measurement (Fig. 21).

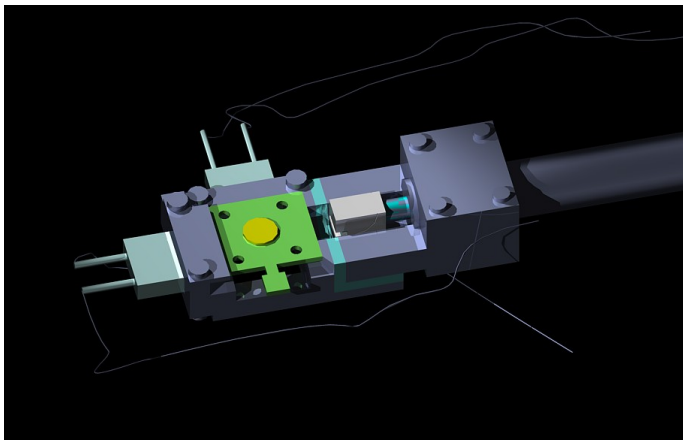

Figure 21: New sample holder for integrated preparation chamber. Samples can be prepared with two independent filaments, electron bombardment included; two separate thermocouples control the temperature simultaneously at two different spots and the sample is electrically isolated from ground.

2.3.2 Actual system with integrated XPS

The next step in 2009 has been to integrate a complete XPS-apparatus in the existing working system (Fig. 22). This consists of a hemispherical electron analyzer and a monochromatic x-ray source mounted in a new XPS-chambe. The photon energy can be chosen in-situ between 1486.6 eV (Al Kα-transition) and 2984 eV (Ag L α –transition) due to two parallel targets. The line width of the radiation is reduced in a monochromator between the x-ray source and the XPS-chamber. In order to be able to rebuild the complete system without finding geometrical constrains, the planning for the positions of all components has been done in a 3D-design program (AutoCAD). After adapting the commercial XPS-chamber in length and dimensions before fabrication, the existing system was demounted completely in order to bring it to the right position on the aluminium frame. Then the XPS-components have been connected and equipped with additional pumping and another precise X-Y-Z-manipulator. In this status the TIREMISU UHV-system provides the possibility to prepare and investigate structurally (LEED and STM) and spectroscopically (XPS with work function measurements) samples on different substrates at variable temperatures in UHV. Samples can be prepared with evaporable materials like organic molecules or metals (several different evaporators form part of the chamber) and even with soluble but not evaporable materials, like big organic molecules, thanks to an electro spray deposition system. Moreover, the possibility exists to grow at variable temperatures while measuring with the STM (see Chapter 5). The chamber also exhibits potential empty flanges at many different positions for more instruments like more evaporators, gas lines and a Helium gas lamp for UPS, for example.

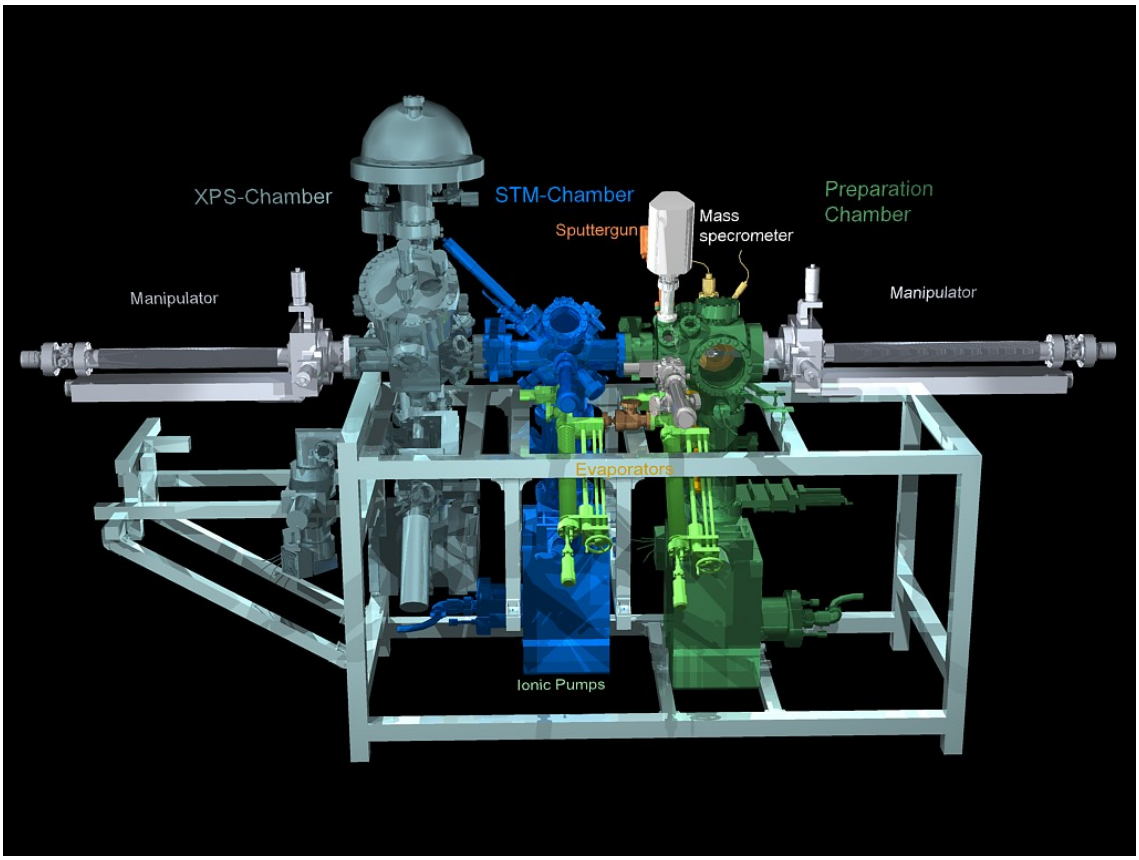

Figure 22: Actual UHV system from 2009 on: The system was extended with a third chamber including a complete XPS-system with x-ray source, monochromator, detector and a liquid nitrogen coolable manipulator. The preparation chamber and the STM-chamber have been maintained while the small MOKE chamber has been removed to provide access between the XPS and the STM chamber. The sample can now be prepared in two different chambers and then be transported to the STM and XPS. This way a spectroscopic and structural characterization of one sample is possible even at variable temperatures. Therefore a further system for a molecule exchange without breaking the UHV has been added pointing onto the STM. Cooling the latter makes it possible to deposit organic material at liquid nitrogen temperature.

2.3.3 Electro spray deposition system

a)

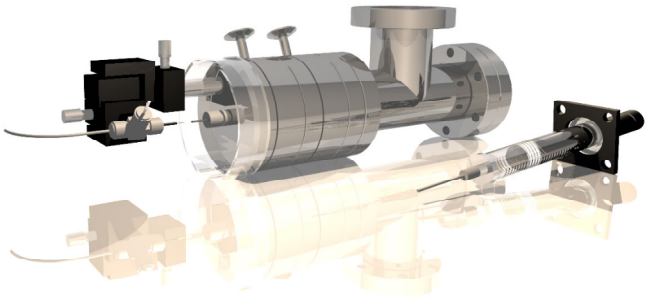

b)

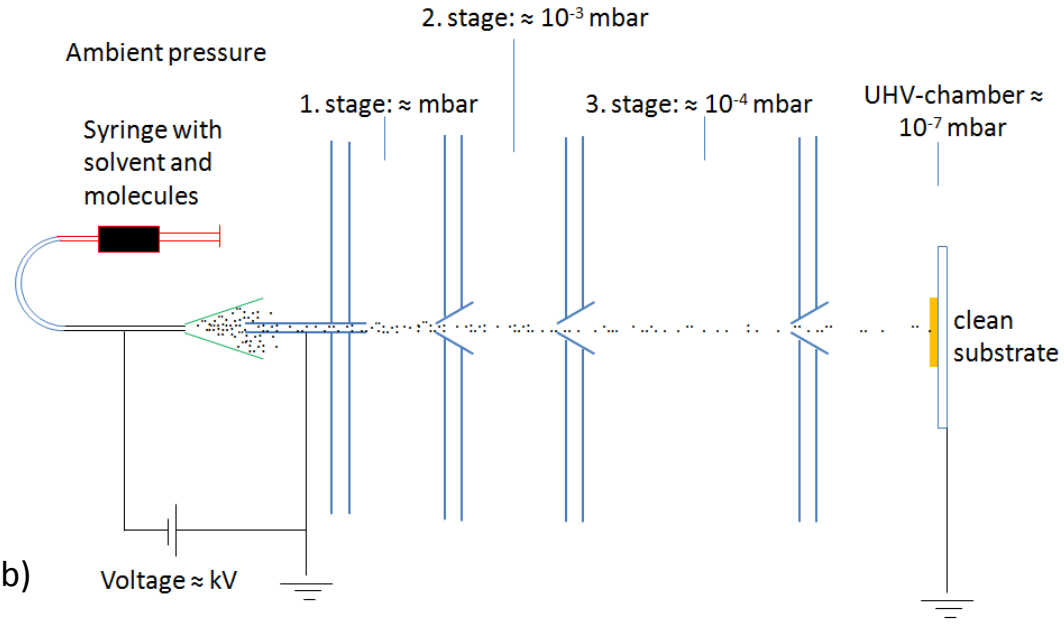

Figure 23: Illustration of the working principle of the electro spray deposition system: **a)** [taken from 16] realistic model of the used apparatus. **b)** Scheme of the electro spray system: The solvent with the molecules is transported from the syringe to a metallic capillary which is connected to negative voltage in the kV-range. The solvent and probably molecules are charged on their way out of the capillary and the electric field accelerates them towards the entrance capillary at the first stage. In the 3-stages differential pumping the pressure is reduced to high vacuum range inside the UHV-chamber. The liquid passes the different stages and the solvent partially evaporates. In the optimum case only the desired molecules without solvent land on the substrate which is connected to ground.

Although not used during this thesis work, in order to be able to investigate under UHV-conditions material which cannot be evaporated, a system (based on several pumping stages, Fig. 23 a) has been installed to inject molecules suspended in a solvent solution from ambient conditions onto a clean substrate inside the UHV-chamber. This solvent is connected to a high voltage source (kV-range) which can partially ionize the liquid with the suspended material (Fig. 23 b). The chamber and the sample are connected to ground, which creates a potential difference leading to the acceleration of solvent droplets with the suspended material towards a capillary entrance at the UHV-chamber. From the entry the solvent with the material passes

three stages with different pumping systems and pressures where most of the solvent is evaporated. Ideally, only the suspended material enters the chamber and lands on the surface. Soft landing is also possible by applying a negative counter voltage on the sample.

This system has been used already with success, although results are yet unpublished (Fig. 24). A solution of a large molecule consisting of a covalent union of an electron donor (pi-extented tetratiafulvalene[17, 18]) and a PCBM-molecule (Fig. 24 a) has been prepared and injected in two solvents, toluene and aceto nitrile (3:1) into the UHV-chamber onto the Au(111) sample. The STM images show that the molecules adsorb first at the step edges and nucleate then on the terraces, preferentially in the "elbows" of the gold reconstruction. At higher coverage they assemble in dimer rows along the fcc-sites of the surface (Fig. 24 b), similar to the PCBM assembly on Au(111)[19]. An XPS-survey spectrum taken at the synchrotron radiation facility indicates that the deposition has been done with success, signs of oxygen, sulfur and carbon can be found (Fig. 25).

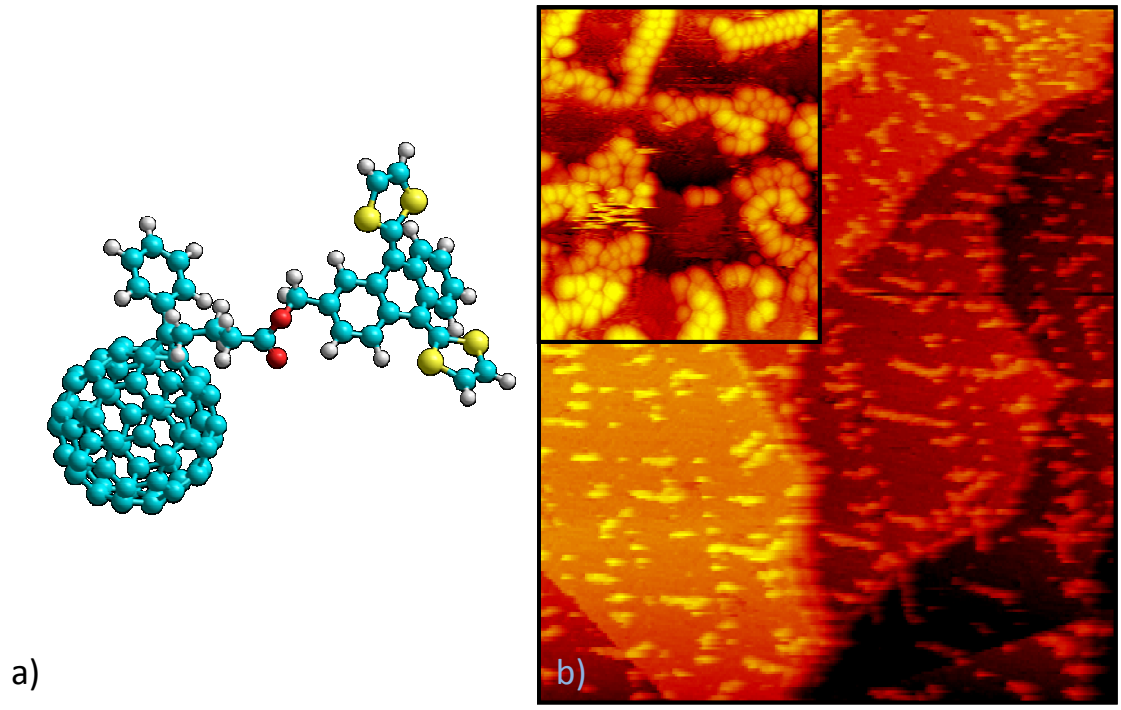

Figure 24: Chemical structure of exTTF-PCBM and STM images: **a)** The chemical model of the deposited donor-acceptor molecule shows the covalent union between them and the element composition, **b)** STM image, taken at 210 K of submonolayer exTTF-PCBM deposited at RT with toluene and aceto nitrile solvent (3:1) by electro spray deposition between 2.8 – 3.5 kV at a background pressure of $1.9 \cdot 10^{-7}$ mbar (2500 Å x 3020 Å, -0.01 nA, -1.8 V): The molecule nucleates at the step edges of the substrate and the "elbows" and grows then along the fcc-sites of the surface reconstruction in dimer rows. The inset (280 Å x 350 Å, -0.24 nA, -2.3 V): shows a close-up where the dimer rows can be observed. A single molecule seems to appear as a single big protrusion.

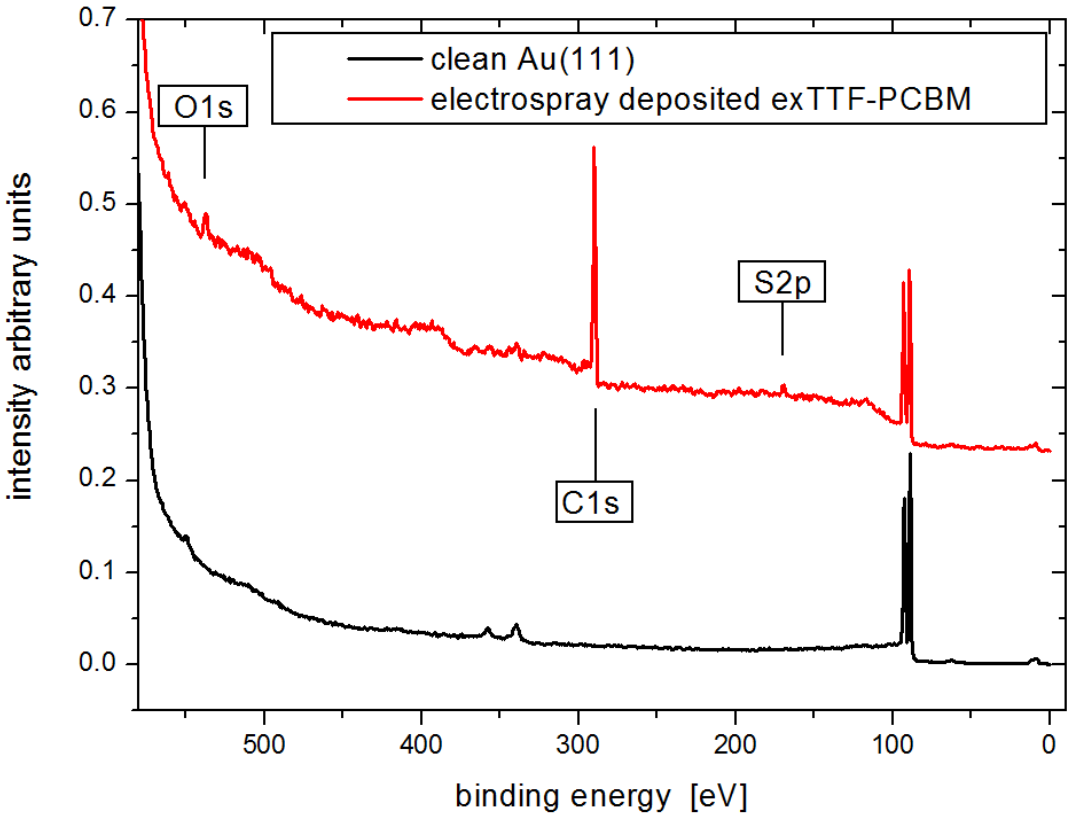

Figure 25: XPS-survey spectra of substrate and ex-TTF-PCBM sample: All expected elements, carbon, oxygen and sulfur, of the donor-acceptor molecule show peaks in the survey spectrum after deposition with the electro spray system.

2.4 Bibliography

References

1. Binnig, G. & Rohrer, H. Scanning tunneling microscopy. *Surf. Sci.* **126**, 236-244 (1983).

2. http://nobelprize.org/nobel_prizes/physics/laureates/1986/index.html.

3. Chen, C. J. Introduction to Scanning Tunneling Microscopy. *Oxford University Press, New York* (1993).

4. Tersoff, J. & Hamann, D. R. Theory and Application for the Scanning Tunneling Microscope. *Phys. Rev. Lett.* **50**, 1998-2001 (1983).

5. Bardeen, J. Tunnelling from a Many-Particle Point of View. *Phys. Rev. Lett.* **6**, 57-59 (1961).

6. http://ulisse.elettra.trieste.it/services/elements/WebElements.html.

7. Miranda, R., Albano, E. V., Daiser, S., Ertl, G. & Wandelt, K. Experimental Evidence of a Roughening Transition in Adsorbed Xenon Multilayers. *Phys. Rev. Lett.* **51**, 782-785 (1983).

8. Zangwill, A. in *Physics at Surfaces* (Cambridge University Press, New York, 1998).

9. Seah, M. P. & Dench, W. A. Quantitative electron spectroscopy of surfaces: A standard data base for electron inelastic mean free paths in solids. *Surf. Interface Anal.* **1**, 2-11 (1979).

10. http://www.specs.de.

11. Bass, M. *et al*. in *Handbook of optics, third edition Volume 1: Geometrical and physical Optics, polarized light, Components and Instruments* .

12. Czanderna, A. W., King, D. E. & Dake, L. S. Ion scattering and x-ray photoelectron spectroscopy of copper overlayers vacuum deposited onto mercaptohexadecanoic acid self-assembled monolayers. *Solid State Sciences* **2**, 781-789 (2000).

13. Seah, M. P., Smith, G. C. & Anthony, M. T. AES - Energy calibration of electron spectrometers I - An absolute, traceable energy calibration and the provision of atomic reference line energies. *Surf. Interface Anal.* **15**, 293 (1990).

14. Vickerman, J. C. & Gilmore, I. S. Surface Analysis: The Principle Techniques, 2nd Ed. (2009).

15. Stöhr, J. & Outka, D. A. Determination of molecular orientations on surfaces from the angular dependence of near-edge x-ray-absorption fine-structure spectra. *Phys. Rev. B* **36**, 7891 (1987).

16. http://www.molecularspray.co.uk/.

17. Molina-Ontoria, A. *et al*. Self-Association and Electron Transfer in Donor-Acceptor Dyads Connected by meta-Substituted Oligomers. *J. Am. Chem. Soc.* **131**, 12218-12229 (2009).

18. Perez, E. M. & Martin, N. Curves ahead: molecular receptors for fullerenes based on concave-convex complementarity. *Chem. Soc. Rev.* **37**, 1512-1519 (2008).

19. Écija, D. *et al*. Crossover Site-Selectivity in the Adsorption of the Fullerene Derivative PCBM on Au(111). *Angewandte Chemie* **119**, 8020-8023 (2007).

3 TCNQ on Cu(100)

3.1 Motivation

The technological importance of tetracyano-*p*-quinodimethane (TCNQ) as an organic material comes from its outstanding properties. TCNQ is one of the strongest electron acceptor ever reported[1] , while some TCNQ-salts show metallic conductivity.

We will show in this chapter that the results of our study on the TCNQ/Cu(100) system affect the general understanding of organic-metal interfaces, due to the discovery of an unexpected molecular assembly mechanism based on the strong interaction betweem the cyano groups of TCNQ with the copper surface as a consequence of the charge transfer from the substrate to the molecule. To our knowledge, previous studies have never proven in this way the causal link between charge transfer, molecular distortion, substrate distortion and molecular self-assembly.

There have already been some studies about the effect that charge transfer may have on the organic-metal interface. Thus, Romaner et al[2] reported on ultraviolet photoelectron spectroscopy (UPS)- and x-ray standing waves (XSW)-experiments, combined with first-principles calculations, of the adsorption of F4-TCNQ on Cu(111). Similar to our case, charge transfer between the substrate and the molecule strongly distorts the geometry of the adsorbate. Although a slight distortion of the surface atoms can be observed in the calculations, no comment is made about the consequences on the molecular order. On the other hand, Bedwani et al[3] have discussed one dimensional structures of TCNE on Cu(100) investigated with STM and density functional theory calculations. In this case, the strong interaction of the molecule with the substrate gives rise to a surface reconstruction with a buckling of some copper atoms. However, a causal connection between the buckling and the 1D-assembly, or between the charge transfer and the geometrical distortion of the molecule, is clearly absent. In a review paper of the same group about TCNE on different metal substrates (Wegner et al[4]) the connection between the Cu(100)-surface stress field and the assembly is depicted in detail as one part of the balance among all active influences, another being the possible lattice mismatch between the adsorbate and the substrate. Summarizing, STM and DFT are the main support for the drawn conclusions but complementary experimental methods are missing, as well as a detailed description of the whole picture of charge transfer and the described consequences.

In our case XAS, XPS and STM measurements are combined with DFT-calculations to demonstrate every step of the causal line drawn between the charge transfer and the self assembly of TCNQ/Cu(100): Charge transfer is the reason of the conformational freedom of TCNQ, which leads to a strong molecule-substrate interaction. The surface is thus distorted which in turn leads to ordered islands. The number of implied steps demonstrates that predictions are very difficult to make about systems with such a complex interplay between substrate and adsorbates. This and the few publications with only moderate experimental support about the observed effect of charge transfer have motivated our experimental and theoretical investigation of TCNQ molecules on Cu(100), a model system for strong acceptor molecules on metal substrates.

3.2 Experimental and computational details

The investigation of TCNQ/Cu(100) has been carried out in collaboration with the x-ray spectroscopic group of Professor Leonardo Soriano at the Universidad Autónoma de Madrid, the surface science group of Professor Klaus Kern at the Max Plack Institute for Solid State Research, Stuttgart, the group of Functional Interfaces of Professor Wöll and the theoretical group of Professor Fernando Martín, also from the Universidad Autónoma de Madrid. The experiments were conducted with two different UHV-STM systems in Stuttgart and Madrid and the spectra of the XPS- and the XAS-experiments have been collected at BESSY in Berlin and a UHV-chamber at Stuttgart, with all data giving compatible results.

TCNQ molecules have been evaporated with a glass crucible resistively heated at 340 K onto the surface of a Cu(100) single crystal held at room temperature (RT), at a deposition rate between 0.06 and 0.8 ML per minute. Most of the UHV-STM experiments were conducted with the microscope at RT. Measurements carried out at nitrogen temperatures revealed the same appearance of TCNQ and the self assembled islands.

DFT calculations were done to calculate the adsorption conformation of a TCNQ molecule on four layers of Cu(100), where the two bottom layers were fixed and all other atoms were allowed to relax. The isolated molecule was simulated with a surface unit cell of 7 a_{Cu} x 5 a_{Cu} in order to exclude any intermolecular interaction. For the calculations of the island assembly, the unit cell obtained experimentally (Fig. 8) was used. The calculations were performed using VASP code with the Perdew-Wang (PW91)[5] functional. The projector augmented wave (PAW) method was used to describe the ionic cores. The Monkhorst-Pack scheme with a k-point mesh of 1 x 1 x 1 k-points was used. A Methfessel-Paxton smearing of 0.4 eV was applied. The energy cut-off in the plane-wave expansion was set to 400 eV. Dipole correction was applied during all the computations. The obtained charge density served to quantify the charge transfer between TCNQ and the Cu-surface based on Baders topological analysis.

3.3 Description of the TCNQ molecule

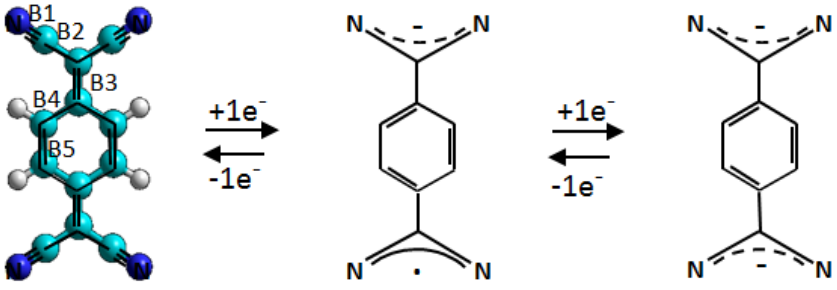

Figure 1: Chemical structure of $TCNQ^0$, $TCNQ^-$ and $TCNQ^{2-}$: An extra negative charge is delocalized in one of the two dicyanomethylene groups and causes bond changes and an aromatization of the central quinoid ring. This has influence on the flexibility of the molecule and thus on the adsorption geometry. A second electron is hosted in the other dicyanomethylene group.

TCNQ consists of 12 carbon, 4 hydrogen and 4 nitrogen atoms. The latter render the molecule a strong electron acceptor[6]. In gas-phase, the neutral molecule adopts a flat geometry with a quinoid carbon ring. Table 1 shows the frontier orbitals of TCNQ in gas phase. In the bottom row of Table 1 constant-charge isosurfaces for neutral ($TCNQ^0$) and charged ($TCNQ^{-2}$) species are shown. On top of these isosurfaces information about the electrostatic potential has been color coded in such a way that blue areas indicate positive and red ones negative potential. They reveal that the charge concentration in the neutral state is negative around the nitrogen atoms, while it is positive close to the hydrogen atoms. In the dianion form the negative charge is increased, mainly on the N-atoms and on the C-atoms which join the cyano groups with the central ring. A slight increase of electron density on the carbon ring can also be noticed (rather yellow color of the $TCNQ^{-2}$ compared to the turquoise tone of the 6-fold carbon ring of $TCNQ^0$). Additional negative charges are hosted mainly along the two dicyanomethylene groups[7] with a contribution on the central carbon ring (Fig. 1), following closely the shape of the LUMO of $TCNQ^0$ (Table 1). All these effects can produce a change in the bond configuration: the extra charges lead to an aromatization of the quinoid ring[8], while the π-bond B3 adopts a more σ-type- and thus more flexible character (Fig. 1). This, as will be seen later, releases structural stress along the molecular backbone upon adsorption on the Cu-substrate and allows the cyano groups to be in closer contact with the surface atoms.

Frontier orbitals **$TCNQ^0$:**	HOMO: -9.6 eV 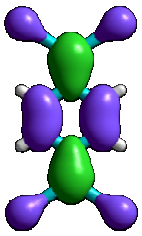	LUMO: -3.07 eV 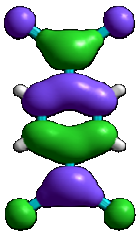
Electrostatic potential projected onto charge density isosurface	**$TCNQ^0$:** 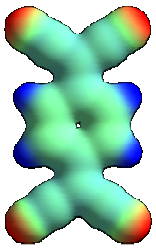	**$TCNQ^{2-}$:** 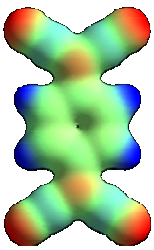

Table 1: The frontier orbitals of the neutral TCNQ molecule in the gas phase: Large parts of the density of an extra charge will be located at the dicyanomethylene groups, as can be seen in the electrostatic potential projected onto a charge density isosurface (red color means negative charge, blue color stands for positive charge).

3.4 Adsorption of TCNQ on Cu(100) - Self assembly of TCNQ

3.4.1 STM Results:

After depositing TCNQ on Cu(100) at RT oval molecular units with an apparent size of 11 Å x 6 Å and a height of 1.3 ± 0.3 Å can be observed similar to the molecules at the step edges in Figure 2. This is compatible with an adsorption geometry where the central carbon ring is parallel to the surface, as observed as well for TCNQ on Cu(111)[9]. The long axis of TCNQ attaches approximately perpendicular to the electron rich step edges of Cu(100). These are fully decorated before island growth sets in, which evidences the high mobility of the adsorbates at RT. At higher coverage two-dimensional islands grow from the step edges into the terraces. Very often the direction of the molecular units inside the island is parallel to the TNCQ molecules adsorbed at the step edge, where the island growth starts from. A direct influence of the step edge direction on the direction of the island constituents and thus on the island direction is therefore concluded. The shape and size of the TCNQ molecules inside the islands is the same as for the molecules at the step edges.

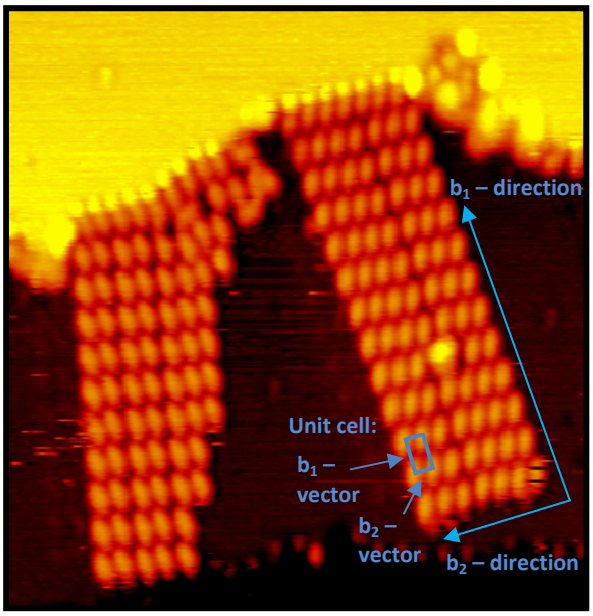

Figure 2: STM image of 0.2ML TCNQ grown at RT on Cu(100) imaged at RT (220 Å x 230 Å, -2.0 V, -0.31 nA): After the step edges are fully covered, almost rectangular islands, with a long side (b_1) and a short side (b_2), start growing from the step edges into the terraces. The initial molecular orientation at the step edge seems to influence the direction of the single molecules in the island and thus the island direction as well.

The orientation of the long molecular axis is not parallel to the high symmetry direction of the Cu(100) surface, forming an angle of 20 ± 3 ° with them. Therefore, and due to the substrate symmetry, four different but equivalent orientations of TCNQ exist and can be found on the surface in different islands (Fig. 3). Although this could give rise to more than four domains, experimentally only four are observed on Cu(100) (Fig. 3), corresponding to four different molecular orientations.

The shape of the islands is elongated and approximately rectangular, as the unit cell is, too, which is also parallel to the sides of the TCNQ islands. We denote as b_1 the unit cell vector parallel to the long side of the island and as b_2 the unit cell vector parallel to the short island side (Fig. 2). The mean aspect ratio of the islands (length of the long side divided by the length of the short side) is 4.3 ± 1.5. Within the islands, and in a non periodic way, there are additional spacings between the molecular rows parallel to the b_1-direction (which we call dislocation lines, Fig. 3).

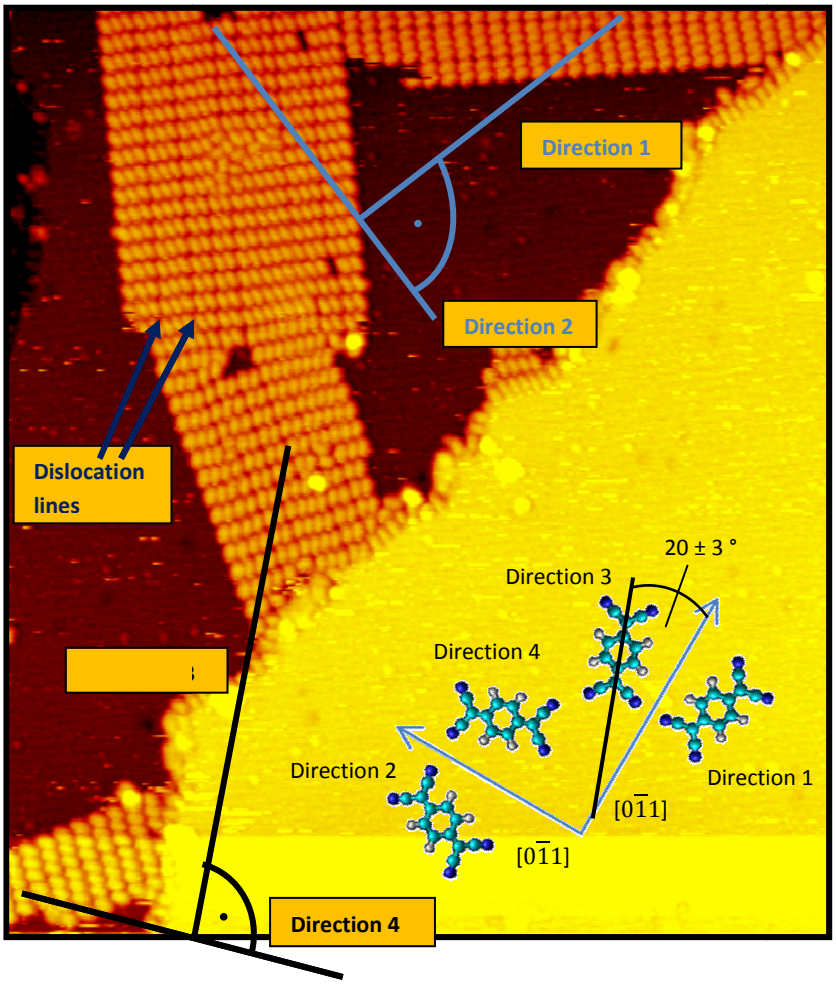

Figure 3: STM image of 0.2ML TCNQ grown at RT on Cu(100) imaged at RT (560 Å x 630 Å, -2.6 V, -0.35 nA): A region of the substrate is shown where all four different directions of the TCNQ molecules are found. The number of four orientations is a consequence of the angle (17 °) that the main molecular axis exhibits with respect to the high symmetry directions of the Cu(100) surface.

From the experimental data we have developed a self assembly model of the TCNQ islands on Cu(100) which explains the observed angles and distances. In matrix notation, for the dislocation free areas (U1 in Fig. 4), the epitaxial relationship between the molecular overlayer and the copper surface can be described with a commensurate unit cell as $\begin{pmatrix} b_1 \\ b_2 \end{pmatrix} = \begin{pmatrix} 2 & 2 \\ -3 & 4 \end{pmatrix} \begin{pmatrix} a_1 \\ a_2 \end{pmatrix}$. This unit cell appears 2.1 ± 0.4 times more often than the one containing a dislocation line (U2 in Fig. 4), with a unit cell of $\begin{pmatrix} b_1' \\ b_2' \end{pmatrix} = \begin{pmatrix} 3 & 2 \\ -3 & 4 \end{pmatrix} \begin{pmatrix} a_1 \\ a_2 \end{pmatrix}$ (Fig. 4). As we shall see later, the molecule-substrate interaction is very strong and localized, so the assumption of a commensurate lattice seems justified.

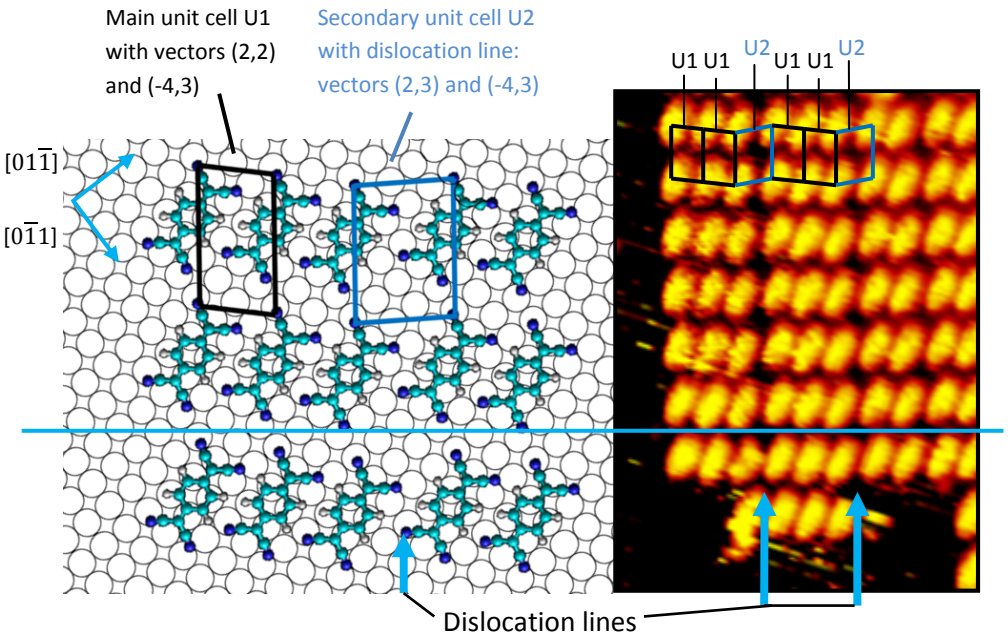

Figure 4: The adsorption model of TCNQ molecules in one of four domains on the Cu(100) surface: The dislocation lines appear when a whole molecular row in a TCNQ island is displaced one Cu-lattice distance; in the case shown here the row movement is parallel to the [01$\bar{1}$]-direction. The main unit cell, which is predominant, consists of the vectors (2,2) and (-4,3) in contrast to the secondary unit cell U2 which includes a dislocation line and thus the first vector is different: (2,3) and (-4,3). In the right part of the Figure both unit cells are superimposed to an STM image of a TCNQ island (80 Å x 130 Å, -0.3 A, -2.0 V), which is aligned with the high symmetry directions of the Cu-surface of the model.

Another interesting observation regarding the dislocation lines is that they can move with time (Fig. 5). The mobility of the rows suggests that the intermolecular interaction perpendicular to the dislocation lines (direction b_2) creates a potential energy landscape with two different positions so similar in total energy that the transition from one position to the other can be overcome by the thermal energy available at RT.

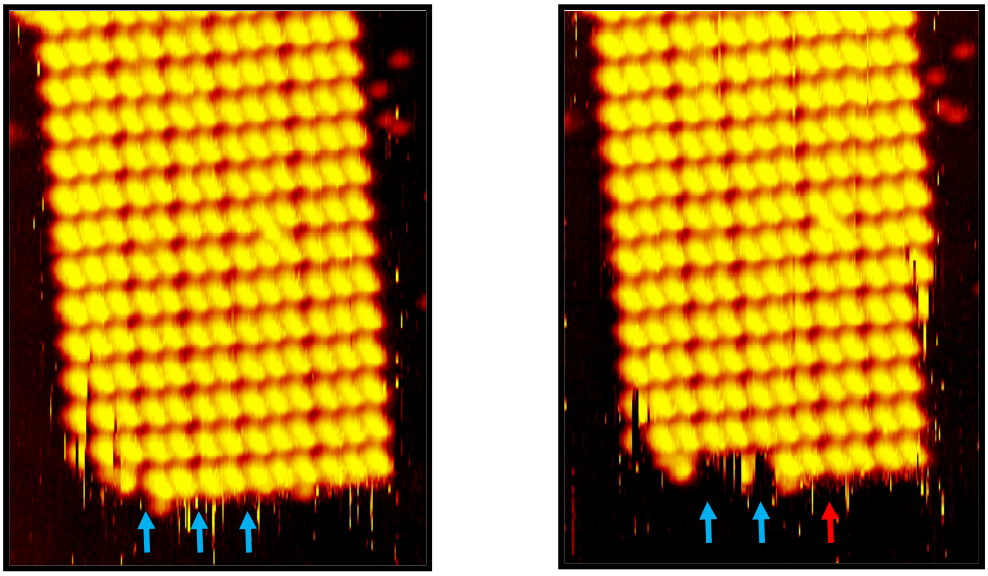

Figure 5: STM sequence (taken 34 seconds) of 0.2 ML TCNQ grown at RT on Cu(100) imaged at RT (140 Å x 190 Å, -2.0 V, -0.29 nA): Apart from the interchange of molecules from the island with the mobile 2D molecular gas on the terraces dislocation lines in the assembly of TCNQ are clearly visible along the b_1-direction of the island. The mobility of those lines becomes obvious comparing the number of molecular rows: in image **a)** the island exhibits every 3, 2, 2 and 3 rows a dislocation line and in **b)** the sequence changed to 3, 2, 3, 2.

In order to understand the interactions that drive the assembly of the islands we have calculated the total energy between two parallel TCNQ molecules in gas-phase as a function of their relative coordinates (Fig. 6, with molecular mechanics using a MM+ force field in the Hyperchem program package). In total four equivalent point-symmetric minima can be identified (black color inside blue areas, Fig. 6). Those are the positions relative to the center of a first TCNQ molecule where a second molecule would nucleate if only intermolecular interactions are taken into account. The energy gain compared to the situation of two molecules separated an infinite distance (this is taken as the zero point of the total energy, Fig. 6) is of 163 meV. This gain is mainly a consequence of the electrostatic attraction between the positively charged hydrogen atoms of one molecule and the negatively charged nitrogen atoms of another TCNQ, as can be seen by drawing the charge density contour isosurface of TCNQ calculated in the gas phase configuration (Table 1 and Fig. 6). Positions closer to the center of the first TCNQ molecule are less favorable because of the strong Pauli repulsion. Further away the electrostatic attraction decreases. The found minima are close to, but not coincide with the experimental results (yellow circles, Fig. 6)

It was mentioned above that these calculations did not include the substrate. However, as also previously stated, the molecular lattice seems to be commensurate with the substrate. In Figure 6 we have overlayed the total energy map of the gas-phase with a grid of lines separated one lattice spacing of the Cu(100) surface (black lines in Fig. 6). The crossings of the lines are representative for equal adsorption positions with respect to the copper lattice. If there is a TCNQ molecule at (0,0), the adsorption position of a second molecule is expected to be at a different node of the grid (commensurability) and close to the calculated minimum (Fig. 6). There are three such sites very close to the absolute energy minimum. In units of the surface lattice vectors, their coordinates are: (3,1), (2,-2) and (2,-3). These positions are marked with yellow circles in Figure 6. The latter two relative positions are precisely the

aforementioned vectors of the unit cells U2 and U1, with and without a dislocation line, respectively, in the short island side direction b_2. Although their relative positions are very similar in total energy, position (2,-3), corresponding to the unit cell U2 with a dislocation line, lies slightly higher (energy gain: 69 meV compared to 95 meV for position (2,-2)) and this may explain the less frequent appearance of the unit cell U2. The first relative position (3,1), which is the one with the highest binding energy gain in gas-phase, it is not observed experimentally, which leads to the conclusion that other forces must also play an important role.

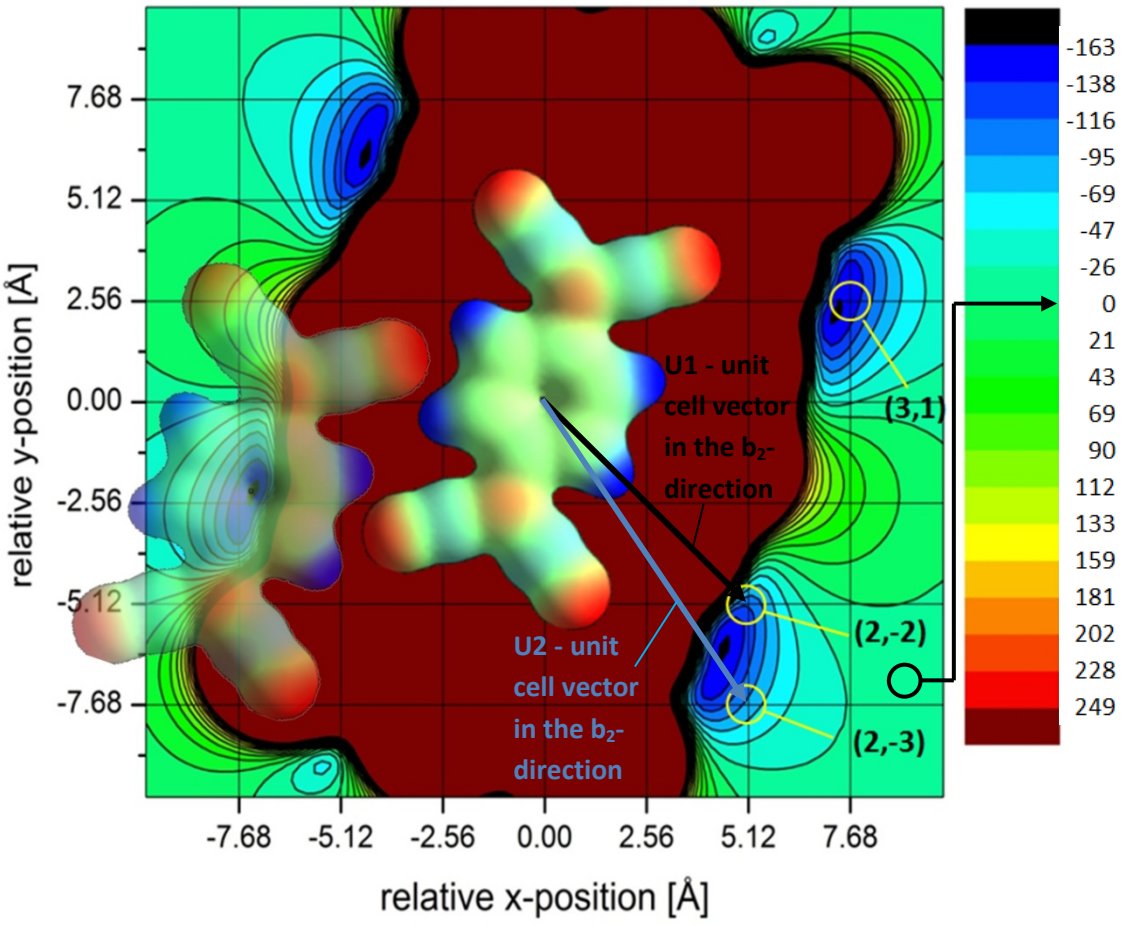

Figure 6: Calculation of the total energy [meV] of two coplanar, parallel TCNQ molecules as a function of their relative position: In this energy map the grid represents the condition of commensurability. Only nodes can therefore be taken into account for the coordinates of a second molecule. The ones close to a minima of the map (black and blue areas) are potential binding sites. This map reveals three positions very close to the absolute minima: (3,1), (2,-2) and (2,-3). The last two correspond to the experimentally observed unit cells.

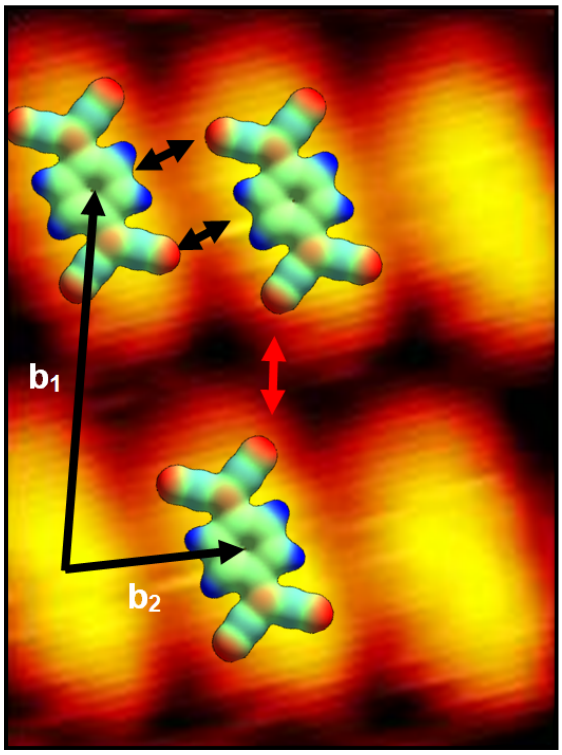

Figure 7: STM image of 0.2 ML TCNQ grown and imaged at RT on Cu(100) (18 Å x 25 Å, -2.1 V, -0.29 nA): Overlaying the electrostatic potential projected onto a charge density isosurface of the TCNQ in gas phases, the interaction of neighboring TCNQ along the b_2-direction can be explained by electrostatic attraction; in this way, however, a repulsive force would be expected in between the lines of assembled TCNQ, contrary to what is observed, because this is the b_1-direction of the island, where the island side is longer than in the b_2 direction.

Electrostatic intermolecular interactions together with the commensurability condition seem to explain the lateral arrangement of molecules along the b_2-direction. However, in the other direction, b_1, no attractive potential from the gas-phase calculations compatible with the experimental observations appears. STM images show that in this direction, nitrogen atoms from molecules of different lines in the islands face each other (Fig. 7), which is energetically costly taking into account the negative charge located around the N-atoms. There must be then another interaction responsible for the assembly of the molecules along this direction. In addition, the fact that the islands are elongated along b_1 can be explained by kinetic or thermodynamic arguments. Although a kinetic effect arising from anisotropic diffusion[10-12] cannot be totally ruled out, it seems unlikely to explain the elongation of the TCNQ islands given the high mobility of the adsorbates. A thermodynamic reason like a larger attractive force between the molecules along b_1 compared with the b_2-direction would be a conclusive explanation but calls for a detailed theoretical investigation.

3.4.2 DFT Calculations:

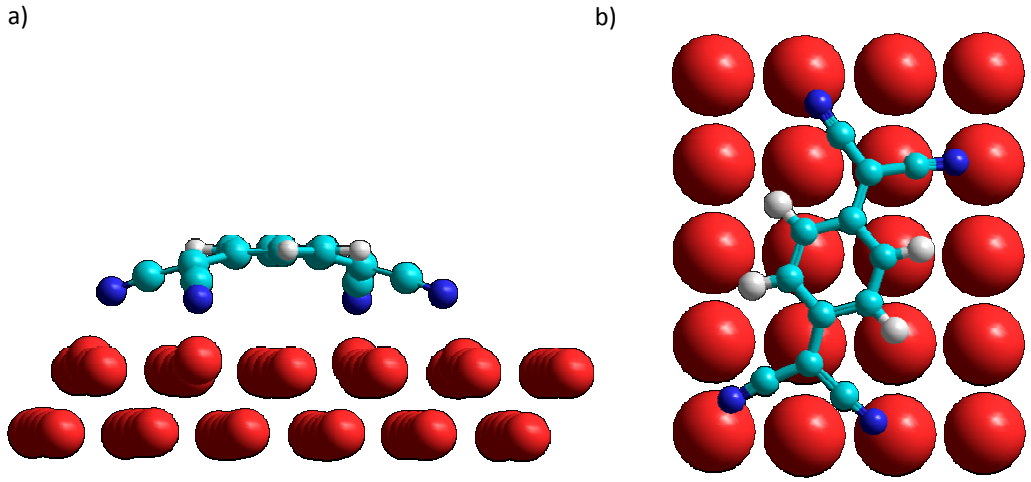

Figure 8: Results of a DFT calculation for the adsorption conformation of a single TCNQ molecule on a 4 layer slab of Cu(100) substrate. **a)** The side view reveals the strong bending of the molecule and the up lift of four Cu-atoms. **b)** In the top view it becomes clear the nitrogen atoms tend to be located close to on top positions on the surface, which leads to a slight distortion of the TCNQ molecule.

As concluded above, gas-phase calculations of TCNQ cannot explain the observed self assembly. Therefore, DFT calculations including the substrate have been carried out. Different initial configurations of a single, isolated TCNQ molecule on Cu(100) were tried, and the obtained theoretical absorption model shown in Figure 8 corresponds to the minimum of all the explored initial configurations. The orientation of the long axis of TCNQ on Cu(100), an angle of 17 ° with the high summetry directions is found in the calculations, is compatible with the experimental results of 20 ± 3°. A calculated binding energy of 2.23 eV indicates a strong chemisorption, which justifies the assumption of a commensurate lattice. The molecule adsorbs with the central carbon ring almost parallel to the surface, but in a conformation where the dicyanomethylene groups are strongly bent towards the surface, with the nitrogen atoms closest to it (Fig. 8a). The distance between the N-atoms and the last surface layer is 2.08 Å, while the C-atoms in the central ring are 0.72 Å higher. The interaction with the substrate also distorts the surface, pulling up some Cu-atoms in the first layer. This causes a buckling of the metal surface (highest Cu-atom in the surface layer is 0.38 Å higher than the lowest). As will be discussed later, this surface distortion is partially responsible for the molecular assembly ("Substrate mediated interaction").

A Mulliken analysis of the charge densities yields a charge transfer close to 2 e^- from the substrate to the adsorbed TCNQ. This facilitates the bending of bond B3 (through the mechanism discussed previously, "Description of the TCNQ molecule", Fig. 1) and the approach of the dicyanomethylene groups towards the surface. A contour of the difference map (Δρ) of the charge densities of the adsorbed molecule ($\rho_{adsorbed\ TCNQ}$) and the superposition of the clean separate surface ($\rho_{surface}$) with the gas-phase TCNQ ($\rho_{TCNQ,\ gas\ phase}$), $\Delta\rho = \rho_{adsorbed\ TCNQ} - \rho_{surface} - \rho_{TCNQ,\ gas\ phase}$), helps us in finding the areas of additional negative charge (blue areas in Fig. 9) as well as areas of depletion of electron density (yellow areas). The shape of the negative charge density contour resembles very well the LUMO orbital of TCNQ, which, as a result of the

charge transfer, is then expected to be filled (Fig. 9 c). This can actually be seen in Figure 10, which shows the calculated density of states (DOS) of the TCNQ/Cu(100)-system. In order to identify the origin of the different features, we have plotted also the energy levels of TCNQ in gas-phase taking into account the measured change in work function upon adsorption, $\phi = 5.1$ eV (see "Work function"), with the result that the LUMO falls below the Fermi level and is therefore fully occupied.

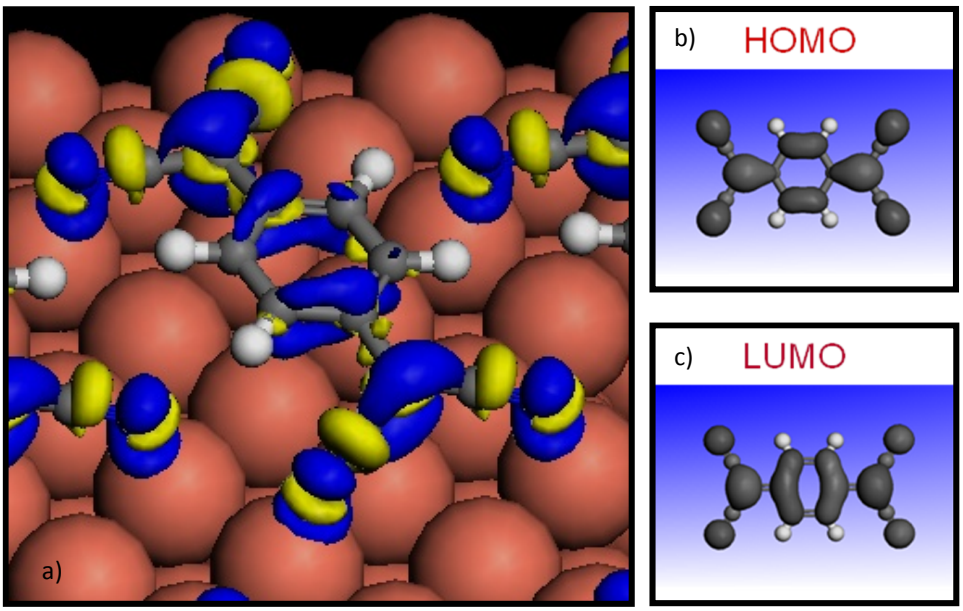

Figure 9: In the electron density difference contour, **a)**, of the origin and final position of transferred electrons the LUMO **c)** can be identified as area where negative charge resides (blue areas). As charge from the surface originates not only in some Cu-atoms but in the electron sea of the whole substrate the amount of charge originated in every single of the surface atoms is too small to be visualized. Yellow areas localize a depletion of negative charge.

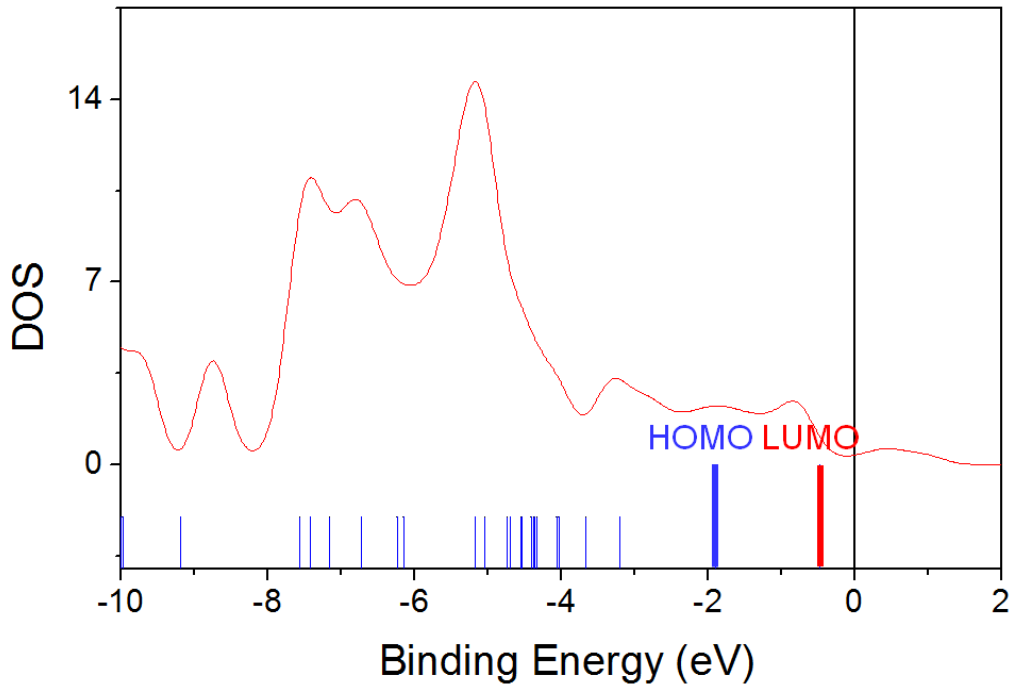

Figure 10: DTF-calculated density of states of TCNQ/Cu(100) (red line). The energy levels of the TCNQ molecule in gas-phase resemble well the electronic structure of the DOS and show that the LUMO falls below the Fermi level. As a consequence of the adsorption of TCNQ on Cu(100) a negative charge transfer from the surface to the LUMO is expected.

3.5 XPS Results

If the results of the DFT calculations are correct, there is an important relation between charge transfer and the structure of the adsorbed molecule. In order to verify the theoretical findings XPS measurements were carried out.

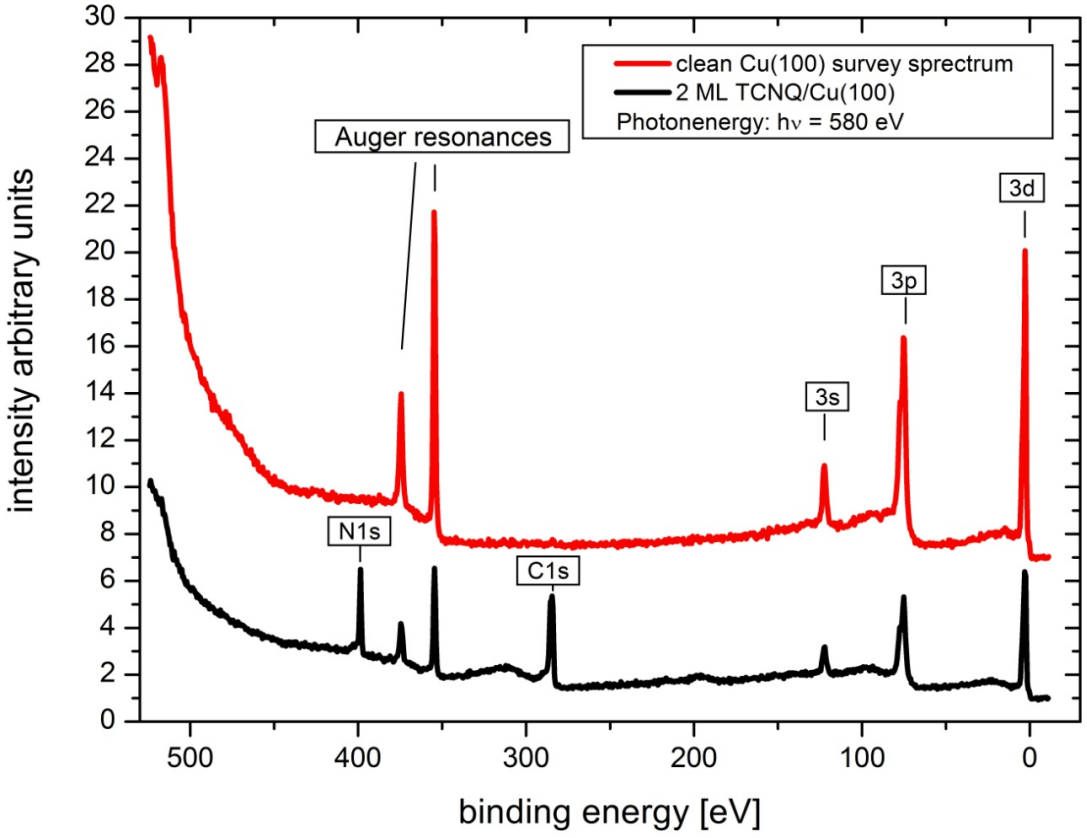

Figure 11: The red curve represents a XPS spectrum of a clean Cu(100) surface at room temperature. The black curve from a TCNQ/Cu(100) sample shows additional resonances in the N1s- and C1s-region (as expected from a molecule consisting of carbon and nitrogen). At the same time the substrate features appear attenuated due to the material on top.

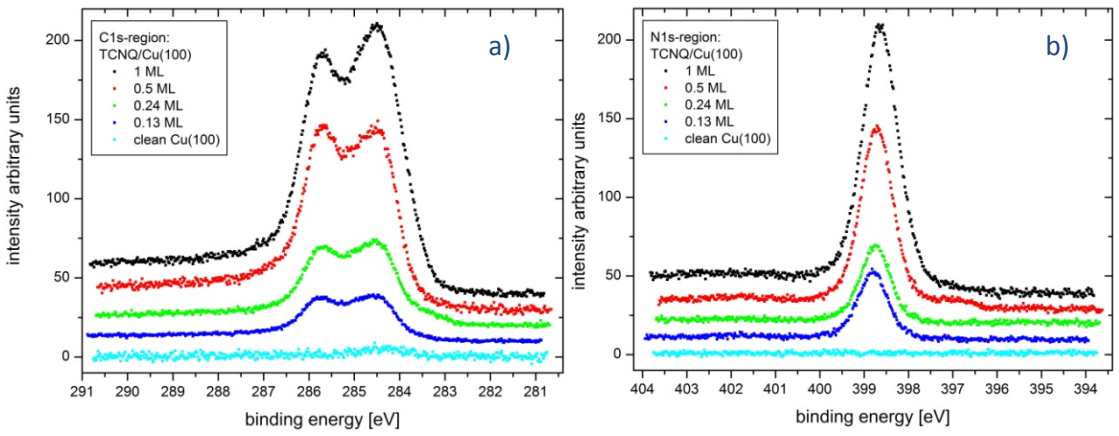

Figure 12: a) Spectra of the C1s- and b) N1s-region of TCNQ/Cu(100) from submonolayer samples: The spectra are displaced vertically for clarity.

3.5.1 Spectra overview:

The overview scan of the clean Cu(100) (taken with a photon energy of 580 eV) shows no peaks of contaminants. After the deposition, clear signs of the TCNQ molecule in the C1s- and N1s-region (Fig. 11) appear. Figure 12 shows high resolution scans in the regions of interest for different submonolayer coverages.

3.5.2 N1s-region

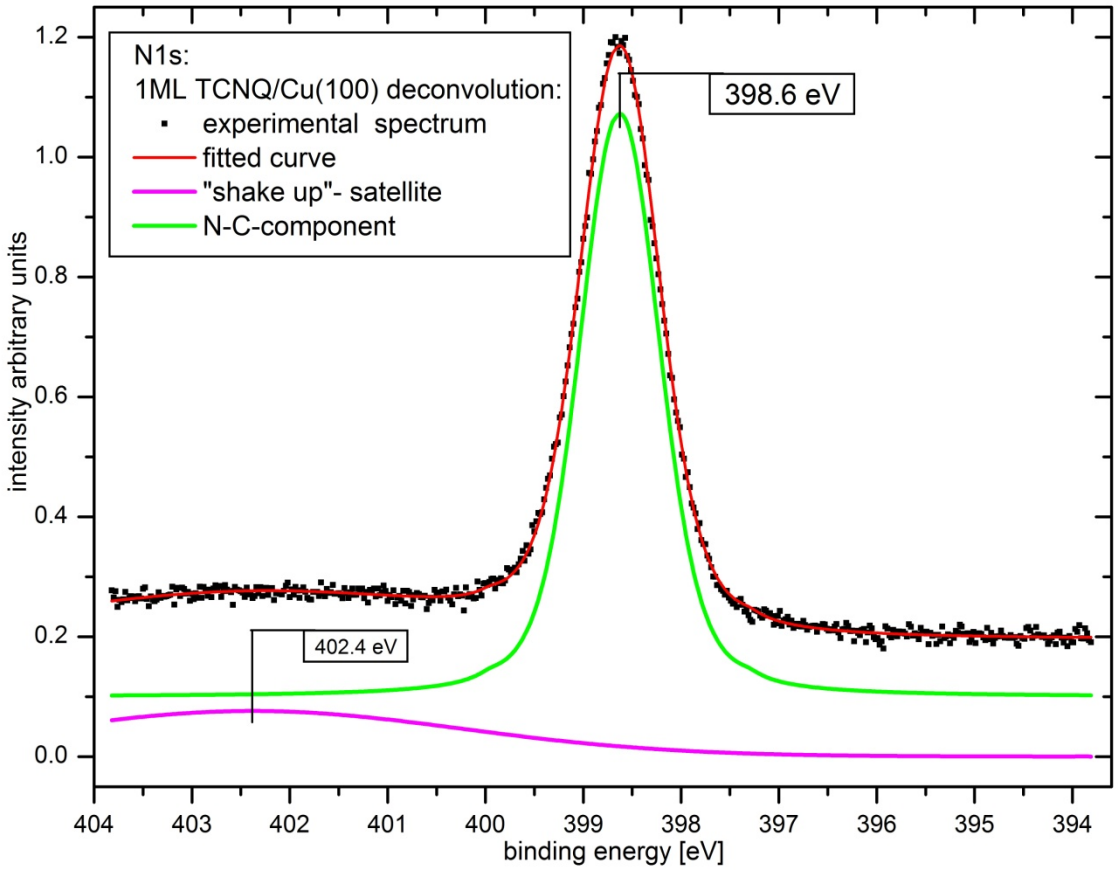

Figure 13: N1s XPS spectrum of 1 ML TCNQ/Cu(100) with the deconvolution peaks: The N1s-region shows the deconvolution of the experimental submonolayer spectra into one main peak and a broader one representing a "shake up" satellite. The energy positions are very close to the binding energies from the nitrogen in charged cyano groups in literature (see text for references).

All submonolayer N1s-spectra of TCNQ/Cu(100) can be deconvoluted into one main component at $E_{1st\text{-}layer}$ = 398.7 ± 0.1 eV with a mix of a Lorentzian and Gaussian components of widths 0.22 ± 0.03 eV and 0.73 ± 0.06 eV, respectively (Fig. 13). The weak "shake-up" satellite is fitted with a very broad component at 402.1 ± 0.5 eV.

The shape and small width of the main peak seems to indicate only one chemical environment for the nitrogen atoms. This supports the former finding of a flat adsorption with all four cyano groups on the Cu-surface. The binding energy is consistent with literature values for TCNQ salts

where the TCNQ molecule is negatively charged[13-15]. On the other hand, for a bulk-like sample (powder sample, Fig. 14), which is expected to be neutral, the main peak is found at E_{bulk}= 399.6 ± 0.1 eV. An energy difference of ΔE = 0.9 ± 0.1 eV between the surface- and the volume component is the result. This seems to indicate a negative charge transfer from the substrate to the molecule. The shift could also be explained by a screening effect in the monolayer sample, but work function measurements, presented in the following ("Work function"), show clearly an increase in work function with growing coverage, proving thus the formation of an interface dipole due to charge transfer to the adsorbed TCNQ molecule.

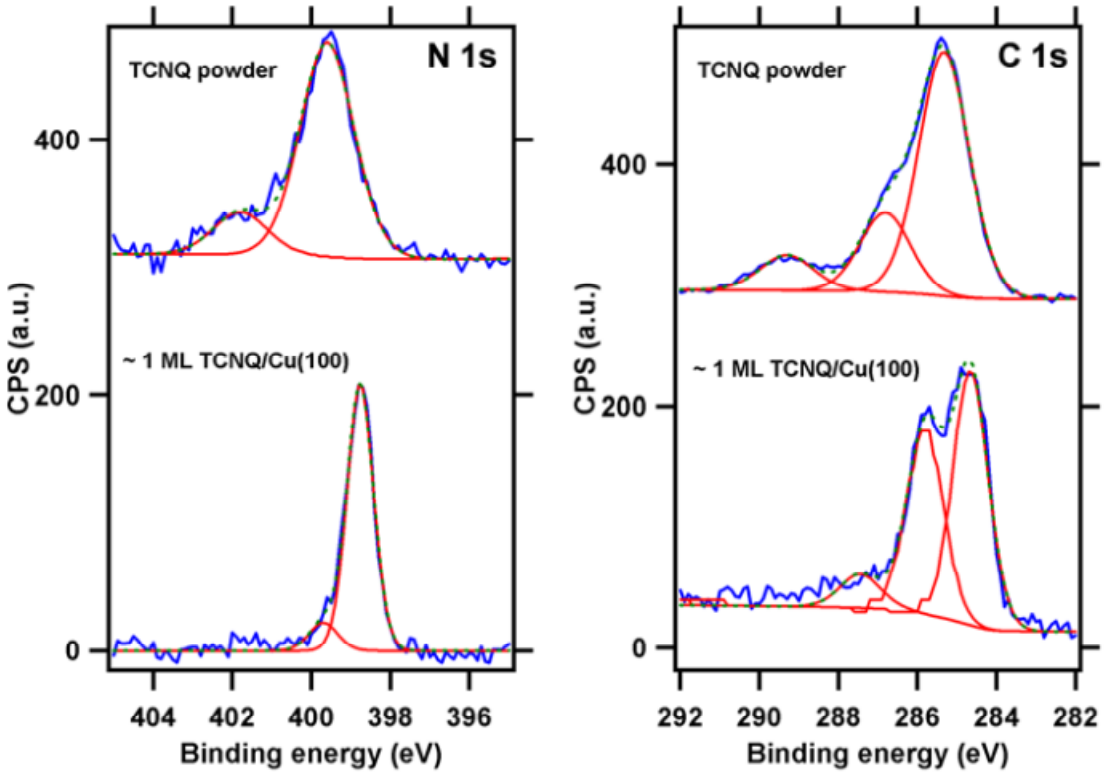

Figure 14: Experimental spectra of the N1s- and C1s-regions of our collaborators in Stuttgart in the group of Professor Kern. The N1s-binding energies are exactly the same as in our measurements at BESSY. The binding energy difference between the nitrogen from the bulk sample and the one from the 1 ML TCNQ/Cu(100) suggests a charge transfer. In the C1s-region a similar trend, more subtle, is observed.

3.5.3 C1s-region

The C1s-spectra of all submonolayer samples can be deconvoluted into three peaks at $E_{1st\text{-}layer,\ C\text{-}N}$ = 285.8 ± 0.02, $E_{1st\text{-}layer,\ C1}$ = 285.0 ± 0.03, $E_{1st\text{-}layer,\ C2}$ = 284.4 ± 0.03 and a broad "shake up"-feature at $E_{"shake\ up"}$ = 286.1 ± 0.4 (Fig. 15). A Lorentzian part of 0.2 eV, as in the N1s-region, and an average Gaussian width of $\Delta E_{G.\text{-}width}$ = 0.75 ± 0.05 eV was found. This is coherent with the binding energies found in the TCNQ-derivative-system described in Chapter 4.

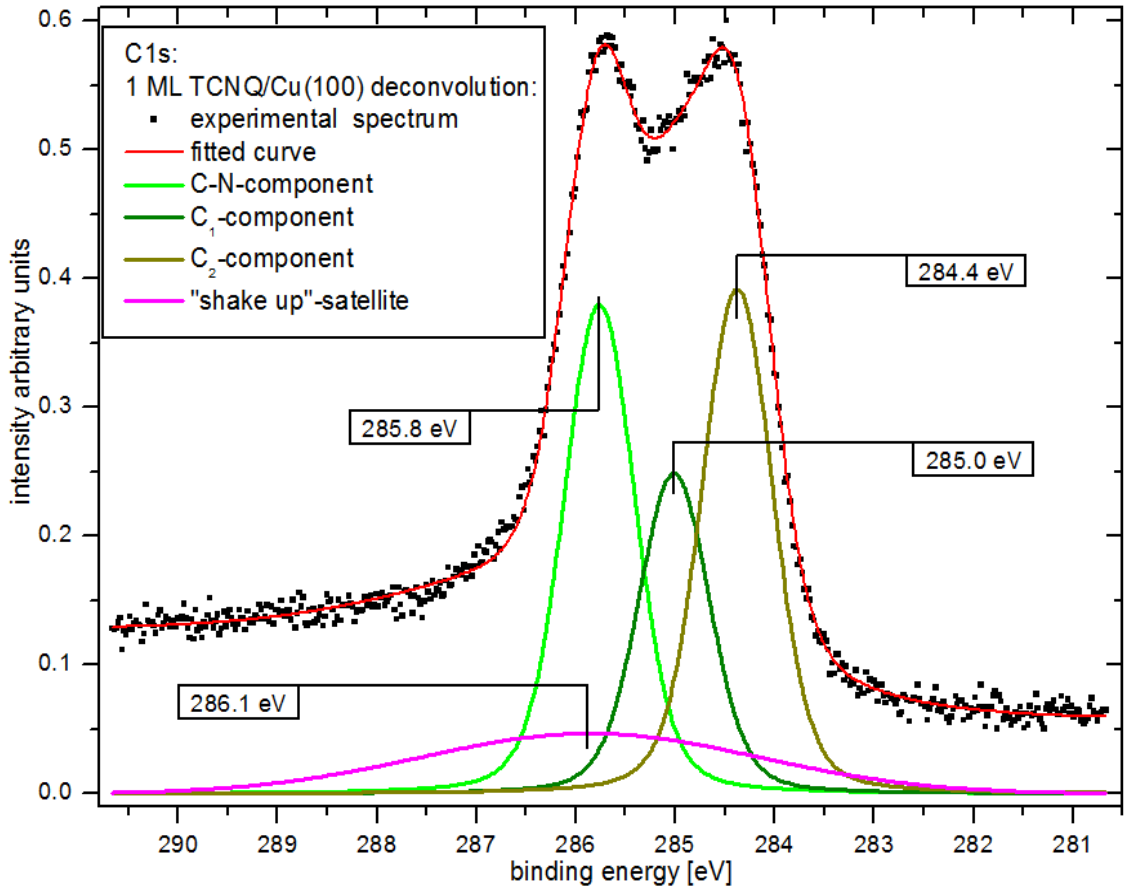

Figure 15: C1s XPS spectrum of 1 ML TCNQ/Cu(100) with the deconvolution peaks: The same sample as in the N1s-region shows exemplifying the deconvolution of the experimental submonolayer spectra into two main resonances and the broader "shake up" satellite. The energy positions are very close to the binding energies from the results of our collaborators from a different XPS machine and underline the finding of a negative charge transfer from the surface to TCNQ/Cu(100).

A Mulliken population analysis of the electronic density of the TCNQ molecule adsorbed on the surface including the charge transfer allows to the assignment of partial charges to all C-atoms (Fig. 16). Three groups with similar charges can be identified this way: 1. Four carbon atoms in the cyano groups exhibit a positive charge around 0.14 e^-, 2. two carbon atoms of the central ring with nearly no charge, 0.06 e^-, and 3. the remaining six carbon atoms with a similar charge of around -0.29 e^-. Since a positive charge on an atom increases the binding energy, the first group, related to the cyano moieties, would thus be expected to appear on the high binding energy side of the spectra; the peak at the low binding energy side of the spectra would correspond to the more carbon atoms, which leaves for the central peak the second group with nearly no charge as origin. The experimental area ratio between the three components, 4:2.8:4.4, is thus qualitatively consistent with the expected ratio from this model of 4:2:6 and can thus explain the C1s-spectra in the monolayer regime. Error sources may be carbon contamination during the time of the measurements and the deficiencies of the Mulliken analysis which otherwise would probably require more deconvolution peaks.

The average peak area ratio between the C- and N-core levels, corrected with the element specific cross section, is a_{C1s}/a_{N1s} = 3.4 ± 0.6, which is within the experimental error the expected from the element ratio in TCNQ with 12 carbon and 4 nitrogen atoms.

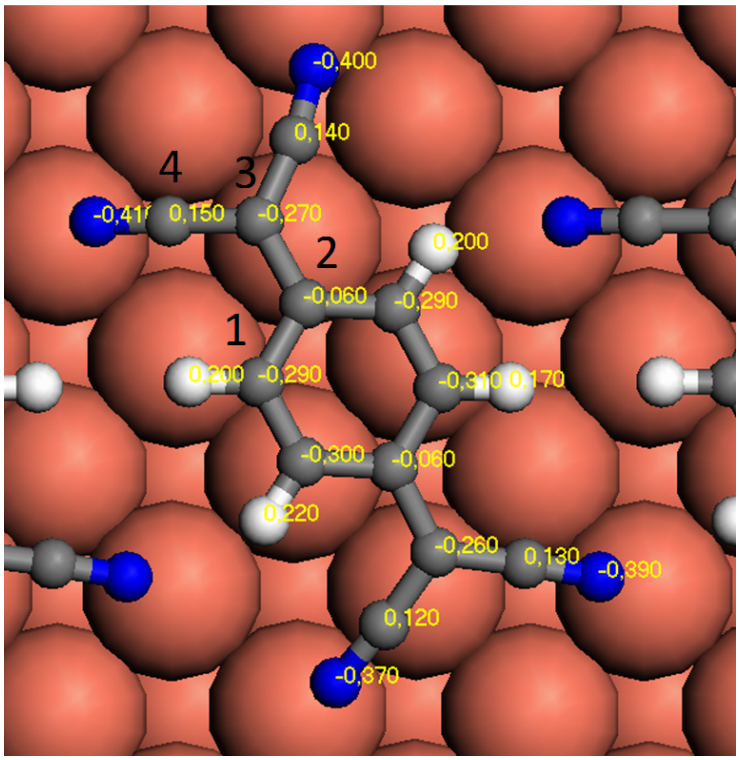

Figure 16: Mulliken analysis of TCNQ/Cu(100): In order to be able to understand the XPS data, a Mulliken population analysis of the electronic densities on every C-atom leads to three different groups with similar charges. Thus the three observed XPS-peak can be assigned to the corresponding C-atoms depending on their charge: The four carbon atoms in direct contact with nitrogen are positively charged which leads to shift in the direction of higher binding energies, two C-atoms of the central ring are basically uncharged and the remaining 6 carbons exhibit a similar negative charge with the consequence of a shift in the direction of lower binding energies. The expected relation would thus be 4:2:6 (from the highest binding energy going to the lowest) which is qualitatively confirmed (4:2.8:4.4).

3.5.4 Work function

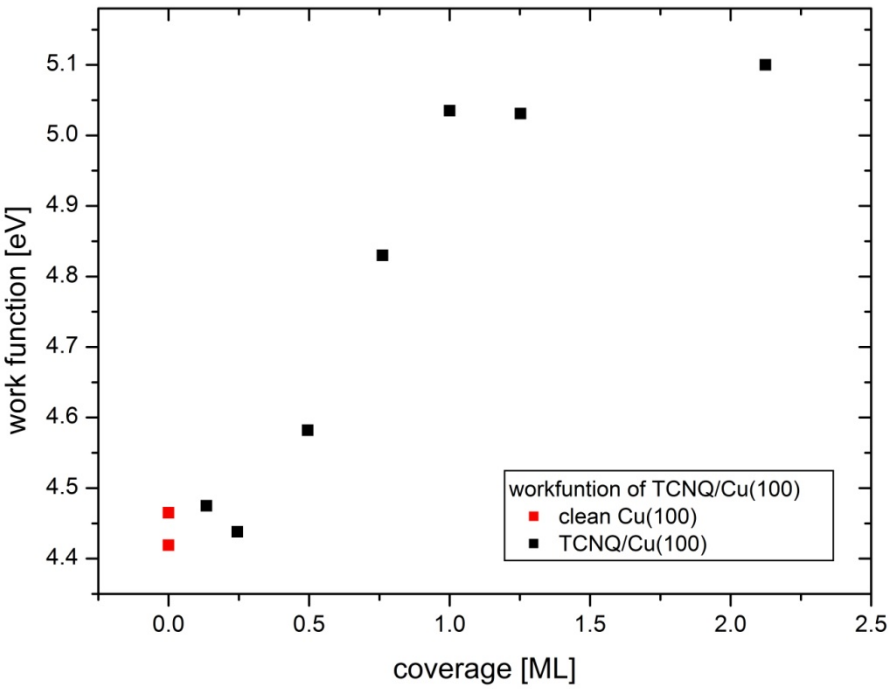

Figure 17: The work function of TCNQ/Cu(100) is represented against the coverage. Up to 0.5 ML only a slight difference is visible compared to the clean samples. Samples with a higher coverage have an increased work function which saturates quickly and stays constant for thicker samples. A total difference of 0.6 eV between the clean substrate and the saturation work function is observed.

In the discussions above we attributed the chemical shift of the neutral bulk-components in contact with the surface to a negative charge transfer from the substrate to the TCNQ molecule. This is justified only if it can be proven that a screening effect can be excluded as being responsible. Work function measurements of samples with coverages from the submonolayer- to the multilayer-regime can doubtlessly confirm a charge transfer. This is found in the case of TCNQ/Cu(100). Up to a coverage of a monolayer the work function increases compared to the pristine Cu-surface in a approximately linear way. For coverages over a monolayer the work function saturates at a value of $\phi = 5.1 \pm 0.1$ eV (Fig. 17). The work function of the metal substrate can thus be increased 0.6 eV by depositing TCNQ molecules.

In conclusion, XPS results support the existence of electron transfer from the substrate to the TCNQ molecules, as evidenced by the core level shift and the change in work function.

3.6 XAS Results

In order to understand and confirm the theoretical results with respect to the strong deformation that TCNQ seems to undergo upon adsorption on the metal surface, XAS experiments were done in collaboration with the group of Professor Wöll. Series of XAS-spectra of the same sample varying the x-ray incidence angle can give insight into the orientation of the unoccupied molecular orbitals of TCNQ and then in principle the adsorption geometry can be obtained.

3.6.1 N K-edge

The XAS spectra of the powder-bulk sample reveal the electronic structure of the unoccupied states of the neutral molecules (Fig. 18 b, upper part). At the N K-edge spectra three clear peaks can be observed: peak 1 at 396.9, peak 2 at 398.9 eV and peak 3 at 400.0 eV (Fig. 18) consistent with literature spectra of neutral TCNQ[16]. The first resonance (1), associated with the transition from the N1s-core level to the LUMO of TCNQ[16], disappears in the N1s-XAS spectra of 1 ML TCNQ/Cu(100) (Fig. 18 a, lower part). This could be a consequence of the charge transfer from the metal substrate to the molecule: since the LUMO is occupied, these transition are no longer possible.

Bässler et al analyzed and presented spectra of a multilayer sample of TCNQ/Ag(111)[17]. Although there is a shift of approximately 1 eV with respect to our data, a comparison of all peaks identifies resonance 2 as originating from the cyano groups (Fig. 18 a), which is in agreement with the identification, based on theoretical and experimental methods, used by Fraxedas et al[16]. The triple bond of the cyano groups exhibits two orthogonal π*-orbitals which in the bulk-like powder or multilayer samples are indistinguishable in energy. This is different in the sample of 1ML TCNQ/Cu(100) due to the interaction of the molecule with the surface and an energy split of resonances 2 into $2'_a$ at 398.7 ± 0.1 eV and $2'_b$ at 399.6 ± 0.1 eV is observed. This behavior has already been observed for resonances originated from molecules containing cyano groups adsorbed on metal surfaces (heteronuclear diatomic CN on Pd(111)[18] and TCNQ on Ag(111)[17]) due to a non-normal bonding geometry with the result of an anisotropic interaction of the π-orbitals with the substrate.

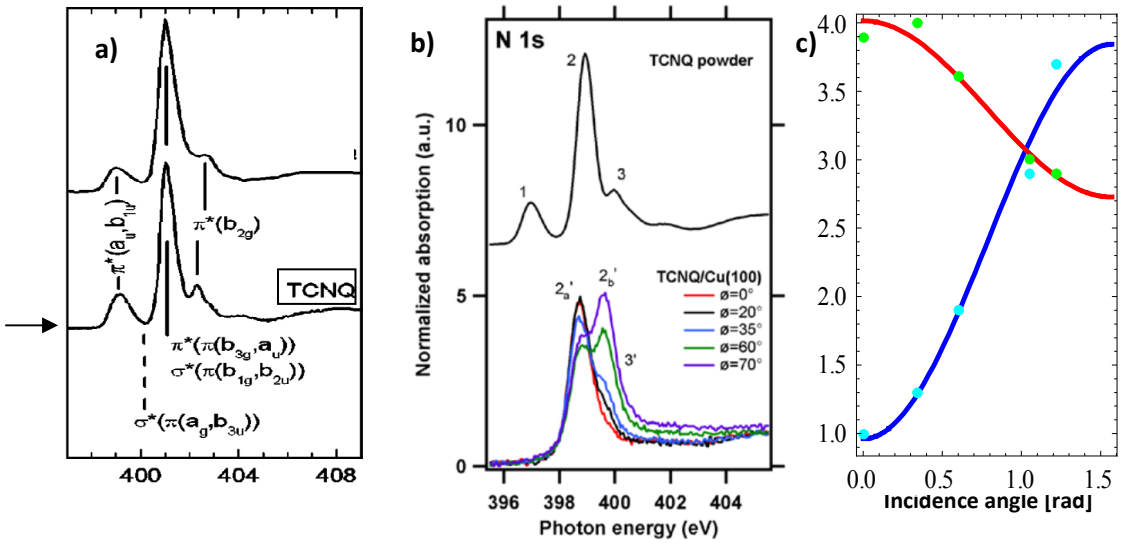

Figure 18: Comparison of XAS results from literature compared to our experiments: In **a)** a bulk TCNQ N K-edge spectrum with the peak identification is shown[taken from 16]. Our experimental N K-edge spectra of a powder sample is shown in **b)** in the upper part while the lower part includes spectra from a monolayer sample depending on the incidence angle. Resonance 1 from the powder sample disappears due to the electron transfer from the sample. Resonance 2 is split two due to the different interaction of the π*-orbitals with the surface. The different peak area evolutions of resonance 2_a' (green dots, c) and 2_b' (cyan dots) with the x-ray incident angle and the fitted curves are shown in **c)**. The area dependence of the peaks with the x-ray incidence angle leads to the interpretation that the cyano groups in contact with the surface exhibit approximately the angle DFT predicts.

As mentioned before, due to the different orientation of the two orthogonal π*-orbitals of the cyano groups with respect to the surface, resonances 2_a and 2_b show a different dependence on the incidence angle (Fig. 18 b): Peak $2'_a$ decreases and resonance $2'_b$ grows with increasing incidence angle (angle between incoming x-ray beam and surface normal). As both N K-edge peaks are different in energy each is fitted assuming a vector-like character for both π*-orbitals (and not with a plane-like character). The regression curves (Fig. 18 c: green and purple straight lines) fit well the experimental peak intensities (Fig. 18 c: green and purple dots) with an angle of the π*-orbitals of the C-N-bond of resonances 2_a of $\alpha_{peak\ 2a} = 61.3 \pm 0.6$ ° and 2_b of $\alpha_{peak\ 2b} = 33.0 \pm 0.3$ ° with respect to the surface normal. If the π*-orbitals are mutually orthogonal, the triple bond of the cyano groups makes an angle with the surface (see Chapter "Experimental methods and theoretical background") of

$$\alpha_{N\ K\text{-}edge} = 14.9 \pm 1.6\ °$$

(Although the error of the fit is small, the typical experimental precision of the whole method is approximately ± 10 ° [19]), which is in very good agreement with the theoretical model of the adsorption geometry: $\alpha_{theory} = 14.1 \pm 2.9$ °. (Here the theoretical error is the standard deviation of the four angle values of all four cyano groups ,which are not equal.)

Resonance 3 has been related to the central carbon ring[16, 17]. In a very similar spectrum of a multilayer sample of TCNQ/Ag(111)[17] the strong dependence of peak 3 on the x-ray incidence angle θ, with a nearly vanishing contribution to the spectrum at θ = 0 °, shows that the central carbon ring is parallel to the surface. In our case peak 3 also disappears at an incidence angle of θ = 0 ° which leads to the same interpretation as in the TCNQ/Ag(111)-system: the central carbon ring is parallel to the surface.

The N K-edge spectra yield therefore experimental arguments for the theoretical adsorption geometry with the result that the TCNQ molecule lies with its central carbon ring flat on the Cu-surface and that the cyano groups are tilted towards the surface.

3.6.2 C K-edge

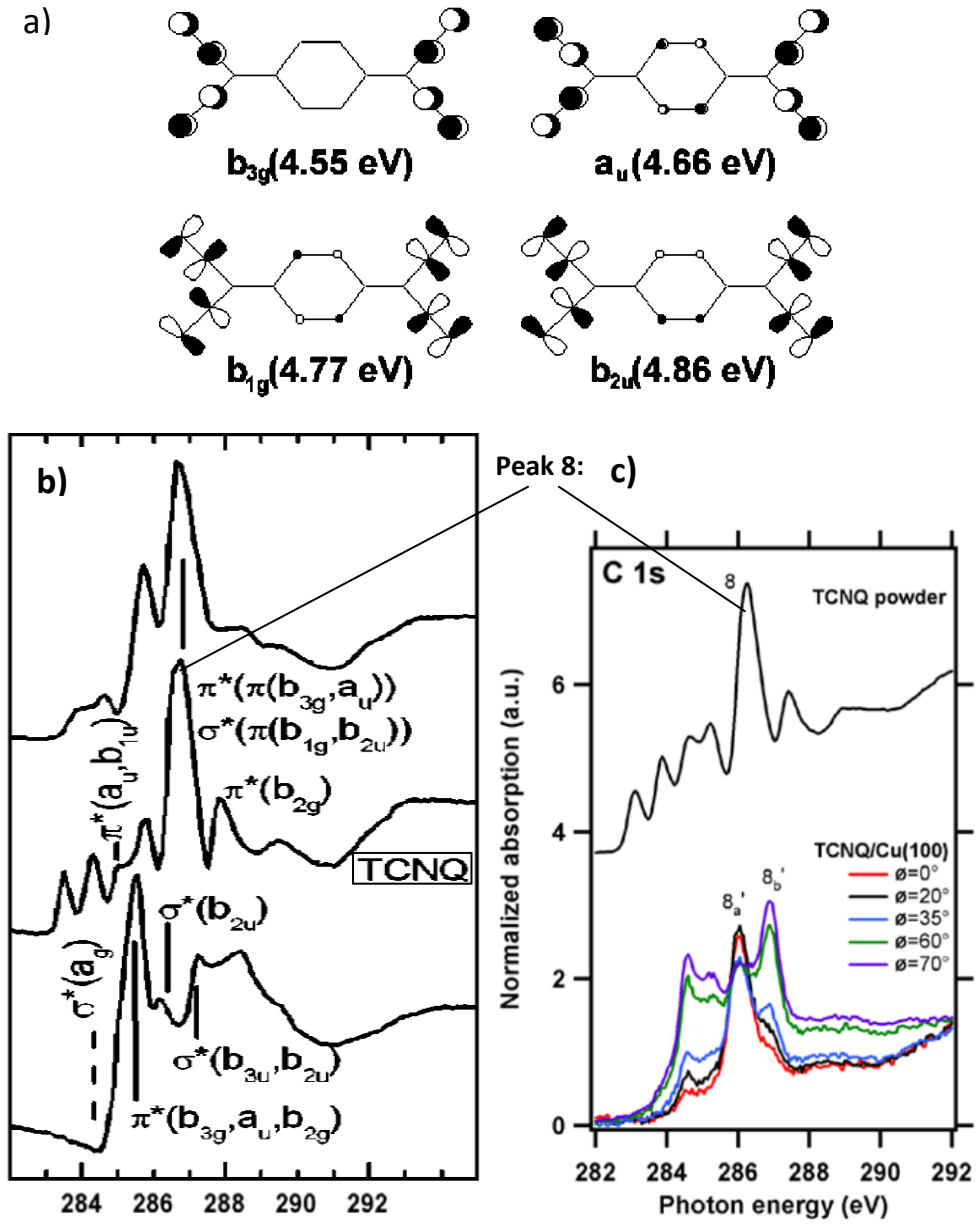

Figure 19, partially taken from Fraxedas et al[16] Molecular orbital- and peak assignation at the C K-edge spectra of TCNQ: **a)** Two schematic calculated unoccupied molecular orbitals of isolated TCNQ related to resonance 8 in the shown XAS spectra. The molecular orbital of peak 8 are mainly located on the cyano groups and thus an angular dependence of the intensity is expected assuming that the former DFT and XPS results are correct. **b) and c):** Experimental XAS spectra from bulk-TCNQ[16] (b), spectrum in the middle) and from our powder TCNQ-samples at the C K-edge (c), upper spectrum). A comparison of both volume-like XAS spectra shows the same peak number with similar energy distances but different intensity relation. Therefore the peak assignment is especially clear for the most intense one, peak 8. In the lower part of c) spectra of a monolayer sample are shown with different x-ray beam incidence angles. Here the assignation is, apart from peak 8, rather problematic.

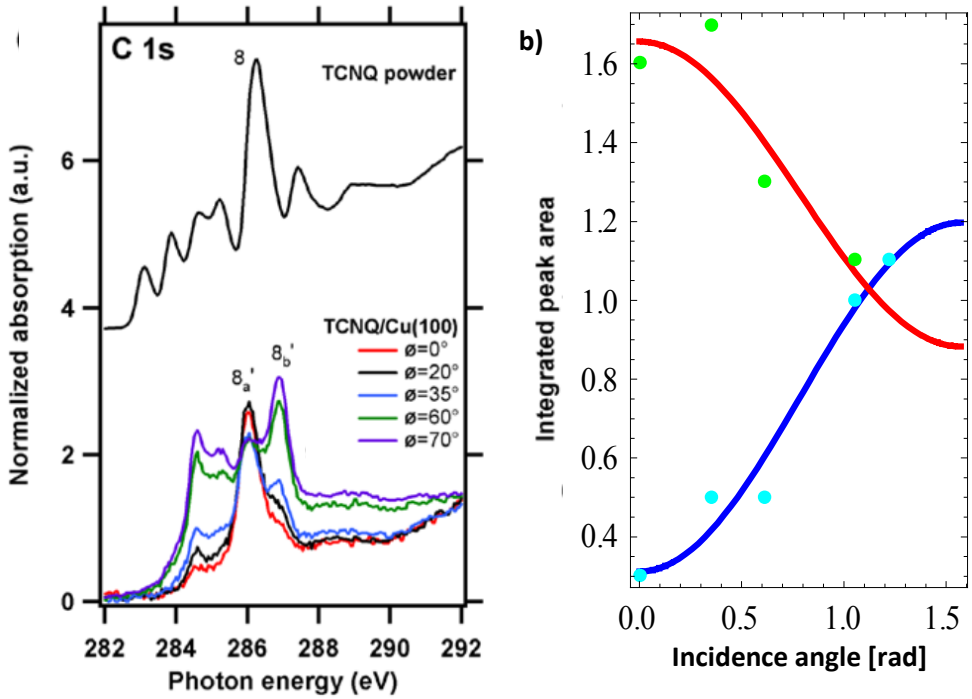

Figure 20: The C1s-XAS spectrum of the powder sample (**a)**, upper part) shows six peaks from which peak 4 has no equivalent peak in the monolayer sample of TCNQ/Cu(100) at different x-ray-incidence angles (**a)** lower part) likely as a consequence of the charge transfer. Peak 6', 7', 8_a' and 8_b' depend strongly on the incidence angle of the x-ray beam with a splitting of peak 8 similar to the N1s-edge for the same reason: the surface vicinity to the cyano bonds and a symmetry breaking. The experimental evolution of the peak areas with the x-ray incident angle for the monolayer sample is illustrated in **b)** (dots) with the theoretical regression curves (straight lines). The different behavior of the curves finds its origin in the geometrical orientation of the p-orbitals of the cyano group atoms with respect to the surface.

The C K-edge of neutral TCNQ yields a more complex spectrum than the N K-edge (Fig. 19 b, upper part). An assignment is therefore more difficult. It seems that the first peak at 283.1 eV of the bulk and powder sample is not any longer present in the monolayer sample. Assigning this first peak to the LUMO, the disappearance of it in the sample with 1ML coverage would be expected because the LUMO is filled by charge transfer and thus unavailable for photo excited electrons. In order to calculate the bond angle of the cyano group with the surface, we concentrated on the strongest peak, denominated "8" at 286.2 eV in the powder sample, which can be identified as related to the electron transition from the carbon core levels of the cyano groups into the molecular π*-orbitals. Also the energy position and the previously described split behavior of the peaks 8_a' at 286.0 eV and 8_b' at 286.8 eV support this assignation. The slight shifts in energy are similar to peak $2_{a,b}$' in the N K-edge spectra. This is confirmed by literature which assigns the π*-orbitals of the resonance 8 to the cyano moieties of the TCNQ molecule.

The resulting angle for peak 8_a' is $\alpha_{peak\ 8a} = 65.5 \pm 0.7$ ° and for peak 8_b' a value of $\alpha_{peak\ 8a} = 33.6 \pm 0.3$ ° is found. These results are consistent with the ones from the split peaks in the N K-edge, and the bond angle of the cyano groups to the surface is calculated to:

$$\alpha_{C\ K\text{-}edge} = 21.5 \pm 1.2\ °$$

This is close to the results from the N K-edge ($\alpha_{N\ K\text{-}edge}$= 14.9 ± 1.6 °) and within the usual error of this method (Δα = ± 10 ° [19]). The average angle of both methods is:

$$\alpha_{surface\ bond} = 17.9 \pm 4.7\ °$$

This result supports the former theoretical findings of a surface geometry with the central carbon ring parallel to the surface (peaks 3' ,N K-edge, with an angle close to 0 °) and the adsorption of the cyano groups with a tilt angle to the substrate plane of $\alpha_{surface\ bond}$ = 18 ± 5 ° (derived from peaks $2'_a$, $2'_b$, $8'_a$ and $8'_b$). Moreover the XAS data is consistent with a charge transfer from the metal substrate and a filling of the LUMO orbital of TCNQ upon adsorption.

3.7 Substrate mediated Interaction

After corroborating the theoretical results of a distorted and bent adsorption model of TCNQ/Cu(100), with a charge transfer of more than one electron from the surface to the molecule, a detailed analysis of the other side of the interface, the surface, as revealed by the DFT calculations, explains the rectangular shape of the island.

Theoretical calculations for the self-assembled layer show that the adsorption geometry of a single molecule does not change significantly due to aggregation with other molecules, that means it is mostly determined by molecule - substrate interactions. The strong chemical interaction between the lone pairs of the nitrogen atoms of TCNQ with the d_z^2-orbitals of the substrate atoms leads to a reconstruction of the surface with a change in z-height of the Cu-atoms in the top layer. (Theoretical calculations on the assembly of another strong electron acceptor, tetracyanoethylene on Cu(100), lead to similar results[20]). The Cu-atoms closest to the cyano groups are lifted 0.22 Å from its equilibrium position (Fig. 21) while other surface atoms are pushed down -0.16 Å relative to its bulk position (maximal corrugation is thus 0.38 Å).

The binding energy for the isolated molecule is slightly smaller (2.23 eV) than the one of a molecule in the complete overlayer (2.35 eV). This extra energy is originated in a larger stabilization through the island assembly, which takes place due to two different interactions. One is the electrostatic attraction between positively charged hydrogen atoms on one molecule and negatively charged nitrogen atoms on the neighboring TCNQ, especially in the b_2-direction (see section "STM Results"). The other interaction is mediated by the substrate and is able to explain the elongation of the TCNQ islands. Some indication that the lifting of the atoms might be related to the assembly in the b_1-direction arises from the realization that the distorted Cu-atoms lie closer together in this direction (Fig. 21). The four Cu-atoms per molecules bound to the nitrogen atom of the cyano groups are strongest lifted. Three of these four surface atoms are in direct contact to another strongest lifted surface atom bond to a different molecule (Fig. 21). As we will see below, the reason for the assembly of the islands along the b_1-direction is that it takes less energy to lift Cu-surface atoms in direct vicinity than isolated Cu-atoms

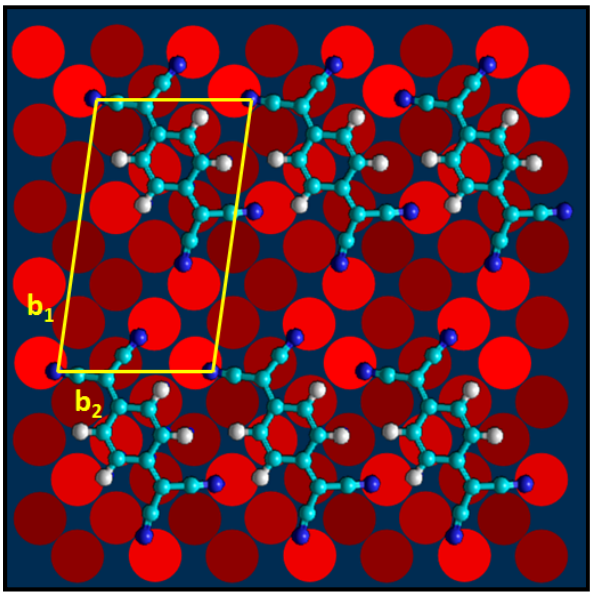

Figure 21: Theoretical calculation of TCNQ/Cu(100) in a periodic unit cell (yellow color) resembling the adsorption of a complete overlayer of TCNQ on Cu(100). The surface atoms with brighter colors are higher (maximum is 0.22 Å above the equilibrium position of the pristine surface, minimum is 0.16 Å below it). The TCNQ island assembly finds its origin in the energy gain of lifted Cu-atoms by being in direct contact with each other.

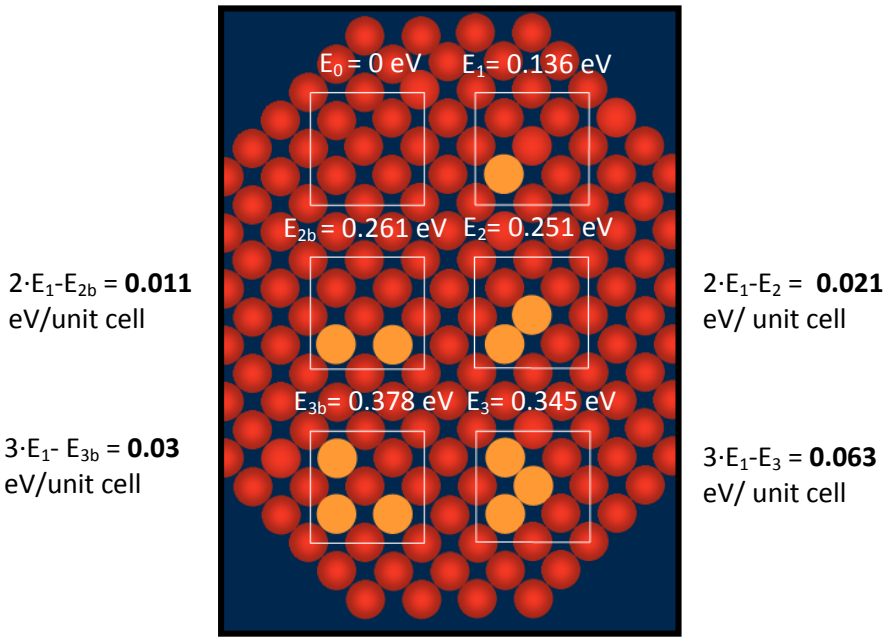

Figure 22: Illustrated are Cu-unit cells with different scenarios of lifted Cu-atoms with its corresponding additional cost in energy. That shows that the surface distortion found theoretically through the strong interaction of TCNQ with the substrate is energetically less costly if the lifted atoms are close together. Most binding energy exhibits the last scenario (lower right corner) with three lifted Cu-atoms close together which represents the maximum number taking into account the geometry of the associated TCNQ molecules in the islands. As a result an energy of 0.063 eV is gained by bringing three lifted Cu-atoms in the nearest neighbor position, the number found in the calculation for the assembly.

The energy gain for a lifted surface atom when it is in direct contact with other lifted Cu-atoms can be calculated comparing the energy it costs to pull an isolated Cu-atom out of its equilibrium position, with the energy it costs to lift adjacent Cu-surface atoms (Fig. 22). That was done in a DFT calculation with a (2x2) unit cell of 4 layers of Cu(100) with different numbers of adjacent surface atoms lifted (Fig. 22). The theoretical result for the above found number of lifted and adjacent Cu-atoms in a TCNQ island (three per molecule, Fig. 21) yields a binding energy gain of 63 meV per molecule. This energy leads to a resulting attractive force between the distorted surface atoms which are bond to TCNQ molecules. The electrostatic interaction along the b_2-direction causes a binding energy with the same magnitude (65 meV and 95 meV for U2 and U1, with and without a dislocation line, respectively) and the superposition of both different forces leads to the observed islands with its peculiar aspect ratio. Without the substrate mediated interaction only small forces in the b_1-direction (for example, Van der Waals) would exist.

3.8 Conclusions

Summarizing, TCNQ/Cu(100) has been investigated with a variety of complementary structural and spectroscopic methods and the experimental results confirm the theoretical findings about the almost planar adsorption of TCNQ on Cu(100), with the central carbon ring parallel to the surface and the dicyanomethylene groups bent towards the surface. This last result is possible due to a conformational change of the molecule, mainly the bending of bond B3 (Fig. 1), enabled by the negative charge transfer from the surface to TCNQ. This strong interaction with the substrate causes a lifting of the surface atoms which are closest to the nitrogen atoms of the four cyano groups, and results in a binding energy gain through the assembly of TCNQ in the observed way because lifted Cu-atoms find themselves coordinated to lifted surface atoms of adjacent molecules. This is energetically less costly and drives thus the self assembly along the b_1-direction, while in the other direction a combination of the electrostatic interaction between the oppositely charged groups of neighboring molecules and this substrate mediated interaction are the reasons.

3.9 Bibliography

References

1. Torrance, J. B. The difference between metallic and insulating salts of tetracyanoquinodimethone (TCNQ): how to design an organic metal. *Acc. Chem. Res.* **12**, 79-86 (1979).

2. Romaner, L. *et al*. Impact of Bidirectional Charge Transfer and Molecular Distortions on the Electronic Structure of a Metal-Organic Interface. *Phys. Rev. Lett.* **99**, 256801 (2007).

3. Bedwani, S., Wegner, D., Crommie, M. F. & Rochefort, A. Strongly Reshaped Organic-Metal Interfaces: Tetracyanoethylene on Cu(100). *Phys. Rev. Lett.* **101**, 216105 (2008).

4. Wegner, D. *et al*. Single-Molecule Charge Transfer and Bonding at an Organic/Inorganic Interface: Tetracyanoethylene on Noble Metals. *Nano Letters* **8**, 131-135 (2008).

5. Perdew, J. P. & Wang, Y. Accurate and simple analytic representation of the electron-gas correlation energy. *Phys. Rev. B* **45**, 13244 (1992).

6. Martin, N., Segura, J. L. & Seoane, C. Design and synthesis of TCNQ and DCNQI type electron acceptor molecules as precursors for 'organic metals'. *J. Mater. Chem.* **7**, 1661-1676 (1997).

7. Milian, B., Pou-Amerigo, R., Viruela, R. & Orti, E. A theoretical study of neutral and reduced tetracyano-p-quinodimethane (TCNQ). *Journal of Molecular Structure: THEOCHEM* **709**, 97-102 (2004).

8. Khatkale, M. The vibrational and electronic spectra of the mono?, di?, and trianon salts of TCNQ. *J. Chem. Phys.* **70**, 1851 (1979).

9. Kamna, M. M., Graham, T. M., Love, J. C. & Weiss, P. S. Strong electronic perturbation of the Cu{111} surface by 7,7',8,8'-tetracyanoquinonedimethane. *Surf. Sci.* **419**, 12-23 (1998).

10. Otero, R. *et al*. Lock-and-key effect in the surface diffusion of large organic molecules probed by STM. *Nat Mater* **3**, 779-782 (2004).

11. Barth, J. V. Transport of adsorbates at metal surfaces: from thermal migration to hot precursors. *Surface Science Reports* **40**, 75-149 (2000).

12. Kwon, K. *et al*. Unidirectional Adsorbate Motion on a High-Symmetry Surface: "Walking" Molecules Can Stay the Course. *Phys. Rev. Lett.* **95**, 166101 (2005).

13. Lindquist, J. M. & Hemminger, J. C. High energy resolution x-ray photoelectron spectroscopy studies of tetracyanoquinodimethane charge transfer complexes with copper, nickel, and lithium. *Chemistry of Materials* **1**, 72-78 (1989).

14. Grobman, W. D., Pollak, R. A., Eastman, D. E., Maas, E. T. & Scott, B. A. Valence Electronic Structure and Charge Transfer in Tetrathiofulvalinium Tetracyanoquinodimethane (TTF-TCNQ) from Photoemission Spectroscopy. *Phys. Rev. Lett.* **32**, 534 (1974).

15. Higo, M., Futagawa, T., Mitsushio, M., Yoshidome, T. & Ozono, Y. Adsorption State and Morphology of Tetracyanoquinodimethane Deposited from Solution onto the Atomically Smooth Native Oxide Surface of Al(111) Films Studied by X-ray Photoelectron Spectroscopy and Atomic Force Microscopy. *The Journal of Physical Chemistry B* **107**, 5871-5876 (2003).

16. Fraxedas, J. *et al*. Characterization of the unoccupied and partially occupied states of TTF-TCNQ by XANES and first-principles calculations. *Phys. Rev. B* **68**, 195115 (2003).

17. Bässler, M. *et al*. Near Edge X-ray Absorption Fine Structure Resonances of Quinoide Molecules. *Langmuir* **16**, 6674-6681 (2000).

18. Somers, J. *et al*. An adsorbed diatomic molecule showing parallel bonding: CN/Pd(111). *Surf. Sci.* **188**, L693-L700 (1987).

19. Stöhr, J. & Outka, D. A. Determination of molecular orientations on surfaces from the angular dependence of near-edge x-ray-absorption fine-structure spectra. *Phys. Rev. B* **36**, 7891 (1987).

20. Bedwani, S., Wegner, D., Crommie, M. F. & Rochefort, A. Strongly Reshaped Organic-Metal Interfaces: Tetracyanoethylene on Cu(100). *Phys. Rev. Lett.* **101**, 216105 (2008).

4 TCPQ and TCTQ on Cu(100)

4.1 Motivation

15,15,16,16-tetracyano-6,13-pentacene-*p*-quinodimethane (TCPQ) and 13,13,14,14-tetracyano-5,12-tetracene-*p*-quinodimethane (TCTQ) belong to the TCNQ family and are interesting from a scientific point of view as well as from a technological perspective because of the variation of the number of central carbon rings. The understanding of the effect that this parameter has on the metal-organic interface including charge transfer, self assembly, adsorption geometry and reactivity, may identify a tool to control interfaces of organic electronics and thus device performance in general. Additionally to this fundamental questions, we show in this chapter that TCPQ and TCTQ are building blocks which are able to form polymeric chains on Cu(100) by a surface assisted reaction. Variable STM and quantitative XPS are combined to identify the reaction mechanism, which is first the radicalization of the units by the removal of two cyano groups, one from each side of the molecule. This is possible due to the charge donating role of the substrate and the thus gained conformational freedom. The chemical interaction of the radicals with the linear chain formation is the second step of the mechanism.

With the concept of supramolecular chemistry many different ordered 1D- or 2D-achitectures of molecular units have been created. Different interactions can be exploited to bring the constituents into programmed order.

- For example Van der Waals forces are weak (0.02 – 0.1 eV[1]) and act only at short distances (< 1 nm)[1] but are for example responsible for the close-packed formation of a tetramesitylporphyrin (TMP) network on Cu(100)[2]. The intermolecular interaction requires therefore certain coverage before the formation of 2D-islands set in[2].

- Hydrogen bonds are responsible for the formation of many different ordered structures with usually larger interaction energy per molecule (0.05 - 0.7 eV[1]) than in islands based on dispersion forces, although both can stand in competition[3]. The relevant distance of hydrogen bonds is 0.15 – 0.35 nm[1]. A higher control over the architectures is possible due to the selectivity and directionality of hydrogen bonds. The building blocks contain very often two or more carboxyl groups which attract each other due to the opposite charge density on the carbonyl and the hydroxyl group with the result of two hydrogen bridges per unit. Terephthalic acid (TPA) on Au(111) is only one of many examples for the formation of supramolecular domains based on the 1D-carboxyl H-bond pairing scheme[4]. 1D-structures can be observed among anthraquinone on Cu(111) where two weak hydrogen bonds (0.05 eV) per molecule are formed based on the attractive interaction of the carbonyl moieties with hydrogen atoms of the C-ring system of adjacent molecules[5]. The same authors describe also an example of hydrogen bonds based on the interaction between sulphur and hydrogen which is even weaker (0.02 eV)[6].

- Metal coordination networks on surfaces are based on the interaction of the building blocks with linker groups like carbonitriles, amines or carboxylic acids containing chemical elements with electron lone pairs and a metal adatom[7, 8 and references therein]. The interaction strength is larger than in hydrogen bond based architectures (0.5 – 2 eV[1]); moreover the bond character is selective and directional and acts over a range of 0.15 – 0.25 nm[1]. The metal atoms can be co-deposited with the organic linkers[9] or are present due to the metal surface in form of diffusing substrate atoms like in the case of bipyridyl molecules on Cu(100)[10]. A very peculiar example of a 1D-metal-oxygen coordination bond is the spontaneous assembly of Zn-porphyrins nanorods on Au(111) and Cu(100) with the interconnected porphyrins standing upright in contrast to the typically found planar adsorption of these kind of molecules on metal substrates. Each Zn-porphyrin is connected with its central metal atom via a coordination bond to two oxygen containing linkers on each side of the main molecular plane. These linkers are then connected to the next Zn-atom in the center of another porphyrin within the rod[11]. The advantages of coordination bonds are their relatively large strength together with a certain reversibility of bonds which can be exploited to achieve higher degree of order. Hydrogen and coordination bonds mimic biological processes which thus can be analyzed and understood in detail. This is partially a motivation for the investigation of these structures.

- An important property of covalent networks is their stronger interactions between the molecular building blocks (several eV)[12]. This is desirable for a higher temperature resistance or a better electronic coupling for charge transport, for example. Covalent networks can be created in several different ways. A very controlled method is the deposition of building blocks with predefined connection and the subsequent activation through thermal energy with the result of a precise chemical reaction between the building blocks. One of the first examples of that approach is the formation of covalent structures from Br-porphyrins as building blocks. These are first deposited on Au(111) where they self assemble in close-packed islands. In a second step the Br-atoms are removed by annealing (single Br-atoms could be removed by the STM-tip, too). The remaining radicals form then, depending on the number and former position of the Br-atoms dimers, 1D-structures or 2D-networks[13]. Nanoporous covalent networks can be achieved in a boronate-based reaction by deposition of 1,4-benzenediboronic acid (BDBA) on Ag(111). The molecules are subsequently dehydrated (- $3 \cdot H_2O$) by annealing and form then arrays of boroxine on the surface. The esterification of BDBA by 2,3,6,7,10,11-hexahydroxytriphenylene (HHTP) on the same surface leads to similar covalent networks, with the size of the initial molecules controling the radius of the formed, thermally very stable (up to 750 K for 5 min.) pores[14]. 1,3,8,10-tetraazaperopyrene (TAPP) on Cu(111) forms three different main assembly structures depending on the active interaction force, which is irreversibly tunable by the substrate temperature. At low temperatures (310 K) close packed islands based on Van der Waals forces and hydrogen bonds are found. Two different coordination networks with Cu-adatoms provided by the surface appear after annealing to 380 - 450 K. Interestingly the ratio between the two types can be adjusted by the annealing temperature. Covalently bound chains which incorporate

Cu-adatoms can be observed after annealing to 550 K[15]. Different graphene nanoribbons can be obtained by the deposition of precursor molecules functionalized at specific positions with two attached Br-atoms (for example 10, 10'-dibromo-9, 9'-bianthryl). These are removed during the sublimation. The remaining biradicals react at the predefined points under a first thermal activation step to form a covalently bound polymer. After a second annealing a surface-assisted cyclodehydrogenation reaction couples further carbon atoms within the polymer and establishes an extended fully aromatic system[16] which is chemically inert in ambient conditions.

In summary, many different complex covalent nanostructures with potential applications in molecular electronics, sensors, surface nanomachines and catalysis have been created[17]. Chemical reactions well known from solution (imine formation, dehydration of boronic acid and esterification[17]) are exploited and also some new have been discovered, due to the surface which confines the processes to 2D, which can lower the reaction energy barriers and catalyses the formation of covalent interactions (for example the homolytic fission of C–Br bonds[12]). Compared to solution a broader range of temperatures for sublimation without the risk of air oxidation or solvent decomposition can be used[17].

In general, the nature of the reactions in all these case is inferred from STM images and tip manipulation experiments, and only few are supported by qualitative XPS, mostly only to show that the halogens have left the surface. For a precise control, however, a complete analysis of all involved parameters will be required. This means to identify the leaving groups, the exact role of the substrate, the reaction mechanism with the activation steps and to determine the diffusion and preorganization of the reactants. In this chapter STM and gas phase calculations are combined with quantitative XPS-analysis to identify most of these parameters concerning the covalent bond formed between the building blocks from the TCNQ family.

4.2 Experimental details

TCPQ molecules have been evaporated with a resistively heated glass crucible at 460 K onto the surface of a Cu(100) single crystal, held at room temperature (RT) with a rate of about 0.1 ML per minute. TCTQ molecules have been deposited as well this way at 420 K onto the same Cu-crystal held at RT. The UHV-STM measurements were conducted with the microscope at a temperature between 100 K and RT. Within this range the appearance of the observed objects did not vary significantly with the imaging temperature.

The STM simulations were done with a modified and tested IGOR macro provided by Oliver Gröning and Roman Fasel at the EMPA in Saint Gallen, Switzerland.

The annealing temperature is defined as the temperature which is finally reached at the surface after annealing with a resistively heated filament during 10 minutes with a certain power. The current was the tuning parameter for the annealing temperature and the temperature at the surface was measured with a thermocouple welded directly to the Cu(100) crystal.

4.3 Description of TCPQ and TCTQ

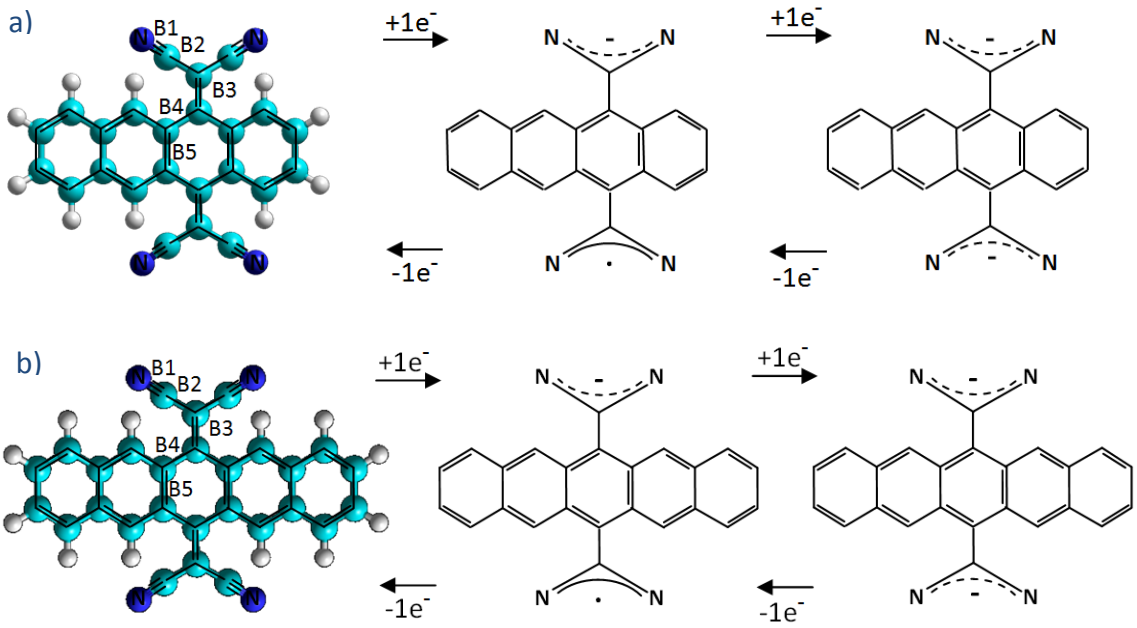

Figure 1: Chemical structures of the neutral, the anion and dianion form of a) TCTQ and b) TCPQ: An additional negative charge is delocalized in one of the two dicyanomethylene groups and causes bond changes and an aromatization of the central pentacene backbone.

TCPQ and TCTQ are organic acceptor molecules from the TCNQ family (chapter 3). TCTQ has a π-electron extension in the form of one naphthalene unit fused to the double bond of the quinone six fold ring and another carbon ring on the other side. TCPQ exhibits this π-extension with two naphthalene units fused to each of the double bond of the quinone six fold ring. This ring with its π-extensions will subsequently be called pentacene backbone.

TCPQ consists of 28 carbon, 12 hydrogen and 4 nitrogen atoms. The latter render the molecule an electron acceptor, although less pronounced than TCNQ[18]. In the neutral form, the steric repulsion between the cyano groups and the hydrogen atoms at the side of the pentacene moieties cause the dicyanomethylene groups to bend in one direction whereas the pentacene backbone bends in the opposite direction, thus acquiring a conformation similar to a horse saddle (conformation A in Table 1)[19].

Due to the strong similarities between TCNQ, TCTQ and TCPQ, they show a similar behavior when they take up an electron[19]. Along the lines of TCNQ, a negative charge is delocalized in the dicyanomethylene groups and thus will affect various parts of the molecule (Fig. 1). Bond B3, originally with π-character, changes to a more σ-type bond and thus becomes more flexible. The aforementioned σ-character of the bond B3 allows the dicyanomethylene groups to rotate around this bond until one cyano group is on one side of the plane of the pentacene backbone and the second on the other side (conformation B in Table 1). A similar behavior has been also described for the anion form of 11,11,12,12-tetracyano-9,10-anthraquinodimethane (TCAQ) molecules, a derivative of the TCNQ family but with only three central benzene rings[20].

We have verified the above results by calculating both conformations for TCPQ, A and B, using the semi-empirical PM3 method (Table 1). Contrary to the neutral TCPQ (conformation A), the amplitudes of the HOMO-1 and HOMO orbitals of the anion form (conformation B) are very small at the pentacene backbone, but are rather high around the dicyanomethylene groups, that is, the additional charge increases the electron concentration around the cyano groups, as can also be seen in the electronic distribution maps of the molecules (Table 1).

	Conformation A	**Conformation B**
	TCPQ:	$TCPQ^{2-}$:
Top view	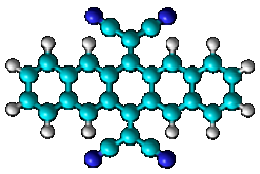	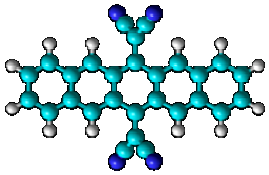
Side view		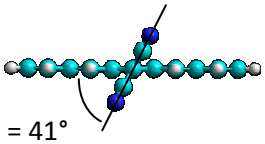
	HOMO: -9.4 eV 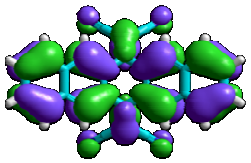	
	LUMO: -2 eV 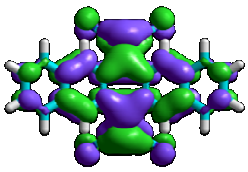	HOMO: -1.3 eV 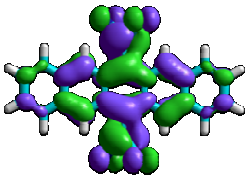
Electrostatic potential projected onto charge density isosurface	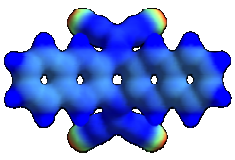	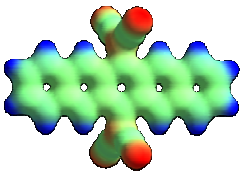

Table 1: Stable gas phase conformations (top and side view) for the neutral and charged TCPQ are illustrated. The LUMO of the neutral molecule in conformation A corresponds to the HOMO of the doubly charged TCPQ in conformation B. The shape of the LUMO of the neutral molecule does not change much when it is populated by two electrons. In the anion (conformation B) the HOMO is rather concentrated on the cyano groups and a bit in the central part of the molecule, meaning that additional charges are localized in those areas (red color in the charge distribution map). The data was calculated with the PM3 method in the Hyperchem program package.

4.4 Adsorption of TCPQ and TCTQ on Cu(100)

4.4.1 STM Results, low coverage

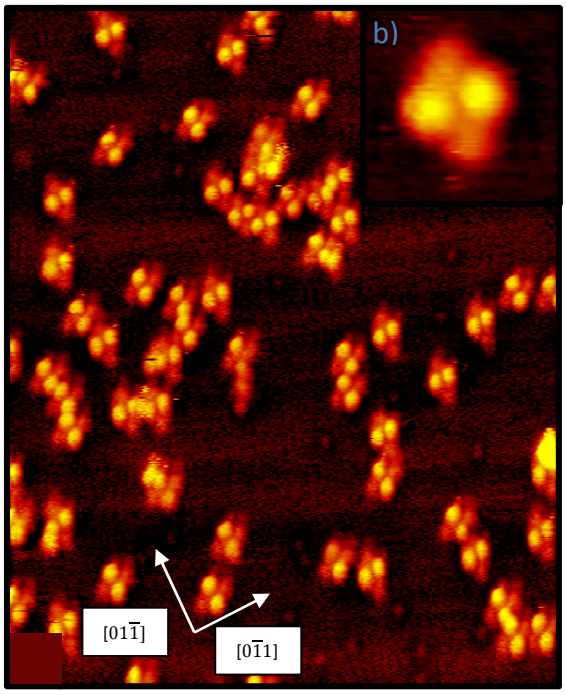

Figure 2: a) STM image (taken at 150 K) of 0.2ML of TCPQ grown at RT on Cu(100) (230 Å x 290 Å, -2 V, -0.19 nA): A random distribution of molecules with a few small molecular aggregates can be observed. The TCPQ molecules, with an apparent dimension of 17 Å x 13 Å, are with its symmetry axis aligned along the high symmetry directions (indicated by the arrows). **b)** STM image (taken at RT) of a single molecule (40 Å x 40 Å, -3.1 V, -0.05 nA).

After depositing 0.2 ML of TCPQ on Cu(100) at RT, STM images taken at 150 K show randomly adsorbed molecular units (Fig. 2a). They have an elongated central part decorated to the left and right of its long axis with two characteristic bright lobes separated 7.9 ± 0.5 Å (Fig. 2b). The presence of only one kind of adsorbate and its apparent size (17 Å x 13 Å) compared with the van der Waals (vdW) size of the chemical models of the TCPQ in gas phase (15.7 Å x 10.2 Å for conformation A and 16.5 Å x 11.7 Å for conformation B) suggests that the molecules are deposited intact. The main symmetry axis of the TCPQ molecules is aligned along one of the two main high-symmetry directions of the substrate. As a consequence two orientations perpendicular to each other can be found (this is different to the adsorption of TCNQ on Cu(100) where the molecular axis have an angle of 17 ° with respect to the high symmetry directions of the substrate, and so four different orientations can be found).

Lack of longe-range order might either arise from weak intermolecular attraction or a reduced mobility. An observation that normally evidences high mobility is a full step edge decoration with adsorbates before nucleation on the terraces starts (compare TCNQ). Here at room temperature the step edges are only partially covered, while growth on the terraces has already begun, which rather indicates a reduced mobility. Apart from a few dimers and trimers, larger islands are not observed in the STM images.

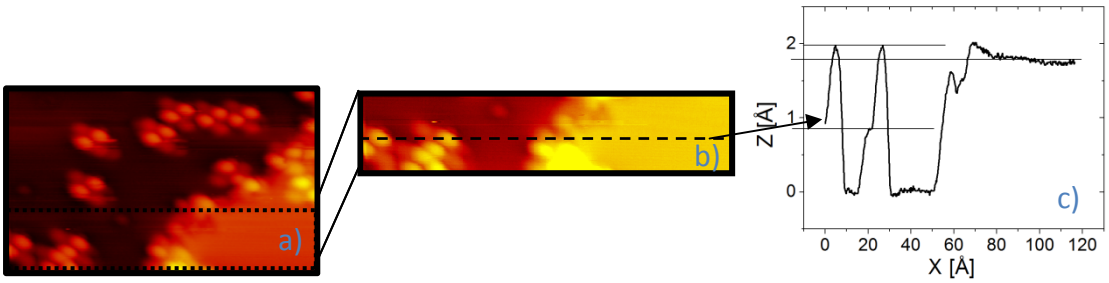

Figure 3: Y-flattened STM image of TCPQ on Cu(100) imaged at 150 K (120 Å x 65 Å, -1.4 V, -0.58 nA): A linescan (**c)** in the fast scanning x-direction (flattening does not affect the measures in this direction) is taken from **a)** to measure the apparent height of the bright lobes of two molecules in comparison to the step edge height (**b)**. This method is applied in all height measurements to increase the reliability.

Height measurements of the dim part and the bright lobes of the molecules have been done for different bias voltages and the mean heights obtained by averaging over the whole voltage range leads to values of 1.1 ± 0.2 Å and 2.0 ± 0.4 Å for the dim and the bright part of the molecules, respectively (Fig. 3). However, some consistent variations with the bias voltage can be observed. The size of the error bars (measured as a 3σ-error) provides evidence that these variations in the height measurements are systematic and may contain, in principle, information about the electronic nature of the molecule. Thus, the increase in the measured height around -1.8 V is probably related to the onset of a new molecular orbital. The fact that the ratio between the bright and dim parts of the molecules is constant, 1.86 ± 0.21 Å, independently of the bias voltage, seems to indicate that this new molecular orbital has a similar weight both at the pentace backbone and at the dicyanomethylene group, in line with the extension of the frontier molecular orbitals in the gas phase calculations (HOMO of different conformations, Table 1).

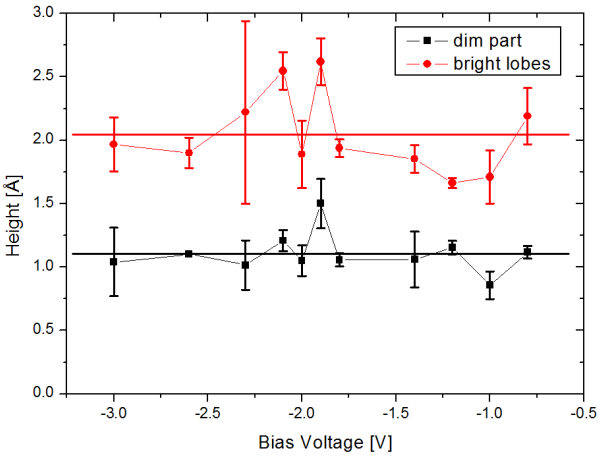

Figure 4: Heights of the lobes and dim parts of the molecules as a function of the bias voltage (extracted from 11 averaged data sets with more than 80 linescans): The dependence is very similar for the dim part and the bright lobes which indicates an electronic structure with similar weight on both parts of TCPQ. The increase around -1.8 V might represent the onset of a molecular orbital.

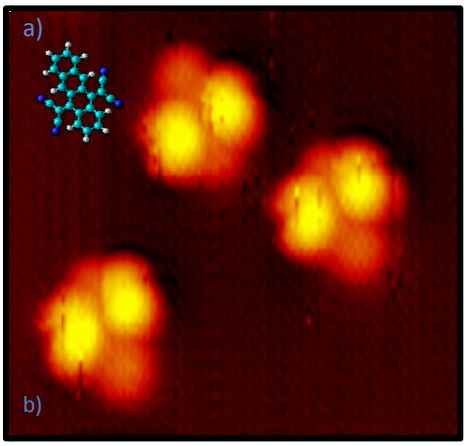

Figure 5: Comparison between the chemical model of the TCTQ control molecule in gas phase and a typical STM image of this control molecule: The asymmetry of the central tetracene part in the model **(a)** helps to identify the dim part of the molecules in the high resolution STM images. **b)** TCTQ grown at 160K on Cu(100) imaged at 160 K (50 Å x 50 Å, -1.8 V, -0.24 nA): The bright lobes represent the dicyanomethylene groups.

In order to know which chemical group causes the bright lobes, a control molecule, TCTQ, has been deposited onto the same Cu(100) single crystal under the same conditions. TCTQ is chemically identical to the TCPQ molecule with one exception: the central backbone possesses four instead of five benzene rings. This leads to a backbone which is shorter than in the TCPQ molecules and thus to a structural asymmetry which can be resolved in the STM images (Fig. 5). On one side of the two lobes the dim part appears shorter than on the other and it is also shorter than one side of the dim part of the TCPQ (compare Fig. 2). We can conclude therefore that the dim part corresponds to the aromatic backbone whereas each bright lobe represents one dicyanomethylene group.

4.4.2 STM Simulation

In order to find out about the reasons behind the bright appearance of the dicyanomethylene groups, simulated STM images, based on different gas phase conformations of the TCPQ molecule, have been calculated. All relevant adsorption geometry models were first relaxed in gas phase with the semi-empirical PM3 method. The eigenenergies and eigenfunctions of the molecular orbitals were then used to calculate, for every molecular state, the 3D electron density probability distribution. Those are then summed up for a number of states from a chosen energy interval. The height above a chosen projection plane for the points with a selected probability (contour value) is used for the z-height in the simulated STM images (this idea and the original program code stems from Oliver Gröning and Roman Fasel at the EMPA in Saint Gallen, Switzerland).

The 3D probability maps $P_{occupied,n}$ and $P_{unoccupied,n}$ have been calculated with the mathematical formalism:

1. for negative voltages: $P_{occupied,n} = \sum_{k=0}^{n}(\mathrm{HOMO} - \mathrm{k})$

2. for positive voltages: $P_{unoccupied,n} = \sum_{k=0}^{n}(\mathrm{LUMO} + \mathrm{k})$.

In order to simulate STM images for different bias voltages, five 3D probability maps have been calculated (n = 0, 1, 2, 3, 4). The possible effects of different tip-sample distances have also been addressed by choosing five different contour values (spanning four orders of magnitude).

In total four different adsorption models have been taken into account. In the case of the conformation A (neutral form) the first model represents the adsorption of TCPQ with the nitrogen atoms bound to the Cu-surface and the pentacene backbone above the dicyanomethylene groups (A1, N down), while in the second model the pentacene backbone interacts directly with the surface and the cyano groups point away from the substrate (A2, N up). The molecule with the conformation B (anion form) can only bind to the surface with two cyano groups while the other two point away from it (conformation B). However, a slightly different conformation may exist if one dicyanomethylene group is turned around bond B3 an angle 180°-α assuming that the other group is turned an angle α (conformation C, see Figures in Table 3).

The STM simulations for each of the four different adsorption geometries consist then of two sets of 25 images, one set for negative and the other for positive bias voltages. Within each set, both the number of contributing orbitals and the probability values are independently varied. However, the images of each set vary very little over a large range of probability contours. Moreover the visible influence of every additional molecular orbital included in the calculation of the images decreases when increasing n and no appreciable change can be found after including two orbitals. This is why for every set of simulated STM images we can chose one to represent the result for the adsorption geometry used in the calculation. We have generated this characteristic image using a contour value of 10^{-5} $e^{-}Å^{-3}$ and n = 2, that is using only two molecular orbitals, HOMO + HOMO-1 for negative voltages, and LUMO + LUMO+1 for positive voltages. This is illustrated in Table 2, which shows the total set of 25 simulated STM images for negative voltages of conformation B of TCPQ.

$TCPQ^{2e-}$

Probability distribution contour:	HOMO	HOMO to HOMO-1	HOMO to HOMO-2	HOMO to HOMO-3	HOMO to HOMO-4
10^{-2} Å^{-3}	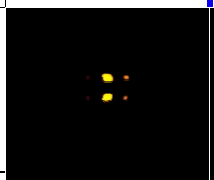	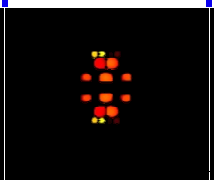	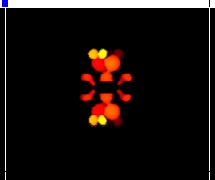	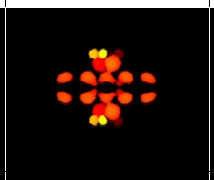	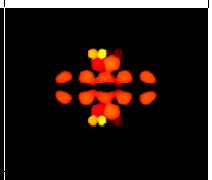
10^{-3} Å^{-3}	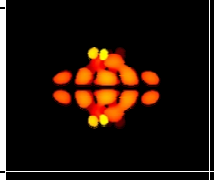	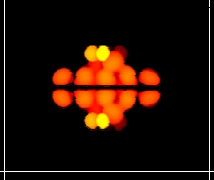	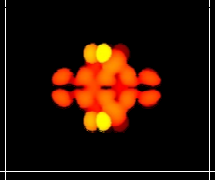	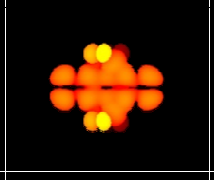	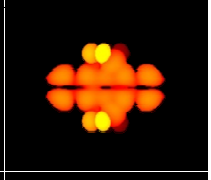
10^{-4} Å^{-3}	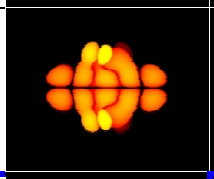	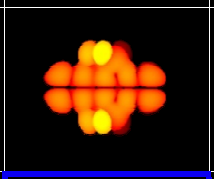	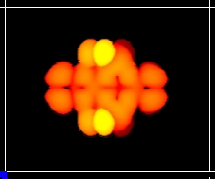	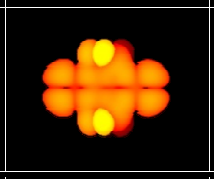	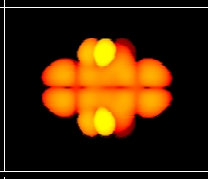
10^{-5} Å^{-3}	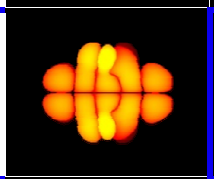	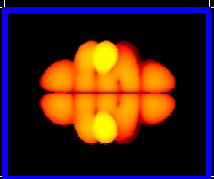	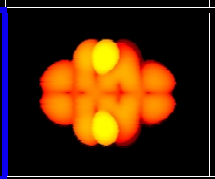	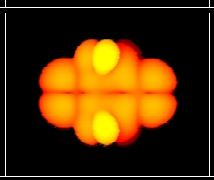	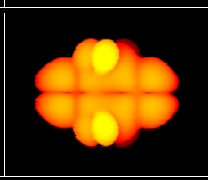
10^{-6} Å^{-3}	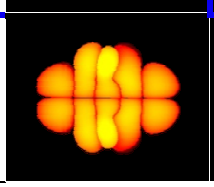	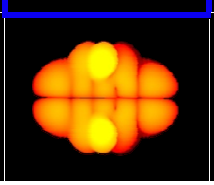	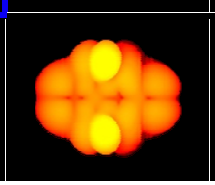	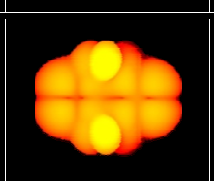	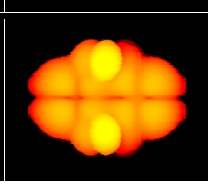

Table 2: Calculated STM images for negative bias voltages using a different number of occupied orbital (n = 0 to 4) and five different probability density contours (ranging four orders of magnitude): The simulation with a contribution from the HOMO and HOMO-1 and a probability density contour of 10^{-5} e^{-}Å^{-3} (blue square) is chosen to represent this set. These parameters are the same for all other characteristic simulated STM images which represent the whole set of calculations for the other models.

Experimentally, the use of positive bias voltages very often leads to tip instabilities for relatively small tunnel distances. Therefore only STM images with negative bias, which show the contributions to the tunnel current from the occupied states of the molecule, can be compared with simulated images.

Finally an influence of the charge state can be excluded, as shown by two representative STM image simulations, A1 and A2, either in their neutral form or with an extra charge of $-2e^{-}$ (Fig. 6). The expected appearance is basically the same. Thus in the following we will only distinguish between the different conformations and the adsorption geometry, which are decisively responsible for the STM appearance, as discussed in the following. It is noteworthy that conformation B and C are only stable when an extra negative charge is taken up from the surface. It does not exist in a neutral state, the amount of charge (one or two extra electrons) and its effect on the STM appearance will be discussed at the end of the chapter.

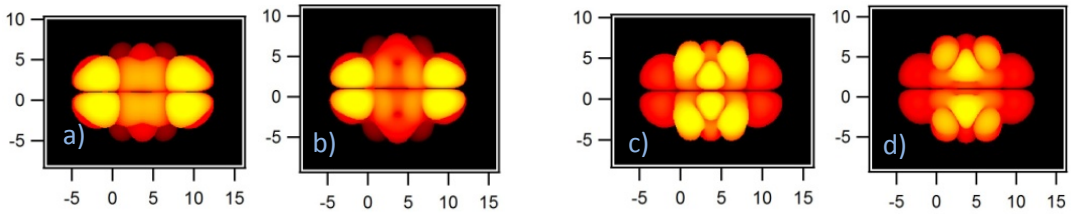

Figure 6: Comparison of the effect of additional negative charge on the different adsorption models of conformation A: The simulated STM image in **a)** shows the neutral TCPQ molecules with the nitrogen atoms bond to the substrate (A1). Image **b)** is obtained simulating the same absorption geometry but with an extra charge of $2e^-$. The difference in appearance is negligible compared to the second absorption geometry, were the cyano groups point into the vacuum (A2): In image **c)** the latter model is simulated with a neutral TCPQ and in **d)** a charge of $2e^-$. Thus the conformation and adsorption geometry of TCPQ are significantly more important for the appearance.

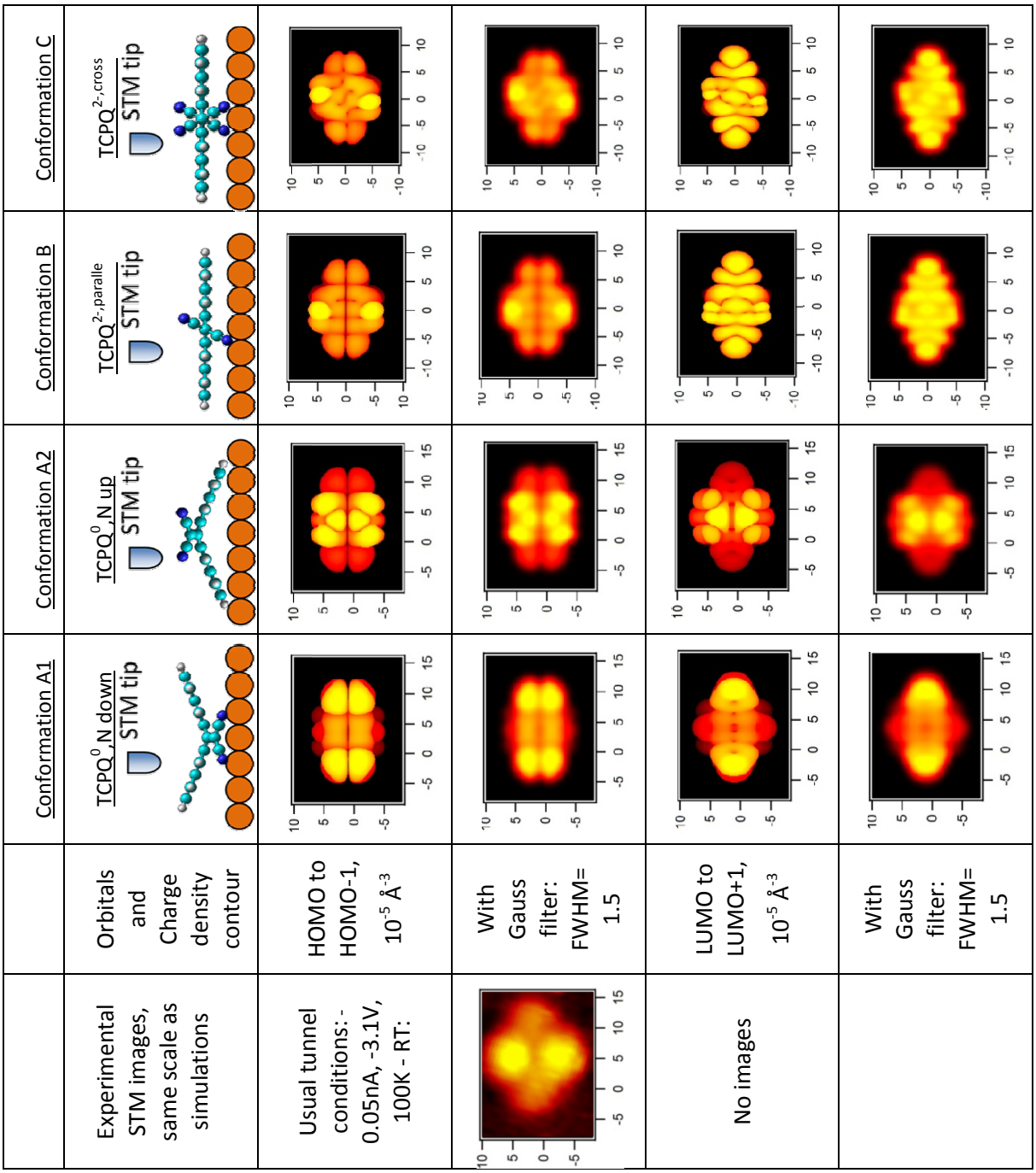

Table 3: The complete comparison of a typical experimental STM image (first column) of a single molecule (-0.05 nA, -3.1 V, RT) with the all simulated STM images for four possible adsorption geometries based on the gas phase calculations of the neutral and the dianion TCPQ: The simulated STM images are shown after applying a Gauss filter (1.5 full width at half maximum, FWHM) in order to simulate the resolution of a finitely sharp STM tip.

The simulated STM images of the conformation A1 of TCPQ (N down) do not resemble well the experimental observations (Table 3), since the simulations predict two bright lobes at both ends of the pentacene backbone, which is the opposite to the observed in the experimental STM images. The predictions for the adsorption geometry of conformation A2 (N up) exhibits a structure which would be resolved with the STM as an elongated dim part with two oval lobes on top of it. Those two ellipses have a very large size and the center to center distance,

measured in the simulated image is only 6 Å, which is probably too small, compared to the separation of the lobes from the experimental images (7.9 ± 0.5 Å). Additionally this adsorption geometry might appear rather unlikely, taking into account that we know from the TCNQ case that the nitrogen atoms interact very strongly with the surface. This cannot be fully compensated by a gain in binding energy due to a stronger interaction of the pentacene backbone with the surface, because the contact area is very small. Thus the adsorption energy of a possible "N down" geometry model is expected to be the smallest of all models and thus rather unlikely.

Contrary to the adsorption models based on conformation A, the two adsorption geometry models based on conformation B and C yield simulated STM images which agree very well with the experimental results (Table 3). They exhibit a central, elongated, dim part, as well as two lobes, which decorate the side of it, nearly at the middle position. Both models are reasonable within the normal experimental resolution. This is confirmed in a direct comparison of the separation between the lobes (Fig. 7).

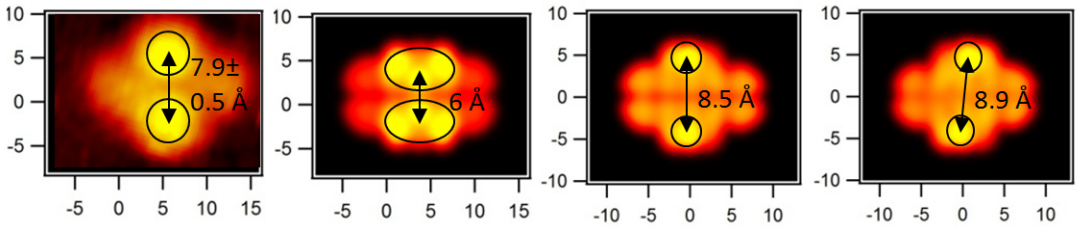

Figure 7: Comparison of the experimental and the predicted distance of the bright lobes from the three most likely adsorption geometries: a) (0.05 nA, -3.1 V, RT): Typical experimental image of a TCPQ molecule, which exhibits two bright lobes with an average separation of 7.9 ± 0.5 Å. **B)** The gauss filtered (1.5 eV at FWHM) simulated image of the "A1" adsorption geometry, with two ellipses which surround the bright lobes 6 Å separated. In **c)** and **d)** gauss filtered (1.5 eV at FWHM) simulated images of the conformation B and C adsorption models, respectively. The separation of 8.5 Å and 8.9 Å are close to the experimental one.

Although in the vast majority of cases the appearance of the TCPQ molecules is the one described above, a clearly different shape could be observed very few times, and always when TCPQ is deposited on the Cu(100)-sample below RT (approximately 140 K). In the STM image shown in Figure 8 there is a molecule with an uncommon appearance adsorbed next to two TCPQ typical units. The fact that both types of molecules are visible in the same STM image, independently of the fast scanning direction, excludes possible tip effects. Moreover the dim part coincides in length with the dim part of the two neighboring molecules, which indicates that it exhibits as well the central pentacene unit. However, instead of the two bright lobes a half-torus-like larger and brighter feature (maximum height is 2.3 Å compared to 2.0 Å of the neighboring molecules) is observed.

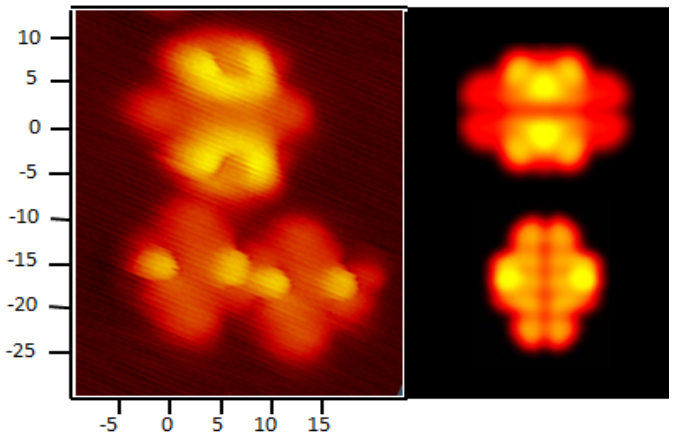

Figure 8: STM image of three TCPQ molecules deposited on Cu(100) at 140 K, imaged at 140 K, (-1.2 nA -1.0 V 35 Å x 50 Å). The experimental image **a)** has been measured in two different scanning directions with the same result to exclude tip- and scan direction effects. The dim part seems very similar in both molecules, what gives a hint that the chemical structure is identical. The simulation of the TCPQ adsorption geometry based on conformation B resembles very well the usual appearance of the molecule, while simulations based on conformation A2 reproduce with the same quality the upper of the three observed molecules. Imaged only rare times, it may represent the unlikely adsorption geometry based on conformation A2 of a TCPQ (N up).

There are quite satisfactory parallelisms between the simulation for the “N up” model based on conformation A2 and the STM image. Therefore, this rarely observed appearance of the TCPQ molecule delivers further argument for excluding the “N up” adsorption geometry model for the primarily observed TCPQ, because at the same time it is able to explain the appearance of the case here discussed.

In order to obtain more information about the conformation of the molecule, from STM images and, in particular, about the expected conformations B and C, we have tried to obtain a better resolution. Having the STM at a temperature of T = 140 K makes it possible to use a very low tunnel resistance with a short tip-sample distance to image the molecules without disturbing them. Figure 9 shows that this procedure does not change the molecular state: after high resolution imaging (Fig. 9b), the “normal” appearance can be recovered by reverting to “standard” tunneling conditions (Fig. 9c). In these “high resolution” images the size of the bright lobes decreases significantly, whereas that of the platform is mostly unaffected. A careful inspection reveals a slight off-centered position of the lobes. Defining the main symmetry axis along the pentacene backbone and the secondary axis as the one perpendicular to it through the center of the molecule, Figure 10 reveals that the lobes are not aligned with the secondary axis. Our experimental STM images (Fig. 10 c)) reveal that two possibilities exist: either the two lobes of a molecule are found on the same side of the secondary axis or one lobe is on one side and the other lob is on the opposite side. Sometimes these two cases can be observed next to each other within a TCPQ island (Fig. 10). Two out of three molecules shown in the center of Figure 10 c) exhibit both lobes displaced off-center in the same direction while the third molecule exhibits two lobes which are displaced in opposite directions. These two kinds of molecule can be explained as arising from conformation B and C, respectively.

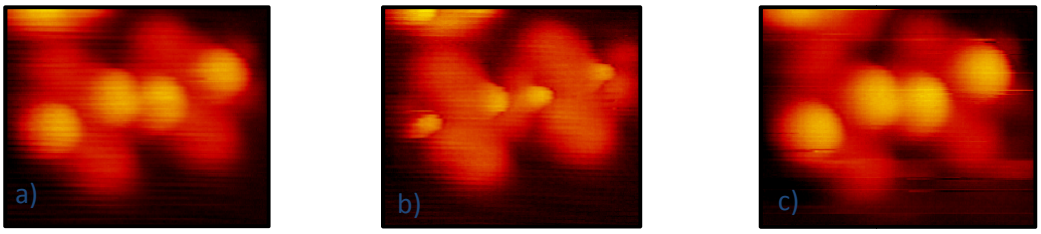

Figure 9: Consecutive STM images of two TCPQ molecules taken at 140 K (26 Å x 19 Å): a) -0.2nA, -1.0V; **b)** -1.2 nA -0.8 V; **c)** -0.84 nA, -1.4 V: The typical two lobes can be observed before and after high resolution imaging at the usual central position of the pentacene backbone with harsher tunneling conditions. This procedure does not change the molecule and provides a possibility to determine the position of the lobes with higher precision.

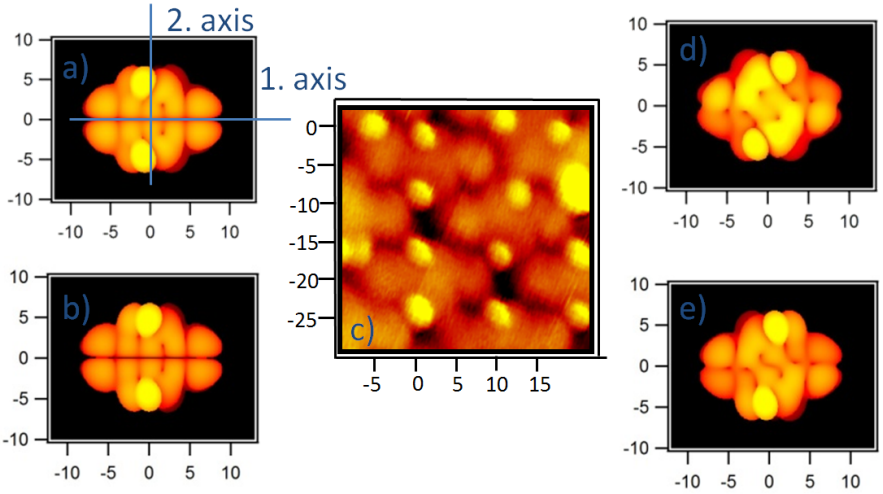

Figure 10: Comparison of experimental and simulated STM images, same scale: a) Representative STM simulation based on the $1e^-$-charged gas phase model with the dicyanomethylene groups turned in the same direction of the TCPQ with definition of main and secondary axis (HOMO to HOMO-1, charge density contour 10^{-5} $Å^{-3}$). **b)** as a) but with a charge of $2e^-$. **c)** (35 Å x 30 Å, -0.7 V, -0.81 nA, 160 K): high resolution STM image with two molecules displaying a displacement of the two bright lobes along the primary molecular axis in the same direction from the pentacene backbone center and one molecule with two lobes, which are on opposite sides of the secondary molecular axis. **d)** Representative STM simulation based on the $1e^-$-charged gas phase model with the dicyanomethylene groups turned in the opposite direction of the TCPQ (HOMO to HOMO-1, charge density contour 10^{-5} $Å^{-3}$). **e)** as d) but with a charge of $2e^-$.

Summarizing, from the experimental images and the comparison to the simulations, we conclude that the adsorption geometry of the TCPQ on the Cu(100) surface is based on the conformation B and C. The fact that both conformations (B and C) are stable only with at least one extra electron is consistent with the charge transfer found in the TCNQ/Cu(100)-system and will be confirmed in the following with spectroscopic data. Similar to the TCNQ case, the negative charge donated from the surface plays also a fundamental role for the observed behavior of the TCPQ and TCTQ molecules. The results obtained from STM simulations for the TCTQ molecule are consistent with the conclusions for the TCPQ molecule and support them.

4.4.3 DFT calculations

Near the completion of this thesis, DFT calculations have been performed and some preliminary results are available. As will be shown, the findings are in complete agreement with those presented previously.

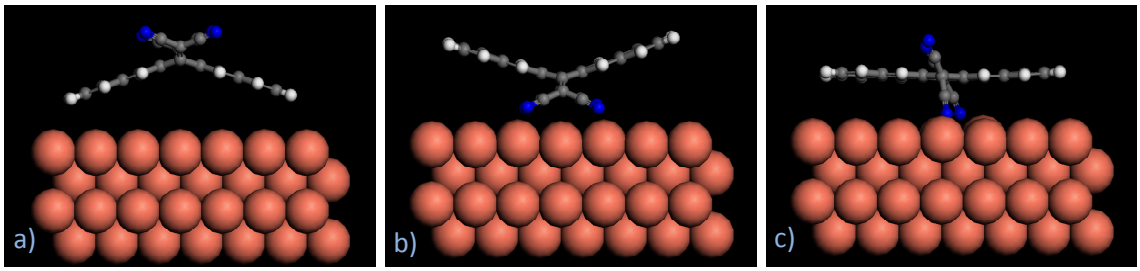

Figure 11: The three adsorption geometries calculated with DFT: Conformation B in c) is the most stable of the shown and exhibits a nearly planar central backbone and two cyano groups on each side of it. This result confirms the STM and gas phase interpretations previously made in this chapter.

Three absorption geometries, corresponding to previously defined conformations A1, A2 and B shown in Figure 11, have been relaxed on a four layer Cu(100)-surface. The most stable is conformation B (Fig. 11 c) with an almost planar pentacene backbone and the symmetric positions of the cyano groups with respect to this central platform. The rotation of the dicyanomethylene group is possible since the C-C-bond linking this side to the pentacene backbone exhibits a marked single bond character with a bond length of 1.49 Å. Thus the steric interaction between the cyano groups and the central platform can be relieved and an angle of about 62 ° for all cyano groups with the pentacene backbone is found. This conformation is very similar to the dianion in gas phase[21]. The calculated total charge transfer from the surface to the molecule is 2.4 e^-. The surface introduces in this conformation an asymmetry for the interaction with the cyano groups. The bond distances between the cyano groups and the C-atom, which links them to the pentacene backbone are smaller for the ones in direct contact with the surface (1.35 Å with a double bond character) than for the two units above the central platform (1.41 Å similar to a single bond length). The molecule-surface-bond is located mainly on the nitrogen atoms of the cyano groups in contact with the substrate. These N-atoms are close to bridge sites of the Cu(100) surface, in contrast to the TCNQ case, where all nitrogen atoms are close to a top position.

The results from the DFT calculations support a charge transfer from the surface and the adsorption geometry of TCPQ in the conformation B, as deduced from the simple gas phase calculations and STM image simulations, previously described. They are thus consistent with all other arguments presented in this chapter.

4.4.4 XPS Results

As we did in the case of TCNQ we will use XPS experiments to confirm the assumption of a negative charge transfer from the surface to the molecule.

4.4.4.1 Spectra overview

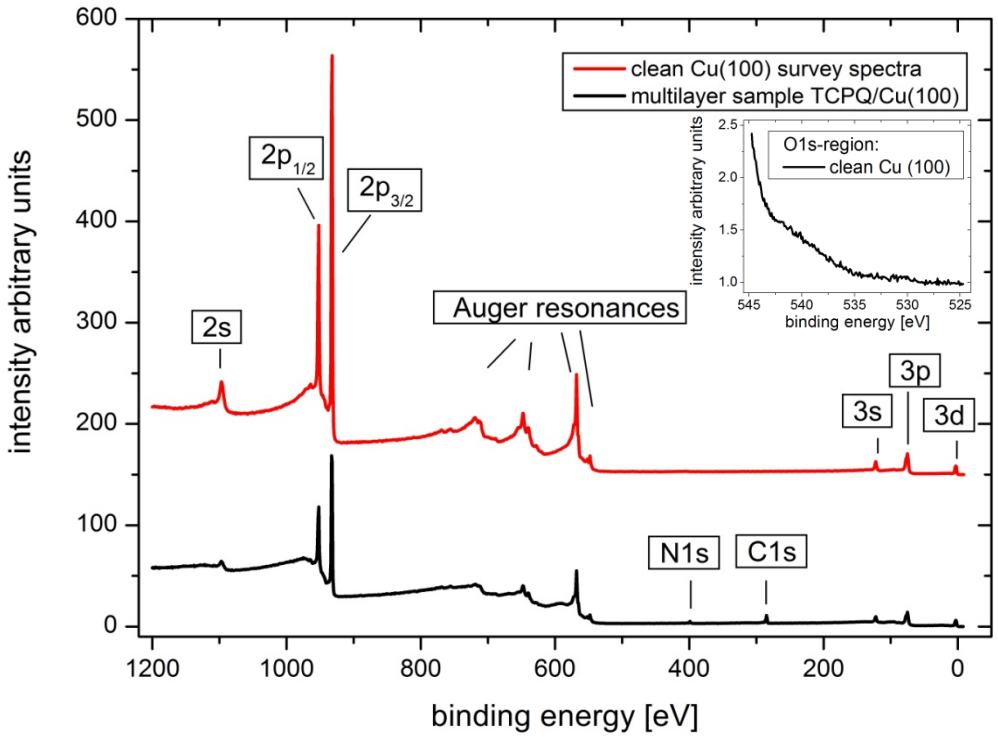

Figure 12: The red curve represents a XPS spectrum of a clean Cu(100) surface at room temperature. Apart from the known peaks of the Cu(100) substrate, others from different elements cannot be found (see as well high resolution scan of the O1s-region, Inset of Fig 12). The black curve from a TCPQ/Cu(100) sample shows additional peaks in the N1s- and C1s-region as expected from a molecule containing carbon and nitrogen atoms. At the same time the substrate features appear attenuated due to the material on top.

Figure 12 shows XPS spectra of the clean Cu(100) substrate (red curve) and after depositing 4.3 ML of TCPQ (black curve), showing the expected peaks in the N1s- and C1s-regions (Fig. 13).

The Cu(100) spectra is well known in literature and shows no additional peaks (red curve Fig. 12). The absence of any peaks In the N1s- and C1s-region confirms the cleanliness of the sample before deposition. The O1s-high-resolution-spectrum proves before and after deposition of TCPQ that no oxygen is present on the surface (inset Fig. 12).

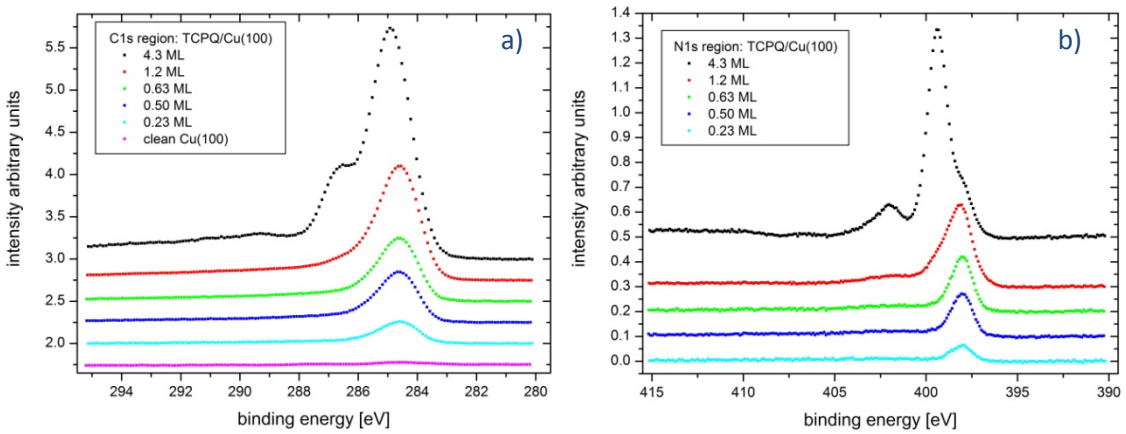

Figure 13: a) C1s- and b) N1s-region spectra of submonolayer and multilayer TCPQ/Cu(100) - samples: The single spectra are displaces for clarity.

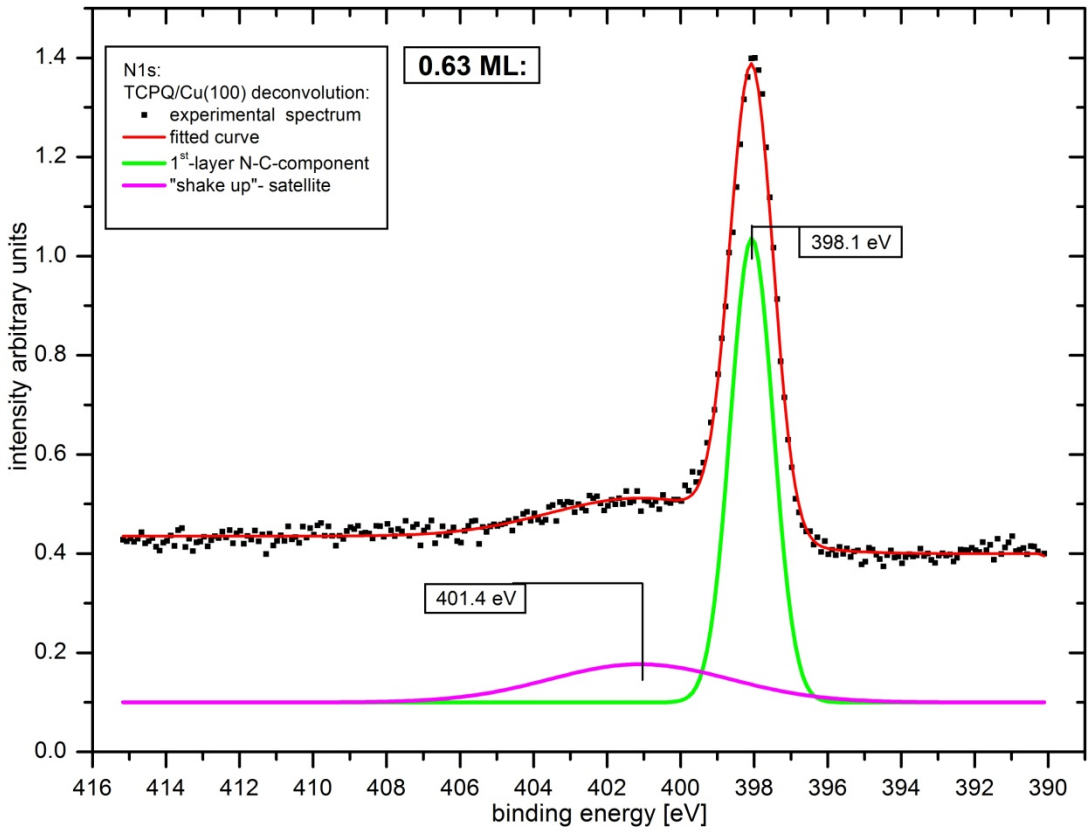

Figure 14: N1s example XPS spectrum of TCPQ/Cu(100) with the deconvolution peaks: A 0.63 ML sample is chosen to represent the submonolayer regime because the spectra of all samples could be fitted with a main peak at the same energy position (398.1 eV) and with the same width plus a broader peak. Only the intensity varies with the coverage.

4.4.4.2 N1s-region

XPS spectra taken in the N1s-region after depositing submonolayer quantities of TCPQ can be deconvoluted into one main peak at $E_{1st,N-C}$ = 398.1 ± 0.05 eV (a Gaussian line shape has been assumed for all peaks with an average width of 1.36 ± 0.01 eV) and a broad feature $E_{shake\ up}$ = 401.7 ± 0.7 eV, with an average Gaussian width of 6.5 ± 1.1 eV (example spectra in Fig. 14). The main N1s-peak found in the submonolayer sample spectra will be referred to as "1st-layer N-C-component" and its binding energy is $E_{1st,N-C}$. For samples with coverages over the monolayer, a new component appears at a different binding energy $E_{multi,N-C}$ = 399.5 ± 0.1 eV (Fig. 15). This new component will be referred to as "multilayer N-C-component". Its energy position does not significantly change with coverage above 1 ML, and it is the only peak which grows in area for thicker films (Fig. 15). The relative insensitivity of the binding energy with thickness (see Appendix, "multilayer sample") is an indication of a weak screening effect, which thus alone cannot explain the binding energy difference of the 1st-layer and the multilayer N-C-component. Additionally, the energy position of the multilayer N-C-component is very close to the N1s-peak, measured in a TCNQ sample in powder form (399.6 eV)[22] and this work Chapter $^{TCNQ/Cu(100)}$, and thus also considered to originate from nitrogen in neutral TCPQ molecules. A shift due to a charge transfer is therefore most likely. The difference between the two main components is $E_{multi,N-C}$ - $E_{1st,N-C}$ = 1.4 eV and thus 0.5 eV larger than the one in the TCNQ/Cu(100) system between bulk and charged surface component. In other words, the binding energy of the 1st-layer N-C-component of TCPQ is 0.6 eV smaller than the charged component of TCNQ on Cu(100) ($E_{N^{charged}}^{TCNQ}$= 398.7 eV). For the latter case work function measurements have demonstrated a charge transfer from the substrate to the molecule. It thus seems natural to explain the N1s-binding energy for submonolayer coverage of TCPQ on Cu(100) by a charge transfer of a probably slightly different amount from the substrate to the molecule. Similar binding energies in both systems (TCNQ/Cu(100) and TCPQ/Cu(100)) and the binding energy difference between the two observed components for each system supports strongly the former STM findings of a negative charge transfer from the surface and are in good agreement with the adsorption geometry derived from the charged conformations B and C and the DFT calculations.

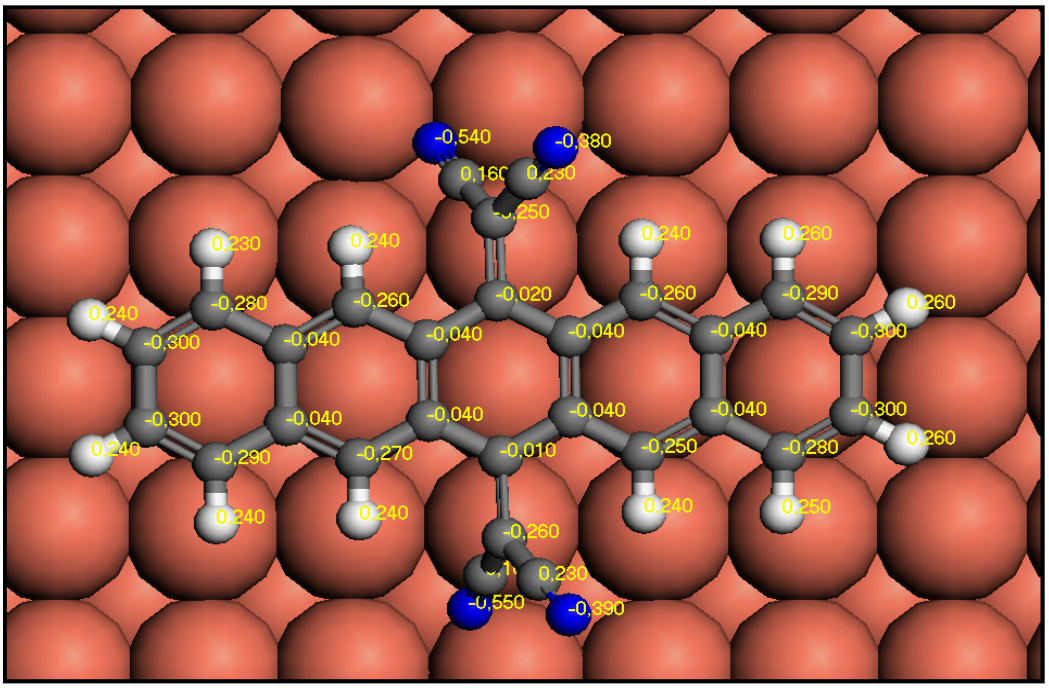

Figure 15: Mulliken population analysis of the electron density: The carbon atoms have to be divided into three groups similar to the TCNQ-case. There are four positively charged carbon atoms in the cyano groups with a similar charge, 10 neutral carbon atoms can be found and at 14 carbon atoms a negative charge is located (4:10:14).

TCPQ contains two different elements, carbon and nitrogen and in bulk all N-atoms are bound in a triple bond to carbon. On the surface, however, only half of the nitrogen atoms interact with the surface. That would imply, in the submonolayer samples, two components in the N1s-region, one from the cyano groups in direct contact with the surface and the other from the nitrogen pointing into the vacuum. Since we observe experimentally only one, slightly broadened component, the energy difference between the two peaks must be too small to resolve them separately (Fig. 14) with our energy resolution (Chapter 2). This is consistent with a Mulliken population analysis of the electron density which assigns a slightly different negative partial charge to the N-atoms in the cyano groups in contact with the surface (-0.54 e^-) compared to those above the pentacene backbone (-0.38 e^-). The difference of 0.16 e^- is probably too small to be detected experimentally.

The similar partial charge of the two, in principle, different nitrogen atoms could be explained by an electronic coupling through the delocalization of the negative charge over the entire dicyanomethylene moities. Actually, a look at the frontier molecular orbitals confirms that the spatial distribution of the extra charge is not limited to one nitrogen atom, but that it is rather extended over the entire dicyanomethylene group, probably as in the TCNQ molecule[23]. As a consequence the extra charge affects the binding energy of both nitrogen species and thus only one peaks is observed in the spectra. Nevertheless, due to the 0.16 e^- partial charge difference, a larger peak width can be expected, compared to the situation with only one pure component. In the case of the multilayer sample the neutral component exhibits indeed only a width of 1.16 ± 0.1 eV (compared to 1.36 eV for the submonolayer samples). The 1st-layer N-C-component in the 4.3 ML sample is smaller (47 %) than in the 1.2 ML sample (100 %) due to the photoelectron attenuation through the material in the second and topmost layers. The multilayer N-C-component dominantes the 4.3 ML sample spectrum (Fig. 16).

The broad component present in all samples at a binding energy of $E_{shake\ up}$ = 401.7 ± 0.7 eV is ascribed to an intramolecular excitation or "shake up" being the result of core level photoelectrons which have lost energy exciting a valence electron from the HOMO to the LUMO ("Shake-up satellites", Chapter 2). The binding energy difference to the main peak, $E_{shake\ up}$ - $E_{1st,N-C}$ = 3.57 ± 0.87 eV, is thus related to the HOMO-LUMO gap (2.64 eV calculated in gas phase for the singly charged specie, $TCPQ^{-1}$). For the multilayer sample an even closer resemblance of this energy gap would be expected, the measured binding energy difference between the "shake-up" and the main component is indeed 2.6 eV. Nevertheless quantitative interpretations are usually difficult to make without sophisticated calculations, because electron transitions participating in a shake-up process are related to the eigenstates of the ionized specie with a core hole: in the case of the TCPQ to the charged molecule with a core hole created by the ionizing x-ray radiation (Shake-up satellites, Chapter 2). However, the shake-up satellites are much less intense than the main components because only a part of the photoelectrons excite electrons across the gap (experimental literature values[24] for nitrogen: 20 %, for carbon: 30 %, in this work experimental for nitrogen: 23 ± 8 %, for carbon: 21 ± 5 %).

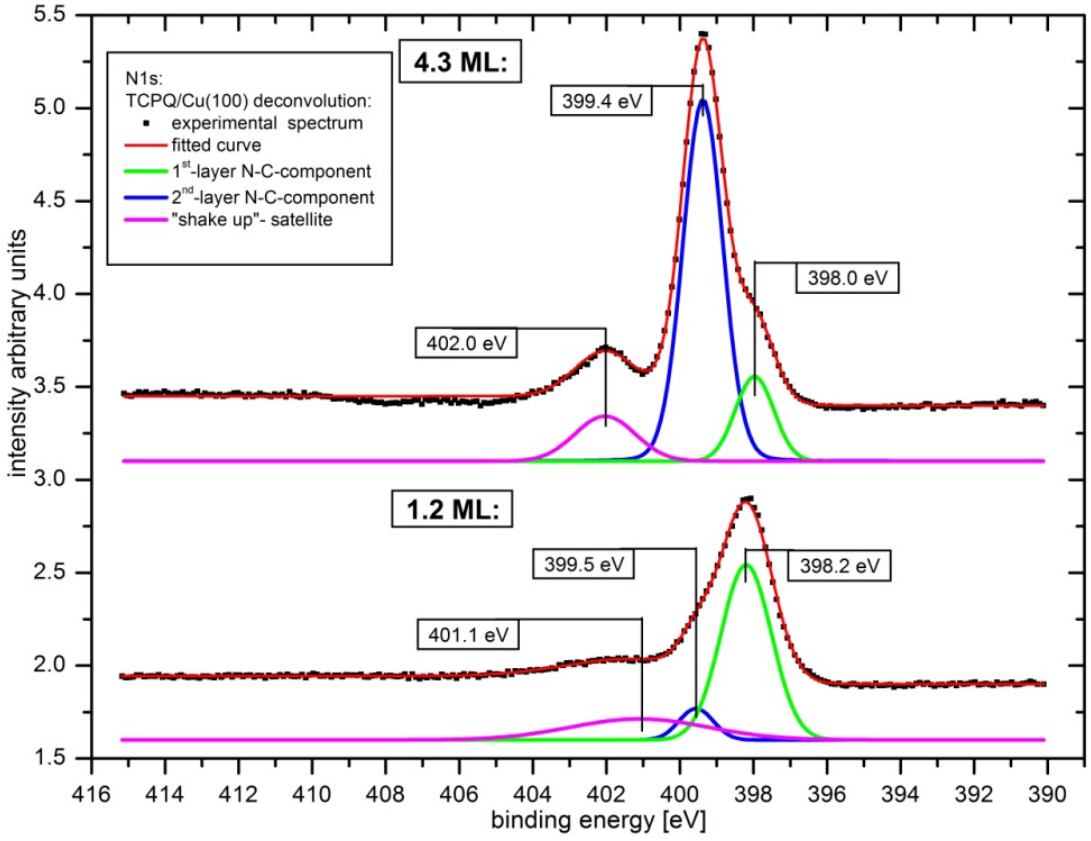

Figure 16: N1s XPS deconvolution spectra of two TCPQ/Cu(100)-samples over the monolayer coverage: After completion of the first monolayer another peak at 399.5 eV is necessary to fit the experimental spectra. This additional line is attributed to the nitrogen atoms of TCPQ from the second layer on. At the same time the peak at 398.2 eV of the 1.2 ML sample exhibits nearly the maximum intensity because only little material on top attenuates the photoelectrons from the first layer. In the case of the 4.3 ML sample the peak representative for nitrogen from the second and topmost layers at 399.4 eV is much larger than the attenuated peak of the cyano groups in the first layer. The average energy difference is 1.4 eV and characteristic for negatively charged molecules. The ratio of the intensities of the 1st-layer N-C-component serves to estimate the attenuation of the photo electrons from the first layer, which provides a method to estimate the coverage more accurately.

4.4.4.3 C1s-region

The deconvolution of the C1s-spectra is more complex because they consist of single asymmetric broad (1.7 eV FWHM) peaks centered around 284.6 eV. However, following the XPS-analysis of the TCNQ-case (Chapter 3), we fitted the submonolayer spectra according to the different groups of C-atoms given by the Mulliken charge population analysis. Three partial charge groups can be identified (Fig. 15). There are four positively charged carbon atoms in the cyano moieties with a similar charge, 10 nearly neutral carbon atoms can be found and a negative charge is located at 14 carbon atoms (4:10:14). Therefore the submonolayer C1s-spectra are deconvoluted into three main components similar to the TCNQ-case: $E_{1st,C\text{-}N}$ = 285.8 ± 0.02 eV, $E_{1st,C1}$ = 285.0 ± 0.01 eV, $E_{1st,C2}$ = 284.3 ± 0.02 eV with a pure Gaussian line shape with a width of 1.13 ± 0.01 eV and a broader peak $E_{shake\text{-}up}$ = 286.6 ± 0.08 eV (Fig. 17). The "shake up"- satellite exhibits an average width of 5.6 ± 0.8 eV, similar to the observation of this feature in the N1s-region. The three main peaks appear at the same energy as the components of TCNQ. The area ration, 2.8 : 10.1 : 14, is qualitatively in agreement with the theoretical one (4 : 10 : 14) based on the Mulliken analysis, as in the TCNQ-case. The total peak area ratio between the C1s- and the N1s-region, corrected with the element specific cross section, is a_{C1s}/a_{N1s} = 7.0 ± 0.6 which is consistent with the expected element ratio from the chemical model of TCPQ with 28 carbon and 4 nitrogen atoms. The analysis of the multilayer spectra is more difficult, although it is clear that a new component at the high binging energy side develops upon increasing the coverage, as in the N1s-region (Fig. 41, appendix).

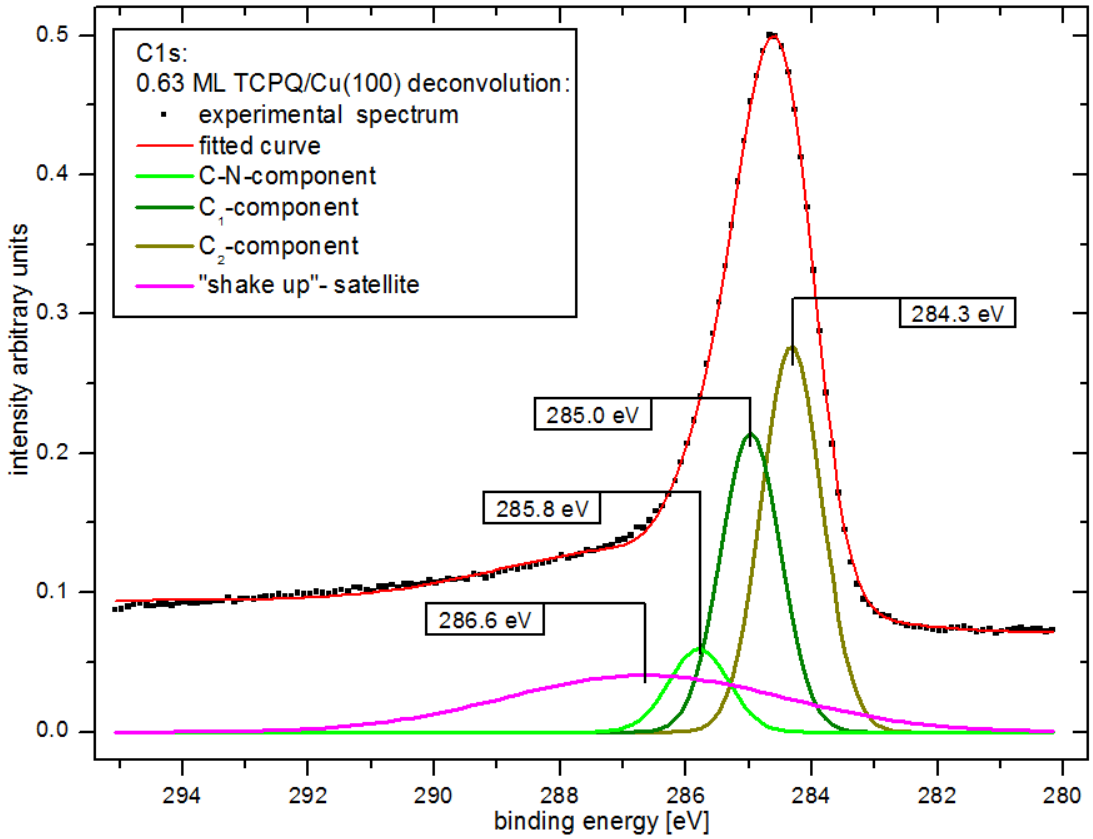

Figure 17: C1s XPS spectrum of 0.63 ML TCPQ/Cu(100) with the deconvolution peaks: The same sample as in the N1s-region exemplifies the deconvolution of the experimental submonolayer spectra into two main peaks and a broader "shake up" satellite. The energy positions are very close to the binding energies measured in TCNQ/Cu(100).

In summary, the XPS results of the C1s- and N1s-regions of the submonolayer and multilayer samples coherently suggest a charge transfer from the substrate to the TCPQ, parallel to the system TCNQ/Cu(100).

4.4.4 Conclusions

To conclude, the adsorption of two electron acceptor molecules from the TCNQ family, TCPQ and TCTQ, on Cu(100) have been investigated with STM and XPS. The rather low mobility of TCPQ and TCTQ, in comparison to TCNQ/Cu(100), is most likely due to a stronger bond to the metal surface based on two different interactions. First, similar to the findings in the TCNQ/Cu(100)-system, a chemisorption of TCPQ and TCTQ on the Cu(100) surface via the lone pairs of the nitrogen atoms in contact with the surface is to be expected. Second an additional molecule substrate interaction due to the extended π-electron system of the aromatized pentacene part must be taken into account. This interaction is probably responsible for the alignment of single units along the main high symmetry directions of the Cu(100) in contrast to the observations of TCNQ/Cu(100), where four (instead of two) nitrogen atoms per unit dominated the interaction with the substrate and thus the orientation of the molecule. The

low mobility due to the strong binding to the substrate and the bulky pentacene backbone may then explain why no island formation at low coverage takes place.

With the help of the asymmetry of TCTQ, the position of the dicyanomethylene groups in the STM images could be identified. This knowledge, in combination with calculated STM images based on stable gas phase conformations of TCPQ, led to the charged adsorption model of TCPQ and TCTQ on the Cu-substrate, in agreement with the XPS results, that suggest a charge transfer between the surface and the TCPQ and TCTQ molecules (as observed in the TCNQ case). The surface has thus a decisive role for the conformation of the adsorbed TCPQ and TCTQ. This conformation, different to the one shown by neutral molecules, is responsible for the appearance of both electron acceptors and would be distinct if no charge transfer would take place.

4.5 Self assembly TCPQ, high Coverage

In order to study the intermolecular interaction of TCPQ, their rather low mobility makes it necessary to increase the molecular density on the surface, which brings the molecules into closer proximity and increases the mutual interaction. After depositing over 0.4 ML of TCPQ on Cu(100), some small close-packed patches can be found among randomly distributed and no equally oriented molecules (Fig. 18). The appearance of the molecules within these arrays is the same as in the low coverage regime, and thus the same charged adsorption geometry can be assumed. The small islands consist of no more than 4 rows, each with up to only 5 molecules whose orientation alternates from row to row (Fig. 18 b). The rectangular unit cell of this assembly Type 1 has the dimensions of 25.3 Å x 10.9 Å and can be described in matrix notation as $\begin{pmatrix} b_1 \\ b_2 \end{pmatrix} = \begin{pmatrix} 3 & -3 \\ 7 & 7 \end{pmatrix} \begin{pmatrix} a_1 \\ a_2 \end{pmatrix}$. A schematic model can be seen in Figure 20 a. Increasing the coverage does not lead to more or larger close packed patches and imperfections remain in the assembly.

Another possibility to improve ordering is to increase the substrate temperature during deposition. This allows the molecules to explore the energy landscape on the surface and to find the optimum conformation not only with respect to the substrate but also regarding intermolecular forces. However, neither a post deposition annealing nor growing the samples at temperatures above RT (380 K - 470 K) does improve notably the degree of order. Small patches are present, some arranged as before (Fig. 19 a) and others exhibiting a new type of order (Fig. 19 b). The latter can be described with a rhombohedral unit cell with a side length of 12.8 Å and an angle of 36.9° with respect to the substrate. For this arrangement, called Type 2, the matrix describing the epitaxial relationship can be written as $\begin{pmatrix} b_1' \\ b_2' \end{pmatrix} = \begin{pmatrix} 3 & 4 \\ 3 & -4 \end{pmatrix} \begin{pmatrix} a_1 \\ a_2 \end{pmatrix}$. The molecular density of the rhombohedral order Type 2 is 14.3 % lower than the rectangular Type 1 order. In both types of order the molecules still exhibit an orientation along the two main high symmetry directions of the substrate.

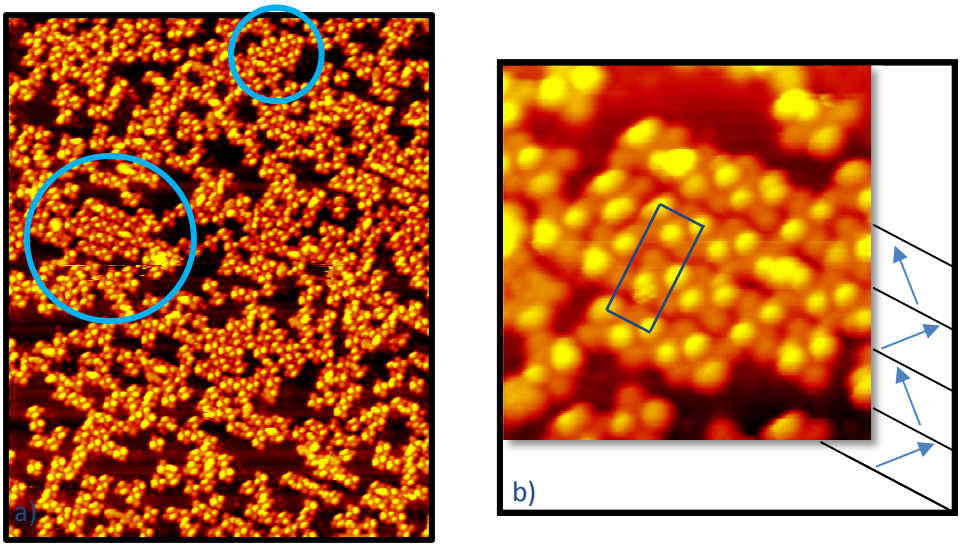

Figure 18: a) Flattened STM image of 0.5 ML of TCPQ on Cu(100) grown at RT and imaged at 130K (350 Å x 430 Å, -1 V, -0.1 nA): Small ordered islands appear with the molecules inside the island alternately oriented along the two main substrate high symmetry directions. The ordered patches occupy less than 1% of the surface of a 0.5 ML sample. **b)** Zoom into the ordered array of a) (70 Å x 70 Å, -1 V, -0.1 nA): The blue arrow point into the direction of the TCPQ main axis in the respective row of molecules. The blue rectangle represents the unit cell of this Type 1 assembly.

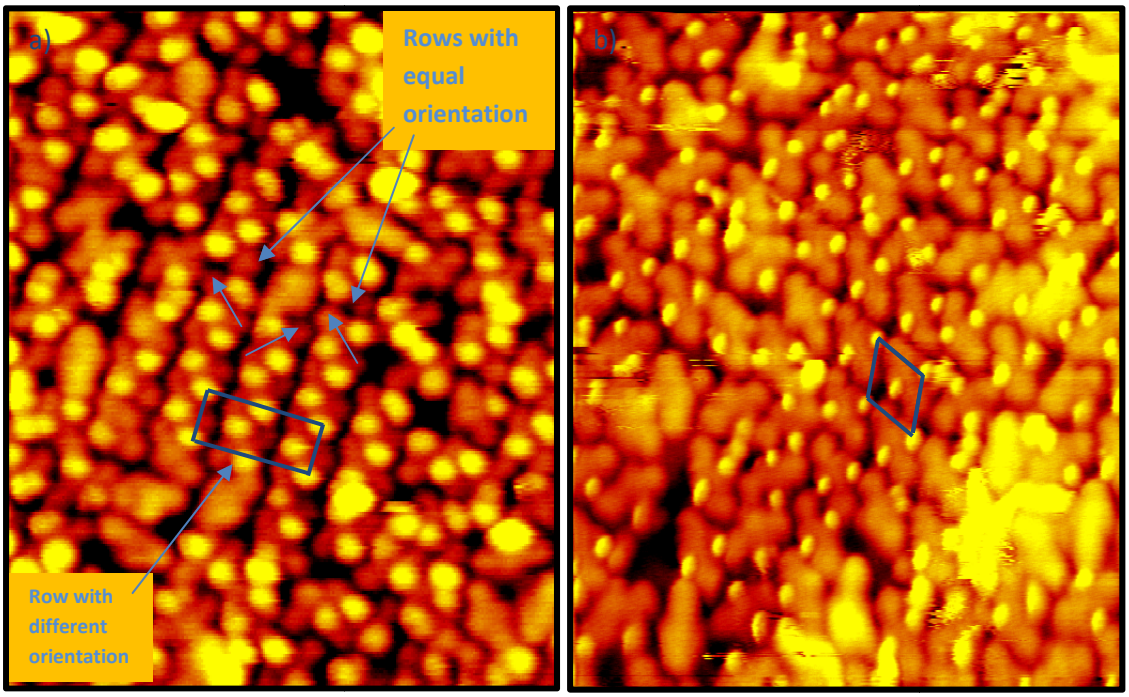

Figure 19. a) STM image of 0.9 ML of TCPQ on Cu(100) grown at 380 K imaged at 160 K (120 Å x 150 Å, -1 V, -0.1 nA): The same molecular arrangement appears under growth at elevated substrate temperatures. The orientation of the molecule in one row is the same and along one substrate high symmetry direction but alternates from row to row. **b)** In a different area of the same sample, (120 Å x 150 Å, -0.7 V, -0.8 nA), another type of ordered arrays (Type 2) with a rhombohedral unit cell can be observed.

Understanding the assembly process of an island means to be able to identify the involved forces. A starting approach, as we did for TCNQ on Cu(100), is to analyze the possible interactions of the molecules in gas phase, without the substrate.

The charge distribution map of TCPQ (Table 1) helps to identify any electrostatic interaction which is positioned in the self assembly pattern of the two described types of order (Fig. 20). The negatively charged nitrogen atoms are located close to the positive hydrogen atoms. We can conclude that electrostatic interaction probably stabilizes the islands.

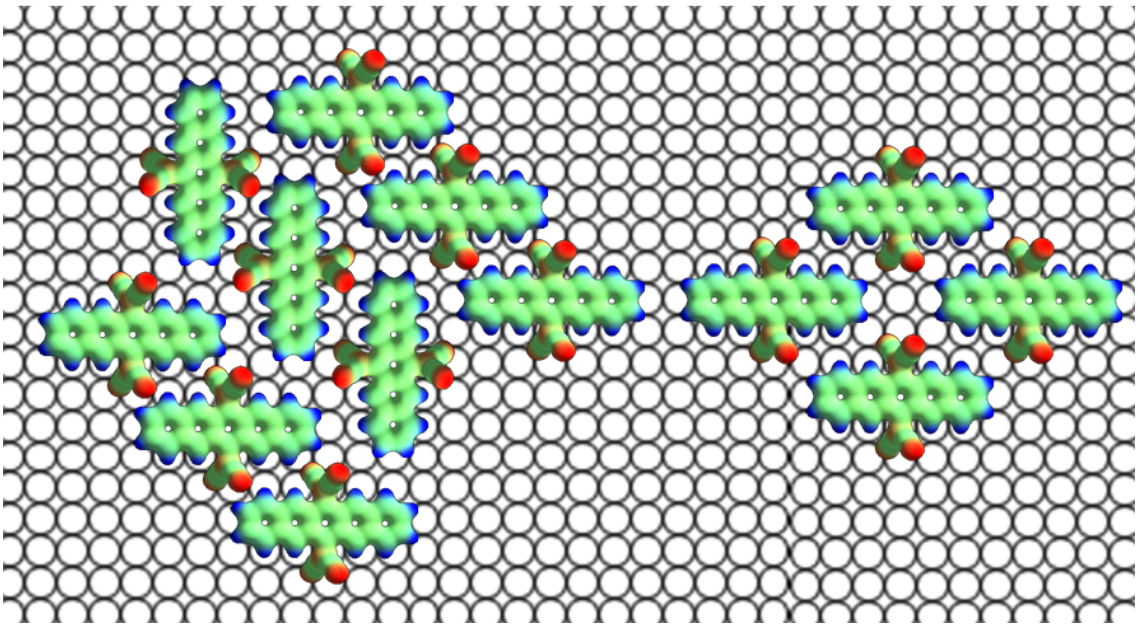

Figure 20: In order to identify the interactions the TCPQ charge density maps are positioned according to the two observed types of order on the Cu(100) surface . Relative displacements (3nn, 3nn) and (4nn, 3nn) are found among neighboring molecules in the rows of the order Type 1 and between TCPQ arranged in the order Type 2, respectively. A closer arrangement would cause an overlap of orbitals at the van der Waals size of the molecule.

This simple approach is supported by gas phase calculations of the total energy of two TCPQ molecules as a function of their relative position in a plane parallel to the surface. The minima in the resulting map indicate where the binding energy for two molecules would be largest. Adding a grid representative of the surface with the nearest neighbor distance of the Cu(100) surface shows the energetically equivalent positions on the substrate and which of them are compatible with the energy minimum of the molecular interaction (Fig. 21).

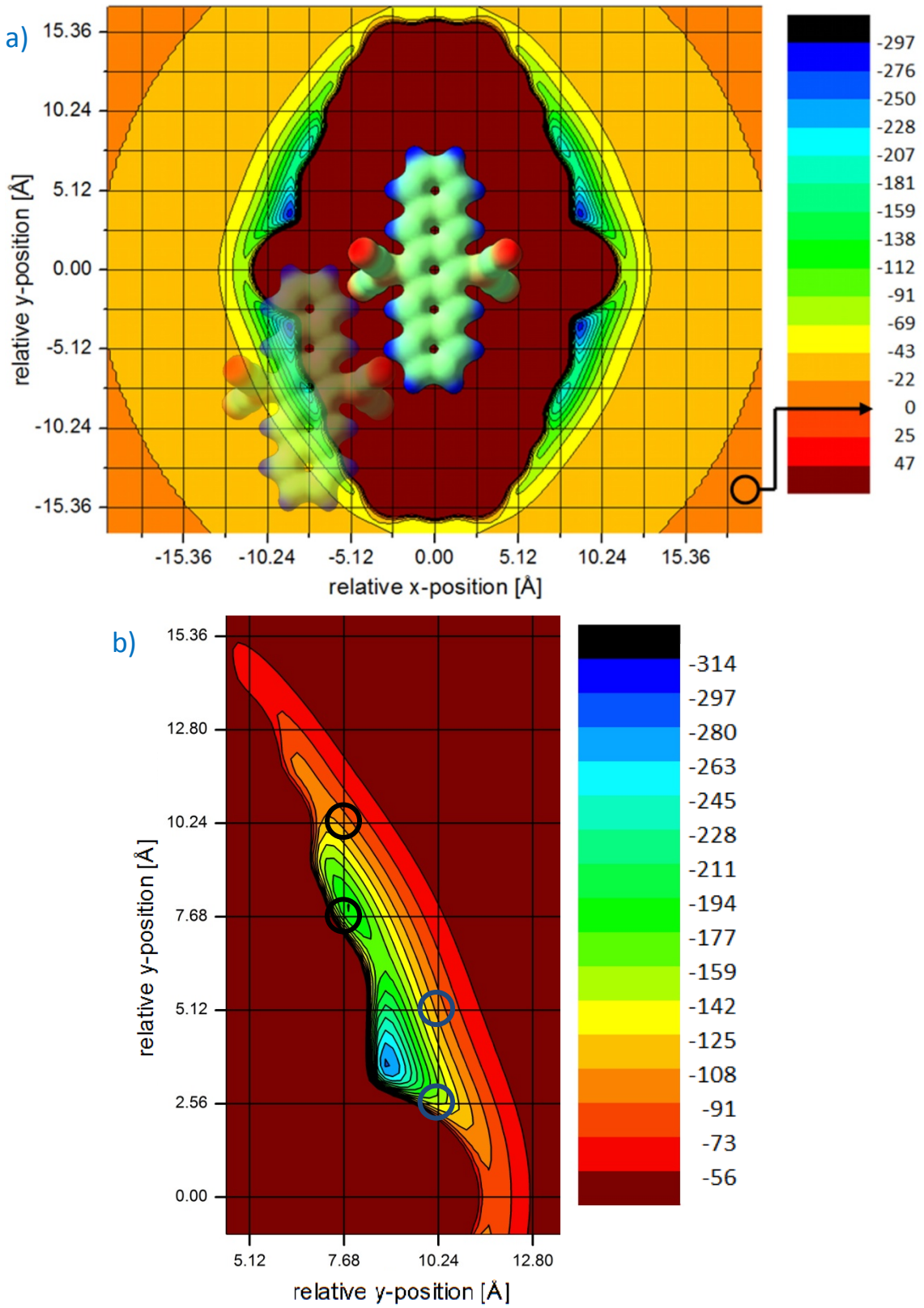

Figure 21: Gas phase calculations of a pair of interacting TCPQ molecules represented in two different color scales. Bluish colors indicate a high binding energy. The influence of the surface is represented by the grid and the nodes are the equivalent adsorption positions on the Cu(100) substrate. The entire interaction energy landscape is show in figure **a)**, which reveals the two mirror symmetry planes. The image in **b)** shows a zoom into a relevant quadrant for more details. In both maps the energy unit is [meV]. The two found unit cells in the assembled islands consist of vectors which are equivalent to the relative positions of the two upper marked adsorption sites (black circles).

Each of the four absolute minima (small black areas in Fig. 21), which are located point symmetrically around (0, 0), are situated in the middle between four such surface positions. Taking into account the strong molecule substrate interaction, it is likely that this forces cause a commensurate assembly. In order to identify the most likely relative positions of a second molecule, the different total energies of the positions at the grid crossing have to be compared. The lowest total energy position compatible with a commensurate lattice is found at (3nn, 3nn) with an energy gain compared to two isolated molecules of 159 meV.

As a matter of fact this relation is observed experimentally among the molecules of the Type 1 arrangement within the same row. In this case a third molecule cannot be assembled into the mirror position at (3nn, -3nn) due to the orbital overlap with the one at (3nn, 3nn) and the resulting Pauli repulsion. This does not occur for two molecules at a very close position, only one nn- distance away in the y-direction, at (3nn, 4nn) and (3nn, -4nn). The difference in total energy from the (3nn, 3nn) to this positions is ΔE = 68 meV (orange area instead of green area in Figure 21 b), 91 meV are gained situating a TCPQ molecule at one of the two mirror positions, (3nn, 4nn) and (3nn, -4nn). The molecules in the arrangement from the Type 2 exhibit this relative position (3nn, 4nn). Other interaction motifs close in energy to the described ones exist and can be observed among few TCPQ molecules but the small, observed islands can be explained based on electrostatic interaction and the positions with the maximal binding energy gain compatible with a commensurate lattice. Even with post-deposition annealing or film growth at elevated substrate temperatures a higher surface fraction of ordered TCPQ islands is not observed probably due to a high energy barrier for diffusion and molecular rotation.

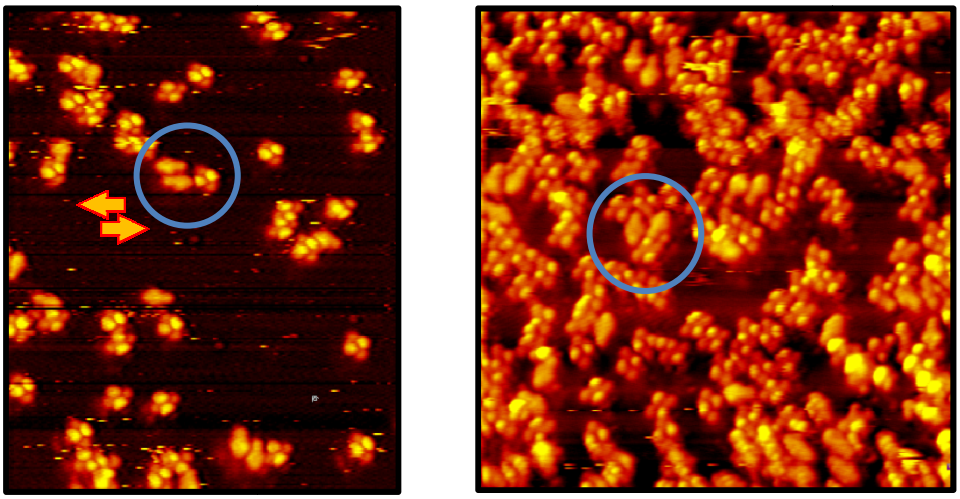

Figure 22: a) STM image of annealed (375 K) TCPQ on Cu(100) taken at 220 K (230 Å x 290 Å, -1.1 V, -0.2 nA): No improvement regarding the degree of order is achieved but the appearance of some molecules has changed (blue circles). The characteristic, two lobes are missing and with a thickening on one end they appear similar to the shape of an arrow (arrows in the image resemble the direction of the two molecules in the blue circle). **b)** STM image of annealed (390 K) TCPQ on Cu(100) taken at 160 K (230 Å x 240 Å, -0.9 V, -0.13 nA): The modified TCPQ molecules appear independently of the coverage, with an orientation different to the unchanged ones.

4.6 Surface induced polymerization

4.6.1 STM results

As can be seen in Figure 22, annealing the substrate temperature over 370 K, after or during the growth of the TCPQ/TCTQ films, induces a change in the appearance of some molecules, independently of the coverage (Fig. 22, blue circles). The modified molecules lack the two bright lobes which are characteristic of the dicyanomethylene groups and are not only oriented along the high symmetry directions of the substrate. The remaining dim, central part exhibits a structure which does not appear oval as would be expected in the case of a pentacene molecule. Rather an elongated object with a thickening on one side, similar to an arrow (Fig. 23), is observed. This indicates that not the whole dicyanomethylene group disappears and that very likely the carbon atom which links the two cyano groups to the pentacene backbone is not detached. This rather speculative interpretation is confirmed by quantitative XPS-results as described in the following sections.

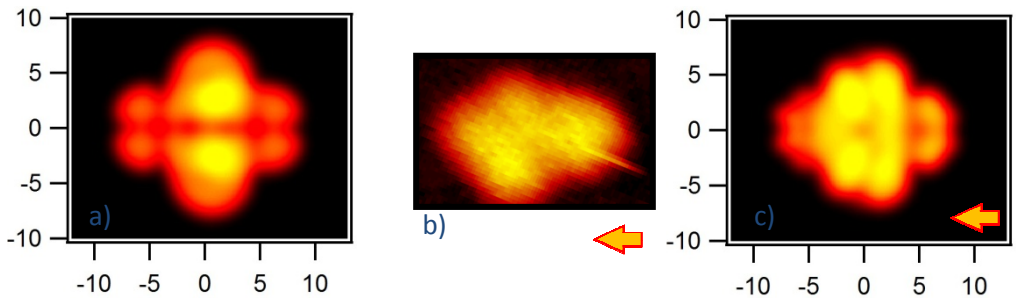

Figure 23: Comparison of the experimental appearance of the changed TCPQ after annealing with two STM simulations based on the charged TCPQ gas phase model (same scale): **a)** Only the two nitrogen atoms above the pentace plane with repect to the surface have been removed for the calculation. Two broad lobes, probably caused by the remaining C-atoms, would be expected to be found in the STM images. **b)** The experimental STM image of a single TCPQ after annealing shows little structure and a rather uniform height with two protrusions not at the center of the long axis of the molecules (imaged at 170 K, 22 Å x 13 Å, -1 V, -0.24 nA). **c)** In this simulation the whole cyano groups on the vacuum side have been removed. A mainly uniform appearance without lobes close to the observation in b) is obtained with this model.

Assuming that only one cyano group of one dicyanomethylene moiety of TCPQ is modified and that this is the one which lies above the pentacene backbone (as suggested by the apparent change in the STM images), STM simulations can provide an argument to distinguish the two remaining possibilities for the chemical change of the TCPQ molecule. This is the detachment of only the nitrogen atom, which would mean a rather unlikely break of a cyano bond with triple character, or the detachment of the cyano group as a whole, breaking a carbon-carbon bond with rather single character.

The simulated STM images (calculated in the same manner as in the previous chapter, “STM Results, low coverage“) are based on the relaxed conformation B of TCPQ in gas phase with an extra charge of $2e^-$, where either only the nitrogen atoms above the pentacene plane with respect to the substrate or the whole cyano group is removed. The latter will be called in the following the “upper cyano groups”.

In the case of the removal of only the nitrogen atoms, the calculated image still preserves two lobes (Fig. 23 a). They are broader than in the images of the original TCPQ and very likely originated in the remaining C-atoms above the plane of the pentacene backbone. In the case of the removal of the whole upper cyano groups, the simulated STM images appear rather uniform and without clear lobes (Fig. 23 c). They show as well a thickening at one end of the central backbone, which resembles very well the arrow shape of the experimental observations. This thickening probably comes from the charge density of the carbon atom which formerly connected the upper cyano groups to the pentacene backbone and which is still fused to the center. This supports the idea of a remaining TCPQ radical where the upper cyano groups have been removed through annealing. The results are in agreement with the DFT calculations, which show an asymmetry between the cyano groups above and below the central pentacene backbone upon adsorption. As mentioned previously, the C-C-distance for the carbon atom of the upper cyano group to the C-atom which connects the cyano group to the pentacene backbone, is 1.41 Å and has a marked single character. The C-C-distance for the carbon atoms of the lower cyano group and the C-atom connecting to the central backbone is only 1.35 Å, similar to a double bond length. We conclude therefore that it is easier to remove and desorb the upper cyano group upon annealing while the lower one remains connected to the pentacene backbone and bound to the surface.

An analysis of height profiles determines the height of the changed molecules to be 1.3 ± 0.1 Å (Fig. 24), with a small lift of 0.2 Å of the pentacene backbone from the surface. This and the new found orientations among the changed TCPQ indicate a slightly modified adsorbate-substrate interaction.

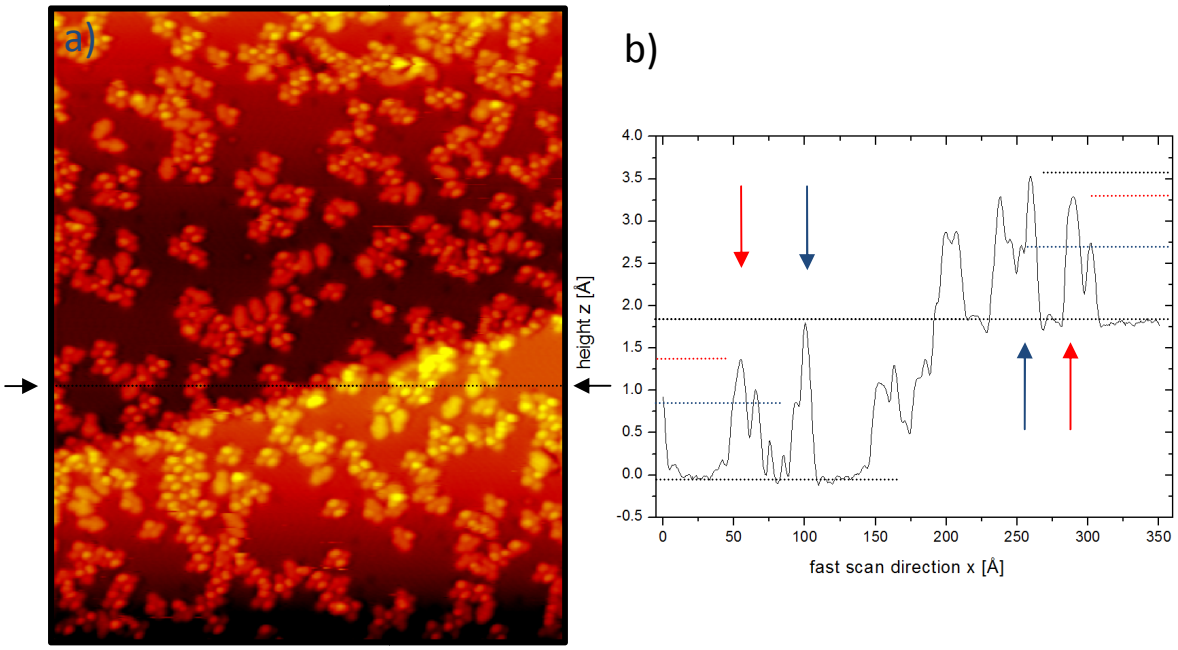

Figure 24: A) STM image of TCPQ grown at 380 K on Cu(100) imaged at 190 K (350 Å x 430 Å, -1 V, -0.12 nA): Due to the moderately higher growth temperature both molecules with two lobes and changed molecules are present on the surface. The linescan (**b)** shows a height comparison of two unchanged molecules (blue arrows) with two changed ones (red arrows) on two different terraces. The step edge serves as reference. The height of a changed molecule lies between the one of the dim part and the lobes of an unchanged molecule (the average height is 1.3Å).

Increasing the annealing temperature leads to more of those new, dim TCPQ radicals without bright lobes. The same process is also observed in the case of growth at elevated substrate temperatures, although here a higher number of molecules with only one lobe are observed. The two different types of experiments can statistically be represented together analyzing the number of "missing" lobes with respect to the total number of dicyanomethylene groups. At 370 K approximately 16.9 % of the bright lobes have disappeared. This number increases with higher temperature and a complete transformation of all the lobes of TCPQ is achieved at an annealing temperature of 490 K (Fig. 25).

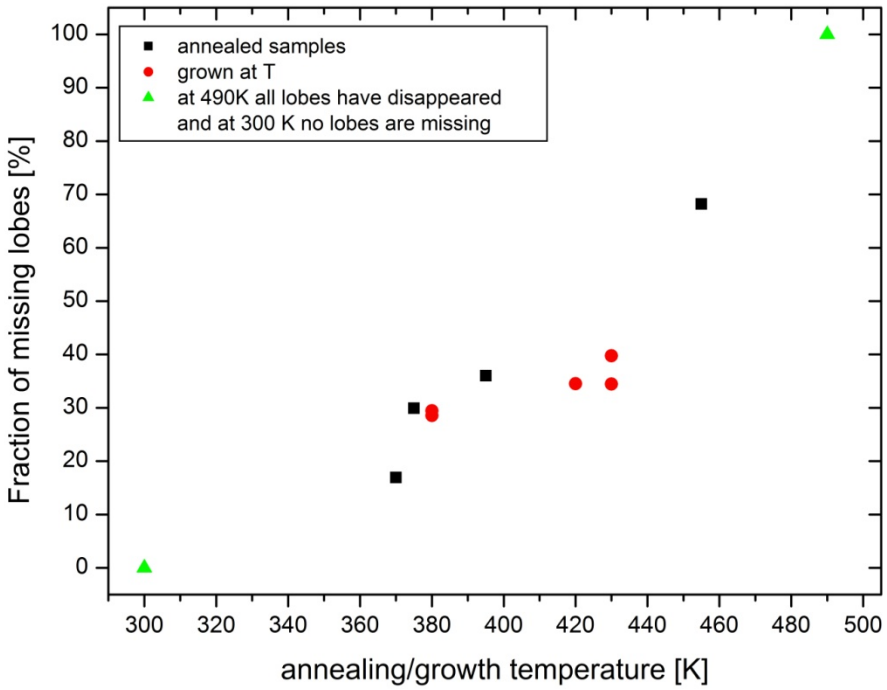

Figure 25: Statistical disappearance of the bright lobes: At 300 K all TCPQ molecules appear with two bright lobes. Annealing (black points) or growth at elevated temperatures (red points) leads to the disappearance of lobes. At 490 K all TCPQ (and TCTQ, too) have lost their bright lobs.

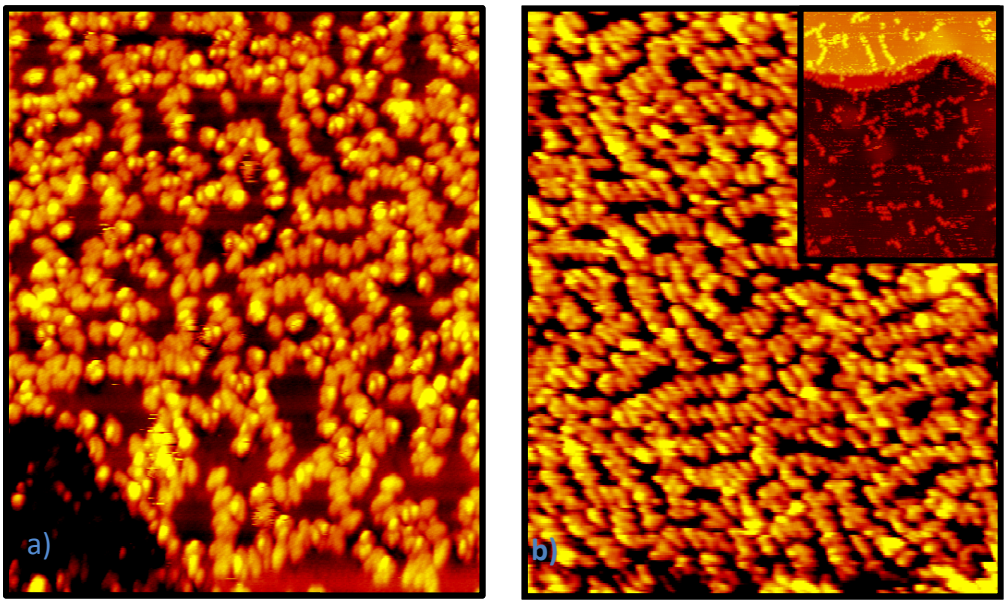

Figure 26. a) STM image taken at 200 K, of 0.5 ML of TCPQ on Cu(100) annealed to 455 K (350 Å x 430 Å, -0.8V, -0.1 nA): Some molecules are still unchanged but a "loosely" assembly in chains starts to appear, following the high symmetry directions of the substrate. **b)** STM image, taken at 100 K of 0.9 ML of TCPQ on Cu(100) annealed to 490 K (290 Å x 380 Å, -1.5, -0.18 nA): The molecular chains seem to be "straightened". All molecules have lost their lobes.. **Inset:** STM image taken at RT of 0.2 ML of TCPQ on Cu(100) annealed to 535 K (590 Å x 720 Å, -2.2, -0.22 nA): The same situation is found for a different coverage, chains without lobes oriented along the high symmetry directions of the substrate.

Together with the disappearance of the lobes, annealing also leads to a new arrangement of the molecular units side by side in chains. These are oriented along the high symmetry directions of the Cu surface and, with higher annealing temperature, grow longer and straighten. A direct comparison at intermediate annealing temperatures between the units with two lobes and the dim ones shows that the length of the long side is unchanged (Fig. 26). Depending on the coverage and annealing temperature, chains with up to 20 molecules can be observed (Fig. 27). The same observation can be found in the TCTQ on Cu(100)-system, too (Fig. 28 and 29).

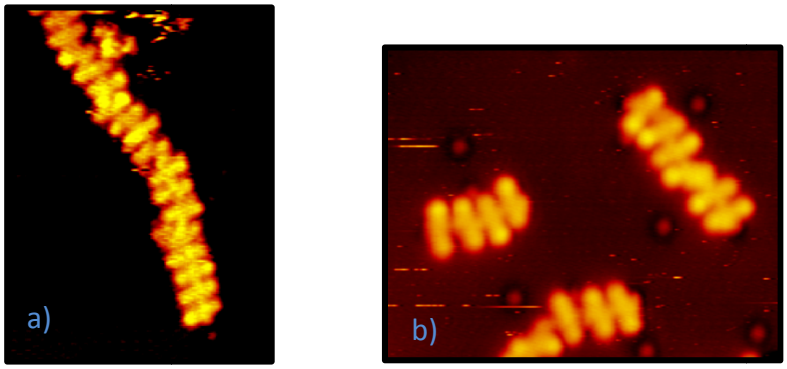

Figure 27: STM images of different chains: a) STM image, taken at 230 K, of 0.2 ML of TCPQ on Cu(100) annealed to 570 K (110 Å x 140 Å, -1.0V, -0.21 nA): **b)** STM image, taken at RT, of 0.3 ML of TCPQ on Cu(100) annealed to 535 K (130 Å x 110 Å, -2.2V, -0.62 nA): Different chain lengths of up to 20 units can be observed depending on the growth and post deposition conditions.

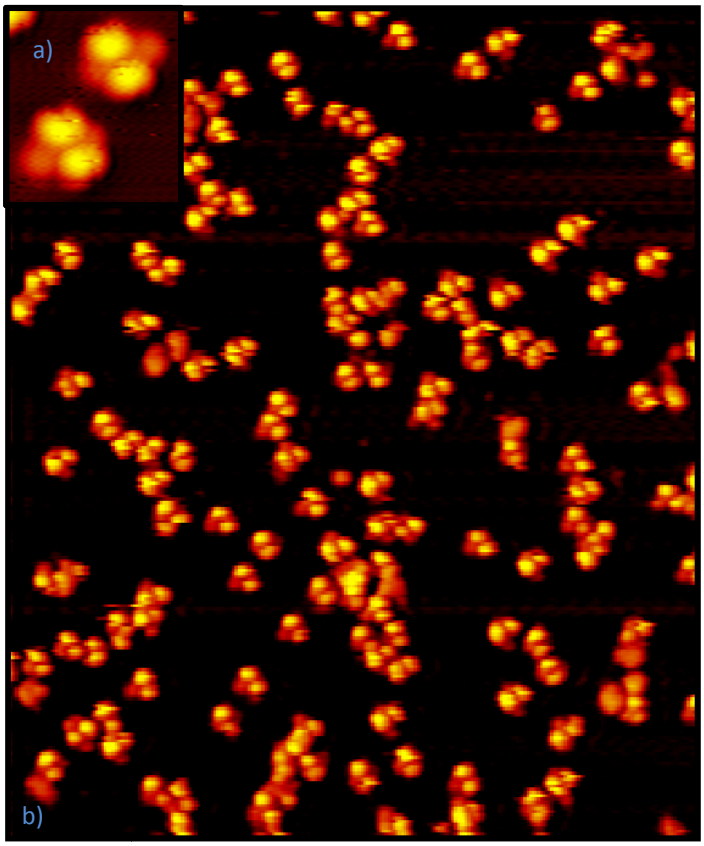

Figure 28. Two STM images (a and b), taken at 160 K, of 0.2 ML of TCTQ on Cu(100), (380 Å x 450 Å, -1.8 V, -0.21 nA): Figure **a)** shows the detailed shape of the TCTQ molecules with its asymmetric structure and the characteristic two bright lobes before annealing, whereas in an overview, Figure **b)**, the lack of long range order becomes visible.

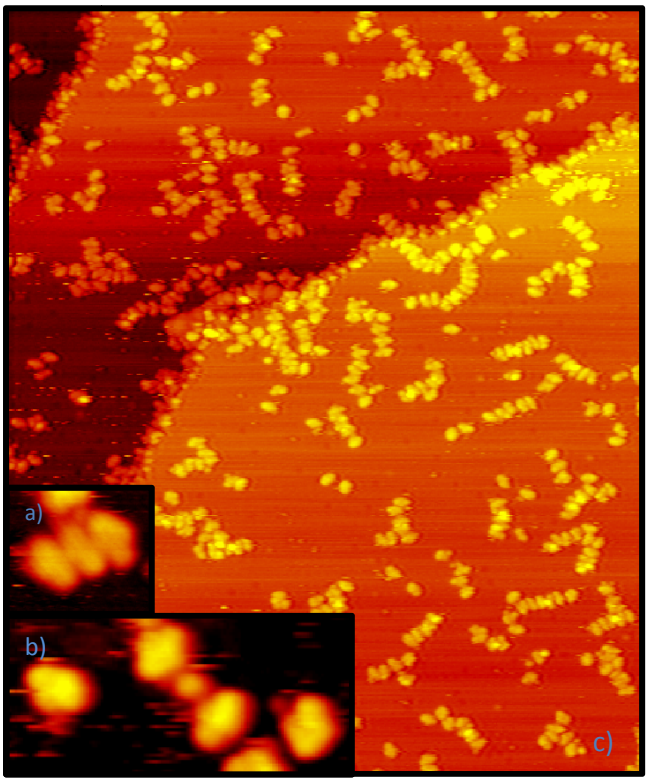

Figure 29. The behavior of TCTQ/Cu(100) is identical to TCPQ/Cu(100). All shown images are from the sample of Figure 28, the insets here are represented at the same scale. In image **a)** after annealing to 460 K a three unit chain consisting of molecules without bright lobes can be observed (35 Å x 30 Å, -1.3 V, -0.12 nA). The changed molecules are present as well in single entities after annealing (Image **b)**: 90 Å x 40 Å, -0.8V, -0.33 nA). They exhibit as well the "arrow" form as in the TCPQ case. An overview (**c)**: 630 Å x 750 Å, -1.1 V, -0.28 nA) shows single TCTQ molecules without lobes and several formed chains, which tend to align along the substrate high symmetry directions, analogue to annealed TCPQ/Cu(100).

The observed order of the molecules after annealing stands in contrast to the mainly disordered close packed arrangement in films around the monolayer coverage at RT. There, the order has been explained based on van der Waals and electrostatic forces. This is different in the case of the annealed samples where the units assemble very close, side by side and with a lateral displacement smaller than the observed arrangement in patches before annealing. This indicates the effect of a new intermolecular interaction with a directional character.

In order to probe the strength of the bond between adjacent molecules within the ordered chains, STM manipulation experiments were performed. A single dim molecule attached to a chain but at a larger distance than the average chain separation can be removed easily with the STM tip (sequence Fig. 30 blue arrows). On the contrary, the individual constituents of the chains at closer distance cannot be separated with these manipulation conditions. Decreasing the STM resistance only leads to a movement or a rotation of the chain as a whole. Manipulations of ordered chains of any length (experiments done for chains up to 10 segments) are only successful in the sense of a movement or a rotation of the whole chain. It was not possible to break any bond within an ordered chain, which suggests a rather strong bond between the units and has usually been interpreted as a probe for covalent bonding[13].

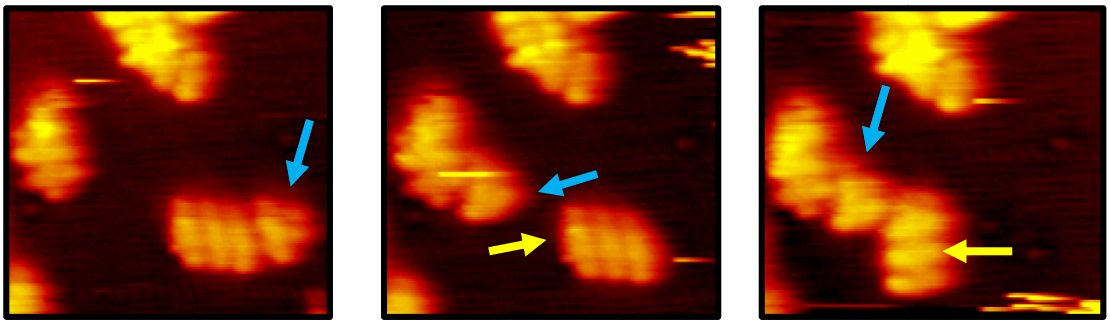

Figure 30: Sequence of three STM images, taken at 110K, of TCPQ grown at RT on Cu(100) and annealed to 490 K (110 Å x 100 Å, -1.5 V, -0.22 nA): In the first image a molecule attached to the chain (blue arrow) can be removed easily and appears to the left of the chain. The attempt to remove one of the remaining three molecules with the same manipulation conditions failed and the chain remained in its place. After increasing the STM impedance for the manipulation the movement of the three molecules as a whole (yellow arrow) can be observed in the subsequent image. That was repeated subsequently (image not shown).

Measuring the total length of the one dimensional assemblies without lobes and dividing it by the number of constituents of samples annealed over 490 K reveals an average separation of 8.8 ± 0.4 Å. Two TCPQ radicals being at this distance brings the remaining side groups close enough that a covalent interaction between neighboring molecules is the most likely scenario (Fig. 31). Two different reaction results are possible: first, a direct connection by the carbon atoms of two different TCPQ molecules which have lost one cyano group (Fig. 31 a and b) and second, a covalent interaction of one carbon atom which has lost a cyano group with a nitrogen from a remaining cyano group of an adjacent molecule (Fig. 31 c and d). The first polymer would exhibit a very short distance of 6.4 Å (gas phase calculation) between the single units constituting the whole chain. This is not compatible with the experimental STM distance. The first polymer model can thus be excluded. The second covalent chain model exhibits a distance of 9.0 Å which is in good agreement with the STM-distance measurements and which therefore is proposed as the result of the polymerization reaction.

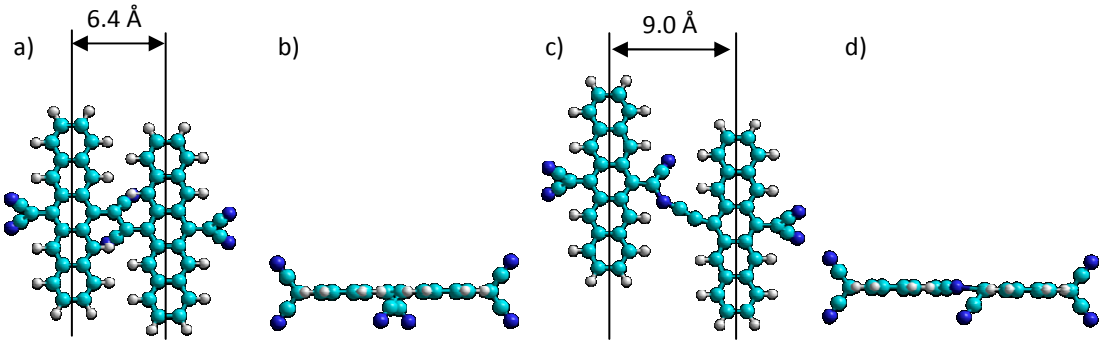

Figure 31: Chemical models of two TCPQ radicals fused together on the Cu(100) surface, a) and c) top views and b) and d) side views: The model with the intermolecular carbon-carbon bond in a) and b) is bond by the the nitrogen atoms of the remaining cyano groups to the surface. The intermolecular unit distance is 6.4 Å and thus too small to explain the STM images. In c) and d) the remaining cyano group of one molecule is lifted and binds to the carbon atom which still exhibits a cyano group bond to the surface. A lateral displacement of the center of two TCPQ molecules in both models along the main axis can be observed. This is observed experimentally, too (Fig. 27 and 30).

Annealing the samples above 600 K, results in the appearance of irregular structures next to few remaining ordered chains (Fig. 32). A structural decomposition of the molecules seems the most likely explanation.

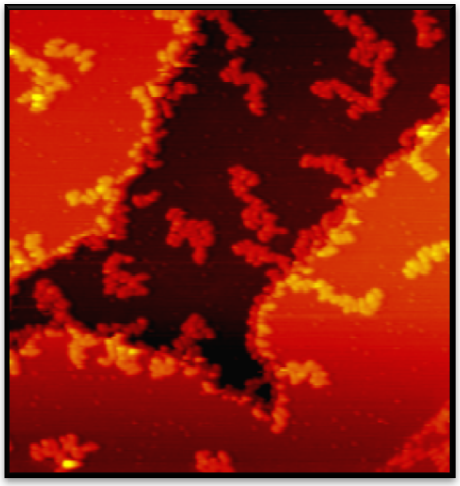

Figure 32. STM image, taken at RT, of 0.2 ML of TCPQ on Cu(100) annealed to 605 K (590 Å x 620 Å, -2 V, -0.12 nA): At this annealing temperature only few ordered chains are left and irregular structures appear.

Concluding the STM results about annealing TCPQ and TCTQ on Cu(100), it has been demonstrated that a one-dimensional order can be achieved by providing the system with thermal energy. This additional energy does not only increase the mobility but also affects the molecules chemically and changes their structure. This is observed in a temperature range from 370 K up to 490 K where the number of bright lobes decreases with increasing annealing temperature. Experimental arguments combined with STM simulations support the idea of a detachment of one entire cyano group per dicyanomethylene moiety, explicitly the CN-part which is located above the pentacene unit, instead of the desorption of only the N-atom of these units. Above 490 K only dim molecules assembled in chains remain. The changed arrangement compared with the ordered arrays seen before, and especially the very close proximity between the radicalized dicyanomethylene groups, which face each other, suggests a new type of interaction. From the impossibility of dividing the chains by tip manipulation, a covalent character of the new formed intermolecular bonds is deduced. Although the molecule - substrate interaction seems to be slightly changed, the still present influence of the surface on the adsorbates becomes clear through the tendency of the chains to follow the close pack directions of the Cu-surface.

4.6.2 XPS results

In order to study the chemical nature of the change of the TCPQ on Cu(100) due to annealing, STM and XPS experiments of the same samples were conducted, in the same UHV system before and after annealing to 490 K, the temperature at which 100 % of the TCPQ molecules have changed.

In this series of experiments the first step after depositing TCPQ on the Cu(100) sample was the structural characterization by STM. Then the samples were transferred in ultra-high vacuum from the STM- to the XPS-chamber, where they were characterized chemically. The third step consisted in the back transfer to the STM chamber and a structural check to exclude radiation damage of the TCPQ/Cu(100). Subsequently the annealing procedure to 490 K in the STM chamber followed. Step number five included another STM check to ensure the complete disappearance of the bright lobes and the formation of the characteristic chains. The sixth and last step was the transfer to the XPS chamber and the x-ray spectroscopy of the annealed TCPQ/Cu(100) assembled in chains and without any bright lobes. An occasional check about the influence of the x-ray radiation on the samples after annealing revealed no difference of the structures found.

4.6.2.1 Structural comparison before and after XPS measurements and annealing

After up to 11 h of x-ray irradiation of the TCPQ/Cu(100)-samples, no change was observed. As mentioned before, after deposition at RT, the molecules are oriented in the close-packed directions of the substrate, do not assemble in ordered islands and exhibit two bright lobes (Fig. 33 and 34, a) and b)). After annealing to 490 K, the expected chains, consisting of molecular units without lobes, are clearly visible and oriented along the two high symmetry direction of the substrate (Fig. 33 and 34, c)).

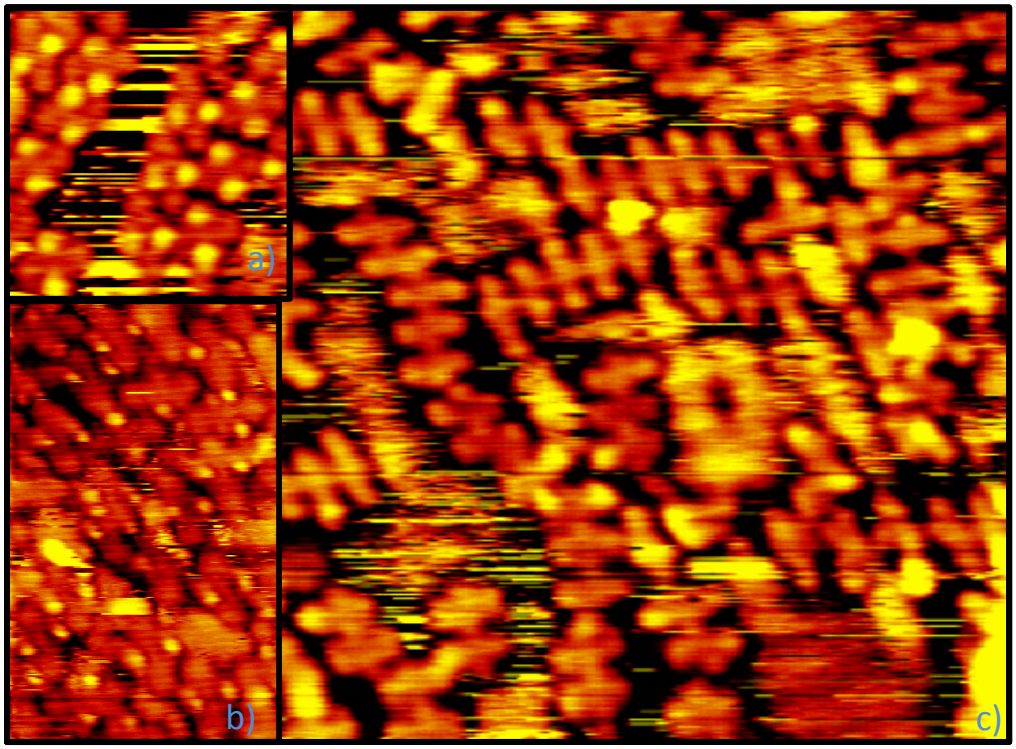

Figure 33. An STM sequence of 0.63 ML TCPQ on Cu(100) is shown, all images were taken at RT and are displayed in the same scale: **a)** (66 Å x 68 Å, -1.6 V, -0.3 nA): Initial situation: Mainly disordered molecules oriented along the two high symmetry directions and with the typical two bright lobes. **b)** (57 Å x 89 Å, -1.6 V, -0.16 nA): The situation is identical after XPS measurement: Different measurement conditions and tip mode let the image appear more defined, nevertheless the molecules are oriented along the close packed directions of the Cu(100), do not show a high degree of order and still posses the two lobes. **c)** (210 Å x 180 Å, -1.5 V, -0.15 nA): After annealing to 490 K the molecules are found forming the expected chains, all have lost their lobes and the chains tend to be oriented along the (011)- and $(0\bar{1}1)$- substrate directions.

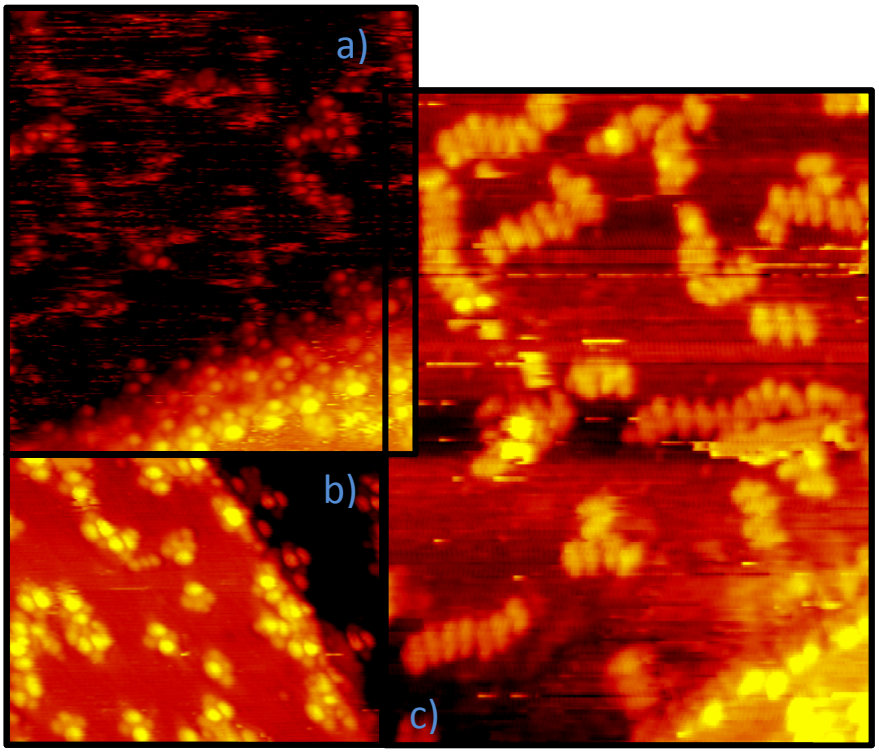

Figure 34. An STM sequence taken at RT of 0.23 ML TCPQ on Cu(100) in the same scale is shown: **a)** (210 Å x 230 Å, -1.6 V, -0.1 nA): Before the annealing the selected image shows an area with substrate steps partially covered by TCPQ molecules. In the trimer on the terrace in a) the usual orientation along the two different substrate directions becomes visible. **b)** (200 Å x 110 Å, -2.8 V, -0.2 nA, imaged at 90 K): After XPS measurement: A very similar situation to a) is encountered, only without any "streaky lines" due to the low STM measurement temperature. The bright lobes are clearly visible. The step edge is partially covered and the TCPQ molecules are oriented along the close pack directions of the Cu(100), ordered islands are not found. **c)** (260 Å x 350 Å, -1.5 V, -0.15 nA, imaged at 105 K): After annealing to 490 K: the lobes have disappeared completely and the molecules form chains oriented along the two high symmetry directions.

4.6.2.2 Spectra overview

The XPS measurements after annealing the samples to 490 K show little changes at the scale of the survey (example survey spectra in Fig. 35). No new peaks can be observed and signs of nitrogen and carbon are still present, which confirms the STM results that the reaction does not imply a detachment of the whole dicyanomethylene group. In the spectrum (black) shown in Figure 35, corresponding to a multilayer film, the substrate features after annealing (compare Fig. 35, Cu3p-peaks) are more pronounced due to thermal desorption of TCPQ molecules. The inset of the O1s-region and the overview scan do not show any measurable sign of oxygen or of any other element.

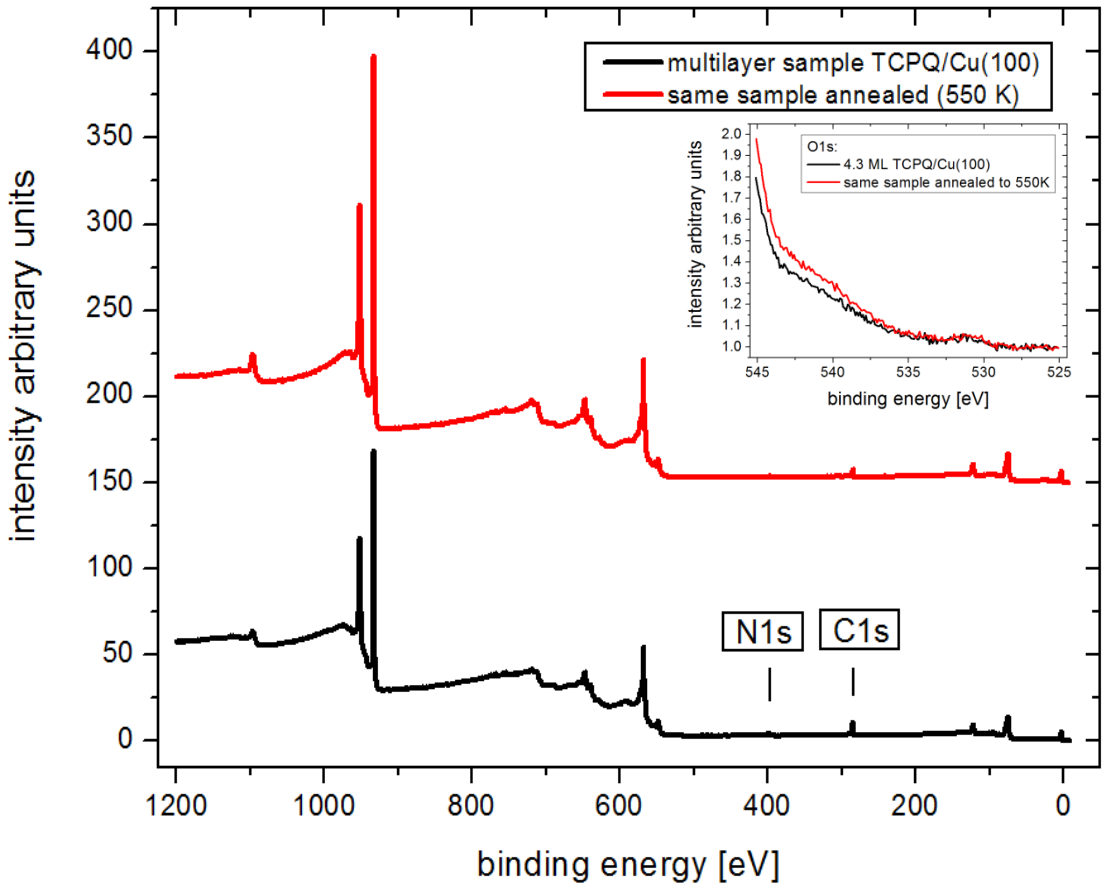

Figure 35: Two XPS spectra of the same sample before and after annealing are represented. The annealed sample shows smaller carbon and nitrogen peaks, as well as stronger substrate features (most clearly around 960 eV). That indicates partial material loss due to annealing. The inset represents the O1s-region (where the Auger background from the Cu(100) is stronger after annealing in line with the aforementioned partially sublimation of TCPQ molecules). No sign of oxygen or any other element than the ones from the molecules can be seen.

4.6.2.3 N1s-region, submonolayer regime

After annealing, all N1s-spectra of submonolayer samples can again be deconvoluted with one main peak (Gaussian width 1.40 ± 0.05 eV) at 398.2 ± 0.05 eV and a broad curve corresponding to the "shake-up"-satellite (Gaussian width 4.0 ± 0.4 eV, Fig. 36). The main component, the 1st-layer N-C-component, is significantly reduced in intensity and thus the total area of the N1s-peak decreases to 55.1 ± 5.6 % of the original value before annealing. This clearly confirms the STM results which assumed desorption of half of the nitrogen of a TCPQ molecule. Additionally the binding energy of this component does only slightly shift (0.09 ± 0.04 eV to higher binding energies), which leads to the conclusion that the adsorbates after annealing remain negatively charged. The average shift of the "shake up"-satellite of 1.4 ± 0.6 eV to lower binding energies may be explained with a smaller HOMO-LUMO-gap in the polymer chains.

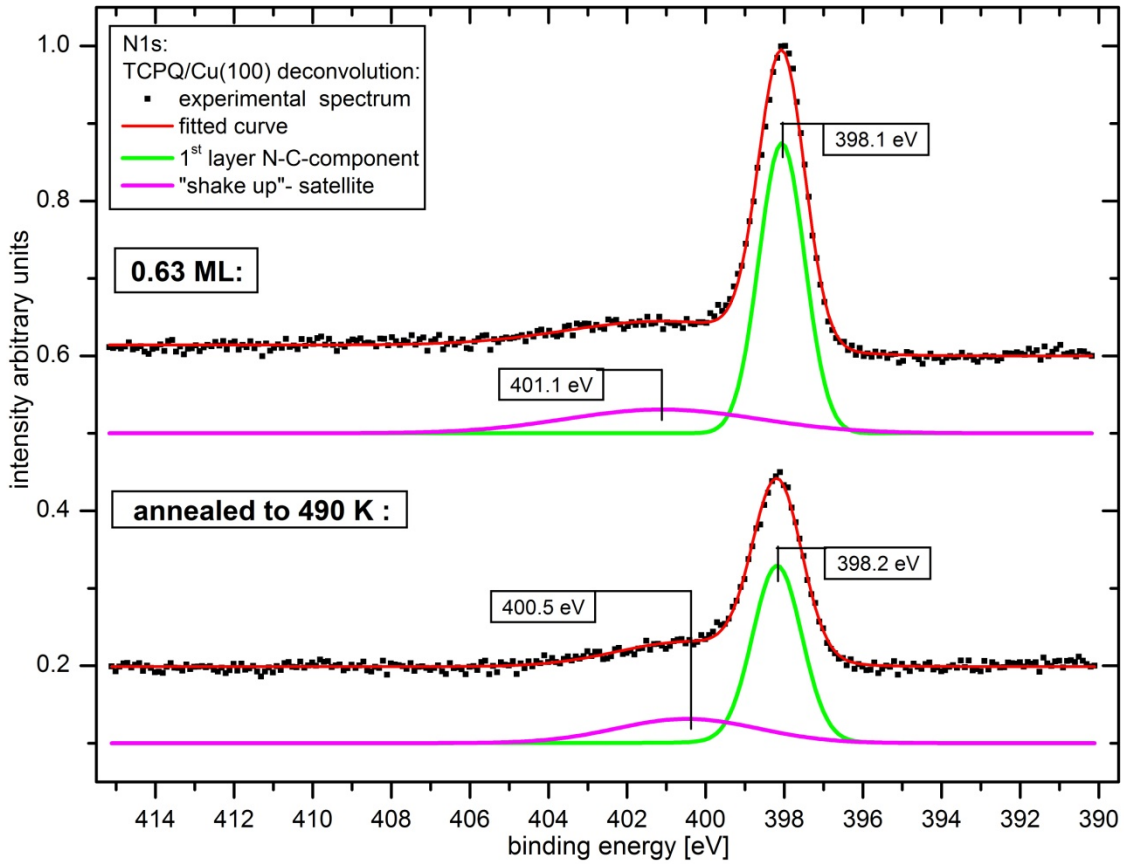

Figure 36: Example XPS spectra from the N1s-region of a submonolayer sample before and after annealing to 490 K. A reduction of about 50 % of nitrogen after annealing is visible. The energy position of the "shake up"-satellite is affected as well by annealing, which may be a hint that the HOMO-LUMO gap has changed.

4.6.2.4 C1s-region, submonolayer regime

The C1s-spectra below the monolayer show a single broad peak centered around 284.6 eV (Fig. 37) and thus cannot be deconvoluted without theoretical support about the partial charges on the atoms of the changed TCPQ molecules. Therefore only the total area is determined. A little reduction can be observed compared to the situation before annealing, in the average 6.7 ± 2.1 % (Fig. 37). This result is compatible with the loss of two entire cyano groups per TCPQ. Two carbon atoms per molecule would correspond to a reduction of area in the C1s-region of 2/28 = 7.14 % very close to the experimental value (4 carbon atoms would account for 14.28 %).

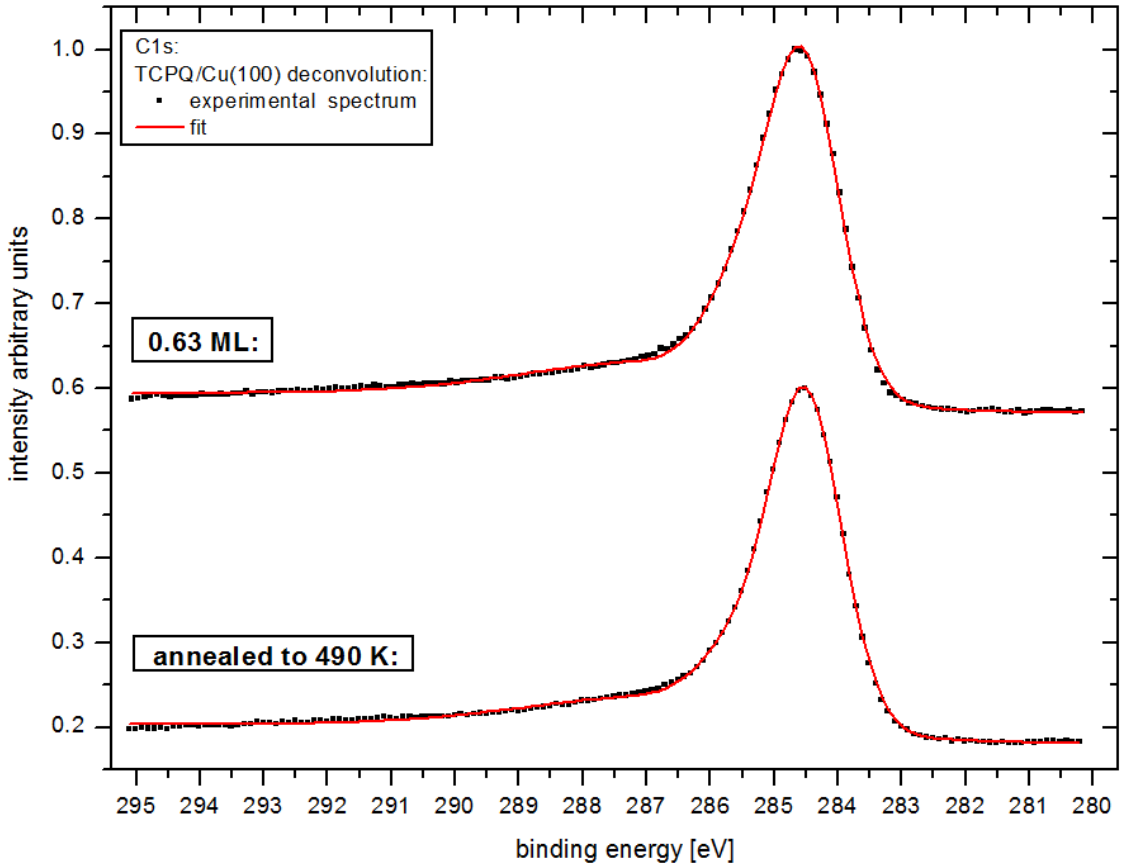

Figure 37: Comparison of an example C1s-spectra from a submonolayer sample before and after annealing: The broad peak is centered at 284.6 eV. The total area is slightly reduced after annealing to about 93 %, consistent with the idea of a desorption of an entire cyano group per dicyanomethylene moiety.

The XPS data of the annealing of the 4.3 ML multilayer sample is discussed in the Appendix due to its rather low relevance for the polymerization reaction and its increased complexity. It shows mainly desorption of material, because of the high initial coverage of TCPQ on Cu(100).

4.6.3 Conclusions

Summarizing the STM and XPS results about the changes experienced by TCPQ and TCTQ after annealing, the following scenario can be depicted. Both experimental methods, STM and XPS, support the detachment of the two upper cyano groups of each initial molecule. The remaining radicals form then chains exhibiting a different order and a closer distance than observed before annealing and with an intermolecular interaction so strong that STM tip manipulations cannot divide the assembled chains. We conclude then the existence of a covalent bond between the constituents of the chains. Annealing samples with coverages over 1 ML leads only to desorption of TCPQ without chemical changes, even at temperatures (550 K) higher than the typical one (490 K) necessary for the reaction in submonolayer samples. This underlines the importance of the surface and the charge transfer which enables the covalent reaction among TCPQ and TCTQ on Cu(100) with coverages of up to around a monolayer. The charge transfer provides the flexibility for the surface conformation of the molecules with two

cyano groups pointing into the vacuum. Preliminary DFT calculations indicate that the charge transfer is responsible for a weakening of the C-C-bond between this upper cyano groups and the methylene atom attached to the pentacene backbone. As a consequence the breaking of this bond is possible through annealing and the cyano groups desorb from the surface. The remaining radicals, provided through the thermal energy with a higher mobility, react with each other and form covalent chains. These are still negatively charged, as deduced from the unchanged N1s-peak after annealing, and the polymers obtained this way, with four (from TCTQ) or five carbon rings (TCPQ), are shown in Figure 38.

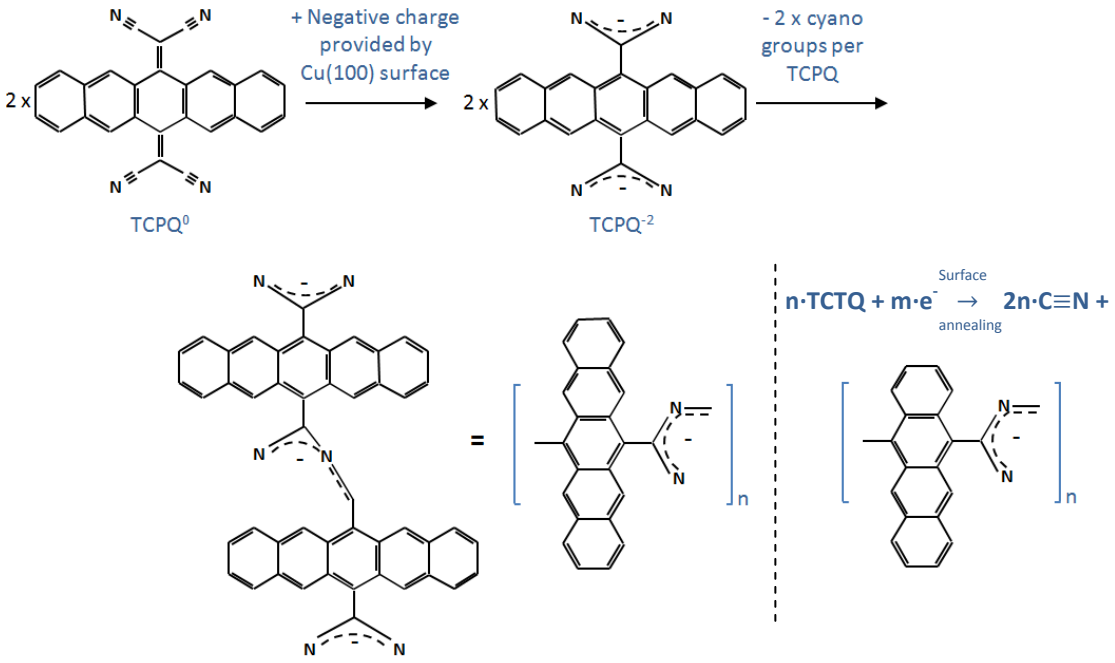

Figure 38: Reaction scheme for two TCPQ molecules (same situation is found for TCTQ): The neutral molecule is negatively charged upon adsorption on the Cu(100)-surface and then two cyano groups per molecule are removed by annealing. The thermal energy increases the mobility, which leads to the reaction of n-radicals to a polymer containing n units.

4.7 Appendix

4.7.1 N1s-region - multilayer regime

The four step sequence of the 4.3 ML sample shows that annealing has a different effect than in submonolayer samples, because the ratio between carbon and nitrogen stays constant over the whole experiment. The main conclusion is that the polymerization of TCPQ previously described does not take place at the same temperature due to the initially larger amount of organic material.

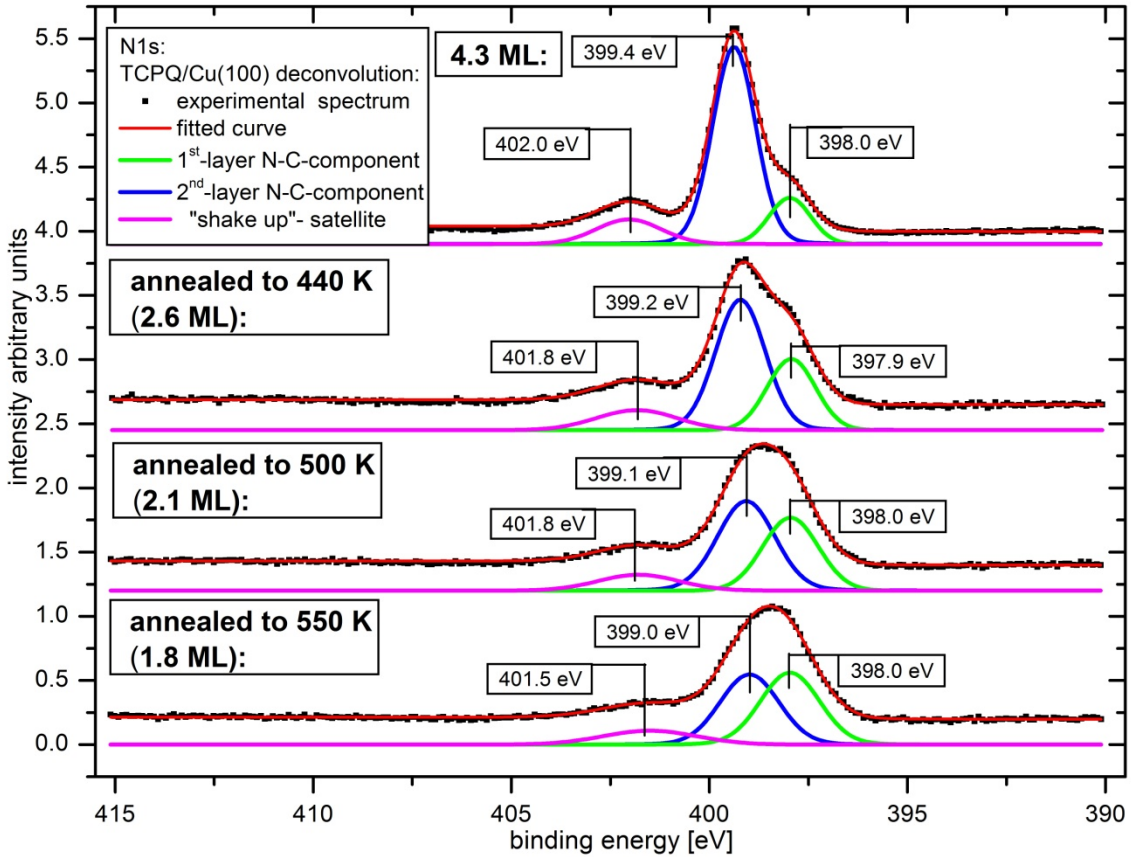

Figure 39: Spectra from the annealing sequence of the multilayer sample with the same deconvolution peaks as described before: multilayer N-C-, the 1st-layer N-C- and a "shake up"- component. The multilayer N-C-line decreases with increasing annealing temperatures and shifts to lower binding energies. The 1st-layer N-C-peak grows slowly and maintains its energy position. The "shake up"-satellite decreases proportional to the amount of nitrogen. In contrast to the other samples the multilayer sample does not exhibit a loss of 50 % nitrogen of the 1st-layer N-C-component which is attributed to a "protecting" effect of the nearly complete second layer after the last annealing step.

The spectra of the annealing sequence of the multilayer sample are deconvoluted as before ("4.7.2.4 C1s-region, submonolayer regime") with two different components and a broad "shake up"-satellite (Fig. 39). This last feature $E_{shake\ up}$ at 402.0 eV decreases in area proportional to the total nitrogen area. The area ratio for the multilayer sample is constant $\frac{a_{shake\ up}}{a_{total\ area}}$ = 13 ± 1 %.

The multilayer N-C-component appearing in topmost layers, which was identified with the line of uncharged nitrogen, is strongly reduced with every annealing step (Fig. 39 and Table 4) and shifts gradually towards lower binding energies, 0.13 ± 0.04 eV with every annealing step, for a total shift of 0.4 eV. Speculating about the origin, a new reaction of the remaining topmost layers might take place, a thermally induced polymerization similar to the beam induced polymerization of thick TCNQ layers on metals[25] or simply a reduccion of a small screening effect of the metal surface (Chapter 2). A parallel desorption of material is supported by the ratio between the total areas of the C1s- and N1s-region. This ratio stays constant along the whole annealing sequence ($r_{C1s/N1s}$ = 7.2 ± 0.4, theoretical = 7, see below).

At the same time the 1st-layer N-C-component grows slightly with every annealing step in accordance with a smaller attenuation due to the loss of material on top. Even after annealing to 550 K a strong multilayer N-C-component remains with an area corresponding to a nearly complete second layer. The presence of this second layer seems to be the reason for the inhibition of the detachment of the cyano groups in both layers. This indicates that the polymerization reaction of the TCPQ molecules, observed in samples with coverages below one monolayer, can only take place for molecules in contact with the surface when there are no others on top.

STM measurements for the multilayer sample could be done only after desorption of some layers of TCPQ due to the difficulties in measuring a tunnel current through several organic layers. The STM images taken after annealing the sample to 500 K show 3D-clustering of the adsorbates and a coverage above 1 ML (Fig. 40 a).

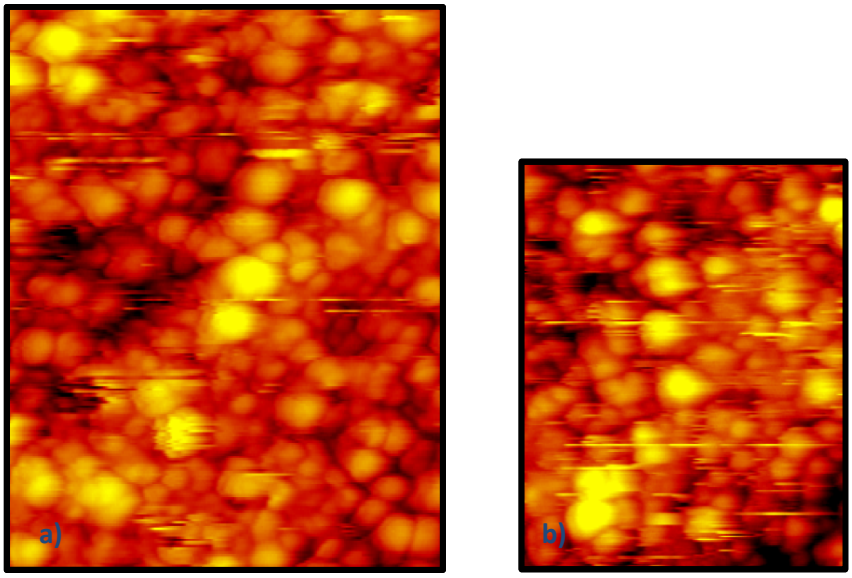

Figure 40. STM images with the same scale of **a)** the 4.3 ML sample annealed to 500 K of TCPQ on Cu(100) at RT (210 Å x 280 Å, -2.2 V, -0.15 nA) with a remaining coverage of about 2.1 ML. A 3D-clustering of the adsorbates with a similar sizes distribution is observed with a coverage over a monolayer.

Multilayer sample:	Development of multilayer peak: $\frac{a_{n,multi-layer}}{a_{0,multi-layer}}$ · 100%	Peak ratio: $P_n = \frac{a_{n,multi-layer}}{a_{n,1st-layer}}$	[1] Attenuation: $A_n = \frac{a_{n,\ 1st-layer}}{a_{1.2\ ML,\ 1st-layer}}$	[2]Coverage: $\theta_n = \frac{A_n P_n}{A_n\ (=1\ or\ A_n)}$ +1ML
TCPQ/Cu(100) (n=0)	100 %	4.51	47 %	4.3 ± 1.2 ML
Annealed to 440 K (n=1)	57 %	1.92	62 %	2.6 ± 0.4 ML
Annealed to 500 K (n=2)	41 %	1.30	67 %	2.1 ± 0.2 ML
Annealed to 550 K (n=3)	33 %	0.97	72 %	1.8 ± 0.1 ML

Table 4: Analysis of the N1s-data after every annealing step of the 4.3 ML multilayer sample. First the change of the multilayer N-C-component normalized to the maximum from the sample before annealing shows the desorption of material. This is why the ratio between the two different components decreases (column 2). The 1st-layer component in comparison to the same component of a sample close to 1 ML reveals the attenuation, which together with the peak ratio can be used to estimate two limiting cases for the coverage (last column).

[1] A detailed argumentation is found in the section "Coverage determination"

[2] Two limiting cases help to determine the coverage and the error. For the first case no attenuation is assumed for the topmost layers, which are all layers but the one in direct contact with the surface. The attenuation in the above simple formula is therefore A_n = 1. An attenuation of the topmost layers equal to the one from the first layer: A = 0.47, 0.62, 0.67, 0.72, is the second limiting case for every annealing step. The average of both cases is calculated for the table with the error including the limiting cases. The calculations were done with the following formula:

$$\theta_n = \frac{1}{2}\left(\theta_{n,lim.case\ 1} + \theta_{n,lim.\ case\ 2}\right) = \frac{1}{2}\left(\frac{A_n P_n}{A0} + 1 + \frac{A_n P_n}{A_n} + 1\right) ML = \left(\frac{(A_n+1)P_n}{2} + 1\right) ML;$$

With n from 0 to 3 being the number of annealing steps, A_n is the attenuation of the 1st-layer N-C component in the N1s-region (A_0=1, no attenuation), P_n is the peak ratio of the multilayer N-C-component divided by the 1st-layer N-C-component.

$$\pm\Delta\theta_n = \frac{1}{2}\left(\theta_{n,limiting\ case\ 1} - \theta_{n,limiting\ case\ 2}\right)$$

4.7.2 C1s-region - multilayer regime

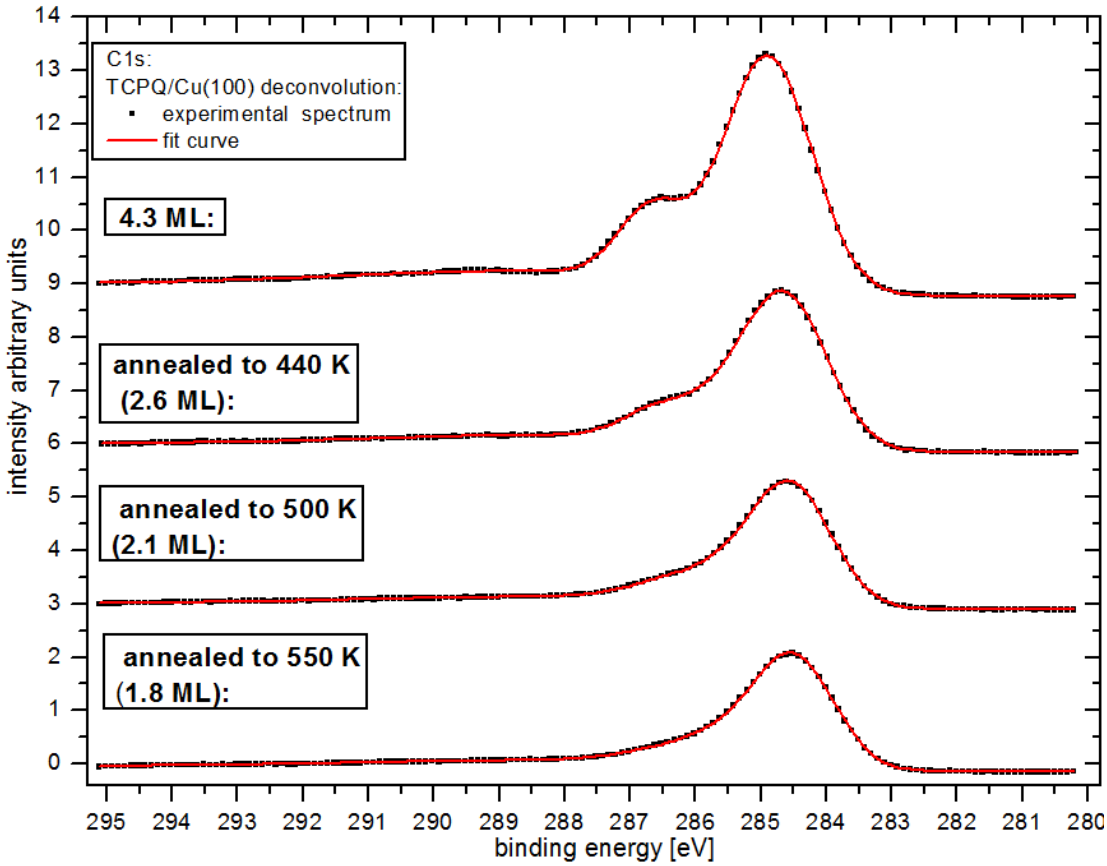

Figure 41: C1s-spectra from the annealing sequence of the multilayer sample with a fit for the total area: The shoulder on the high binding energy side decreases parallel to the strong component of the spectra with every annealing step. The area analysis reveals a constant C : N – ratio which is consistent with a desorption of material with the element ratio of the TCPQ molecule.

The C1s-spectra are only fitted for the determination of the total area, due to the increased complexity for samples over the monolayer which makes a precise deconvolution impossible without sophisticated theoretical support. A direct visible result (Fig. 41) is a reduction of the total carbon area after every annealing step from 100 % to 70.2 %, 60.2 % and 56.7 %, respectively. The ratio between the total area of the C1s- and the N1s-region stays constant after every annealing step, with a value of 7.2 ± 0.4, the same ratio is found for submonolayer samples before annealing. From this can be deduced that, first, the elements are adsorbed on the surface in the ratio expected from the chemical model of TCPQ (ratio = 28 C-atoms/4 N-atoms = 7) and second, that annealing the multilayer sample only desorbs material with the ratio of the molecule.

In summary, the polymerization reaction which takes place in the submonolayer regime, simply does not occur in the case of a 4.3 ML sample, although the coverage is reduced down to about 2 ML through desorption of material. This suggests that without the Cu(100) surface and the missing charge transfer the above describe submonolayer polymerization cannot take place. Parallel to desorption of material a gradual binding energy shift of the N1s-multilayer

component is observed. The latter result may suggest a small screening effect or an unknown reaction among neutral TCPQ in the remaining topmost layers without any element ratio change.

4.7.3 STM height measurement method

The STM height measurements of the dim part and the bright lobes of the molecules have been done for different bias voltages and always in comparison to a known value (Fig. 24), the step edge height of the Cu(100) surface (a_{Cu} = 1.8 Å). This is more time consuming but increases the reliability compared to height measurements which are based on a former calibration of the STM. The latter method suffers usually from slightly different measurement conditions during the calibration compared to the conditions during the measurements of molecules (STM temperature, measurement history, creep and drift). Several images for each of the 11 different bias voltages were thus analyzed with a total of more than 80 linescans.

4.7.4 XPS-spectra background treatment

The highest XPS peak, $Cu2p_{3/2}$, was used for the count optimization and for the energy scale calibration (the average of all $Cu2p_{3/2}$ from pristine Copper of the NIST-database was used: 932.6 eV) in all high resolution spectra. In the nitrogen region no spectrum of a clean sample is shown because it was subtracted from all N1s-spectra to eliminate the broad Auger background. This subtraction causes a little dip of the background of the thickest sample, where the organic material already attenuates the Auger Cu features.

XPS-spectra of samples with organic material exhibit in some regions an overlap of spectral features due to the contributions of electrons from the adlayer and the surface. In order to distinguish between the contributions from the substrate and the adsorbates in the N1s-ragion, a subtraction of a previously measured spectrum from the clean surface has been done for all sample spectra in this region for the system TCPQ/Cu(100). The data acquisition in the case of the clean substrate was extended over the maximum time for the measurement of the N1s-ragion of the samples with the molecular material. This way a better signal-to-noise ratio is achieved and thus the sample spectra exhibit after the treatment the signal-to-noise ratio of the original measurement. The broad feature in the N1s-region of clean Cu(100) (Fig. 42 a) is eliminated and only the peaks related to the TCPQ-molecules remain (Fig. 42 b) which can be fitted for the quantitative analysis more easily and probably more accurate.

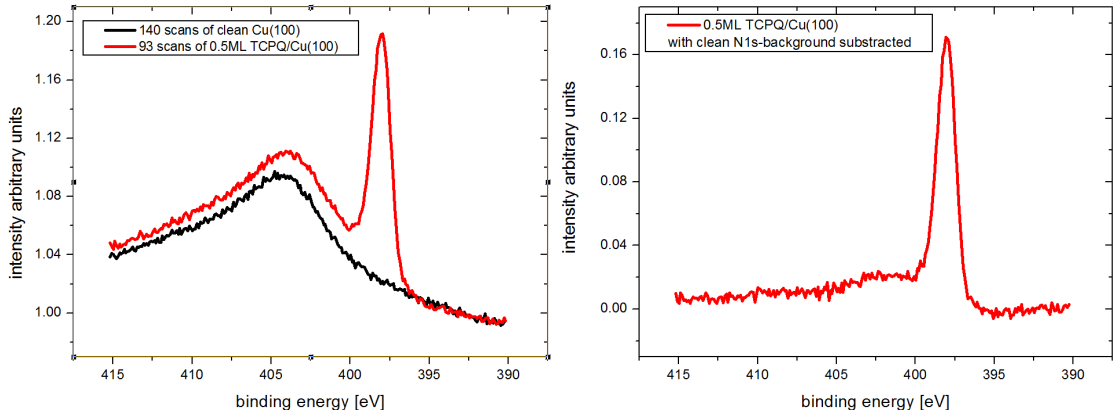

Figure 42: Comparison of spectra of a clean Cu(100)-surface and of a 0.5 TCPQ/Cu(100) sample. The broad substrate feature disturbs the analysis of the N1s-region and has been subtracted from all spectra in this region. The result in the case of the 0.5 ML sample is a sharp peak with a small shake-up contribution (b).

4.7.5 Coverage determination

The determination of coverages of organic material adsorbed on surfaces is in general a difficult topic and connected with several sources of errors, especially when combining structural and spectroscopic methods from two separate chambers. Coverage values from XPS suffer often errors originated in differences of experimental parameters from one chamber to the other (deposition geometry, the evaporator temperature, background pressure) and need a reliable calibration method. The STM-coverage determination is only of local nature and breaks down for coverages of multilayers.

The advantage in the TIREMISU-UHV system is that the same sample is measured with two different methods. On one hand this ensures that XPS and STM experiments are done for exactly the same sample with the same amount of material on top and on the other that through the combination not only the reliability is increased but coverages can be determined which would not be accessible to only one method. Additonally, XPS, being an averaging method (x-ray spot-radius > 1 mm), verifies the local (maximum area 1 μm^2) STM coverage determination (error in a linear regression is in the TCPQ-case below 1.3 %).

The first step in determining the coverages of the submonolayer samples with STM was to analyze statistically several images from all samples with respect to the area covered with TCPQ molecules. A monolayer is defined as the amount of molecules necessary to fully cover an observed surface area in a close packed way. The example in Figure 43 describes how this was done for one image.

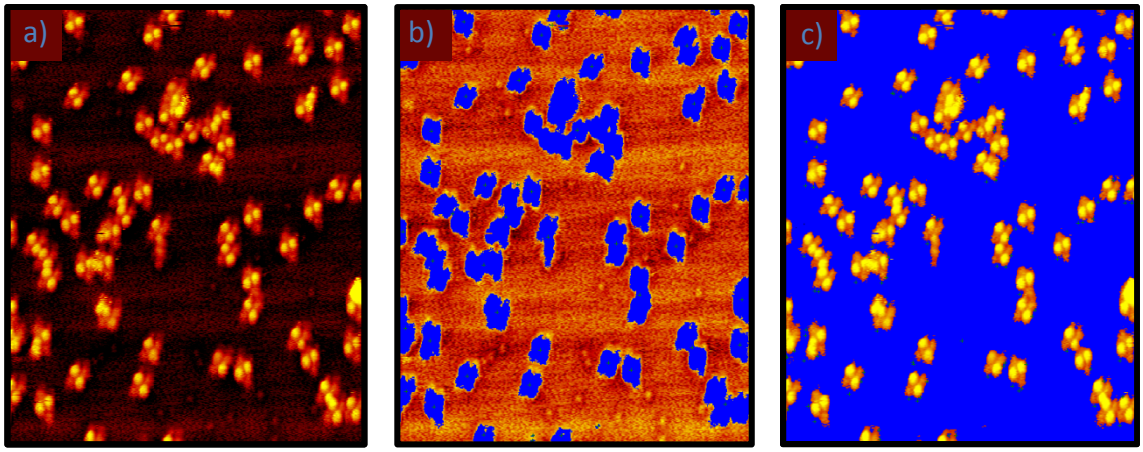

Figure 43: a) STM image taken at 150 K of 0.2ML of TCPQ grown at RT on Cu(100), (230Åx290Å, -2V, -0.19nA): In order to determine the coverage of the sample, first the surface area of all objects with a height bigger than the surface was measured, b) blue area 19.71%). The inversion was also measured, c), with a result of 80.11%. The average was round to full decimals and result thus in a coverage of 0.20 ML for one image. Several images from each sample were analyzed this way to determine the final coverage for one sample.

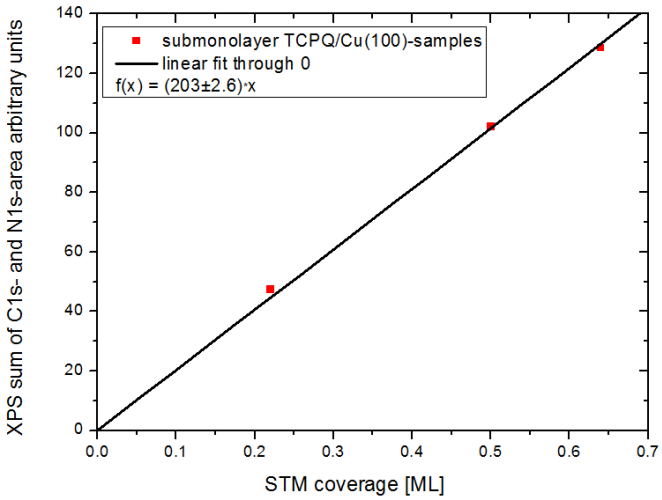

Figure 44: The points represent TCPQ/Cu(100) samples measured with STM and XPS in the same UHV-system. The total coverage analysis of both methods is shown: the abscissa represents the STM value in monolayers and the ordinate axis shows the sum of the XPS peak areas from the two elements the molecule contains. With the linear regression the XPS values are calibrated and thus the determination of a lower limit of coverages for multilayer samples, measured with XPS, is possible. At the same time it is assured by an averaging method (XPS) that the STM coverage determination was done with sufficient statistics is not only valid on a local scale.

In a second step the STM coverage results were compare to the total amount of material determined by XPS measurements (Fig. 44). This is the sum of the total areas of the C1s- and N1s-peaks from the high resolution XPS measurements, corrected with a factor for the different cross sections of each chemical element (taken from the Trieste synchrotron homepage "Elettra" based on data from[26, 27]). With the help of a linear regression a calibration of the XPS measurements for coverage values below the monolayer can be obtained.

This method yields for samples over a monolayer only a minimum value, because the photoelectron attenuation due to the topmost layers is. The area appears smaller due to the

attenuation and the coverage of multilayer samples is therefore underestimated. This problem can be resolved if a component can be found which changes in binding energy due to a direct surface contact. The N1s-component in the TCPQ-case provides this due to the charge transfer which affects the N1s-binding energy only in the first layer. Based on this component another coverage estimation method is presented in the following.

4.7.6 Coverage estimation based on charge transfer

In the TCPQ/Cu(100) system the binding energy of the photoelectrons from nitrogen depends on the charge on the TCPQ molecules. In the topmost layers which are not in direct contact with the substrate, no charge transfer to the molecules occurs and the binding energy of the N1s-level is higher compared to the case of an extra charge located on the TCPQ molecules. In a submonolayer sample the area of the peak at the characteristic binding energy for nitrogen with an extra charge, $E_{1st,\,N\text{-}C}$ = 398.1 eV, is therefore a measure how many molecules are found in direct contact with the surface. The area of this peak grows with increasing material but reaches a maximum at 1 ML because nitrogen of the molecules on top of the first layer exhibits a higher binding energy, $E_{multi,N\text{-}C}$ = 399.5, due to the neutral charge state of TCPQ. The 1st-layer component decreases due to attenuation by further material on top.

This way the area of the 1st-layer component represents in multilayer samples the equivalent for an amount of material of one monolayer. This area has to be corrected for the attenuation by division of the attenuation coefficient. This coefficient can be extracted from the N1s-regime comparing the areas of the 1st-layer components of the multilayer sample with a sample around 1 ML, where the attenuation is negligible (in our case a 1.2 ML-sample).

Comparing now this corrected area of the 1st-layer component with the remaining area of the multilayer component, provides a measure for how much material is found above the first layer. The multilayer area has to be corrected, too, due to attenuation. As there does not exist any experimental measure for the attenuation of the topmost layers, two extreme cases can be assumed as the limits of attenuation for the topmost layers. One is that no attenuation takes place with the result of a minimum coverage value, because thus the corrected area of the multilayer component is minimal. The other limit is given by assuming an equal attenuation in the 1st-layer as in the topmost layers. This represents the case of maximal attenuation because the amount of attenuating material is less for the topmost layers than for the first layer due to less material on top (at least one layer less). Therefore photoelectrons from the layers except the first one should be less attenuated than electrons from molecules in direct contact with the surface.

Calculating the average of the two limiting cases yields a result with a reasonable error and, as expected, above the minimum values obtained by using the STM-coverage calibration for the XPS areas without taking into account the effect of attenuation. Most important it is coherent with all experimental findings of the TCPQ/Cu(100) system being thus able to explain all observations.

In order to clarify this method the example of the 4.3 ML sample before annealing is calculated step by step in the following: Here the area a_{multi} in the N1s-region called "multilayer component" originates from the material on top of the first layer.

This area is 4.48 times larger than a_{1st} which is the area from the peak associated with the elements in contact with the surface. If a_{1st} originates from 1 ML and the topmost layer cause an area 4.48 times larger, than in a picture without attenuation of the topmost layers an amount of material on top of the first layer of 4.48 ML and in total 5.48 ML would be expected. Introducing the two cases of the assumed attenuations of the topmost layers of first, no attenuation and second, the same attenuation as the first layer exhibits, two limiting cases can be calculated this way:

First no attenuation is assumed for the topmost layers, A0 = 1:

$$\theta_{n,lim.case\,1} = \frac{1}{2}\left(\frac{A_n P_n}{A0} + 1\right) ML = \left(\frac{0.47 \cdot 4.48}{1} + 1\right) ML = 3.10\ ML;$$

With $P_n = \frac{a_{\boldsymbol{multi},N1s}}{a_{\boldsymbol{1st},N1s}} = \frac{1.12}{0.25} = 4.48$ and $A_n = \frac{a_{n,\ N-C}}{a_{1.2\ ML,\ N-C}} = \frac{0.25}{0.53} = 0.47$ (from the N1s-regime)

Second, an attenuation of 0.47 is assumed for the topmost layers, the same value as measured for the first layer:

$$\theta_{n,lim.case\,2} = \frac{1}{2}\left(\frac{A_n P_n}{A_n} + 1\right) ML = \left(\frac{0.47 \cdot 4.48}{0.47} + 1\right) ML = 5.48\ ML;$$

The average of both limiting cases is the final result for the coverage:

$$\theta = \frac{1}{2}\left(\theta_{n,lim.case\,1} + \theta_{n,lim.\ case\,2}\right) = 4.3\ ML;$$

The error is $\pm\Delta\theta = \frac{1}{2}\left(\theta_{n,lim.case\,1} - \theta_{n,lim.\ case\,2}\right) = \pm 1.2\ ML;$

This way all other coverages of the multilayer sample are calculated (Table 4). This method represents an independent coverage estimation with better results than by extrapolation from the submonolayer regime and can be applied in general to systems which exhibit an XPS-component which changes the binding energy upon contact with the surface.

4.8 Bibliography

References

1. Barth, J. V. Molecular Architectonic on Metal Surfaces. *Annu. Rev. Phys. Chem.* **58**, 375-407 (2007).

2. É cija, D. *et al*. Molecular Conformation, Organizational Chirality, and Iron Metalation of meso-Tetramesitylporphyrins on Copper(100). *J. Phys. Chem. C* **112**, 8988-8994 (2008).

3. Xu, W. *et al*. Probing the Hierarchy of Thymine?Thymine Interactions in Self-Assembled Structures by Manipulation with Scanning Tunneling Microscopy. *Small* **3**, 2011-2014 (2007).

4. Clair, S. *et al*. STM Study of Terephthalic Acid Self-Assembly on Au(111):â€‰ Hydrogen-Bonded Sheets on an Inhomogeneous Substrateâ€ . *J Phys Chem B* **108**, 14585-14590 (2004).

5. Pawin, G. *et al*. A Quantitative Approach to Hydrogen Bonding at a Metal Surface. *J. Am. Chem. Soc.* **129**, 12056-12057 (2007).

6. Kwon, K. *et al*. Unidirectional Adsorbate Motion on a High-Symmetry Surface: "Walking" Molecules Can Stay the Course. *Phys. Rev. Lett.* **95**, 166101 (2005).

7. Schlickum, U. *et al*. Metalâˆ'Organic Honeycomb Nanomeshes with Tunable Cavity Size. *Nano Lett.* **7**, 3813-3817 (2007).

8. Pawin, G. *et al*. A Surface Coordination Network Based on Substrate-Derived Metal Adatoms with Local Charge Excess. *Angewandte Chemie International Edition* **47**, 8442-8445 (2008).

9. Stepanow, S. *et al*. Steering molecular organization and host-guest interactions using two-dimensional nanoporous coordination systems. *Nat Mater* **3**, 229-233 (2004).

10. Tait, S. L. *et al*. One-Dimensional Self-Assembled Molecular Chains on Cu(100): Interplay between Surface-Assisted Coordination Chemistry and Substrate Commensurability. *J. Phys. Chem. C* **111**, 10982-10987 (2007).

11. Trelka, M. *et al*. Surface assembly of porphyrin nanorods with one-dimensional zinc-oxygen spinal cords. *CrystEngComm* **13**, 5591-5595 (2011).

12. Gutzler, R. *et al*. Surface mediated synthesis of 2D covalent organic frameworks: 1,3,5-tris(4-bromophenyl)benzene on graphite(001), Cu(111), and Ag(110). *Chem. Commun.*, 4456-4458 (2009).

13. Grill, L. *et al*. Nano-architectures by covalent assembly of molecular building blocks. *Nat Nano* **2**, 687-691 (2007).

14. Zwaneveld, N. A. A. *et al*. Organized Formation of 2D Extended Covalent Organic Frameworks at Surfaces. *J. Am. Chem. Soc.* **130**, 6678-6679 (2008).

15. Matena, M., Riehm, T., Stöhr, M., Jung, T. & Gade, L. Transforming Surface Coordination Polymers into Covalent Surface Polymers: Linked Polycondensed Aromatics through

Oligomerization of N-Heterocyclic Carbene Intermediates. *Angewandte Chemie* **120**, 2448-2451 (2008).

16. Cai, J. *et al*. Atomically precise bottom-up fabrication of graphene nanoribbons. *Nature* **466**, 470-473 (2010).

17. Gourdon, A. On-Surface Covalent Coupling in Ultrahigh Vacuum. *Angewandte Chemie International Edition* **47**, 6950-6953 (2008).

18. Martin, N., Segura, J. L. & Seoane, C. Design and synthesis of TCNQ and DCNQI type electron acceptor molecules as precursors for 'organic metals'. *J. Mater. Chem.* **7**, 1661-1676 (1997).

19. Viruela, R., Viruela, P. M., Orti, E. & Martín, N. Molecular and electronic structure of a largely extended tetracyanoquinodimethane. *Synth. Met.* **70**, 1031-1032 (1995).

20. Gomez, R., Seoane, C. & Segura, J. L. The first two decades of a versatile electron acceptor building block: 11,11,12,12-tetracyano-9,10-anthraquinodimethane (TCAQ). *Chem. Soc. Rev.* **36**, 1305-1322 (2007).

21. Viruela, R., Viruela, P. M., Orti, E. & Martín, N. Molecular and electronic structure of a largely extended tetracyanoquinodimethane. *Synth. Met.* **70**, 1031-1032 (1995).

22. Tseng, T. *et al*. Charge-transfer-induced structural rearrangements at both sides of organic/metal interfaces. *Nat Chem* **2**, 374-379 (2010).

23. Lindquist, J. M. & Hemminger, J. C. High energy resolution x-ray photoelectron spectroscopy studies of tetracyanoquinodimethane charge transfer complexes with copper, nickel, and lithium. *Chemistry of Materials* **1**, 72-78 (1989).

24. Persson, P., Lunell, S., Szöke, A., Ziaja, B. & Hajdu, J. Shake-up and shake-off excitations with associated electron losses in X-ray studies of proteins. *Protein Sci* **10**, 2480-2484 (2001).

25. Wells, S. K., Giergiel, J., Land, T. A., Lindquist, J. M. & Hemminger, J. C. Beam-induced modifications of TCNQ multilayers. *Surf. Sci.* **257**, 129-145 (1991).

26. Yeh, J. J. & Lindau, I. Atomic subshell photoionization cross sections and asymmetry parameters: 1 < Z < 103. *Atomic Data and Nuclear Data Tables* **32**, 1-155 (1985).

27. Yeh, J. -. Atomic calculation of photoionization cross-sections and asymmetry parameters. *Rapid Communications in Mass Spectrometry* **8**, 579-579 (1994).

5 DCNQI on Cu(100)

5.1 Motivation

Dicyano-*p*-quinonediimine (DCNQI) is an electron acceptor molecule as strong as TCNQ[1], and it belongs to a family of molecules which form a large number of charge transfer and coordination compounds[2] exhibiting metallic conductivity[3] and interesting magnetic[4, 5] and optical properties. The study of such organic materials offers wealth of information on fundamental solid state chemistry and physics, relevant for far reaching technological applications within molecular electronic devices[6].

Additionally, the goal of further miniaturization proposes applications which use single molecules adsorbed on surfaces[7] to act, for example, as switches[8, 9] for logical operations[10] and for data storage. Therefore, a transition between two thermally stable and preferably reversible states with a measurable difference in its physical properties is required. A molecule with two isomeric forms provides all that, if an external stimulus can drive the isomerization reaction in the desired direction. For the integration in circuits these molecular switches have to be deposited on a surface and although isomerization reactions are well known in solution, on solid substrates the mixing of the molecular-orbitals with the surface-states can quench excitations which are necessary for the transition from one isomer to the other[11]. Additionally, surfaces play an important role as they can suppress or enable the isomerization for the same molecule on different substrates[12, 13]. Even novel, stable isomers are observed due to the influence of the surface, as in the case of stilbene molecules on Si(100)-2x1[14].

Azobenzene is an important example of a molecule with two isomers but only the trans-form is observed on Cu(110)[15] due to the strong molecule - surface interaction. In contrast, several azobenzene derivatives have been investigated on a variety of surfaces with a successful reversible transition between the trans- and the cis-form. In one of the first STM-studies, the isomerization transition of molecules containing azobenzene was reversibly induced at the liquid/graphite interface by irradiation with UV light[16 and later 17]. Tunneling electrons can also provoke the reversible cis-trans isomerization of azobenzene derivatives on Au(111)[18, 19] and on an ultrathin film of insulating NaCl/Ag(111)[20]. The electric field of a STM junction without tunneling electrons is also able to provide the necessary energy to overcome reversibly the barrier between the two different isomer-states, as in the case of another azobenzene derivative[9]. In a few systems thermal energy has been applied, too, to provoke an isomerization in one direction[13, 21, 22].

In summary, isomerization reactions of azobenzene derivatives have been extensively investigated by STM and sometimes with HREELS on a variety of surfaces with different excitation mechanisms[10], but studies of molecules from a different family are scarce. Up to now only Bis(4,4'-(m,m'-di(dodecyloxy)phenyl)-2,2'-difluoro-1,3,2-dioxaborin)[13], *cis*-1,2-dicyano-1,2-bis(2,4,5-trimethyl-3-thienyl)ethene[23] and two chlorobenzene derivatives have been investigated to our knowledge.

DCNQI derivatives have only been investigated in solution[24] but not on surfaces which motivates therefore detailed studies. We have investigated the DCNQI/Cu(100)-system in a

wide range of substrate temperatures. Depending on the temperature, two different phases of DCNQI appear related to the two isomers of the molecule. We will show that a charge transfer from the surface to the DCNQI-molecules is the reason for a decrease in the transition energy barrier for isomerization. Thus, this is on one hand one of the few molecule-on-surface systems where isomerization due to thermal energy has been studied in detail[13, 21, 22] and on the other hand, reactive surfaces, like Cu(100), are usually not successfully used for molecular switching between isomers. In the majority of the cases, isomer transitions have been observed only on Au(111)[10], which exhibits a smaller reactivity than copper. According to previous work, physisorption and the decoupling of the adsorbates from the substrate were believed to be necessary conditions to observe isomerization reactions[25]. In the case of DCNQI/Cu(100), the reactivity of the surface and the strong adsorbate-surface interaction, which results in charge transfer to the molecules is identified as the reason for the lowering of the transition barrier and thus of the observed isomerisation by thermal energy at 245 K. This counter-intuitive result opens a new perspective for the role of the substrate in isomerization reactions.

5.2 Experimental and computational details

DCNQI molecules have been evaporated with a resistively heated glass crucible at temperatures between 350 K and 380 K, onto the surface of a Cu(100) single crystal held at temperatures between 145 K and RT at a deposition rate between 0.01 and 0.03 ML per minute.

DFT calculations were done for the assembly of DCNQI molecules in gas phase without the surface in collaboration with the theoretical group of Professor Fernando Martín of the “Universidad Autónoma de Madrid”.

5.3 Description of the DCNQI molecule

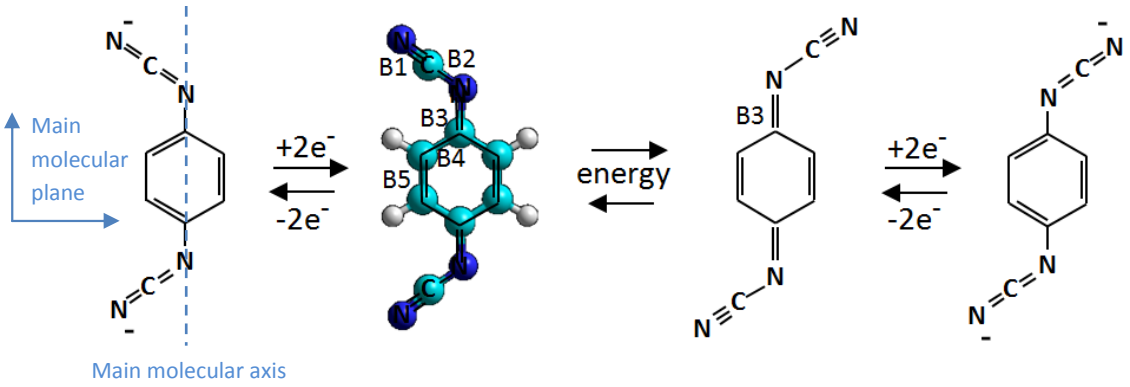

Figure 1: Chemical structure of cis- and trans-DCNQI under reduction: Additional electrons are delocalized along the cyano-imine groups with the effect of aromatization of the quinoid central carbon ring and the reduction of the double bond character of B3 to a more σ-type bond which is thus more flexible in turns of rotation..

DCNQI consists of 8 carbon, 4 hydrogen and 4 nitrogen atoms (Fig. 1). The latter render the molecule an electron acceptor (similar to the TCNQ- and TCPQ-cases). In gas-phase the neutral molecule adopts a flat geometry with a quinoid carbon ring. In the neutral form the bond B3 with its double bond character exhibits a high energy barrier for the transition of one cyano group from one side of the main axis to the other. Therefore two stable isomers of DCNQI exist: while the trans-form exhibits two cyano groups on opposite sides of the main molecular axis, in the cis-isomer these functional groups are on the same side (Fig. 1). The isomerization reaction occurs when one of the two functional groups changes from one side of the main molecular axis to the other. The transition mechanism among imine systems can be a pure inversion, a rotation or an intermediate mechanism between the two[26]. The inversion reaction in a simple picture is the rotation of the cyano group in the plane of the quinoid ring (main molecular plane) around the imine nitrogen atom (Fig. 2) until a mirror image of the original side group with respect to the main molecular axis is created. The rotation mechanism is the rotation of the cyano group out of the main plane around the main molecular axis until it lies again within the main plane. In literature, calculations in solution and gas phase for DCNQI derivatives identify an inversion reaction at the imine nitrogen as the isomerization mechanism[24, 27]. Experimental data reveal that for DCNQI, and also for other DCNQI-substituted molecules[24] the trans-form is the more stable isomer in gas phase and solution[28], which is consistent with our calculations for DCNQI in gas phase, presented later in this chapter. The reason for the higher stability of the trans-configuration is the reduction in the dipole interaction of the two cyano groups[28].

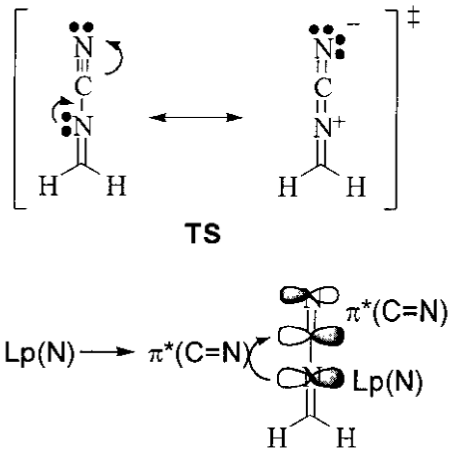

Figure 2[taken from 24]: Transition state in the inversion mechanism of *N*-cyanomethanimine involving the LUMO of the functional group. The isomerization in this molecule takes place nearly exclusively by this mechanism of an inversion which be considered as an in plane rotation of the cyano group around the imine nitrogen atom.

As mentioned above, DCNQI is a strong organic acceptor and an additional negative charge will be hosted along the cyano-imine groups similar to the case of TCNQ and TCPQ. The electrostatic potential maps for the neutral and the dianion of both isomers help to visualize the effect of a negative extra charge. At the bottom row of Table 1 and Table 2 we show constant-charge isosurfaces for neutral ($DCNQI^0$) and double negatively charged species ($DCNQI^{-2}$) of the trans- and the cis-form of DCNQI on top of which information about the electrostatic potential has been color coded, in such a way that blue areas indicate positive and red ones negative potential (Table 1 and 2, bottom line). The blue color located on the central carbon ring of the neutral molecules appears less intense compared to the dianion, which represents a reduction of positive potential, while the red color on the nitrogen atoms is extended in the negatively charged DCNQI-forms. Thus, an additional charge increases the electron concentration around the nitrogen atoms and also on the central carbon rings, following the spatial distribution of the LUMO orbital of the neutral $DCNQI^0$ (Table 1 and 2). With respect to the bond configuration, the effect of an additional charge is similar to the cases of TCNQ and TCPQ, the quinoid rings of both isomers convert into an aromatic moiety and the π-bond B3 adopts a more σ-type character becoming therefore more flexible (Fig. 1).

	HOMO: -10.1 eV	LUMO (empty): -2.63 eV
	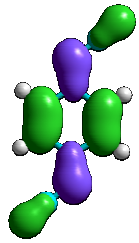	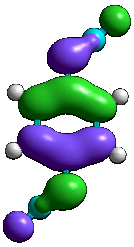
Electrostatic potential projected onto charge density isosurface	$DCNQI^{0}$: 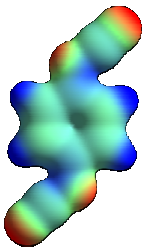	$DCNQI^{-2}$: 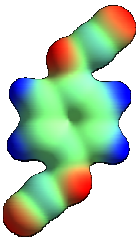

Table 1: Two different charge states of the trans-DCNQI molecule are represented with its occupied and unoccupied molecular orbitals. Large parts of the density of an extra charge on the molecule will be located at the nitrogen atoms of the functional groups attached to the central carbon ring. This can be seen in the electrostatic potential projected onto a charge density isosurface in the last line.

	HOMO: -10.1 eV	LUMO (empty): -2.63 eV
	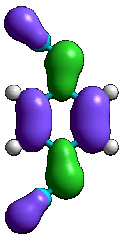	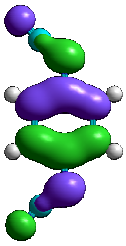
Electrostatic potential projected onto charge density isosurface	$DCNQI^{0}$: 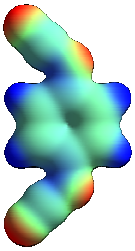	$DCNQI^{2-}$: 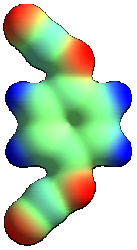

Table 2: Two different charge states of the cis-DCNQI molecule are represented with its occupied and unoccupied molecular orbitals. As in Table 1 large parts of the density of an extra charge on the molecule will be located at the nitrogen atoms of the functional groups attached to the central carbon ring. This is reflected in the electrostatic potential projected onto a charge density isosurface in the last line.

5.4 Adsorption of DCNQI on Cu(100) – Self assembly of DCNQI

5.4.1 STM Results

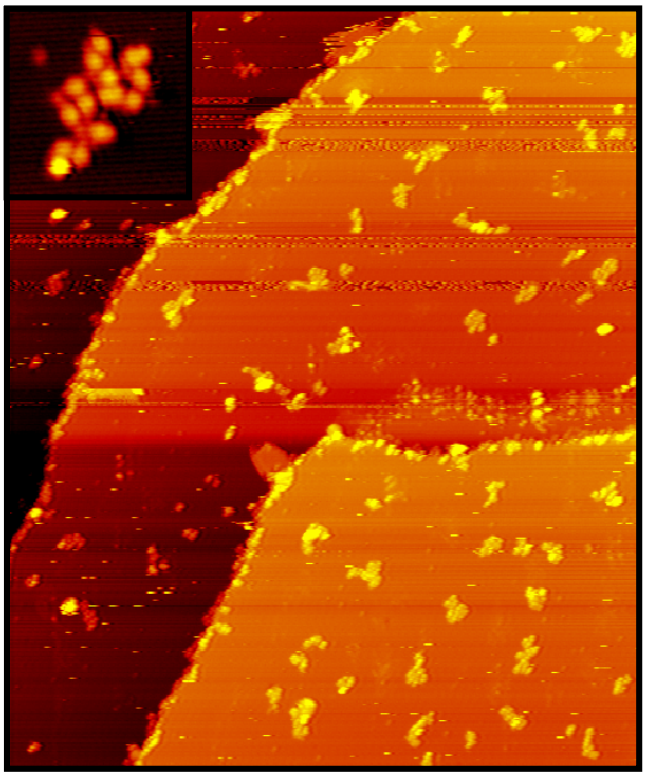

Figure 3: STM image of 0.03 ML DCNQI grown at 145 K on Cu(100) imaged at 158 K (1250 Å x 1500 Å, -2.1 V, -0.18 nA): The step edges are nearly fully covered, small disordered islands are found on the terraces which evidences the high mobility of the molecules on this substrate. The inset shows a close-up of a cluster of molecules (imaged at 143 K, 77 Å x 80 Å, -1.7 V, -0.26 nA).

After depositing 0.03 ML of DCNQI on a Cu(100) single crystal held between 145 K – 160 K the step edges are nearly fully covered and small clusters with up to 30 molecules with an average distance of 130 ± 30 Å can be found on the terraces (Fig. 3). Both observations evidence some mobility of DCNQI/Cu(100) at this temperature. Increasing the substrate temperature above 160 K, leads to the formation of short, elongated 1D-structures consisting of up to 7 molecular units, in coexistence with the 2-dimensional disordered clusters (Fig. 4). Higher temperatures promote the growth of more 1D-chains at the expense of the clusters until at 235 K 2D-islands with a high degree of order appear (Fig. 5), while the short chains disappear. These big DCNQI-islands (denominated "LT-Phase") with long range order exhibit a unit cell which in matrix notation can be defined as $\begin{pmatrix} b_1 \\ b_2 \end{pmatrix} = \begin{pmatrix} 4 & 3 \\ -3 & -4 \end{pmatrix} \begin{pmatrix} a_1 \\ a_2 \end{pmatrix}$ (Fig. 5 and 7). The pure LT-Phase is observed in all occasions only in a small sample temperature range and increasing further the temperature causes these islands to reorganize their structure in a 1.39 times denser assembly (denominated "RT-Phase") with a new unit cell: $\begin{pmatrix} b_1' \\ b_2' \end{pmatrix} = \begin{pmatrix} 0 & 6 \\ 6 & 0 \end{pmatrix} \begin{pmatrix} a_1 \\ a_2 \end{pmatrix}$ (Fig. 6 and 7). The sample temperature for the start of the formation of the RT-Phase is 245 ± 5 K. Both phases coexist (Fig. 8) until a sample temperature of 255 ± 5 K from where the transition of the LT- to the RT-

phase is complete. The RT-phase islands are stable up to at least 440 ± 20 K. STM-movies at the transition temperature show that the constituents of the rectangular LT-phase islands gain mobility and single molecular units start to detach and disappear. This leads to a reduction of the island size until it disappears while at the same time the RT-phase islands grow (Fig. 9). Higher sample temperatures increase the average size of the RT-islands while its number is reduced due to the process of Oswald-ripening (Fig. 10).

The shape of isolated molecules is that of an elongated protrusion of 11 Å x 7 Å. DCNQI units within the LT- and RT-phase islands, as will be discussed later, exhibit a somewhat different appearance, but with similar dimensions. The molecular shapes of DCNQI are compatible with an adsorption geometry where the central carbon ring is parallel to the surface, as observed also for TCNQ and TCPQ on Cu(100).

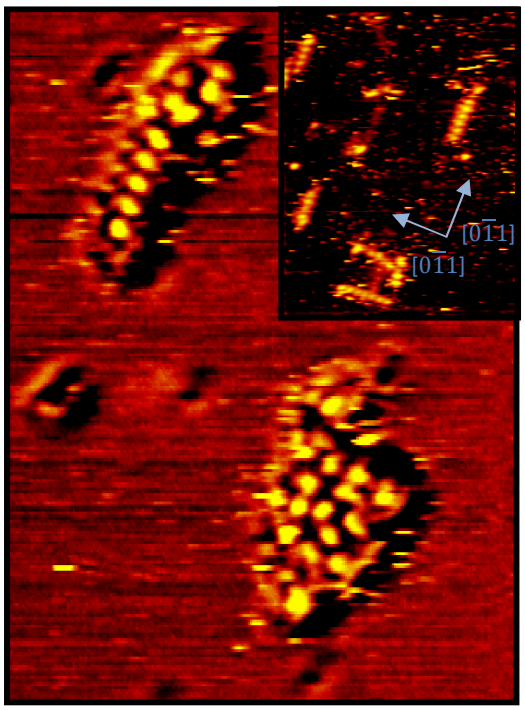

Figure 4: STM image of 0.03 ML DCNQI grown at 145 K on Cu(100) imaged at 189 K (160 Å x 220 Å, -1.3 V, -0.13 nA): Next to the disordered island chain-like one-dimensional (1D) structure start to appear aligned along the high symmetry directions of the substrate. The inset shows a sample region with more DCNQI chains in both high symmetry directions of Cu(100) at a slightly higher temperature while fewer cluster remain (imaged at 198 K, 77 Å x 80 Å, -1.7 V, -0.26 nA).

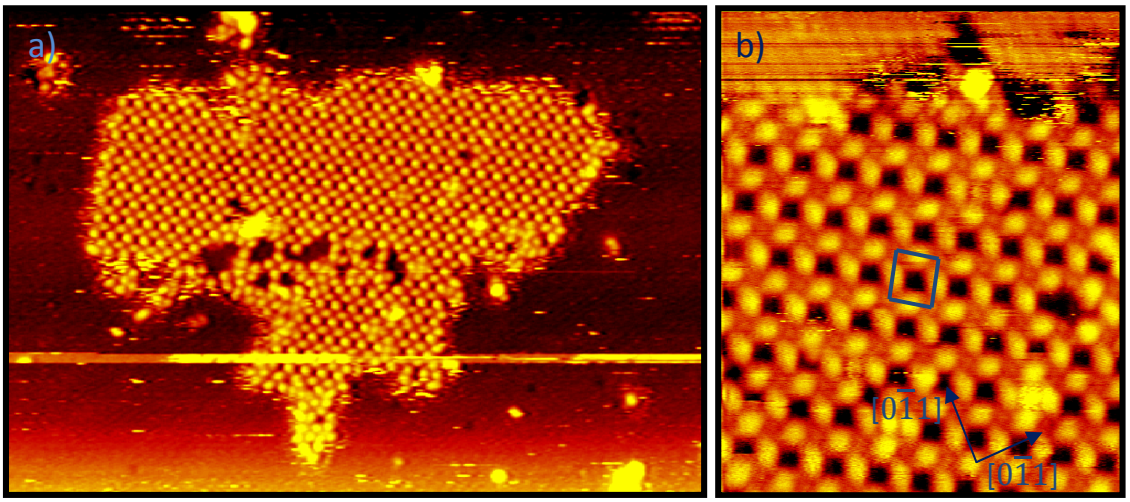

Figure 5: STM images of 0.03 ML DCNQI grown at 145 K on Cu(100) imaged at 255 K (**a)**: 580 Å x 400 Å, -1.5 V, -0.2 nA, **b)** 130 Å x 150 Å, -1.0, -0.21 nA): From a substrate temperature of 245 K on bigger ordered islands appear, called "LT-Phase", with the square unit cell shown in figure b). The substrate close-pack directions are indicated.

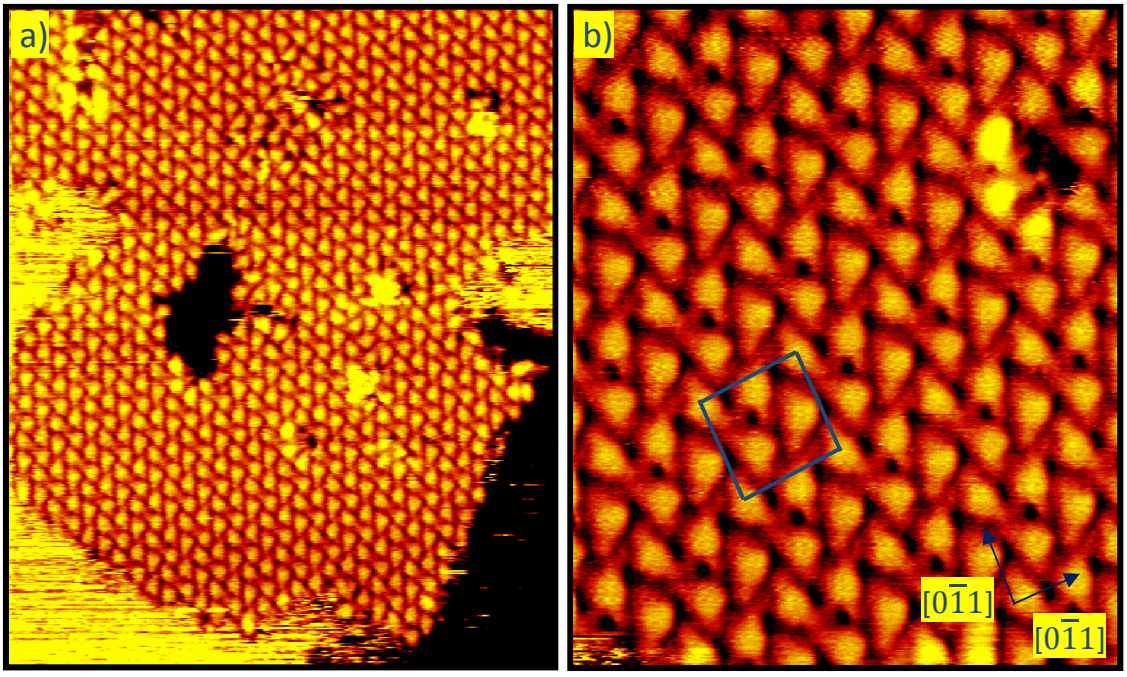

Figure 6: STM images of 0.23 ML DCNQI grown at RT on Cu(100) imaged at RT (**a)**: 250 Å x 300 Å, -1.24 V, -0.43 nA, **b)** 90 Å x 100 Å, -1.24, -0.48 nA: The new RT-phase appears from a substrate temperature of 245 K on. Until 255 K both phases can be found, above that temperature the LT-phase disappears completely. The unit cell and the substrate high symmetry directions are indicated in b).

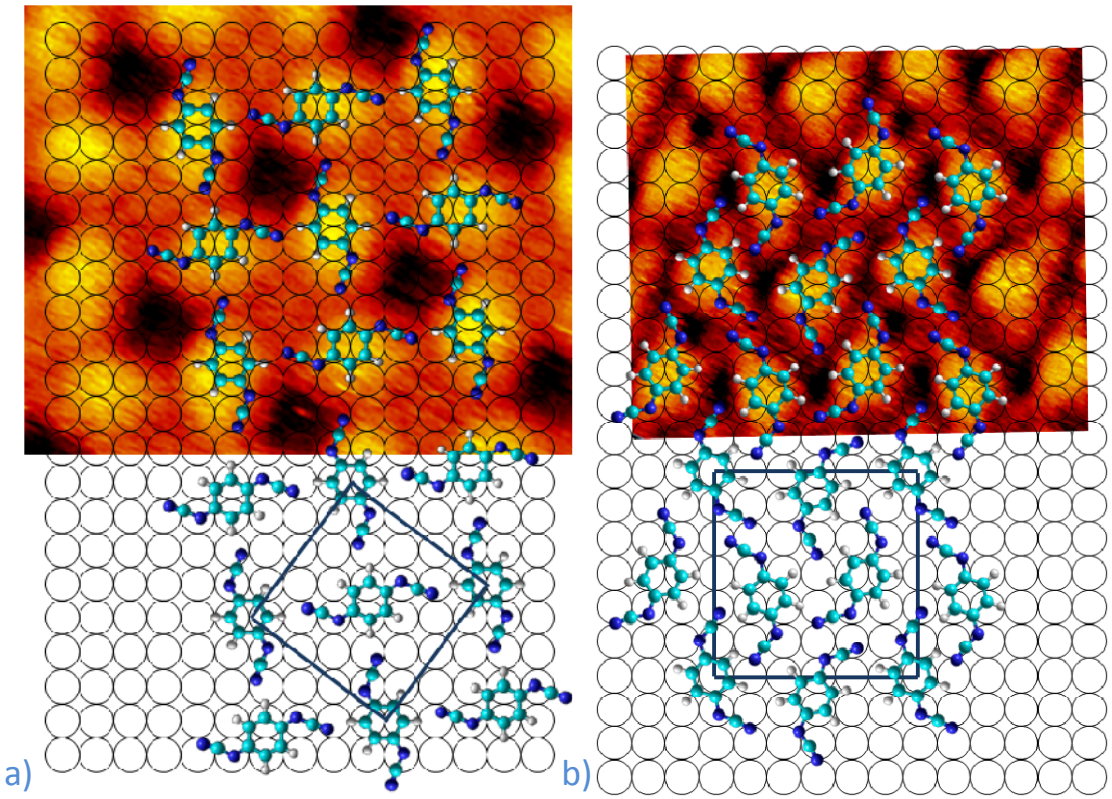

Figure 7: STM images of the two different DCNQI-phases on Cu(100) with assembly model and unit cell deduced from the experimental measures (details in the text) **a)**: LT-phase island of DCNQI imaged at 236 K (25 Å x 28 Å, -1.0 V, -0.21 nA)), **b)** 0.23 ML DCNQI grown at RT on Cu(100) imaged at RT 90 Å x 100 Å, -1.24, -0.48 nA

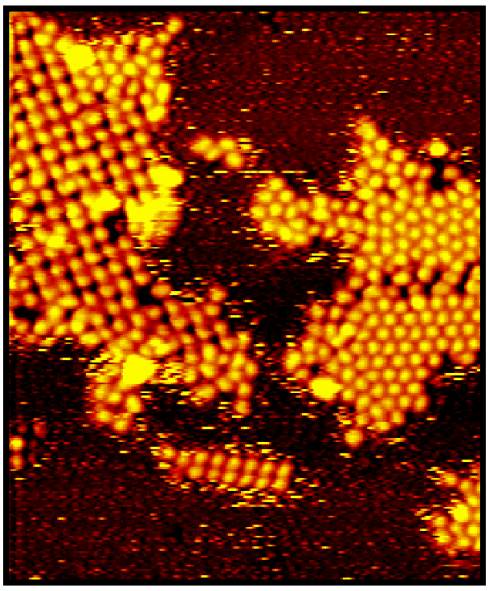

Figure 8: STM images of 0.3 ML DCNQI grown at 240 K on Cu(100) imaged at 250 K (250 Å x 300 Å, -1.8 V, -0.22 nA): The LT-phase can still be observed on the left side while on the ride side the RT-phase is already present. Both island types are found simultaneously until a sample temperature of 255 ± 5 K.

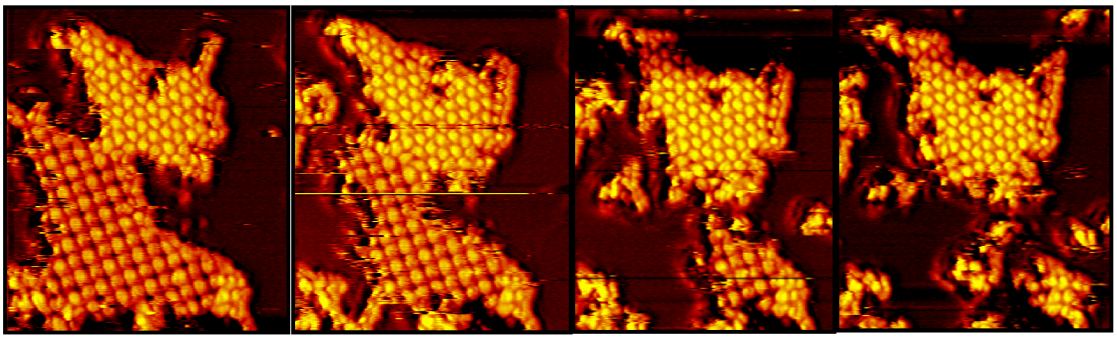

Figure 9: Sequence of STM images (every 40 s) of 0.2 ML DCNQI grown at 220 K on Cu(100) imaged at 252 K (200 Å x 220 Å, -1.7 V, -0.23 nA): The LT-phase of DCNQI in the lower part of the images disappears slowly while the RT-phase (upper part) maintains basically its size.

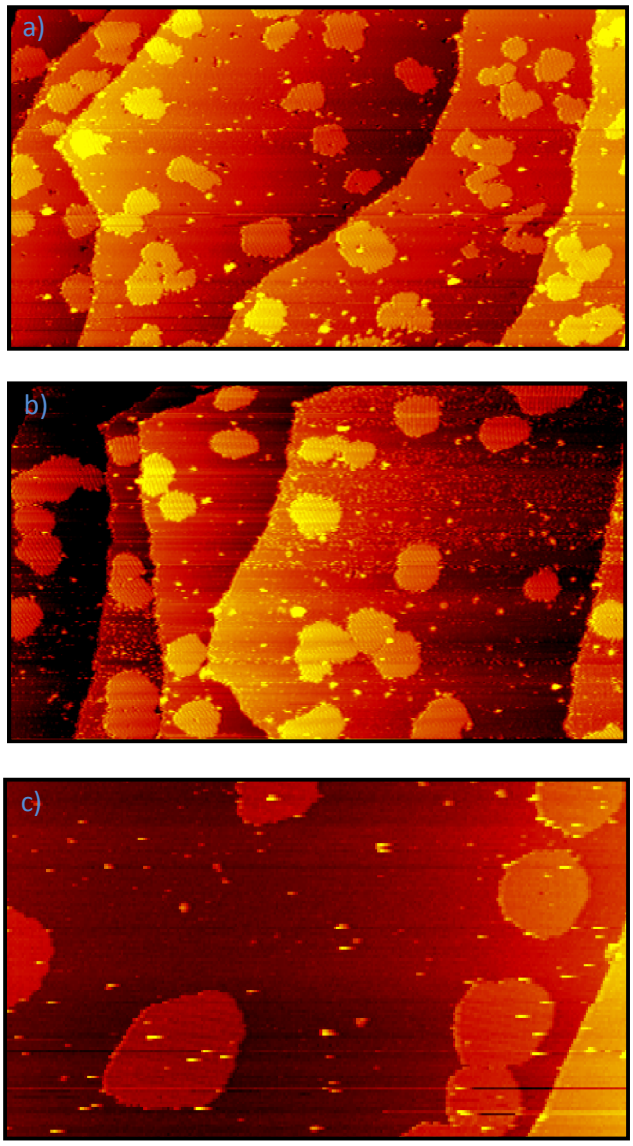

Figure 10: Sequence of annealed STM images of 0.2 ML DCNQI in the same scale, grown at 220 K on Cu(100), **a)** annealed to RT, imaged at 265 K (2500 Å x 1370 Å, -2.4 V, -0.23 nA), **b)** annealed to 360 K, imaged at 268 K (2500 Å x 1440 Å, -1.6 V, -0.25 nA), **c)** annealed to 420 K, imaged at 274 K (2500 Å x 1440 Å, -2.9 V, -0.03 nA): The growth of the average island size with increasing annealing temperature can clearly be observed as a result of the effect of Oswald ripening.

5.4.2 Structural conclusions of the STM Results

We propose based on three structural arguments that only the trans-form of DCNQI is observed on the Cu(100)-surface in both, the single units and the LT-island phase, when the molecule is deposited on the substrate held within the previously mentioned temperature range (145 -245 K). First, the unit cell of the LT-phase islands of DCNQI exhibits a C_2-symmetry, which implies at least the same point symmetry for the single molecular units. Then the shape of isolated DCNQI units on Cu(100) and the appearance of single molecules within the LT-phase islands is elongated and seems also symmetric to an in-plane rotation of 180 ° (Fig. 5 b). Third, calculations show (described in the following) that trans-DCNQI exhibits a higher binding energy in gas phase than the cis-form of the molecule. The experimentally found unit cell in the assembly of DCNQI and the shape of the single molecules in islands below 245 K can then be well understood (Fig. 7 a). STM simulated images based on gas phase calculated images (like in Chapter 4) corroborate this result (Fig. 11). Two sets of simulated images for the trans-isomer have been calculated to account for the possible charge states ($DCNQI^0$ or $DCNQI^{-2}$). For each set two images with the same parameters as in chapter 4 (HOMO plus HOMO-1 depicted with a contour value of 10^{-5} $Å^{-3}$) have been chosen (Fig. 12 a and b). All the simulated STM images of the trans-DCNQI resemble very well the molecular shape in the LT-phase islands and fit also well in the unit cell (Fig. 12 a).

The unit cell of the RT-islands exhibits no symmetry and is thus lower than the C_2-symmetry found in the LT-phase. This is not necessarily incompatible with the symmetry of the trans-isomer of DCNQI, but the shape of the single units in the RT-islands is different to the molecules in the LT-phase and it is not symmetric (Fig. 6). The trans-isomer therefore does neither reproduce well the shape of the single molecules in the RT-islands nor the unit cell in the assembly (Fig. 7). It is therefore excluded to explain the RT-island assembly The cis-isomer instead resembles well the shape of the individual molecules and the experimental unit cell of the RT-phase (Fig. 7 b) which is suggested by the two simulated STM images (Fig. 11 e and f) with an excellent reproduction of the assembly (Fig. 12 b). We conclude therefore that the RT-islands consist only of cis-DCNQI molecules.

An explanation for the different appearances is that the DCNQI-molecules adsorb on the Cu(100)-surface below a substrate temperature of 245 K in the trans-form and assemble in the LT-phase at about 235 K, where enough thermal energy is present for the necessary mobility. STM movies (Fig. 9) reveal that increasing further the substrate temperature over 245 K leads to the disintegration of the LT-phase islands and to the formation of the RT-islands which are stable up to 440K. An isomerization reaction taking place while the molecules detach from the LT-islands and reattach to the RT-structures at about 245 K explains the new shape of the molecules and the new assembly type in islands. The average island distance l and the flux of molecules *F* during the deposition are experimental values which provide an estimation of the average time t a DCNQI molecule diffuses over the surface before it is again incorporated into an island. The average diffusion time t is related to the diffusion coefficient *D* by:

$$t \approx \frac{l^2}{D}$$

The saturation island density reflects the mean free path for monomer diffusion and allows estimating the diffusion coefficient D[29]:

$$D \approx \frac{l^6}{\ln(l^2)} F \approx (5.9 \pm 5.8) \cdot 10^6 s$$

At a deposition temperature of 240 ± 5 K (before the LT-islands begin to disintegrate) the average island separation l = 142 ± 48 Å and the flux F = (2.0 ± 0.6)·10^{-6} Å^2·s^{-1} lead to an estimation of the time a molecule diffuses before finding an island:

$$t \approx \frac{\ln(l^2)}{l^4 F} \approx (3.8 \pm 3.5) \cdot 10^{-2} s$$

During this time the molecule diffuses freely without being bound in an assembly and this situation allows the isomerization reactions, since we observe the two different forms of DCNQI. Therefore a number of reversible trans-cis transitions will have occurred before a diffusing molecule meets an island which can be from the two observed phases. Therefore four different scenarios after diffusion over the terraces can occur:

1. The molecule interacts in the trans-form with an LT-island and may attach for a short time again, but the experimentally observed disintegration shows that this situation is not stable at the transition temperature and the DCNQI molecule will detach again.

2. The molecule meets in the trans-form a RT-island and cannot be integrated due to its different conformation with the consequence of a reduced time of stay and a subsequent detachment because mixed phases are never observed experimentally.

3. The molecule finds in the cis-form of DCNQI a LT-island. The interaction must be low because, again as in case 2., an island consisting of two types of isomers are not observed, and therefore the molecule will continue diffusing after probably a very short stay-time.

4. The molecule interacts in the cis-form with a RT-phase island of DCNQI. A stronger attractive intermolecular interaction than in the LT-islands stabilizes the molecule in the denser RT-phase, as will be shown in our gas phase DFT calculations in the following, preventing also further isomerization reactions, so that the stay time is much larger.

All scenarios together lead to the growth of the RT-islands and the disappearance of the LT-phase, as experimentally observed. The mechanism is based on the detachment, the isomerization during diffusion and a final stronger interaction of the molecule with an RT-island in the final cis-isomer form.

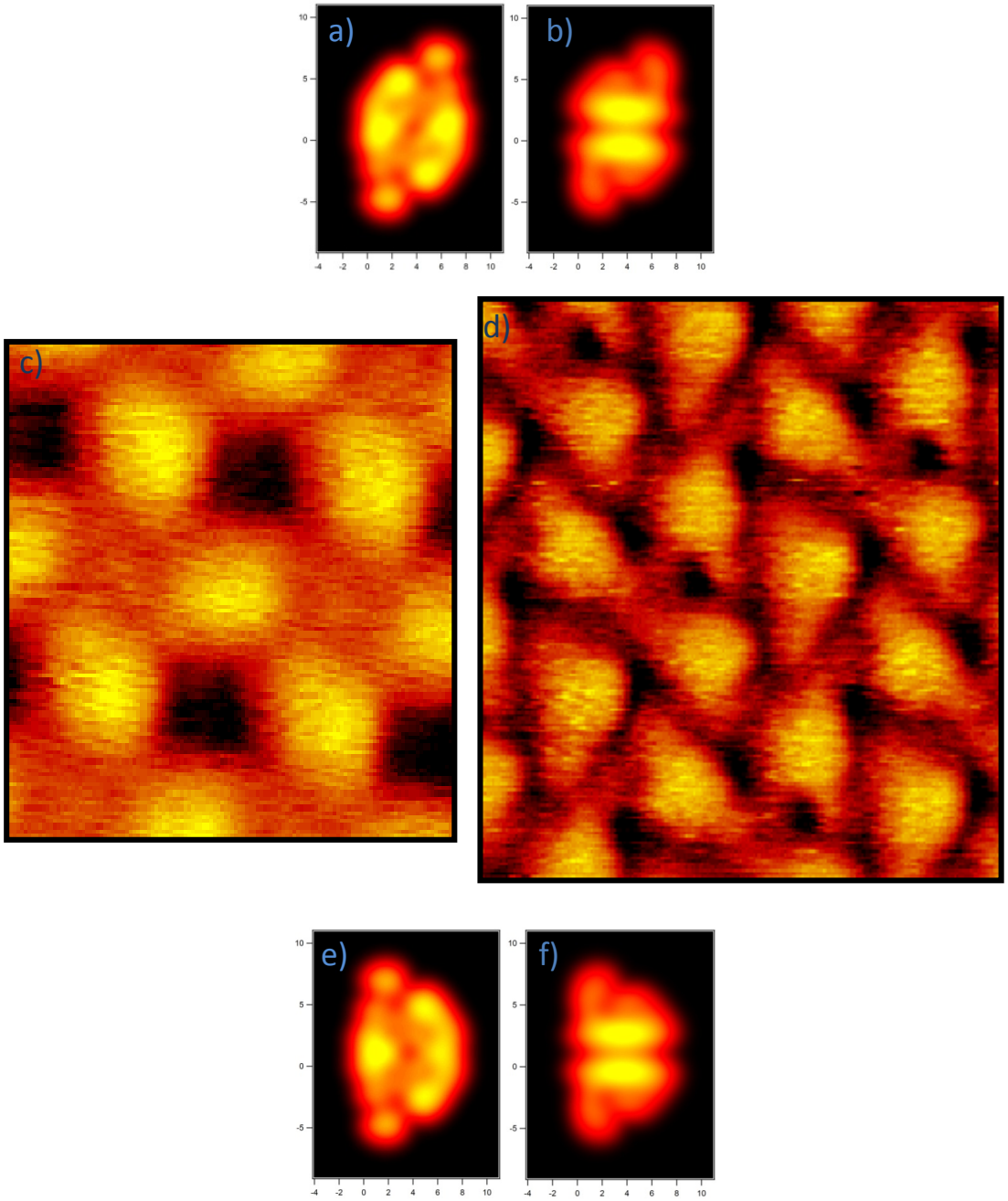

Figure 11: Comparison of experimental STM-images with simulated ones based on the neutral and charged models of the two isomers of DCNQI. The simulated images of the trans-forms, **a)** neutral- and **b)** dianion-form, resemble very well the point symmetric appearance of an isolated and a single DCNQI-molecule within the LT-phase arrangement (an entire unit cell is shown in **c):** LT-phase of DCNQI imaged at 236 K (25 Å x 28 Å, -1.0 V, -0.21 nA). This reflects a temperature range of 145 K to 245 K. **d):** unit cell of RT-phase of DCNQI imaged at RT (28 Å x 32 Å, -1.24 V, -0.48 nA)). The changed appearance of the single molecules is well represented by the simulations based on the cis-isomers **e)** (neutral) and **f)** (dianion) which fit in accordance with the orientation and size perfectly the RT-phase islands above 245 K.

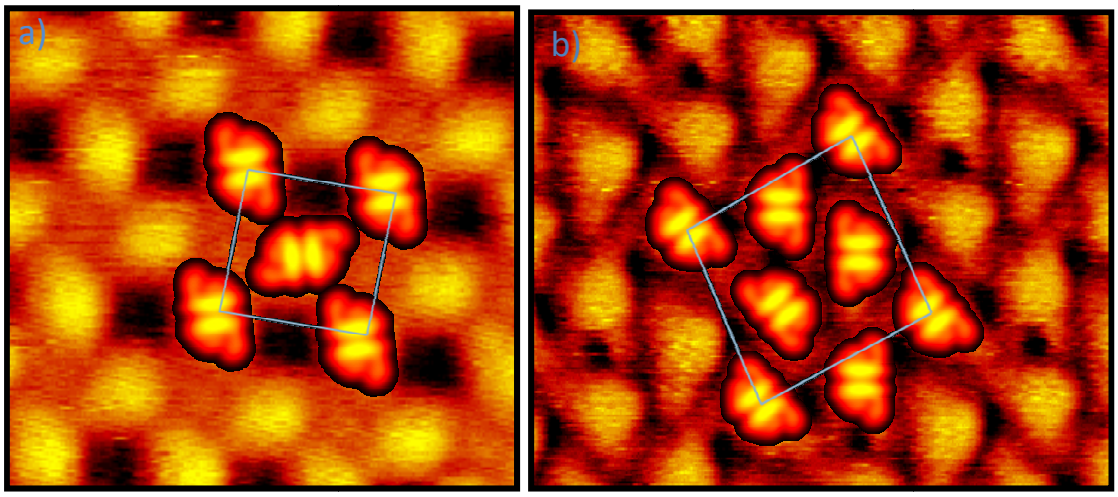

Figure 12: Experimental STM-images overlaid with simulated ones based on the charged model of DCNQI. The trans-form resembles very well the LT-phase arrangement (**a)** imaged at 236 K (25 Å x 28 Å, -1.0 V, -0.21 nA)) while the cis-isomer is in high accordance with the LT-phase of DCNQI, **b)** DCNQI imaged at RT (28 Å x 32 Å, -1.24 V, -0.48 nA)).

5.4.3 DFT gas phase calculations

In order to find out about the forces that stabilize the islands, we collaborated with the theoretical group of Prof. Martín and carried out DFT calculations without the substrate. Different initial configurations of DCNQI molecules in a periodic unit cell of both observed assemblies without the Cu-surface were tried and the obtained theoretical assembly model corresponds to the minimum of all the explored configurations. The position of the molecules in the minimum energy configuration is consistent with the experimental distances and orientations. Each molecule in the LT-phase forms four weak hydrogen bonds between the nitrogen atoms of each cyano group and a hydrogen atom from the central ring of an adjacent trans-DCNQI molecule (Fig. 13). The calculated binding energy per molecule is 0.18 eV. The arrangement changes in the RT-phase, as seen before, and the number of weak H-bonds per unit cell doubles to eight. Thus the binding energy is slightly higher with 0.22 eV per cis-DCNQI molecule (Fig. 14).

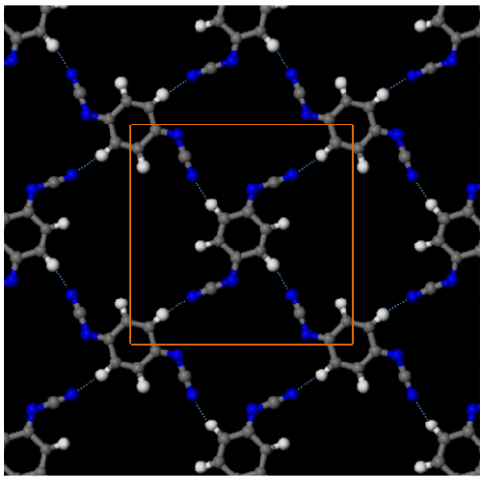

Figure 13: Result of DFT-calculations for the LT-islands of DCNQI in gas phase: Every nitrogen atom from a cyano group binds to a hydrogen atom from an adjacent molecule and forms thus four weak hydrogen bonds. The bond energy is 0.18 eV per molecule. The unit cell of the experimental image is very well reproduced.

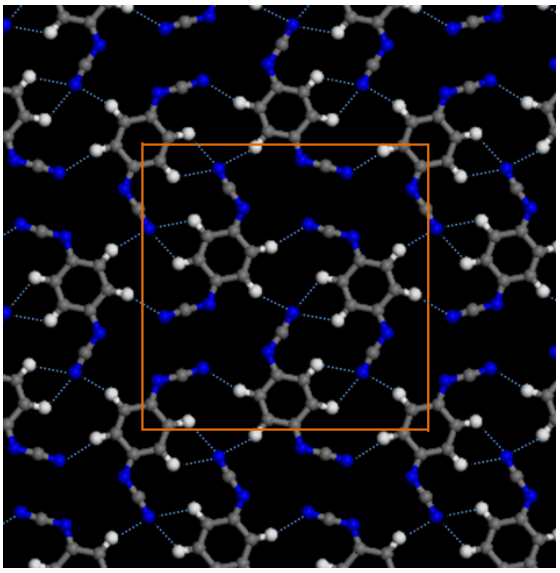

Figure 14: Results of DFT-calculations for the RT-islands of DCNQI in gas phase: Nitrogen atoms from the cyano groups bind to hydrogen atoms from adjacent molecules and form thus eight weak hydrogen bonds. The bond energy is 0.22 eV per molecule. The unit cell of the experimental RT-islands is very well reproduced.

5.4.4 Isomerization reaction and the role of charge transfer

In order to take into account the very likely reduction of DCNQI/Cu(100) due to the expected charge transfer from the surface, the transition states (TS) of the isomerization from the trans-DCNQI to the cis-form have been calculated in gas phase for three different charge states of DCNQI; the neutral, the single negatively charged and the dianion form of DCNQI (Fig. 15). The geometry of the TS is depicted in the center part of the three charge states of the molecule between the two isomers in Figure 15 a), b) and c). The cyano group of the TS^0 of the neutral DCNQI molecule reveals inversion around the iminic nitrogen atom as the isomerization mechanism. An alternative transition structure involving an out of plane rotation of the

functional group was not found for the neutral DCNQI molecule which is consistent with literature results of neutral DCNQI derivatives[28, 30, 31, 32 and 33]. The total energy of the TS^0 is 0.66 eV and thus comparable to experimental and theoretical values of several neutral DCNQI derivatives in gas phase and in solution which lie between 0.57 and 0.6 eV[24].

While a trans-DCNQI molecule is diffusing, it must be able to isomerize in order to meet a RT-island in the cis-form. The average time for an isomerisation t_{iso} event depends on the energy barrier between the two possible states and can be estimated at the transition temperature (245 K) based on the transition state theory[34, 35] and assuming a typical attempt frequency[29] of $\nu_0 = 10^{12}\ s^{-1}$ (K_b is the Boltzmann constant):

$$\nu = \nu_0 \cdot e^{-\frac{\Delta E_{trans-cis}}{k_b T}} \rightarrow t_{iso} = \frac{1}{\nu_0} \cdot e^{\frac{\Delta E_{trans-cis}}{k_b T}}$$

For the neutral molecule the energy barrier is $\Delta E_{trans-cis} = 0.66\ eV$ and $t_{iso} \approx 40\ s$ is the time necessary for a transition event. This is three orders of magnitude larger than the time a molecule diffuses on the terraces without meeting any island ($t \approx (3.8 \pm 3.5) \cdot 10^{-2} s$). We thus conclude that a neutral molecule would not have the time to isomerize to the cis configuration, before it finds one of the RT-islands contrary to our observation of RT-islands consisting only of the cis-isomer of DCNQI. A charge transfer seems therefore very likely, especially taking into account that DCNQI is an electron acceptor molecule like TCNQ, TCPQ and TCTQ. An extra charge actually does change the time necessary for an isomerization event, as will be shown in the following. As mentioned in the description of the molecule, an additional charge leads to an aromatization of the planar central carbon and the carbon-imine double bond (B3) adopts a more single character, similar to a σ-bond. As a consequence, the conformational effect of the extra charges allows the cyano-imine groups to rotate easier around bond B3. The isomerization of the anionic-species, with the cyano-imine group in the TS^{-1} exhibiting an angle out of the molecular plane (Fig. 15 b), includes rotation around bond B3 as part of the transition mechanism. An isomerization is thus more likely than for the neutral DCNQI molecule and indeed the energy barrier is slightly lower with 0.63 eV. This trend continues in the transition of the dianion form where the TS^{-2} reveals a cyano-imine group with an even larger angle out of the carbon ring plane (Fig 15 c). The total energy of the TS^{-2} is only 0.26 eV larger than the trans-isomer of $DCNQI^{-2}$ and a rotation of the cyano-imine group plays an important part in the mechanism of isomerization. That is shown also by the calculation of a forced transition by rotation of only the cyano-imine group around bond B3. Starting from the trans-form of the differently charged DCNQI molecules, one cyano-imine group on a single molecule is forced to rotate around the bond B3 out of the main molecular plane over a range of 180 °. At every new rotation position (13 in total) of the cyano-imine group, the molecule is relaxed with the rotation angle of this cyano-imine group fixed and the total binding energy is calculated. This way the total energy, dependent on the forced rotation angle of the cyano-imine group, grows until 90 ° and decreases before it reaches the total energy value of the cis-form of DCNQI (Fig. 16). In the case of the neutral molecule the height of the energy barrier is 0.96 eV and thus larger than in the previous calculation of the transition pathway. This is expected, as the mechanism for the isomerization is an inversion, consistent with literature[27], and not a rotation of the cyano-imine group. The dianion form of DCNQI reveals the same barrier height, 0.26 eV, as in the previously calculated TS^{-2} of the molecule which shows clearly the importance of rotation as part of the transition mechanism in the dianion of DCNQI.

However, for the dianion form of DCNQI, the energy barrier is lowered by charge transfer to $\Delta E_{trans-cis} = 0.26\,eV$ and thus the time for a transition event is estimated to $t_{iso} = 2.3 \cdot 10^{-7}\,s$, which is short enough to overcome the barrier from the trans- to the cis-form of DCNQI during the time of diffusion ($t \approx (3.8 \pm 3.5) \cdot 10^{-2} s$). While a trans-isomer continues simply to diffuse on the terraces, a cis-DCNQI can meet others of the same kind and nucleate forming an RT-island or simply attach to existing RT islands. These are more stable due to the higher binding energy per molecule as seen in the gas phase calculations. As described before, the phase transition of the LT- to the RT-islands takes thus place in three steps: the detachment from the LT-phases, the diffusion on the terraces with a number of isomerization events and the attachment to an RT-island, because LT-islands are not stable at this temperature. The charge transfer plays in this process a fundamental role because by lowering the energy barrier for the isomerization, the transition probability is increased and DCNQI molecules can isomerize during the short time of diffusion and before meeting the next island. Therefore and because of the larger stability per molecule the RT-islands are already observed at a temperature of 245 K.

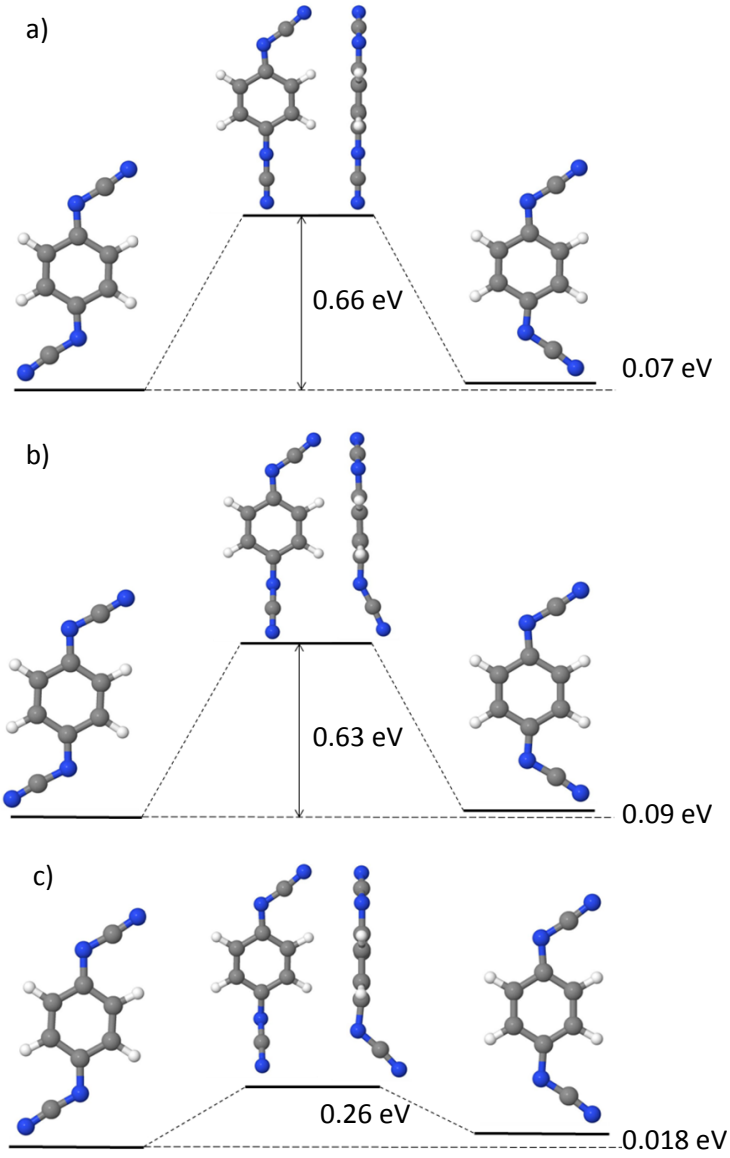

Figure 15: Representation of DFT calculations in gas phase of the trans-cis-transition: Shown are the geometries of the starting point of the transition of differently charged trans-DCNQI molecules, the transition state in the center of the figure and the final cis-state. The transition state reveals the mechanism of the isomerization reaction which take place in the uncharged specie through an inversion in contrast to the charged DCNQI molecules where an out of plane angle of the cyano-imine group is observed which reveals rotations of the functional group as part of the transition. The cis-form is always slightly higher in total energy than the trans-form. In **a)** the energy barrier difference for the neutral molecule of the transition state to the trans-state is 0.66 eV, very similar to the single charged DCNQI, **b)**. Only the dianion, in **c)**, has a noticeably lowered transition energy barrier of 0.26 eV.

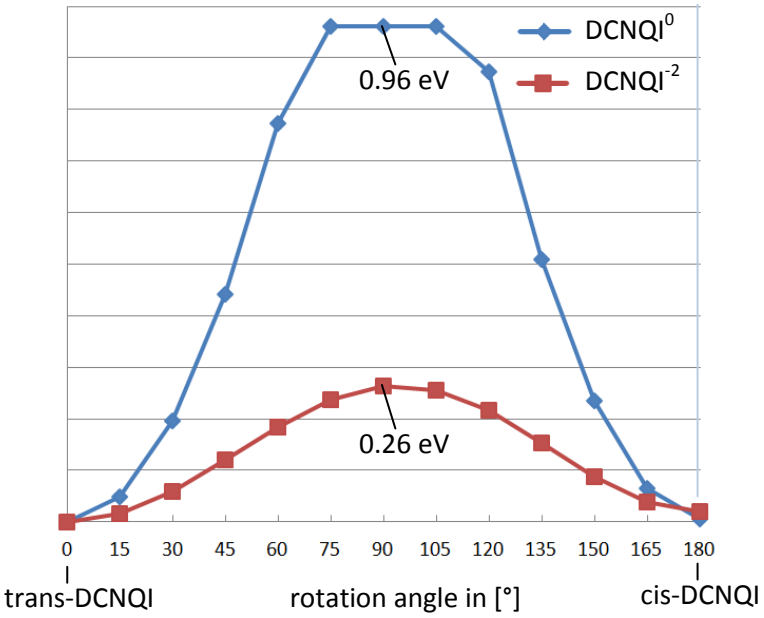

Figure 16: The total energy pathway for a forced transition by rotation of the cyano-imine group from the trans to the cis-isomer of DCNQI: The neutral form exhibits the clearly higher barrier with 0.96 eV compared to the one of the dianion-isomer (0.26 eV). This is because the isomerization does not take place by a rotation of the cyano-imine group, it is, as in literature, rather a inversion which leads to the transition from the trans- to the cis-form. In contrast to the dianion-form which isomerizes due to rotation and thus the energy barrier in both calculations is the same (transition state and forced rotation transition).

5.5 Conclusions

In conclusion, DCNQI, a molecule representative for a whole electron acceptor family has been proven to show an isomerization reaction on a rather reactive metallic surface different to Au(111). For that, the adsorption of DCNQI on Cu(100) has been studied with STM over a wide range of temperatures (145 – 440 K). Apart from a basically disordered cluster growth below 235 K, two types of islands with long range order have been identified. The one observed at lower growth temperatures, the LT-phase, starts to convert into the 1.39 times denser RT-phase at 245 K. The molecular units of the LT-islands have been identified as the trans-isomer of DCNQI by various structural arguments and STM image simulations. On the same basis, the RT-phase has been shown to consist of the cis-DCNQI. Calculations of the DCNQI-assembly without the substrate resemble well the experimental unit cells. These gas phase calculations reveal that in both island types, hydrogen bonds stabilize the structures but the binding energy per molecule in the RT-phase is 30 meV higher than in the LT-phase. As a negative charge transfer from the surface to the electron acceptor molecule is expected, similar to TCNQ, TCPQ and TCTQ, the bond configuration of DCNQI is probably affected, with the consequence of a higher flexibility which renders the rotation of the cyano-imine group around bond B3 less costly than in neutral molecules. Also gas phase calculations for the dianion identify the transition mechanism from the trans- to the cis-DCNQI as nearly pure rotation of the cyano-

imine group. In the neutral species the isomerization occurs via a pure inversion of the cyano-imine group with a larger energy barrier. The charge transfer is therefore the reason for the smaller transition barrier which thus increases the transition probability during the diffusion of the molecular units. Comparing the average time a molecule diffuses to the necessary time for an isomerization event, reveals that only the dianion form of DCNQI isomerizes before it interacts with another island due to its lowered transition energy barrier. Only in the case of the cis-isomer the interaction is large enough to form stable islands, due to formation of eight hydrogen bonds per molecule with the consequence of a higher binding energy per molecule. Thus the structure of the DCNQI islands is affected by the charge transfer which is fundamental for the lowering of the transition barrier and thus the accessibility to both isomers by thermal energy below RT. This knowledge can be applied in device architecture, for example, to tune the transition barriers of molecular switches. This opens up, on one hand, a whole family of organic molecules for the field of single molecular switches and on the other, it brings reactive types of surfaces back into the focus of possible electronic devices based on isomerization reactions. In summary, the causal connection between charge transfer and the isomerization reaction of DCNQI/Cu(100) has been described in detail as a further example of the consequences charge transfer might have.

5.6 Bibliography

References

1. Hüning, S. Aromatic/quinoid systems: principles and applicatios. *Pure & Appl. Chem.* **62**, 395-406 (1990).

2. Mori, T., Inokuchi, H., Kobayashi, A., Kato, R. & Kobayashi, H. Electrical conductivity, thermoelectric power, and ESR of a new family of molecular conductors, dicyanoquinonediimine-metal [(DCNQI)_{2}M] compounds. *Phys. Rev. B* **38**, 5913-5923 (1988).

3. Sinzger, K. *et al*. The organic metal (Me2-DCNQI)2Cu: Dramatic changes in solid-state properties and crystal structure due to secondary deuterium effects. *J. Am. Chem. Soc.* **115**, 7696-7705 (1993).

4. Kato, R., Kobayashi, H. & Kobayashi, A. Crystal and electronic structures of conductive anion-radical salts, (2,5-R1R2-DCNQI)2Cu (DCNQI = N,N'-dicyanoquinonediimine; R1, R2 = CH3, CH3O, Cl, Br). *J. Am. Chem. Soc.* **111**, 5224-5232 (1989).

5. Takahashi, T. *et al*. Magnetism of DCNQI-Cu salts. *Synth. Met.* **56**, 2281-2288 (1993).

6. Bryce, M. R. Recent progress on conducting organic charge-transfer salts. *Chem. Soc. Rev.* **20**, 355-390 (1991).

7. Gimzewski, J. K. & Joachim, C. Nanoscale Science of Single Molecules Using Local Probes. *Science* **283**, 1683-1688 (1999).

8. Feringa, B. L. & Browne, W. R. in *Molecular switches* (Wiley-VCH Verlag GmbH, 2001).

9. Alemani, M. *et al*. Electric Field-Induced Isomerization of Azobenzene by STM. *J. Am. Chem. Soc.* **128**, 14446-14447 (2006).

10. Morgenstern, K. Switching individual molecules by light and electrons: From isomerisation to chirality flip. *Prog Surf Sci* **86**, 115-161 (2011).

11. Dulic, D. *et al*. One-Way Optoelectronic Switching of Photochromic Molecules on Gold. *Phys. Rev. Lett.* **91**, 207402 (2003).

12. Alemani, M. *et al*. Adsorption and Switching Properties of Azobenzene Derivatives on Different Noble Metal Surfaces: Au(111), Cu(111), and Au(100). *J. Phys. Chem. C* **112**, 10509-10514 (2008).

13. Rohde, D., Yan, C., Yan, H. & Wan, L. From a Lamellar to Hexagonal Self-Assembly of Bis(4,4'-(m,m'-di(dodecyloxy)phenyl)-2,2'-difluoro-1,3,2-dioxaborin) Molecules: A trans-to-cis-Isomerization-Induced Structural Transition Studied with STM. *Angewandte Chemie International Edition* **45**, 3996-4000 (2006).

14. Riedel, D. *et al*. Surface-Isomerization Dynamics of trans-Stilbene Molecules Adsorbed on Si(100)-2x1. *J. Am. Chem. Soc.* **131**, 5414-5423 (2009).

15. Miwa, J. A. *et al*. Azobenzene on Cu(110): Adsorption Site-Dependent Diffusion. *J. Am. Chem. Soc.* **128**, 3164-3165 (2006).

16. Vanoppen, P. *et al*. Solvent Codeposition and Cis-Trans Isomerization of Isophthalic Acid Derivatives Studied by STM. *J. Phys. Chem.* **100**, 19636-19641 (1996).

17. Feng, C. L. *et al*. Completely interfacial photoisomerization of 4-hydroxy-3′-trifluoromethyl-azobenzene studied by STM on HOPG. *Surf. Sci.* **513**, 111-118 (2002).

18. Choi, B. *et al*. Conformational Molecular Switch of the Azobenzene Molecule: A Scanning Tunneling Microscopy Study. *Phys. Rev. Lett.* **96**, 156106 (2006).

19. Morgenstern, K. Isomerization Reactions on Single Adsorbed Molecules. *Acc. Chem. Res.* **42**, 213-223 (2009).

20. Safiei, A., Henzl, J. & Morgenstern, K. Isomerization of an Azobenzene Derivative on a Thin Insulating Layer by Inelastically Tunneling Electrons. *Phys. Rev. Lett.* **104**, 216102 (2010).

21. Óvári, L., Wolf, M. & Tegeder, P. Reversible Changes in the Vibrational Structure of Tetra-tert-butylazobenzene on a Au(111) Surface Induced by Light and Thermal Activation. *J. Phys. Chem. C* **111**, 15370-15374 (2007).

22. Mielke, J. *et al*. Imine Derivatives on Au(111): Evidence for "Inverted" Thermal Isomerization. *ACS Nano* **5**, 2090-2097 (2011).

23. Bellec, A. *et al*. Distinguishing Different Isomers of the Photochromic CMTE Molecule on the Si(100) Surface Studied by STM. *J. Phys. Chem. C* **111**, 14818-14822 (2007).

24. Cossío, F. P. *et al*. Determination of syn/anti Isomerism in DCNQI Derivatives by 2D Exchange Spectroscopy: Theoretical Underpinning. *European Journal of Organic Chemistry* **2000**, 2407-2415 (2000).

25. Bazarnik, M., Henzl, J., Czajka, R. & Morgenstern, K. Light driven reactions of single physisorbed azobenzenes. *Chem. Commun.* **47**, 7764-7766 (2011).

26. Gálvez, J. & Guirado, A. A theoretical study of topomerization of imine systems: Inversion, rotation or mixed mechanisms? *Journal of Computational Chemistry* **31**, 520-531 (2010).

27. Eliel, E., Wilen, S. H. & Mander, L. N. Stereochemistry of Organic Compounds. , 550-555 (1994).

28. Aumüller, A. & Hünig, S. Multistep Reversible Redox Systems, XLVI N,N'-Dicyanoquinonediimines - A New Class of Compounds, I: Synthesis and General Properties. *Liebigs Ann. Chem.* **1986**, 142-164 (1986).

29. Brune, H. Microscopic view of epitaxial metal growth: nucleation and aggregation. *Surface Science Reports* **31**, 125-229 (1998).

30. Erk, P. *et al*. Reversible Redox Systems, LXII. 2,3-Disubstituted 1,4-Benzoquinones and Their N,N?-dicyanimines: Syntheses, Physical Properties, and CT Complexes with TTF. *Liebigs Annalen* **1997**, 1235-1243 (1997).

31. Hünig, S. *et al*. 2,5-Disubstituted N, N'-Dicyanoquinone Diimines (DCNQIs) - Syntheses and Redox Properties. *European Journal of Organic Chemistry* **1998**, 335-348 (1998).

32. Hünig, S. *et al*. Tethered 1,4-Benzoquinones and Their DCNQI Derivatives: Syntheses, Electronic Interactions, Redox Properties, Charge-Transfer Complexes, and Copper Salts. *European Journal of Organic Chemistry* **1998**, 1977-1988 (1998).

33. Martín, N. *et al*. Synthesis, Characterization, and Theoretical Study of Sulfur-Containing Donor-Acceptor DCNQI Derivatives with Photoinduced Intramolecular Electron Transfer. *J. Org. Chem.* **61**, 3041-3054 (1996).

34. Eyring, H. The Activated Complex in Chemical Reactions. *J. Chem. Phys.* **3**, 107 (1935).

35. George H., V. Frequency factors and isotope effects in solid state rate processes. *Journal of Physics and Chemistry of Solids* **3**, 121-127 (1957).

6 General conclusions

Four different organic electron acceptor molecules have been deposited on Cu(100) and investigated with variable temperature STM, XPS and XAS in combination with sophisticated theoretical support.

In all four different systems charge transfer has been identified as a driving force with very different consequences. A causal link has been established between charge transfer and several effects, like substrate reconstruction that controls molecular self assembly, the increased chemical reactivity and the resulting covalent polymerization, and the lowering of the energy barrier between the trans- and cis-isomers of a molecule with the consequence of the activation of an isomerization reaction by thermal energy below RT.

For the investigated molecules, all which belong to the TCNQ family, the charge transfer in all cases results in an increased conformational freedom, that has a number of different consequences depending on the specifics of the molecules under consideration. i) In the case of TCNQ, a stronger interaction with the substrate which is therefore distorted, mediates the island assembly of the adsorbates. ii) The charge transfer in the TCTQ and TCPQ cases enables the rotation of the dicyanomethylene groups which makes the two upper cyano groups to detach from the molecular backbone when annealing the sample. The remaining radicals react then with each other and form polymer chains. iii) The higher flexibility of the cyano-imine group in DCNQI due to charge transfer allows the isomerization from the trans-isomer to the cis-isomer by rotation instead of inversion as transition mechanism which exhibits a lower energy barrier that can be overcome by thermal energy around 20 meV. A probability for isomeization several orders of magnitude higher is the result of the charge transfer.

All these consequences of charge transfer change the role of the surface in organic-metal systems. If a charge transfer is likely to occur, the mentioned effects have to be taken into account and they may be used to control the desired properties of potential applications. The results of the studied systems affect the general understanding of organic-metal interfaces and future investigations have to consider our results about ultrathin acceptors on metal surface.